

International Workshop on Beam Cooling and Related Topics

8th – 13th October 2023

Royal Plaza Hotel

Montreux, Switzerland



PROCEEDINGS

The 14th International Workshop on Beam Cooling and Related Topics, COOL'23 returns as an in-person meeting in the beautiful lakeside town of Montreux, Switzerland.

The workshop will highlight the latest developments in the field of particle beam cooling, including the following topics:

- Electron cooling
- Stochastic cooling
- Laser cooling
- Muon cooling
- Ionization cooling
- Existing and future facilities
- Storage and cooling of particles in traps
- Other methods of phase space manipulation
- Cooled beam dynamics

Local Organising Committee:

Madeleine Catin (Secretary)

Alexandre Frassier

Ghanshyambhai Khatri

Lars Varming Joergensen

Gerard Alain Tranquille (Chair)





Preface
Photo

Preface

The 14th International Workshop on Beam Cooling and Related Topics, COOL'23, was hosted by CERN, the European Laboratory for Particle Physics, from the 8th to the 13th of October 2023. It was the first in-person meeting of the beam cooling community in four years due to the covid-19 pandemic and was held on the shores of Lake Geneva at the Royal Plaza Hotel in Montreux.

Due to the difficult geopolitical and economic situation, the organisation of the workshop proved to be very challenging. Nevertheless, it was attended by nearly fifty participants from countries in Europe, America, and Asia. Twenty-nine oral contributions were presented in sessions covering all aspects of particle beam cooling including status reports from existing and planned facilities. In the dedicated poster session on the Thursday afternoon, eighteen posters were displayed enabling the participants to further discuss recent advances and new techniques. The workshop concluded on Friday with a special lecture entitled "Fundamental Physics with Antihydrogen" given by Professor Geoffrey Hangst of Aarhus University.

As is custom since COOL'13, the Dieter Möhl medal was awarded to our colleagues who have made significant contributions to the field of beam cooling. This year five awards were given, two for early-stage researchers and three for lifetime achievements.

The scientific program was complemented with several social events to enable the participants to fully appreciate the Montreux Riviera region. A boat trip on the lake with wine tasting accompanied with local specialities concluded the first day of the workshop. An afternoon excursion to the Rochers-de-Naye was organised on Wednesday with spectacular views of the Alpes extending beyond the Bernese Oberland. The workshop banquet took place on the final evening and, for the first time, prizes for the three best poster contributions were awarded.

The organisers are grateful to the staff of the Royal Plaza Hotel and to the Montreux Tourist Office for their help in ensuring the success of the workshop.

Special thanks should be given to the conference secretary Madeleine Catin and to the local organising committee members; Alexandre Frassier, Lars Joergensen and Gunn Khatri, who prepared and managed the workshop with high efficiency and great enthusiasm. A special mention to our editors Christine Petit-Jean Genaz, and Volker RW Schaa for the publication of the workshop in the JACOW system and for their exceptional editorial work.

Finally, we would like to express our sincere appreciation to all the participants for their active participation in this workshop.

The next COOL workshop will be held in 2025 in the United States of America under the auspices of Stony Brook University in New York state. We look forward to seeing you there!

G rard Alain Tranquille
COOL'23 chairman

International Advisory Committee (IAC)

Toshiyuki Azuma	RIKEN	Japan
Alexei Fedotov	BNL	USA
Jürgen Dietrich	Univ. Dortmund	Germany
Takeshi Katayama	Nihon University	Japan
Vladimir Litvinenko	Stony Brook Univ.	USA
Sergei Nagaitsev	JLab	USA
Dieter Prasuhn	FZ Jülich	Germany
Markus Steck	GSI	Germany
Gérard Tranquille	CERN	Switzerland
Masanori Wakasugi	RIKEN	Japan
Andreas Wolf	MPI Heidelberg	Germany
Xiaodong Yang	IMP Lanzhou	China
Katsuya Yonehara	FNAL	USA

Local Organizing Committee (LOC)

Madeleine Catin	CERN	Switzerland
Alexandre Frassier	CERN	Switzerland
Ghanshyambhai Khatri	CERN	Switzerland
Lars Varming Jørgensen	CERN	Switzerland
Gérard Alain Tranquille	CERN	Switzerland

JACoW Editorial Team (JET)

Zhichu Chen	SARI	China
Christine Petit-Jean-Genaz	CERN	Switzerland
Michaela Marx	DESY	Germany
Volker RW Schaa	GSI	Germany

JACoW Editorial Board (JEB)

Gérard Alain Tranquille	CERN	Switzerland
Christine Petit-Jean-Genaz	CERN	Switzerland
Lars Varming Jørgensen	CERN	Switzerland
Volker RW Schaa	GSI	Germany

Contents

Preface	i
Foreword	iii
Committees	iv
Contents	v
Papers	1
MOPAM2R1 – Accelerator Physics Requirements for Electron Cooler at the EIC Injection Energy	1
MOPPM1R3 – Specifications and Status of the New Electron Cooler for the CERN Antiproton Decelerator (AD)	5
TUPAM1R3 – Dynamic Aperture and Frequency Analysis in ELENA with Electron Cooler Magnetic Field Included	11
TUPAM2R1 – Status of Beam Instrumentation at the Electron Beam Test Stand at CERN	16
TUPPM1R2 – Development of Stochastic Cooling Components for HIAF Spectrometer Ring	22
TUPPM1R3 – Numerical Study of the Wiggler-Based Microbunching Amplifier for EIC	26
WEPAM2R1 – Self Bunching, RF Bunching and Cooling of Ions in an Electrostatic Ion Beam Trap	29
THPAM1R1 – Theoretical and Simulation Study of Dispersive Electron Cooling	32
THPAM1R2 – Sustaining Competences for Electron Cooling at HESR	37
THPAM1R3 – Status of E-Cooling Characterisation at 100 keV in ELENA	40
THPOSRP01 – Influences of the Longitudinal Shift of the Electron Bunch to the Longitudinal Cooling Rate	46
THPOSRP02 – Advancements and Applications of Cooling Simulation Tools: A Focus on Xsuite	49
THPOSRP03 – Influences of Beam Parameters on the Interaction Between Ion and Electron Beams	54
THPOSRP04 – Explicit Expressions for Non-Magnetized Bunched Electron Cooling	58
THPOSRP06 – A Test Bench for Characterizing Electron Cooler Components at up to -80 kVDC	61
THPOSRP07 – An Optimized Delay Line with Temperature Compensation	65
THPOSRP09 – H0 Diagnostics for the ELENA Electron Cooler	68
THPOSRP10 – Development of a Field Emission Electron Gun for Low Energy Electron Cooling	72
THPOSRP13 – Investigation of Ion Trapping and Beam-Induced Fluorescence at the Electron Cooler Test-Bench at HIM	76
THPOSRP14 – JSPEC: A Program for IBS and Electron Cooling Simulation	79
THPOSRP15 – Influence of Energy Shift of Electron Beam on the Electron Cooling in EicC	83
THPOSRP17 – Development of an ERL for Coherent Electron Cooling at the Electron-Ion Collider	87
THPOSRP18 – Simulation Study of a Multi-Stage Rectilinear Channel for Muon Cooling	91
THPOSRP20 – Beam Measurements of a Palmer Pick-up for the Collector Ring of FAIR	95
THPOSRP21 – How to Adjust Stochastic Cooling Systems	98
THPOSRP22 – Experience with Beam Transfer Function Measurements for Setting-up the Stochastic Cooling System in the CERN Anti-Proton Decelerator (AD)	102
THPOSRP23 – Kicker for the CR Stochastic Cooling System Based on HESR Slot-Ring Coupler	106
FRPAM1R2 – Electron Cooling in NICA Acceleration Complex	109
FRPAM1R3 – Experiments on Electron Cooling and Intense Space-Charge at IOTA	114
Appendices	121
List of Authors	121
List of Institutes	124

ACCELERATOR PHYSICS REQUIREMENTS FOR ELECTRON COOLER AT THE EIC INJECTION ENERGY*

A.V. Fedotov[#], D. Kayran, S. Seletskiy
Brookhaven National Laboratory, Upton, NY, U.S.A.

Abstract

An electron cooler using RF-accelerated electron beam is presently under design to provide required cooling of protons at the EIC injection energy of 24 GeV. In this paper, we describe accelerator physics requirements and design considerations of such 13 MeV electron cooler, including associated challenges.

INTRODUCTION

The Electron-Ion Collider (EIC) is a partnership project between Brookhaven National Laboratory (BNL) and Thomas Jefferson National Accelerator Facility (TJNAF) to be constructed at BNL, using much of the existing infrastructure of the Relativistic Heavy Ion Collider (RHIC); a layout of the EIC is shown in Fig. 1. Collisions occur between the hadrons in the Hadron Storage Ring (HSR) and the electrons supplied by the Electron Storage Ring (ESR), in order to maintain a high average polarization of the ESR, bunches are frequently replaced using the Rapid Cycling Synchrotron (RCS) [1].

In order to achieve the design emittances of the hadron beam, hadron beams are injected into the HSR and pre-cooled to the target emittances at injection energy of protons of 24 GeV. After the target emittances are achieved, the HSR is ramped to the collision energy, and the hadron beam is cooled during collision using high-energy cooling system. Several options of such high-energy cooling system, based on Coherent Electron Cooling (CeC) [2, 3] and on Electron Cooling using storage ring [4-6], are being considered.

Precooling of protons at 24 GeV will be done using conventional electron cooling technique which requires 13 MeV electron accelerator. The design of such a Pre-cooler is based on RF-accelerated electron bunches, similar to LEReC [7], but scaled to higher energy. The Pre-cooler energy can be extended to 22 MeV to provide cooling of protons at collision energy of 41 GeV.

COOLER REQUIREMENTS

The Precooler design is based on the non-magnetized cooling approach with zero magnetic field on the cathode and no magnetic field in the cooling region [7].

The friction force acting on the ion with charge number Z inside a non-magnetized electron beam with velocity distribution function $f(v_e)$ is

$$\vec{F} = -\frac{4\pi n_e e^4 Z^2}{m} \int \ln\left(\frac{\rho_{\max}}{\rho_{\min}}\right) \frac{\vec{V}_i - \vec{v}_e}{|\vec{V}_i - \vec{v}_e|^3} f(v_e) d^3 v_e, \quad (1)$$

where e and m are the electron charge and mass, V and v_e are the ion and electron velocities respectively, and n_e is electron density in the particle rest frame (PRF).

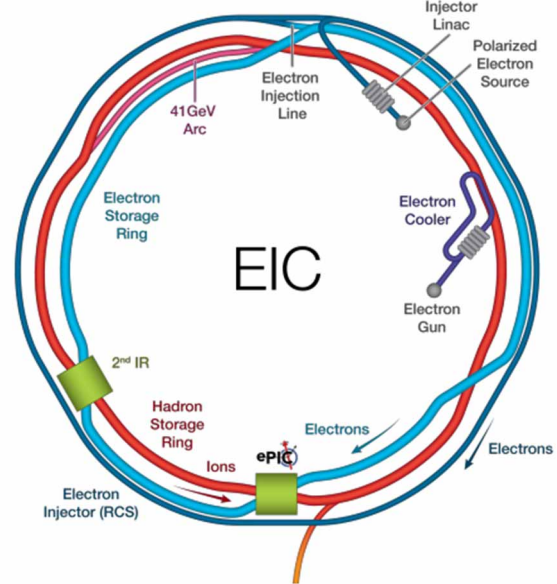


Figure 1: The layout of the Electron-Ion Collider (EIC). The Hadron Storage Ring (HSR), Electron Storage Ring (ESR), and the Rapid Cycling Synchrotron (RCS) labels are color-coded to their respective rings; the current and proposed IRs are shown at IR6 and IR8, with both Pre-cooler and high-energy cooling systems located in IR2.

As cooling of protons ($Z=1$) is the most challenging task compared to cooling of heavy ions, in this report we focus on cooler parameters considering only proton beams.

To maximize the cooling power and to preserve transverse distribution of hadrons under cooling, the electron beam rms velocity spreads are chosen close to those of the hadron beam. At injection energy in the EIC with $\gamma=25.4$, the proton beam with bunch intensities $N=2.8 \times 10^{11}$ will have rms longitudinal momentum spread of about $\sigma_p=5-6 \times 10^{-4}$. This sets the requirement for the rms momentum spread of electron beam $< 5 \times 10^{-4}$. For the rms normalized emittance of the proton beam around $2 \mu\text{m}$ and 200 m beta function in the cooling section, the hadron beam rms angular spread in the lab frame is 0.02 mrad. This gives the requirement for the electrons angular spread θ in the cooling section around 0.02 mrad (as presented in Table 1).

*Work supported by the US Department of Energy under contract No. DE-AC02-98CH10886.
#fedotov@bnl.gov

Table 1: Electron Beam Parameters in the Cooling Section

Electrons kinetic energy, MeV	12.5
Charge per single electron bunch, nC	1.3-2
Number of bunches in macrobunch	2-3
Total charge in macrobunch, nC	4
Average current, mA	98
RMS normalized emittance, μm	< 1.5
Angular spread, μrad	< 25
RMS energy spread	$< 5 \times 10^{-4}$
RMS bunch length, cm	5
Beta function, m	150
Length of cooling sections, m	120

With the friction force maximum being located close to the longitudinal rms velocity spread of the electrons, one gets a requirement for matching electron and beam energies to better than the rms velocity spread, which for our parameters is about 3×10^{-4} . Energy stability of the electron beam should be better than this, at about 1×10^{-4} rms.

The largest contributions to the angles in the cooling section come from the electron beam emittance and the space charge of electron and proton beams. In addition, to keep the transverse angle of the electron beam trajectory $< 10 \mu\text{rad}$ an integral of residual transverse magnetic field in cooling region should be kept below 1 Gauss $\cdot\text{cm}$. A shielding of residual magnetic field to such level will be provided by several concentric cylindrical layers of high permeability alloy [8]. Some cooling section space will be taken up by short solenoids (to control angular spread due to the transverse space charge of electron beam), steering dipoles and beam position monitors to keep the electron and ion beam in close relative alignment.

In simulations shown in Fig. 2, we assumed the total angular spread of the electrons in the cooling section to be $20 \mu\text{rad}$. Both horizontal and vertical emittances are being cooled to slightly different values due to different IBS rates in the two planes. For IBS calculations we assumed single harmonic RF with Gaussian proton bunches and uncoupled betatron motion so that IBS in the vertical plane is minimized. Presently, a plan is to provide cooling in both transverse planes simultaneously until lifetime of cooled protons becomes affected by the space charge. The cooled proton beam with small emittances in both planes will then be accelerated to the top energy at which the horizontal emittance can be increased to a required level.

The goal of precooling is to provide strong cooling in the vertical plane only. Using 24.6 MHz RF for protons at injection energy allows us to have long bunch length, around 0.8 m rms. However, even for long proton bunches, the space charge for the protons could become very large due to cooling of beam emittances which would affect protons lifetime.

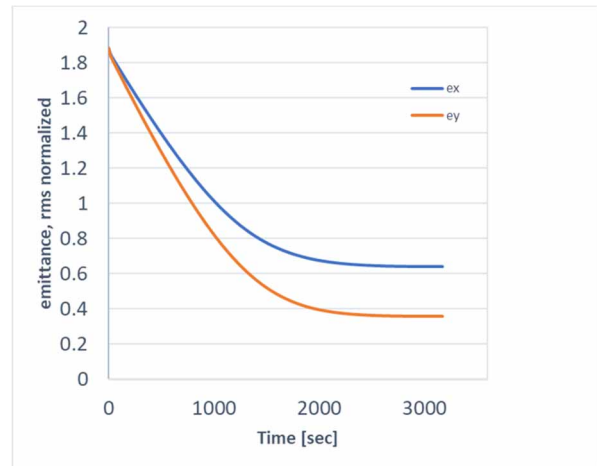


Figure 2: Cooling of protons at $\gamma=25.4$, with decoupled transverse motion (simulations with IBS, using single harmonic RF, and cooling only). Horizontal emittance (top curve, blue) and vertical emittance (bottom curve, orange).

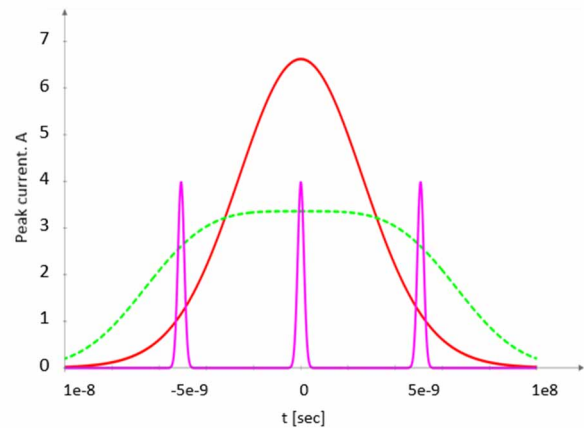


Figure 3: Three electron bunches (magenta) spaced by 5.1 ns placed on a single proton bunch (red: single RF harmonic; green: double RF harmonic).

To mitigate space-charge effects during cooling, one can provide heating of emittance in the horizontal plane while cooling in the vertical plane, however this will slow down vertical cooling due to large horizontal angles [9]. Instead, space charge for cooled protons bunches could be alleviated using second harmonic RF which allows us to produce flattened distribution of proton bunches (green curve in Fig. 3) with peak current reduced by a factor of two compared to a single harmonic RF (red curve in Fig. 3). A similar approach was used during RHIC operation at low energies with electron cooler LEReC [10]. With the second harmonic RF (peak current of 3.35 A) for proton beam emittances at the end of cooling shown in Fig. 2, space-charge tune shifts for proton beam are estimated to be 0.06 and 0.11, for the horizontal and vertical planes, respectively. For flattened protons bunches with second harmonic RF, IBS will be reduced as well due to reduced peak current. As a result, one should be able to provide even stronger cooling than shown in Fig. 2 (where single harmonic RF was assumed) if the space charge of protons bunches can be mitigated further.

ELECTRON ACCELERATOR

Electron beam will be generated by illuminating a multi-alkali CsK₂Sb photocathode with green light (532 nm) from a laser. The photocathode is inserted into a DC gun with design operational voltage of around 400 kV. The 197 MHz laser will produce bunch trains with individual electron bunches of about 500 ps full length at 24.6 MHz bunch train repetition frequency. The bunch train repetition rate will be the same as the repetition rate of proton bunches in the HSR at injection energy.

After the gun, an electron beam is first accelerated in 3 MeV injector and then merged into the 197 MHz linac and accelerated to final energy of 13 MeV. Simulations of electron beam dynamics show that required electron beam parameters can be obtained at the end of 13 MeV linac for electron bunches with 2 nC charge, Figs. 4-5.

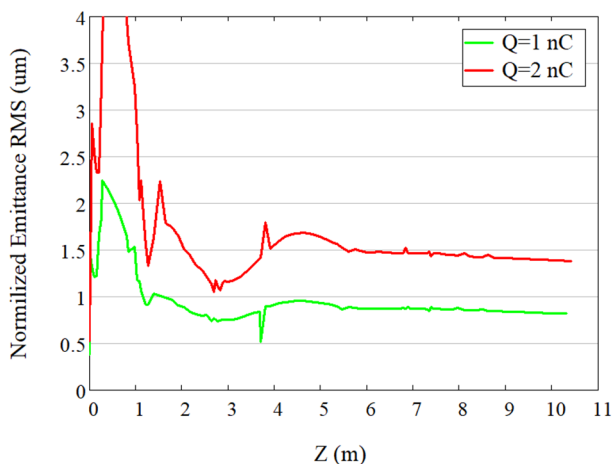


Figure 4: Simulated emittance for electron bunch charges of 1 and 2 nC at the end of 13 MeV linac.

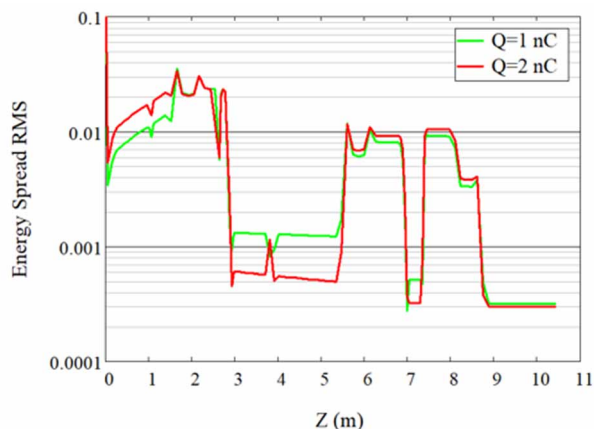


Figure 5: Simulated energy spread for electron bunch charges of 1 and 2 nC at the end of 13 MeV linac.

The 197 MHz repetition rate of electron bunches, corresponding to 5.1 ns spacing, allows us to place either two electron bunches with 2 nC charge each or three electron bunches with 1.33 nC charge (as shown in Fig. 3) on a single proton bunch to provide total required charge of electrons of 4 nC per proton bunch. Simulations shown in Figs. 4-5 include main 197 MHz RF and 3rd harmonic RF

for energy correction. Adding higher RF harmonic cavity (9th harmonic of 197 MHz) could allow us to operate with longer electron bunches and achieve even better electron beam parameters. The corresponding optimization is presently in progress.

After acceleration to 13 MeV, an electron beam is transported to the first cooling section in the HSR ring, cools protons in the first cooling section, separated from hadrons after the first cooling section to bypass hadron beam chicane (required for high-energy cooler based on the CeC), transported and merged again with the protons in the second cooling sections, turned around and transported to the beam dump. Present integration of injection energy Precooler with high-energy cooler based on the CeC is reported in [11].

Design of electron beam optics in the mergers and cooling sections is ongoing and aims to provide largest space available for effective cooling and to minimize contribution to electron angles from the space charge of electrons.

CHALLENGES

Presently, maximum available space for the cooling sections is limited to about 120 m total length due to integration of Precooler with the high-energy cooler based on the CeC approach. This requires CW operation of Precooler electron accelerator with high beam current of up to 98 mA. If length of cooling section can be increased, for example to 180 m, as in the design assumed in [4-6], required current for Precooler can be decreased to about 65 mA.

The easiest operation of Precooler would be similar to LEReC, sending electron beam after cooling sections directly to a beam dump without energy recovery. If electron beam, after interaction with protons in two cooling sections and with resulting large tails in beam distribution due to the space charge, needs to go through return beam line for energy recovery in the linac, it would require special consideration of collimation of the tails of beam distribution.

The attainment of required low energy spread in the electron bunch relies on RF gymnastics. A tight requirement on impedance budget requires detailed wake fields simulations and special design of every vacuum element including instrumentation devices. The repeatability of low energy electron transport is challenging due to remnant fields in the optics and hardware. Quality of electron beam should be preserved through the entire beam transport since the same beam will be used in two cooling sections of the HSR.

The achievement of very low transverse angular spread for the electron beam should be addressed by a proper beam transport and engineering design of the cooling sections. The required electron angles in cooling section are about factor of five smaller than achieved in LEReC.

Integration of 13 MeV Precooler with high-energy cooler based on the CeC approach adds additional constraints: 1) limited space for effective cooling, 2) additional merges and optics matching section due to split into two separate cooling sections, 3) finding proper solution

for mu-metal shielding of cooling sections with many magnetic elements. These challenges are presently being addressed by optimization of Precooler and high-energy cooler parameters.

SUMMARY

Electron cooler based on the RF acceleration of electron bunches is being developed to provide cooling of protons at the EIC injection energy of 24 GeV. Various challenges are being addressed by a proper physics and engineering design.

ACKNOWLEDGMENTS

We would like to thank members of the EIC team at Brookhaven and Jefferson Laboratories and members of the Collider-Accelerator Department Beam Cooling group. Special thanks to Erdong Wang and Sergei Nagaitsev for many useful discussions and help.

REFERENCES

- [1] C. Montag *et al.*, “Design status of the Electron-Ion Collider”, in *Proc. IPAC’23*, Venice, Italy, May 2023, pp. 136-139. doi:10.18429/JACoW-IPAC2023-MOPA049J
- [2] E. Wang *et al.*, “The Accelerator Design Progress for EIC-Strong Hadron Cooling”, in *Proc. IPAC’21*, Campinas, SP, Brazil, May 2021, pp. 1424–1427. doi:10.18429/JACoW-IPAC2021-TUPAB036
- [3] C. Gulliford *et al.*, “Design and optimization of an ERL for cooling EIC hadron beams”, in *Proc. IPAC’23*, Venice, Italy, May 2023, pp. 73-76. doi:10.18429/JACoW-IPAC2023-MOPA016
- [4] H. Zhao, J. Kewisch, M. Blaskiewicz, and A. Fedotov, “Ring-based electron cooler for high energy beam cooling”, *Phys. Rev. Accel. Beams*, vol. 24, p. 043501, 2021. doi:10.1103/PhysRevAccelBeams.24.043501
- [5] J. Kewisch *et al.*, “Optics for an electron cooler for the EIC based on electron storage ring”, presented at FLS’23, Luzern, Switzerland, Aug. 2023, paper WE4P24, to be published.
- [6] S. Seletskiy, A. Fedotov, J. Kewisch, “Parameters optimization for EIC ring cooler”, presented at COOL’23, Montreux, Switzerland, Oct. 2023, paper WEPAM1R1, this conference.
- [7] A.V. Fedotov *et al.*, “Accelerator Physics Design Requirements and Challenges of RF Based Electron Cooler LEReC”, in *Proc. NAPAC’16*, Chicago, IL, USA, Oct. 2016, pp. 867–869. doi:10.18429/JACoW-NAPAC2016-WEA4C005
- [8] S. Seletskiy *et al.*, “Magnetic Shielding of LEReC Cooling Section”, in *Proc. NAPAC’16*, Chicago, IL, USA, Oct. 2016, pp. 1030–1032. doi:10.18429/JACoW-NAPAC2016-WEPOB61
- [9] S. Seletskiy and A. Fedotov, “Explicit expressions for non-magnetized bunched electron cooling”, presented at COOL’23, Montreux, Switzerland, Oct. 2023, paper THPOSRP04, this conference.
- [10] C. Liu *et al.*, “Gold-gold luminosity increase in RHIC for a beam energy scan with colliding beam energies extending below the nominal injection energy”, *Phys. Rev. Accel. Beams*, vol. 25, p. 051001, May 2022. doi:10.1103/PhysRevAccelBeams.25.051001
- [11] K.E. Deitrick *et al.*, “Development of an ERL for coherent electron cooling at the Electron-Ion Collider”, presented at COOL’23, Montreux, Switzerland, Oct. 2023, paper THPOSRP17, this conference.

SPECIFICATIONS AND STATUS OF THE NEW ELECTRON COOLER FOR THE CERN ANTIPROTON DECELERATOR (AD)

A. Rossi*, C. Accettura, W. Andreazza, A. Bollazzi, C. Castro Sequeiro, J. Cenede, N. Chritin, Y. Coutron, A. Frassier, G. Khatri, D. Gamba, L. Joergensen, C. Machado, O. Marquversen, L. Ponce, A. Pikin, J. A. Ferreira Somoza, M. Sameed, Y. Thurel, A. Sinturel, T. Todorovic, G. Tranquille, L. von Freeden, CERN, Geneva, Switzerland

Abstract

A new electron cooler for the Antiproton Decelerator (AD) is being designed at CERN, and will replace the current device (in operation for more than 40 years), during the next Long Shutdown (2026-2028). The functional specifications, recalled in this paper, favour high reliability, with improved performance in terms of time of cooling, obtained mainly with better field quality and possibly higher electron beam current. The status of the new electron cooler design is presented, showing an evolution that aims at easing integration, installation and maintenance.

INTRODUCTION

The AD (Antiproton Decelerator) ring decelerates antiprotons (\bar{p}) from 3.5 GeV/c to 100 MeV/c which are then injected into the ELENA (Extra Low ENergy Antiproton) ring. To counteract beam blow up during deceleration, stochastic cooling and electron cooling are carried out during the AD cycle, with electron cooling operating at 300 and 100 MeV/c momentum of the circulating beam [1]. While the AD ring has been operating since the year 2000, the current electron cooler is around 40 years old, being recovered from the Low Energy Antiproton Ring (1982-1997) [2]. The magnets are even older and the companies who produced them no longer exist. A replacement for the electron cooler is therefore envisaged, in the frame of the Consolidation Project at CERN. The new device aims at a high reliability, by design and robustness of the ancillary equipment. Moreover, it is expected to have improved performance in terms of time of cooling, mainly obtained by limiting the electron transverse and longitudinal temperature and switching on/off the electron beam during the energy ramps, as described in the following. In this paper we give the main parameters of design of the new cooler, explaining the technical choices implemented as an evolution of what was presented in [3]. A brief overview of planning for installation will also be given.

SPECIFICATIONS FOR THE NEW ELECTRON COOLER

The specifications [4] for the new electron cooler are listed in Table 1 where the main design parameters are compared to the one of the presently installed electron cooler, with blue font highlighting the main differences. The cooling will act at the same momentum plateaux as for the current AD cycle,

* adriana.rossi@cern.ch

Table 1: Main Parameters of the Present and New E-Cooler

	Present	This Spec.
Gun:		
Magnetic field [T]	0.06	0.24 †
Perveance [$\mu\text{AV}^{2/3}$]	0.58	2.5
Cathode radius [mm]	25	12.5
Toroid:		
Magnetic field [T]	0.06	0.06
Angle ϕ_0 [rad]	0.6283	0.6283
Radius r_{tor} [m]	1.133	1.133
Integrated \perp field [T·m]	~ 0.016	≤ 0.016
Cooling region:		
Vacuum pressure [mbar]	$\sim 10^{-10}$	$< 10^{-10}$
Length [m]	< 1	~ 1
Radius [mm]	25	≥ 25
Magnetic field [T]	0.06	0.06
$(B_{\perp}/B_{\parallel})_{\text{max}}$	10^{-3}	10^{-4}
$(B_{\perp}/B_{\parallel})_{\text{rms}}$	n.a.	$< 10^{-4}$
$e^- k_B T_{\perp}$ [meV]	100	≤ 100
$e^- k_B T_{\parallel}$ [meV]	—	≤ 1
$r_{e\text{-beam}}$ [mm]	—	up to 25
E_{e^-} [keV]	2.9 _{100 MeV/c}	2.9 _{100 MeV/c}
	25.5 _{300 MeV/c}	25.5 _{300 MeV/c}
E_{e^-} resolution [eV]	1	0.1 _{2.9 keV}
	—	1 _{25.5 keV}
E_{e^-} stability [eV]	—	< 0.1 _{2.9 keV}
	—	< 1 _{25.5 keV}
e^- current I_0 [A]	2.4	2.4 nominal
	—	4.8 ultimate
Stability [$\Delta I/I_0$]	—	$\sim 10^{-4}$
Relative losses [$\delta I/I_0$]	—	$< 10^{-4}$
Max time to vary from 25.5 keV to 2.9 keV [s]	> 5	~ 1
e^- beam start/stop [s]	—	$\ll 1$
BPM relative e^-/\bar{p} accuracy [μm]	—	≤ 100
E-cooler availability	—	99%

† The main differences are highlighted in blue in the text

i.e. 300 and 100 MeV/c momentum of the circulating beam. In designing the new electron cooler, we tried to improve its performance and reduce the time of cooling, as well as guarantee good reliability. This is approached by trying to limit the transverse and longitudinal electron velocity

spreads, and reduce the angle between \vec{p} and e^- trajectories in the cooling region (see also [4]).

In the following, the technical choices taken to achieve the specified values are detailed.

TECHNICAL SPECIFICATION AND TYPOLOGY CHOICES

The main technological novelty for the new electron cooler will be the electron gun and collector.

Gun, Collector and High Voltage Powering

The first design for the new electron cooler thermionic gun was presented in [3]. In a thermionic gun the minimum electron transverse temperature at the gun will be determined by the temperature of the cathode, which, for the types of cathode material employed will be around 1000 °C, corresponding to ~ 0.1 eV. The design is based on simulations [5], showing that a flat cathode geometry would be best to emit as uniformly as possible and with a limited transverse e^- energy as pictured in Fig. 1, which will depend on the magnetic field in which the gun is immersed. The shape of the electrodes was slightly modified (see also [3]), and modelled into COMSOL to check electrostatic and magnetic properties. The final 3D model and prototype are shown in Fig. 2. The estimated perveance of the gun is between 2.2 and 2.5 $\mu\text{AV}^{2/3}$; it follows that to extract 2.4 A (nominal) and 4.8 A (ultimate) electron current —as indicated in Table 1—the required grid-cathode (see Fig. 2) potential difference (V_{grid} in Fig. 3) will be ~ 11 kV and 17 kV, respectively. It should be noted that even if theoretically the time of cooling is inversely proportional to current, in practice electron space-charge and other effects in the cooling region might limit the electron beam transport efficiency and cooling performance, therefore, the optimal current value will be determined experimentally.

The presence of the grid allows to regulate current extraction and e^- velocity independently, and therefore to suppress the beam while ramping the cathode power supply. To reach the required e^- energies (namely 2.9 keV for cooling at 100 MeV/c and 25.5 keV for cooling at 300 MeV/c), the cathode to ground potential (V_k in in Fig. 3) of the present electron cooler is set to 3 kV and 27 kV, respectively. For the new electron cooler the power supply nominal rating is 30 kV. The actual values for operation will be evaluated experimentally. The whole High Voltage system, i.e. grid, collector pot and collector electrodes potentials are referred to the cathode potential, as shown in Fig. 3. This avoids dumping the whole e^- beam power to ground, thereby limiting the size of the power supplies required. Moreover, control of electron losses to ground is automatically done, since if the leakage current is larger than the limit current of the power supply, the HV system will switch off, preventing damage to the vacuum chambers¹. In the frame of consolidation and reliability improvement, all power supplies in

¹ Similarly, other interlocks on magnet cooling water temperature and vacuum will also stop the electron beam and avoid damage.

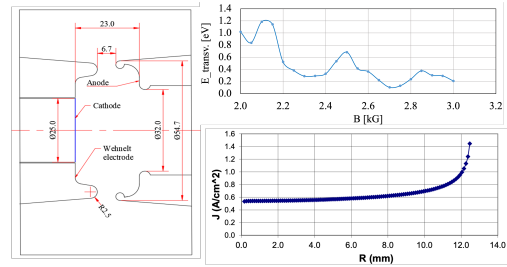


Figure 1: Top: Dependence of maximum transverse electron energy on magnetic field for electron gun with flat cathode and flat electrodes @ $I_{e^-} = 2.5$ A, $E_{e^-} = 27.0$ keV. Bottom: electron gun 2D design and radial distribution of the emission current density for a $r = 12.5$ mm cathode @ $I_{e^-} = 3.5$ A, $V_{\text{grid}} = 12.15$ keV.

the block diagram of Fig. 3 will be renewed, and provided with spares. The electron energy resolution and stability, and the subsequent requirements imposed upon the powering [6] were taken into account in the selection of the new equipment.

As a way to lower the transverse temperature of the electrons, the electron beam is going to be adiabatically expanded [7, 8] by a factor of two. The resulting transverse electron temperature and density after expansion are expected to be $T_{\perp} = T_{\text{cathode}} \frac{B_{\text{cool}}}{B_{\text{cathode}}}$ and $n_{\text{cool}} = n_{\text{cathode}} \frac{B_{\text{cool}}}{B_{\text{cathode}}}$. Given that in the cooling region the required electron beam radius is 25 mm, and the magnetic field is the same as the one of today's electron cooler, i.e. 0.06 T, this imposes a cathode radius of 12.5 mm and a gun solenoid (called *expansion solenoid*) field intensity of 0.24 T, as $r_{\text{cool}} = r_{\text{cathode}} \sqrt{\frac{B_{\text{cathode}}}{B_{\text{cool}}}}$. The actual cathode will be of 1" diameter (2.54 mm) from Spectra-Mat, Inc.

The gun prototype is presently under test: it passed the vacuum test, with an ultimate vacuum of 5×10^{-8} mbar without bake-out; a potential of 27 keV could be applied between both cathode and grid to ground and cathode to grid—with the cathode at room temperature, and no spark or problem was observed. The gun thermal tests, heating the cathode

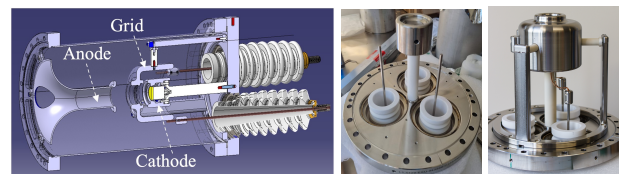


Figure 2: Left h.s.: 3D drawing of the new AD cooler electron gun. Middle: photos of the cathode mounted on the flange, and right: assembly cathode plus grid.

up to nominal and ultimate temperature, are also successfully completed, and the gun is now install in the test stand where current can be extracted and measured. As already described in [8], development for a new collector design started already after a water leak into the vacuum of the present collector. The design was made compatible with the

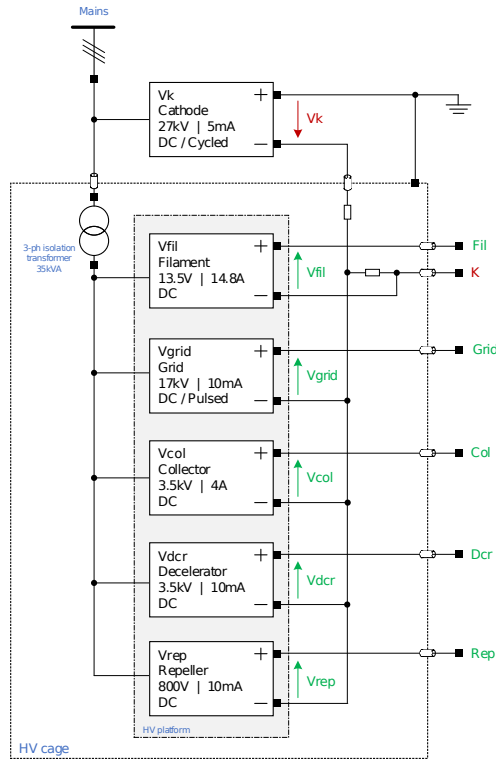


Figure 3: HV powering block diagram.



Figure 4: Collector 3D model (left) and prototype (right).

new electron cooler. A picture of the collector 3D design and the prototype built is shown in Fig. 4. The cooling water circuit runs only at the bottom of the collector. The collector features two electrodes, the first to slow down the e^- beam before hitting the collector pot, set at potential V_{dcr} in Fig. 3 ~ 3 kV difference from the cathode potential, the second to repel electrons that are reflected or desorbed at the collector pot surface, set at a potential V_{rep} in Fig. 3 close to the cathode potential (only ~ 800 V difference). This collector has already been tested for several days at 3 kV with a beam of 2 A DC, and the cooling water temperature increased by about 15°C . Further tests and calculations are to be carried out to validate the design to the maximum power to be absorbed (i.e. $3\text{ kV} \times 4.8\text{ A}$).

Magnetic System and Powering

To limit electron temperature heating and improve magnetised cooling time, the field quality in the cooling region solenoid is required to be $\leq 10^{-4}$, a value calculated the-

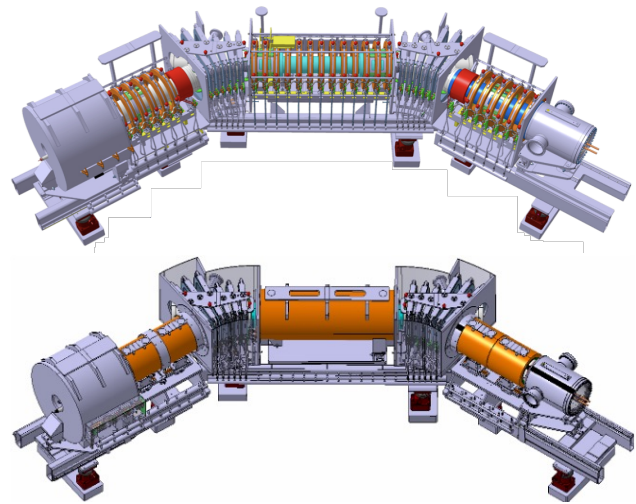


Figure 5: Pancake (top) and complete (bottom) magnetic system design. The ‘complete’ solenoid system has been chosen for the new design.

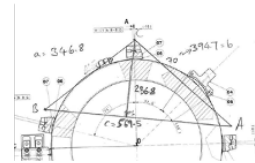


Figure 6: Pancake coil pivot supports.

oretically [4] and confirmed by experimental evidence by several experts around the world [9], observing a degradation of the cooling time when the field quality was worse than this value. It should be noted that the field quality measured for the present cooling region solenoid, before installation in LEAR, is in the order of 10^{-3} [10], which may partially justify why the cooling time at AD is about three times longer than initially foreseen [11]. Two different topologies, depicted in Fig. 5, have been analysed for the new AD cooler design; the first with a full pancake system as in [3] and the second with complete solenoids in the cooling region and the gun and collector arms. A comparison of performance of the two typologies in the cooling region was presented in [12]. The field quality in the pancake system (13 pancake coils) can be tuned by tilting the pancake coil around three pivot points (see Fig. 6; it was found that the system would approach the required field quality if the pancakes were aligned to better than $200\ \mu\text{m}$. For the complete solenoid the field can be adjusted by regulating the current in the corrector coils (8 horizontal and 8 vertical). Figure 7 shows the magnetic field intensity calculated in the cooling region, for the *perfect* case, and compares to measurements performed for the currently installed electron cooler [10]. A Monte-Carlo analysis was carried out [12] to quantify the field quality expected of the built system. The following assumptions were made:

- The adjustment of each of the three pivot points of the pancakes is normally distributed with $3\sigma = 200\ \mu\text{m}$, the

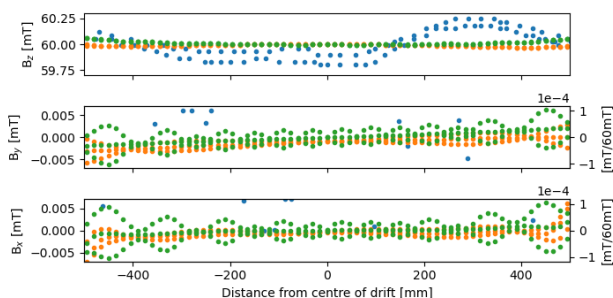


Figure 7: Magnetic field along the direction of motion of the e^- beam (B_z), perpendicular to the bending plane (B_y) and in the bending plane (B_x), estimated in the cooling region for the pancake (orange) and complete (green) typology, for the *perfect* case, i.e. all coils positioned and powered exactly. The values as extracted and scaled for the present magnetic system from [10] are shown in blue, but hardly visible since outside the scale chosen for B_x and B_y .

long term stability is normally distributed with $3\sigma = 20 \mu\text{m}$;

- The current in the corrector coils has a resolution vs. nominal normally distributed with $3\sigma = 5 \text{ PPM}$, a ripple of 1 mA RMS, and a long term stability of $3\sigma = 1000 \text{ PPM}$.
- Mechanical tolerances should be the same for the pancake and complete solenoid, and therefore are not discussed.

The results show that the two magnet configurations would be expected to give similar performance once built, with a field error of $\sim 2 \times 10^{-4}$ due to correction tolerance for the pancake case and $\sim 5 \times 10^{-5}$ for the complete case. It was decided to go for the complete cooling region solenoid which features active control of the magnetic field. With the pancake system the main concern was the tight tolerances needed in adjusting the coils position (better than $200 \mu\text{m}$) to achieve the required field quality. Besides being tight, the adjustment might be time/resource consuming, and, if any of the pancakes moved or broke during operation, very difficult to reproduce, especially considering that once the cooler is installed it would no longer be possible to measure the magnetic field. As for the magnets in the gun and collector arms, the choice of complete solenoids was made for economical reasons (less costly, especially if the main solenoid is a complete magnet) and for space constraints, to allow the integration of new orbit correctors adjacent to the electron cooler, made necessary by the fact that the new cooler is horizontal and not vertical [3].

The new magnet system is composed of

1. The gun expansion complete solenoid (nominal field 0.24 T, field quality $\leq 10^{-3}$), adiabaticity in expansion 0.93 T/m;
2. The arms solenoid (both on the gun and collector side) split in two complete magnets (0.06 T, field quality $\leq 10^{-3}$). The arm solenoids closest to the drift are fitted with horizontal and vertical steering coils;

3. The toroid solenoids (0.06 T), formed from 6 coils per side arranged to guarantee as a uniform bending toroidal field as possible, and shape to allow insertion and extraction of the e^- beam into and out of the AD ring; the toroids are also equipped with bending dipole magnets (shaped to match the toroid) to compensate for the residual vertical field from the toroid;
4. The cooling region complete solenoid (0.06 T, field quality $\leq 10^{-4}$), equipped with eight horizontal and eight vertical corrector magnets (0.34 mT), plus horizontal and vertical steering magnets to adjust the angle of the electron orbit (0.38 mT);
5. Collector squeeze coil, to compress the e^- beam before the collector entrance.

To optimise procurement time and costs, development work and spares availability, the type of power converters already available at CERN were taken into account when dimensioning the new magnetic system. The layout of the magnet powering is shown in Fig. 8, where almost all parameters have already been fixed. It should be noted that the SMILE type converters for the corrector and steerer magnets are already available as they can be recovered from the present installations and spares that we have at CERN.

Vacuum System

The design of the vacuum system is shown in Fig. 9 and have not significantly changed since [3]. The diameter of the vacuum chamber is everywhere the same as the adjacent chambers in the AD ring (145 mm inner diameter, and round shape). This is an improvement with respect to the present cooler as it provides smoother transition at insertion and extraction of the e^- beam. This also means that the need of clearing electrodes in the toroid chambers (to suppress ions and electrons either created by ionisation of the residual gas or by reflection from the collector) seems unlikely. This aspect is subject to ongoing investigation. The vacuum chambers of the gun and collector arms are identical, but rotated because it was decided to use the same collector design as for the present cooler, with inlet flange of DN150. Vacuum requirements for the new AD cooler impose the coating with NEG wherever possible (for its properties of pumping, low electron stimulated desorption, and to reduce the size of the vacuum chamber and design complexity), the use of NEG strips where the gas load is larger (close to the gun and collector), and the employment of NEXtoor pumps. The average pressure evaluated assuming a secondary electron yield at the collector after one day of operation is estimated to be in the order of $\sim 5 \times 10^{-10}$ mbar. Without NEG coating, the pressure would be at least an order of magnitude larger [13, 14].

Beam Position Monitors — BPM

One way for speeding the cooling time is to be able to align the e^- and \bar{p} beams to better than $300 \mu\text{m}$ which translate into a required relative measurement resolution of the BPM reading of $\leq 100 \mu\text{m}$. The new BPM design, presented in Fig. 10, is estimated to have a resolution of $\sim 90 \mu\text{m}$.

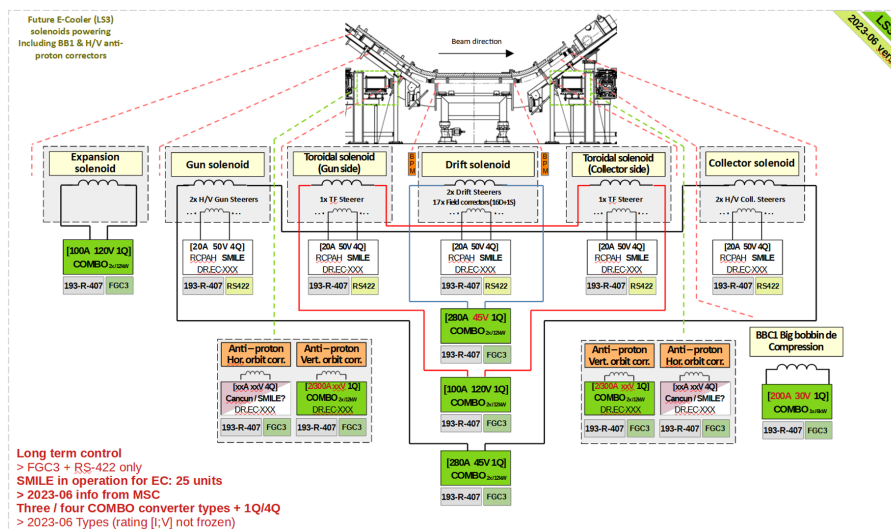


Figure 8: Magnet powering schematics for the new AD cooler.

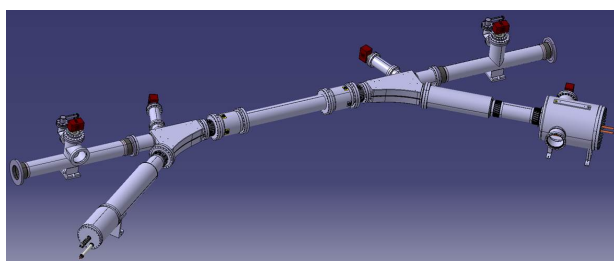


Figure 9: Vacuum chambers for the new electron cooler.

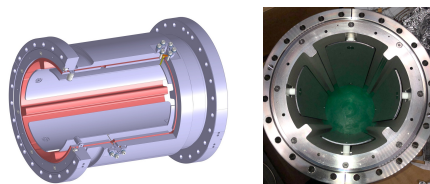


Figure 10: BPM for the new AD cooler.

TESTING STRATEGY AND SCHEDULE

All components of the new AD electron cooler will be tested separately in the laboratory. Magnets will be tested individually for acceptance and to tune correctors current, plus as an ensemble mounted on the support system to measure steering magnets strength and prepare for operations. Gun and collector are being tested individually, in a straight configuration, with magnets equivalent to those for the final electron cooler. Vacuum chambers and powering system will be tested individually. The magnet powering will be used for the complete magnet test. The de-installation of the current electron cooler will start when all components are proven to work as expected. In the present schedule, this should happen in the second quarter of 2026. After that the new electron cooler will be installed, connected to power, baked and commissioned, with operation to be started after

June 2027, i.e. after the end of the Long Shut Down 3 for the CERN injectors.

CONCLUSION

In this paper the main specification parameters and the newest design of the electron cooler replacing the one installed in the AD ring were presented. The new device aims at improving reliability as well as performance. The magnet design has evolved to complete solenoids which can produce a high quality field with active correction and avoid lengthy and difficult alignment, given the tight requirements. The design is mature and close to completion, and procurement will start in the beginning of year 2024. Provided the testing campaign for all components is successful, the decommissioning of the present electron cooler will start in the second quarter of 2026, and commissioning of the new device in 2027.

REFERENCES

- [1] P. Beloshitsky and T. Eriksson, “The CERN Antiproton Decelerator (AD) operation, progress and plans for the future”, presented at the 2nd International Workshop on Atomic Collisions and Atomic Spectroscopy with Slow Antiprotons, Aarhus, Denmark, 14–15 Sep 2001, CERN-OPEN-2002-041, CERN-PS-OP-NOTE-2002-040. <https://cds.cern.ch/record/561996>
- [2] G. Tranquille, “Recent highlights from the CERN-AD”, *Nucl. Instrum. Meth. A*, vol. 532, pp. 111–117, 2004. doi:10.1016/j.nima.2004.06.036
- [3] G. Tranquille *et al.*, “A New Electron Cooler for the CERN Antiproton Decelerator (AD)”, in *Proc. COOL’21*, Novosibirsk, Russia, Nov. 2021, pp. 95–97. doi:10.18429/JACoW-COOL2021-P2004
- [4] D. Gamba *et al.*, “Functional Specification for the New AD electron cooler”, Rep. AD-LNT-ES-0001, EDMS 2772724, CERN, 2023. <https://edms.cern.ch/document/2772724>

- [5] A. Pikin, “Simulations of e-gun for AD e-cooler”, presented at the E-coolers and e-lenses simulations - joint BE-ABP / BE-BI meeting, CERN, Geneva, 10 Jan. 2019. <https://indico.cern.ch/event/774322/>
- [6] C. Machado, “High Voltage powering for the New AD Electron Cooler”, Rep. EDMS 2938278, CERN 2023. <https://edms.cern.ch/document/2938278/>
- [7] H. Danared *et al.*, “Studies of electron cooling with a highly expanded electron beam”, *Nucl. Instrum. Meth. A*, vol. 441, pp. 123–133, 2000. doi:10.1016/S0168-9002(99)01121-3
- [8] G. Tranquille, L. Jørgensen, D. Luckin, and R. Warner, “The CERN-ELENA Electron Cooler Magnetic System”, in *Proc. IPAC’18*, Vancouver, BC, Canada, Apr. 4, 2018, pp. 842–845. doi:10.18429/JACoW-IPAC2018-TUPAF056
- [9] Discussion at the #12 AD E-Cooler Meeting: AD cooler specs, gun and magnetic system, CERN, 28 Feb. 2023. <https://indico.cern.ch/event/1248937/>
- [10] A. Wolf, L. Hütten, and H. Poth, “Magnetic field measurements for the electron cooling device for LEAR”, Rep. CERN-EP-INT-84-01, CERN, Geneva, 1984.
- [11] S. Baird *et al.*, “The anti-proton decelerator: AD”, *Nucl. Instrum. Meth. A*, vol. 391, pp. 210–215, 1997. doi:10.1016/S0168-9002(97)00359-8
- [12] L. Von Freeden, presentation at the #12 AD E-Cooler Meeting: AD cooler specs, gun and magnetic system, CERN, 28 Feb. 2023. <https://indico.cern.ch/event/1248937/>
- [13] J.A. Ferreira Somoza, presented at the New AD Electron Cooler Project Review, CERN, Geneva 2022. <https://indico.cern.ch/event/1157504/>
- [14] C. Castro Sequeiro and J.A. Ferreira Somoza, presented at the AD-CONS ELECTRON COOLER PROCUREMENT READINESS REVIEW, CERN, Geneva 28 June 2023. <https://indico.cern.ch/event/1298443/>

DYNAMIC APERTURE AND FREQUENCY ANALYSIS IN ELENA WITH ELECTRON COOLER MAGNETIC FIELD INCLUDED

Lajos Bojtár, CERN Beams Departement

Abstract

We present a new tracking algorithm and its implementation called SIMPA. It has the unique feature of long-term tracking of charged particles in arbitrary static electromagnetic fields in a symplectic way. It is relevant to beam dynamics and optics studies whenever the usual hard-edge model cannot describe the accelerator elements accurately or the beamline contains complex magnetic or electric fields. Such a situation arises in the ELENA machine at CERN and many other rings containing an electron cooler. The magnetic field of the electron cooler has a significant influence on the beam dynamics. Frequency analysis and dynamics aperture studies in ELENA are presented with the electron cooler magnetic field included.

INTRODUCTION

Long-term tracking of charged particles is a fundamental problem of accelerator physics, plasma physics, and it is important in astrophysics. In earlier papers [1, 2] we described a new algorithm allowing long-term symplectic integration of charged particle trajectories in arbitrary static magnetic and electric fields. The approach to particle tracking we described naturally includes the end fields for all kinds of magnets and special elements, like the magnetic system of an electron cooler, with the same treatment. The aim of this paper is to introduce the SIMPA algorithm and software [3] to the cooling expert community. The beam dynamics studies made on the Extra Low ENergy Antiproton (ELENA) ring [4] with SIMPA can be applied to other rings.

THE SIMPA ALGORITHM

We recommend reading the previous papers [1, 2] to understand the algorithm in detail, as only a summary is provided here.

Symplectic integrators keep the conserved quantities bounded, but cannot cure the errors coming from the representation of the fields. These are two separate sources of errors. It is crucial to have a physically valid representation of the fields obeying Maxwell's equations close to machine precision, otherwise there is a spurious energy drift during the tracking. This requires a continuous description of the electromagnetic fields in the entire beam region without any cuts. This is an important difference between SIMPA and other tracking codes which usually make element by element tracking and do not handle the electromagnetic field of the ring or beam line as a whole.

The Modified Surface Method

Surface methods describe the fields on the boundary surrounding the region of interest. Field values on the surface

determine the magnetic or electric fields in a source-free region. This is true because these fields are harmonic functions satisfying the Laplace equation which has a unique solution for a given boundary condition.

As a first step, the potentials are expressed analytically in terms of point sources. Sources are placed outside the volume of interest, at some distance above the boundary, and their strength is calculated by a system of linear equations such that they reproduce the magnetic or electric field at the boundary. In case of a static electric field, electric point sources are used, since the normal component of the field on the boundary surface is sufficient to describe the field inside the volume. For a static magnetic field this is not always true [1]. For example a field of a solenoid coil can not be reproduced by magnetic monopoles. In early versions of SIMPA, additionally to the magnetic monopoles, current loops were also used. This approach however has several drawbacks. Dirac's magnetic monopoles has singularities which must be directed such, that they do not intersect the volume of interest. The Dirac string singularities also prevent using the Fast Multipole Method [5] for the calculation of field maps. For these reasons the magnetic monopoles recently has been replaced by current point sources. These are two infinitesimally small wires perpendicular to each other and parallel to the boundary surface. Instead of the normal component, two tangential component are matched to the given magnetic field. This modification doubles the number of unknowns to be solved in the resulting linear system of equations, but allows the use of the Fast Multipole Method and eliminates the problem with the Dirac strings and current loops. The Fast Multipole Method can also be used to accelerate the iterative solver, largely compensating for the bigger number of variables.

The relative precision of the reproduction of the magnetic field is typically about 10^{-3} using 10^4 sources for a magnet with length of 1 meter. The precision can be made better by increasing the number of point sources. Regardless of the error relative to the reference field, the reconstructed field is continuous and satisfy Maxwell's equations close to machine precision anywhere inside the volume of interest. This is a key feature of the SIMPA algorithm, and it is the reason of the reconstruction of the field with point sources.

The distance of the point sources from the surface is a free parameter, but it must be chosen carefully. The elevation should be such, that the point sources are not too close to the boundary surface of the element, because the point sources can not be inside the balls of the cover or too close to them. When the sources are too close to the balls, the field expansion will require higher degree spherical harmonics which will make the field map slower and bigger or even impossible to achieve the required level of discontinuity between

the balls, which should be in the order of $B_{max} \times 10^{-10}$ or smaller for long-term tracking. On the other hand, when the sources are too far from the boundary surface, the solving of the strengths of the point sources will be difficult, the matrix describing the linear system of equations will be ill-conditioned. As a rule of thumb, the elevation should be about the same as the distance between the points on the boundary surface.

After the potentials are reproduced at the boundary by the point sources, they can be evaluated analytically anywhere inside the volume. However, this method is too slow to be practical.

Solid Harmonics

Several orders of magnitude speed improvement can be achieved by using a local description of the potentials. The value of the potentials can be evaluated inside a sphere with radius R with the following expression. In fact, this is the well known formula for regular real solid harmonics inside a unit ball, scaled by R .

$$f(r, \theta, \phi) = \frac{1}{R} \sum_{\ell=0}^{\ell_{max}} \sum_{m=-\ell}^{\ell} r^{\ell} c_{\ell m} \tilde{P}_{\ell}^m(\cos \theta) \Phi(\phi; m) \quad (1)$$

We denoted the ϕ dependent part as $\Phi(\phi; m)$ given by

$$\Phi(\phi; m) = \begin{cases} \sqrt{2} \sin(|m|\phi) & \text{if } m < 0 \\ 1 & \text{if } m = 0 \\ \sqrt{2} \cos(m\phi) & \text{if } m > 0 \end{cases} \quad (2)$$

In the expression above, $\tilde{P}_{\ell}^m(\cos \theta)$ is the orthonormalized associated Legendre polynomial, given as:

$$\tilde{P}_{\ell}^m(\cos \theta) = \sqrt{\frac{(2\ell+1)(\ell-|m|)!}{4\pi(\ell+|m|)!}} P_{\ell}^m(\cos \theta). \quad (3)$$

$P_{\ell}^m(\cos \theta)$ is calculated without the Condon-Shortley phase.

In Eq. (1), $r = |r_e - r_c|/R$ is the scaled distance between the sphere center r_c and the evaluation point r_e .

The real-valued coefficients $c_{\ell m}$ are pre-calculated by the following integral:

$$c_{\ell m} = \int_{S^2} \varphi(\theta, \phi) \tilde{P}_{\ell}^m(\cos \theta) \Phi(\phi; m) d\Omega, \quad (4)$$

where $\varphi(\theta, \phi)$ is the potential to be approximated, and S^2 denotes the surface of the sphere. There are several ways to do this integration. An elegant one is, to sum values $\varphi(\theta, \phi)$ on the surface of the sphere at the t -design points with equal weights. A spherical t -design is a set of N points on the sphere, such that a quadrature with equal weights using these nodes is exact for all spherical polynomials of degree at most t . More on t -designs can be found in [6]. An advantage of integrating on a sphere with t -designs is that the sample points have a uniform distribution, contrary to the often used Gaussian quadrature, which has a denser sampling around the poles. As [7] points out, when the sampling points are distributed uniformly on the sphere, the

error in the integral is minimized, assuming the errors in the sample values have a normal distribution.

For a set of N points $\{x_i\}$ in a t -design the following expression is exactly true for all spherical polynomials of maximum degree t or below.

$$\int_{S^2} \varphi(x) d\Omega = \frac{4\pi}{N} \sum_{i=0}^{N-1} \varphi(x_i). \quad (5)$$

Combining Eqs. (4) and (5), the spherical harmonics coefficients can be calculated with the following sum:

$$c_{\ell m} = \frac{4\pi}{N} \sum_{i=0}^{N-1} \varphi(x_i) \tilde{P}_{\ell}^m(\cos \theta(x_i)) \Phi(\phi(x_i); m), \quad (6)$$

where N is the number of quadrature points in the t -design. The spherical coordinates $\theta(x_i)$ and $\phi(x_i)$ are expressed in terms of the vectors x_i pointing to the quadrature points. The author of [6] has published a set of files containing t -designs up to degree 325 on his website for download. A subset of these files has been used in our implementation.

Regular solid harmonics are the canonical representation for harmonic functions inside a sphere. A key characteristic of the algorithm is the description of vector and scalar potentials by solid harmonics inside a set of overlapping spheres covering the volume of interest.

The potentials satisfy exactly the Laplace equation inside the spheres. The discontinuity between the spheres decrease exponentially with the degree of solid harmonics expansion and can be easily kept close to machine precision. The representation of the potentials in terms of solid harmonics is optimal in terms of memory and allows fast evaluation.

Field Map Preparation

1. The workflow starts with modeling individual magnets with CAD software or measurement data.
2. The strengths of the point sources are calculated for each type of magnet as described earlier.
3. The next step is to assemble the sources according to the lattice of the machine. This is done by rotating and translating the collections of sources to the correct place.
4. The boundary of the volume of interest is described by a Standard Tessellation Language (STL) file. SIMPA provides functionality to create the STL files to describe the beam region. It also can be taken from CAD models.
5. Next, the beam region is filled with overlapping spheres, such that the entire beam region is covered without gaps. For simple beam lines with uniform aperture a single line of spheres is often sufficient. For more complicated geometries HCP lattice is recommended. It leads to several times faster field maps [2]. The spheres should be small enough to not overlap with the sources. The coordinates of the sphere centers on an infinite HCP lattice can be obtained by three simple expressions.

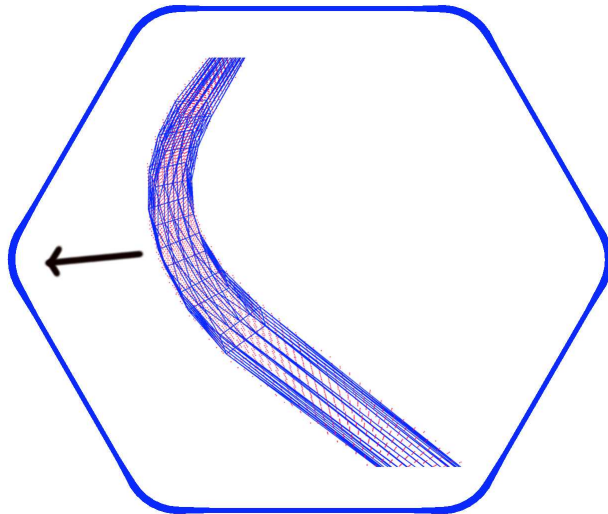


Figure 1: Triangulated boundary of the ELENA beam region. The interior plot is an expanded 3D view of an arc. The red dots are the centers of the covering spheres located on an HCP lattice.

Only those spheres are kept from the infinite lattice which are necessary to cover the beam region. Figure 1 shows the ELENA beam region and the centers of the covering spheres. The radius of the spheres was 1 cm in this study and about 76000 of them were needed to cover the beam region of ELENA.

6. The magnets of the beam line or ring are organized into magnet groups. Usually, a magnet group consists of magnets connected to the same power supply.
7. For each magnet group, a field map is produced by calculating the solid harmonics coefficients in each ball in the cover. These field maps are scaled individually, then combined into a global field map. A global field map is a scaled superposition of group field maps. All magnet group field maps are calculated using the same ball cover to allow efficient calculation of their superposition.

Once a global field map is prepared as described above, symplectic tracking can be performed. The motion of a charged particle calculated by the usual relativistic Hamiltonian

$$H = \sqrt{m^2 c^4 + c^2(p - qA)^2} + qV_E, \quad (7)$$

where A is the vector potential, V_E is the electric scalar potential, p is the canonical momentum and q is the charge of the particle.

Integrating these equations with classical methods like the Runge-Kutta introduces errors, like the drift of energy or non-preservation of phase-space volume. Symplectic integration methods don't suffer from these problems.

An explicit second-order method for general Hamiltonians, symplectic in extended phase space, is described in [8].

We implemented this integrator, which has the correct long-time behavior.

FREQUENCY ANALYSIS

The Method

The drift in the tunes can serve as an early indicator of the long-term stability of the motion [9]. For initial conditions corresponding to chaotic trajectories, the frequency can only be defined for a given time interval. Calculating this local frequency for two consecutive time intervals and taking their difference we can calculate tune shifts $\Delta Q_{h,v}$. For a coasting beam, the figure of merit can be defined as:

$$D = \log_{10}(\sqrt{\Delta Q_h^2 + \Delta Q_v^2}) \quad (8)$$

D calculated with this definition can be used to identify stable areas in the tune diagram.

The tunes were scanned in 160 steps in both directions giving 25600 initial conditions. Each particle was tracked for 300 turns and the phase space variables were saved at a single longitudinal position for each turn. The tracking result is post-processed with the NAFF algorithm [10]. To calculate $\Delta Q_{h,v}$, we split the 300 turns into two sets. Then the figure of merit D in Eq. (8) was calculated for each point in the diagram and plotted as colors.

Results

Figure 2 shows the figure of merit D for the bare ELENA machine with bending magnets and quadrupoles only, plotted against the tunes as colors. The exercise was repeated with the magnetic elements of the electron cooler included. Figure 3 shows the numerically measured tunes with the electron cooler included. Figure 4 shows the magnetic field of the electron cooler. It is apparent that the magnets of the electron cooler have a significant effect on the beam dynamics. Many resonance lines became stronger and wider and particle losses are more frequent at the strongest resonance lines.

On both plots, many higher-order resonance lines can be seen. It should be emphasized, these resonance lines are present also in a perfectly manufactured, built, and aligned machine. We have not put any imperfections into the model. All the resonance lines are the results of the fringe fields of the bending magnets and the quadrupoles. They are the direct consequence of the geometry of the magnets.

DYNAMIC APERTURE

The dynamic aperture of six working points has been calculated and displayed in Table 1 to compare resonance conditions with a non-resonant case. The selected set of tunes is indicated in Fig. 3. These resonance lines were selected because they are close to the region where the working point of ELENA was set during the commissioning. The first working point was chosen to be far from the strong resonance lines at $Q_h = 2.455$, $Q_v = 1.415$. The other five points were placed on resonance lines with various orders.

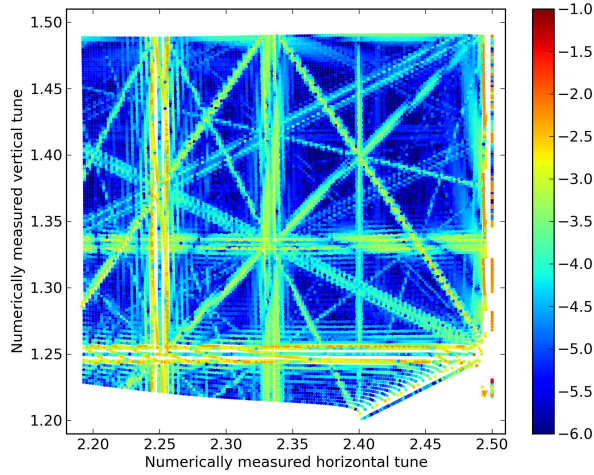


Figure 2: D plotted as colors against the numerically measured tunes for the bare ELENA machine, consisting of only the main bendings and the three quadrupole families.

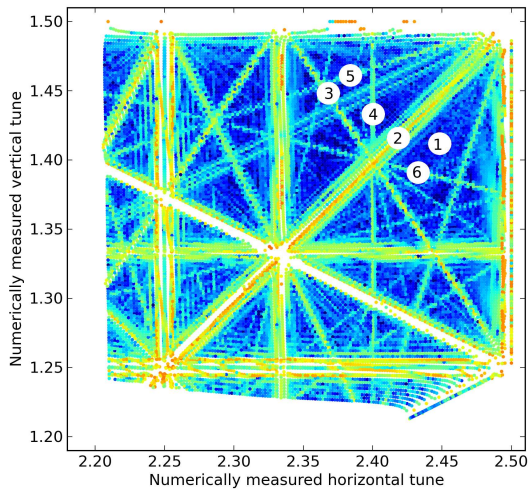


Figure 3: D plotted as colors on the same scale as above against the numerically measured tunes for the ELENA machine with the electron cooler included. The numbered white points in the tune diagram indicate the tunes where the dynamic aperture was calculated.

Stability diagrams are given in Fig. 5 for each point in Fig. 3, which survived $N = 10^4$ turns. In these diagrams, instead of the usual convention of using the physical beam dimensions in units of sigmas of the beam distribution on the axes, we used the single-particle emittances. We did so, because in ELENA, the beam size depends on the performance and duration of the electron cooler, so there is no nominal emittance we could use for comparison.

In Fig. 5 it is apparent that some of the resonance lines make the dynamic aperture significantly smaller than the physical aperture. The transverse acceptance of ELENA is determined by the size of vacuum chambers and the optics.

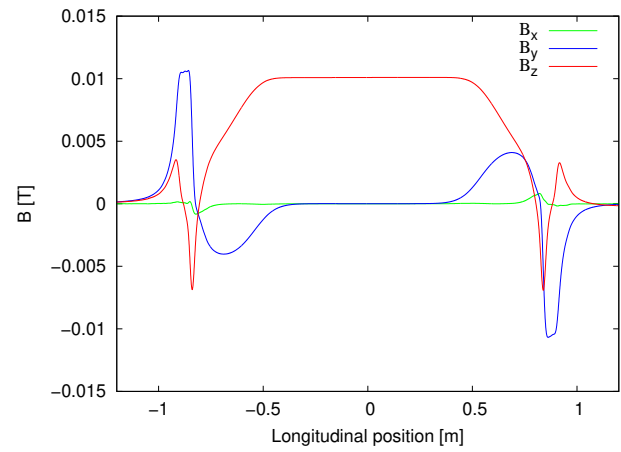


Figure 4: The magnetic field components of the electron cooler plotted against the longitudinal position with transverse coordinates $x = y = 2$ cm referenced to the design orbit.

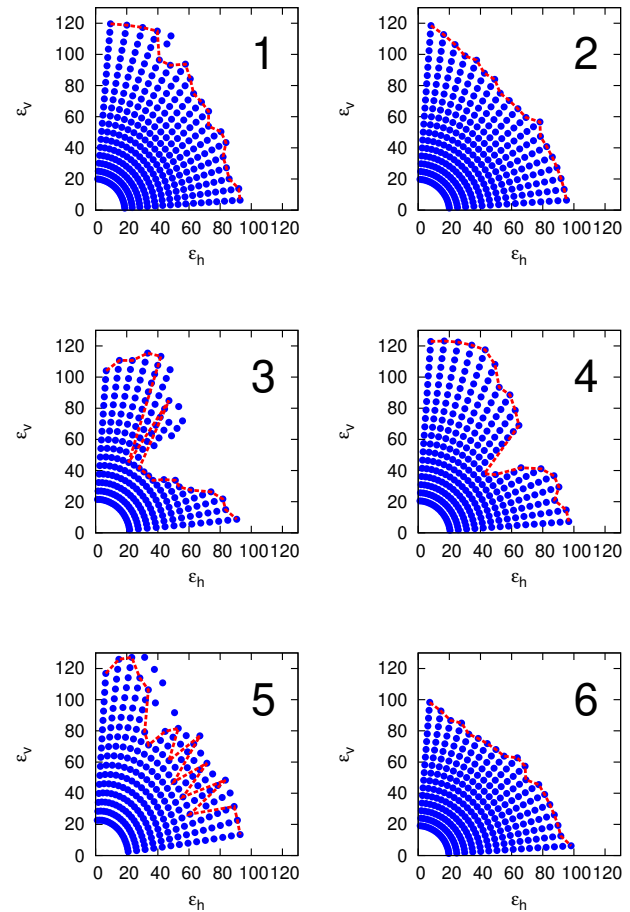


Figure 5: Initial emittances plotted in units of π mm mrad for particle with $dp/p = 0$. Only those initial conditions are plotted which survived $N = 10^4$ turns. The numbers in the upper right corners correspond to the numbering in Fig. 3. The lines indicate the last connected initial emittances for each angle α_k .

Table 1: Dynamic apertures r_d for the six points in Fig. 3 calculated with averaging over the dynamics, see [2]. M is the angular grid size for R_d calculation.

Point	r_d [m]	M	Resonance condition
1	0.0115	14	NA
2	0.012	8	$Q_h - Q_v = 1$
3	0.01	6	$3Q_h + 2Q_v = 10$
4	0.0117	3	$5Q_h = 12$
5	0.0113	9	$-Q_h + 3Q_v = 2$
6	0.0113	8	$Q_h + 4Q_v = 8$

THE SIMPA SOFTWARE

SIMPA is an open source software written in JAVA for physically valid representation of electromagnetic fields and symplectic tracking. That implies compliance with Maxwell’s equations close to machine precision. Symplectic long-term tracking in general electromagnetic fields is a difficult problem and was not fully solved before, to our best knowledge.

At the time of writing the papers [1, 2] the code was experimental and hard to use. Since, the core functionality has been refactored and separated into the ‘core’ library which can be used for many purposes where a representation of the EM field is needed. The accelerator-specific part was refactored into the ‘simpa-acc’ package. A command interface was developed, so the user doesn’t need to know JAVA programming to set up a simulation. The ‘simpa-acc’ package has most of the functionality available from the command line interface. Common tasks such as assembling beam lines, tracking particles, calculating optics, matching beam lines are performed with writing text files containing SIMPA commands. Examples are available in the GITLAB source repository [11]. More elaborate tasks such as frequency analysis and dynamical aperture studies described in this paper should use the JAVA API provided. Even in these cases most of the work is done from SIMPA command files and only simple coding is needed.

JAVA used to have a reputation of being slow, however this is not the case anymore. The tracking speed using a single core of an Intel i5-11500 CPU is about 90 turns/seconds in the ELENA machine with 30 meters circumference. It can be further improved using the vector instruction set of the CPU. The vector API is only a preview feature in JDK21, the final implementation comes later.

In the future SIMPA will handle time-varying EM fields at any frequency as well. A number of successful tests has been done aiming in this direction.

CONCLUSIONS

We have applied the SIMPA code for long-term symplectic charged particle tracking in arbitrary static electromag-

netic fields on the ELENA machine.

The frequency and dynamic aperture analysis identified a number of 4th and 5th order resonance lines in the tune diagram strong enough to reduce the dynamic aperture below the physical one. What made the frequency and dynamic aperture analyses different, is the fact that we have not introduced any multipole error into our model apart from the multipole components due to the geometry of the magnets, which are inevitable. All the resonances seen in the frequency analysis are direct consequences of the geometry of the fields, even if the magnetic elements are manufactured perfectly.

We showed in the frequency analysis section the effect of the magnetic system of the electron cooler on the beam dynamics by comparing the two cases, with and without electron cooler. The electron cooler introduced non-negligible magnetic perturbations, strengthening many resonance lines. To our best knowledge there was no similar study done before with electron coolers.

REFERENCES

- [1] L. Bojtár, “Efficient evaluation of arbitrary static electromagnetic fields with applications for symplectic particle tracking”, *Nuclear Instruments and Methods A*, vol. 948, p. 162 841, 2019. doi:10.1016/j.nima.2019.162841
- [2] L. Bojtár, “Frequency analysis and dynamic aperture studies in a low energy antiproton ring with realistic 3d magnetic fields”, *Phys. Rev. Accel. Beams*, vol. 23, no. 10, p. 104 002, 2020. doi:10.1103/PhysRevAccelBeams.23.104002
- [3] <https://simpa-project.web.cern.ch/>
- [4] V.K. Chohan *et al.*, “Extra Low ENergy Antiproton (ELENA) ring and its transfer lines: Design report”, CERN, 2014.
- [5] V. Rokhlin, “Rapid solution of integral equations of classical potential theory”, *Journal of Computational Physics*, vol. 60, no. 2, pp. 187–207, 1985. doi:10.1016/0021-9991(85)90002-6
- [6] R. S. Womersley, “Efficient spherical designs with good geometric properties”, 2017.
- [7] V. I. Lebedev, “Quadratures on a sphere.”, *USSR Computational Mathematics and Mathematical Physics*, 16, 1976.
- [8] M. Tao, “Explicit symplectic approximation of nonseparable hamiltonians: Algorithm and long time performance”, *Phys. Rev. E*, vol. 94, no. 4, p. 043 303, 2016. doi:10.1103/PhysRevE.94.043303
- [9] E. Todesco, M. Giovannozzi, and W. Scandale, “Fast indicators of long term stability”, *Particle Accelerators*, vol. 55, pp. 27–36, 1996.
- [10] J. Laskar, “The chaotic motion of the solar system: A numerical estimate of the size of the chaotic zones”, *Icarus*, vol. 88, no. 2, pp. 266–291, 1990. doi:10.1016/0019-1035(90)90084-M
- [11] <https://gitlab.cern.ch/lbojtarsimpa/-/tree/master/examples>

STATUS OF BEAM INSTRUMENTATION AT THE ELECTRON BEAM TEST STAND AT CERN

M. Sameed*, M. Ady, S. Burger, J. Cenede, A. Churchman, T. Coiffet,
W. Devauchelle, A. Ganesh, A. Kolehmainen, S. Mazzoni, D. Perini, M. Plantier,
A. Rossi, S. Sadovich, Y. Sahin, G. Schneider,
O. Sedlacek¹, C. Castro Sequeiro, K. Sidorowski, R. Veness, F. Guillot-Vignot, M. Wendt
CERN, Geneva, Switzerland
P. Forck, S. Udrea
GSI, Darmstadt, Germany
O. Stringer, C. Welsch, H. Zhang
The University of Liverpool, Liverpool, UK
¹also at The University of Liverpool, Liverpool, UK

Abstract

The Electron Beam Test Stand (EBTS), a collaborative effort at CERN with the Accelerator Research and Innovation for European Science and Society (ARIES) project, has been purpose-built within the High Luminosity Large Hadron Collider (HL-LHC) initiative. This comprehensive test facility features a high-perveance electron gun producing a hollow electron beam, supported by a magnetic system comprising normal conducting solenoid magnets with horizontal and vertical correctors. The EBTS boasts an array of advanced beam instrumentation, including YAG:Ce screens, a multi-channel Pin-Hole Faraday cup, a Beam Position Monitor (BPM), and a Beam Gas Curtain (BGC) profile monitor integrated with an optical transition radiation (OTR) screen. Additionally, it includes an electron collector.

This paper offers an overview of the EBTS, emphasizing the design and capabilities of its various beam instruments. It further provides insights into some prototype test results with pulsed electron beams, and upcoming tests with DC beams. The EBTS holds great potential as a valuable tool for advancing electron beam technologies, particularly in the realm of sources and instrumentation for electron cooling devices.

INTRODUCTION

The EBTS at CERN has been designed and constructed to address the objectives outlined in ARIES WP16 (Intense, RF Modulated, E-Beams (IRME)) [1–3], as well as HL-LHC WP5 (Collimation) and WP13 (Beam Instrumentation) [4]. The key objectives include:

- Designing and building a test stand capable of evaluating an electron gun, equipped with instrumentation for measuring both transverse and longitudinal profiles of the RF-modulated electron beam.
- Conducting measurements to characterize the properties of the RF-modulated electron beam generated by the gun within this test stand.

- Prototyping components, such as the electron gun, collector, and BPM, to potentially implement hollow electron lenses (HEL) for active beam-halo control in the HL-LHC.
- Developing a gas curtain monitor to precisely align the electron and proton beams within the hollow electron lens.

Although the ARIES project concluded in 2022, the R&D part of the HL-LHC project remains ongoing. This section will delve into specific aspects of the HEL and their implications on the design of the EBTS. The EBTS will be described in subsequent sections along with an update on the current status of beam instrumentation at this facility.

High Luminosity LHC Hollow Electron Lens

The purpose of HEL is to enhance the transverse beam halo diffusion and provide controlled halo depletion for HL-LHC proton beams [5]. By superimposing a low-energy (about 10 keV), high-current (5 A) counter-propagating hollow electron beam with the proton beam, halo particles in the proton beam experience non-linear transverse kicks, while the particles in the beam core remain unaffected. Over time, these kicks accumulate, diffusing and eventually removing halo particles through downstream collimation. The electron beam must be concentric with the proton beam (within 100 μm) over a three-meter interaction region to achieve 90% halo depletion in five minutes [6, 7].

The key components for HEL, as depicted in Figure 1, include the electron gun and pulse modulator for generating the pulsed hollow electron beam. Two beam position monitors are employed to precisely locate the proton and electron beams in the interaction region. The minimally invasive beam profile monitor, known as the BGC (for Beam Gas Curtain monitor) [8–14], acts as an overlap monitor for both beams. Additionally, a collector serves as an electron beam dump. The setup also features superconducting solenoids, compensation magnets, and steering coils to guide and control the beams within their designated orbits.

The HEL prototype components to be tested at the EBTS include the electron gun, BPM, BGC, and electron collector.

* m.sameed@cern.ch

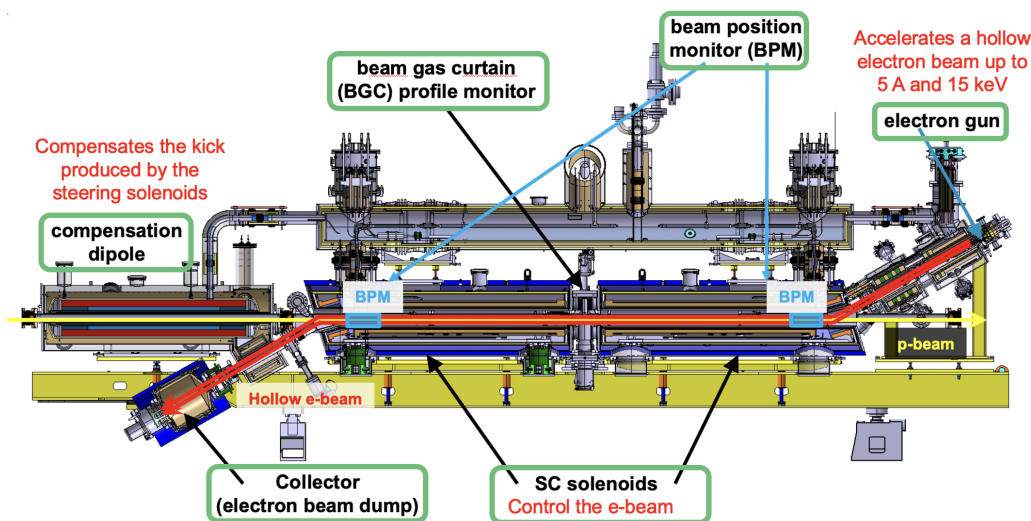


Figure 1: 3D model of a preliminary design of the HEL for HL-LHC.

ELECTRON BEAM TEST STAND (EBTS)

The EBTS layout, shown in Figure 2, emphasizes HEL components outlined in green. Resistive solenoids, capable of producing a maximum axial magnetic field of 0.4 Tesla, guide the electron beam, each featuring horizontal and vertical correctors for precise beam control. A sector valve divides the EBTS into two independent volumes, allowing separate interventions. The upstream volume houses the Beam Diagnostic Box (BDB), providing electron beam assessment even when downstream instruments are unavailable.

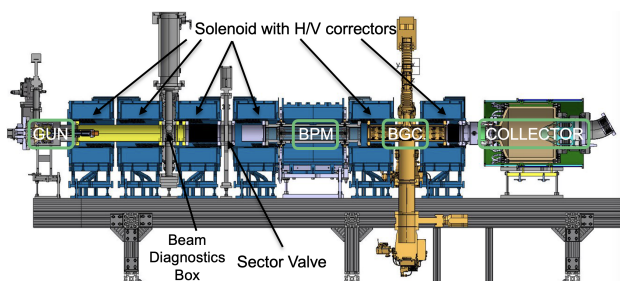


Figure 2: 3D model of the EBTS.

The EBTS supports modular installations, offering versatility for testing electron guns, collectors, beam profile monitors, beam position monitors, pulse modulators, power converters (including high voltage ones), and control and interlock systems.

In the remainder of this section, we will provide a concise overview of the electron gun and the parameters of the generated electron beam, followed by descriptions of the various beam instruments currently operational within the EBTS in the next section.

Electron Gun

The EBTS currently employs the HEL Gun v3, as depicted in Figure 3. This gun features a hollow cathode with

a 16.10 mm outer diameter and 8.05 mm inner diameter, capable of providing a current density of 3.33 A/cm² at an operating temperature of 950 °C. Within the EBTS, the electron gun delivers a beam current of up to 5 A and a beam energy of up to 15 keV.

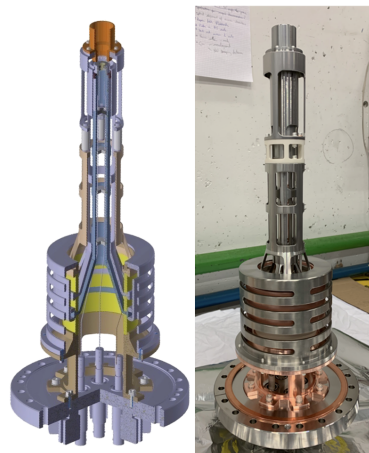


Figure 3: HEL electron gun 3D model (left) and image of the assembled gun (right).

For pulse modulation, a Marx generator [15] is used, offering a rapid 200 ns rise/fall time and an adjustable pulse duration ranging from 1 to 100 microseconds. The system supports a repetition frequency between 1 Hz and 1 kHz.

Both the cathode and electron gun's performance have undergone validation, with testing conducted at FNAL (using HEL Gun v1) and CERN (using HEL Gun v3) [16, 17]. Figure 4 showcases the results of this characterization and provides a comparison of the experimental data with the outcomes from three distinct simulation programs.

Content from this work may be used under the terms of the CC-BY-4.0 licence (© 2023). Any distribution of this work must maintain attribution to the author(s), title of the work, publisher, and DOI

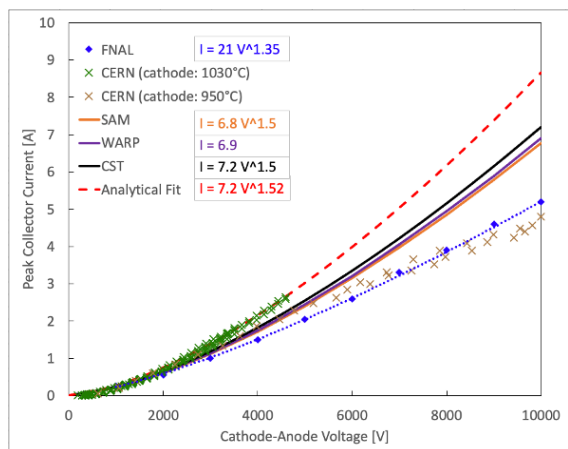


Figure 4: Characterization of the HEL electron gun.

BEAM INSTRUMENTATION

The beam instrumentation at the EBTS consists of beam profile monitors, a beam position monitor (BPM), and an electron collector.

Beam Profile Monitors

The EBTS is equipped with four beam profile monitors, each serving specific functions:

1. YAG:Ce screens
2. Pin-Hole Faraday cup
3. BTV screen
4. BGC

The YAG:Ce screens and Pin-Hole Faraday cup are positioned at the BDB location, while the BTV screen and BGC are located at the position labelled BGC in Figure 2.

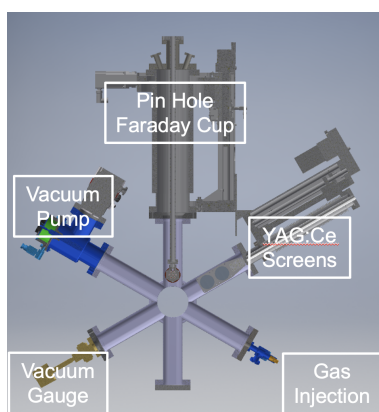


Figure 5: 3D model of the BDB.

YAG:Ce Screens The BDB, depicted in Figure 5, includes a pair of 50 mm diameter, 0.1 mm thick YAG:Ce screens mounted on the diagonal linear translator. One screen is coated with a 100 nm thick aluminum layer which reflects photons generated normal to the screen surface, increasing the signal intensity by a factor of 2. This works well when the signal intensity is low. The second screen

is coated with a 20 nm thick indium tin oxide (ITO) layer which is transparent and minimizes smearing of the beam profile. This works well when the signal intensity is high. Both aluminum and ITO are conductive layers that prevent charge buildup on the YAG:Ce screens.

A YAG:Ce screen, when inserted into the beamline, is perpendicular to the electron beam direction of motion. The photons generated at the screen travel downstream and pass through an optical viewport before they are collected by a scientific camera (Manufacturer: Thorlabs, Model: CS135MU).

YAG:Ce screens offer benefits such as high photon yield, rapid decay time, and exceptional image resolution. However, they can encounter challenges like image saturation and screen damage when exposed to high-intensity or prolonged electron beam operation.

In this paper, only measurements with the aluminum coated YAG:Ce screen are shown. The beam profile acquisition and analysis procedures for these screens have been entirely automated. Figure 6 illustrates an example of the acquired image and the subsequent beam profile analysis.

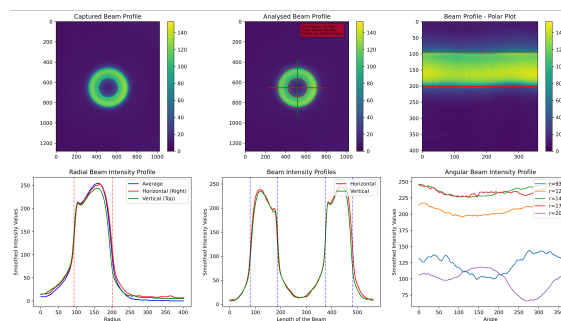


Figure 6: Transverse profile of a 4 keV, 25 mA, 25 μ s long hollow electron beam as measured with a YAG:Ce screen.

Pin-Hole Faraday Cup The Pin-Hole Faraday cup, located on the vertical linear translator on the BDB (Figure 5), consists of seven pins with a 10 mm pitch in a hexagonal arrangement, each pin featuring a 0.2 mm aperture. The entire Faraday cup assembly is adjustable in XYZ directions within a range of ± 20 mm.

This type of Faraday cup offers the advantage of withstanding very high electron beam intensities. Furthermore, acquiring the beam profile only necessitates an electrical feedthrough, eliminating the need for a camera or viewport. However, one notable challenge is the time required for profile acquisition; for an image with 900 data points on a grid, this process can take up to 30 minutes. On the other hand, a fast acquisition is possible if one wants to only check the uniformity of emission over few points.

The current status of the Pin-Hole Faraday cup is as follows: individual testing of each pinhole with nominal electron beam parameters has been successfully conducted. Additionally, the automation of beam profile acquisition and analysis has been implemented. Unfortunately, a setback occurred just before the first fully automated acquisition,

when the PXI scope card experienced a malfunction. The card has been repaired and is scheduled for reinstallation at the EBTS by the end of 2023.

BTV Screens The BTV (or Beam TV [18]) consists of a screen positioned at an angle (between 45 and 60 degrees depending on the light emission pattern) w.r.t. the electron beam direction of motion, and a camera (Manufacturer: Basler, Model: acA1920-40gm) collecting the light through a viewport perpendicular to the beam direction. A high speed gated intensifier (Manufacturer: Hamamatsu, Model: C9547-01) is optionally used.

At the EBTS, two distinct types of BTV screens have been tested [19]. The first type is Chromox (scintillating screen), known for its high photon yield but long decay times [20]. One challenge associated with Chromox screens is the accumulation of charge which may blur or completely distort the profile image as evident in Figure 7.

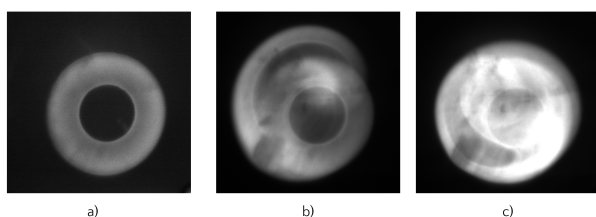


Figure 7: Transverse profile of a 7 keV, 3 μs long hollow electron beam as measured with a Chromox screen. The beam current is a) 2 mA b) 44 mA c) 87 mA. The image distortion is visible in b) and c).

The second type of screen tested at the EBTS is glassy carbon (OTR screen). These screens offer a low photon yield but boast an exceptionally short decay time [20]. This characteristic makes them suitable for examining longitudinal beam slices (when used with a gated intensifier) and evaluating the electron beam's uniformity in the longitudinal direction as depicted in Figure 8. Glassy carbon screens at the EBTS do not encounter saturation issues. Generally, BTV screens are capable of withstanding high beam intensities and extended pulse durations, exhibiting good radiation resistance and response linearity.

However, it is important to note that the image resolution, especially with glassy carbon screens, is inferior to that of YAG:Ce screens. Additionally, longer acquisition times may be necessary for beam intensities that are not significantly high.

Notably, at the EBTS, the Chromox screen displayed limited effectiveness for beam currents exceeding 5 mA or pulse durations extending beyond 3 μs. This limitation primarily stems from the aforementioned charge accumulation issue. In contrast, the glassy carbon screen has been thoroughly tested, commissioned, and operates effectively.

Beam Gas Curtain (BGC) The EBTS incorporates a minimally invasive beam profile monitor known as the

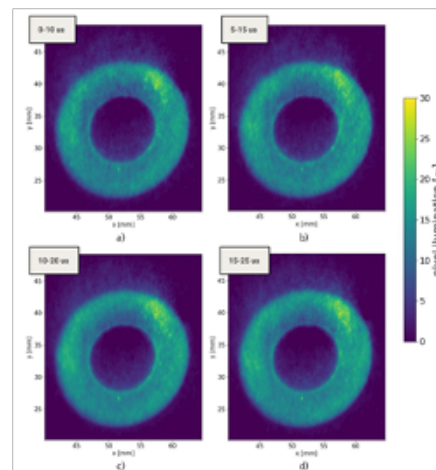


Figure 8: Transverse profile of a 7 keV, 1.2 A, 25 μs long hollow electron beam as measured with a glassy carbon screen. Each distribution corresponds to a longitudinal slice: a) 0-10 μs i.e. first slice (head) of the beam b) 5-15 μs i.e. second slice of the beam c) 10-20 μs i.e. third slice of the beam and d) 15-25 μs i.e. final slice (tail) of the beam.

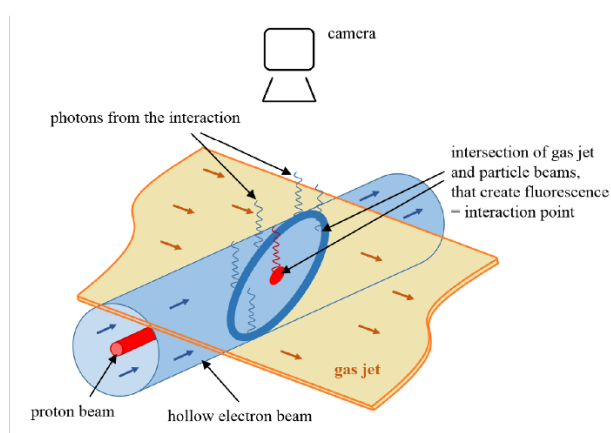


Figure 9: Working principle of the BGC.

BGC [8–14]. This monitor generates a thin and dense supersonic gas sheet by directing high-pressure gas through a series of skimmers. The particle beam interacts with this gas sheet to produce beam-induced fluorescence photons that can be captured by a camera to produce a transverse beam profile (Figure 9). The gas sheet (or curtain) dimensions depend by the apertures of the skimmers installed. The intensity of the signal vary with the gas type injected.

The advantages of the BGC include its minimally invasive approach to beam profile measurement and bidirectionality, enabling the examination of reflected and secondary electrons at the EBTS or the counter-propagating proton beam at the HEL.

However, the BGC does present challenges, such as prolonged acquisition times and the need for active gas pumping in vacuum. Additionally, its intricate setup, considerable footprint, and high manufacturing costs are notable drawbacks.

The BGC, originally designed for HEL as an overlap monitor for the electron and proton beams, was successfully tested and commissioned at the EBTS by the end of 2022. A BTV screen was used to validate its performance. Figure 10 shows the electron beam transverse profiles acquired by the BGC using different working gases. Preliminary analysis suggests that the BGC can achieve the required 100 μm resolution for HEL [21].

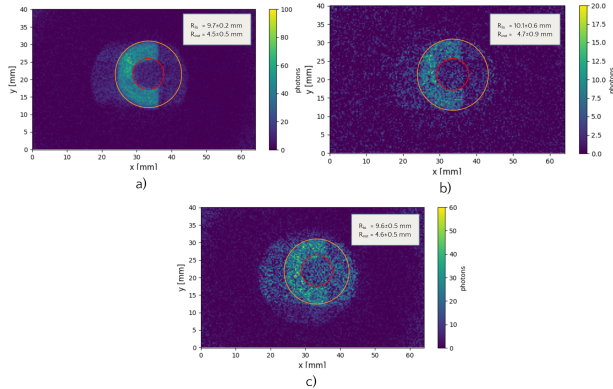


Figure 10: Transverse profile of a 7 keV, 1.5 A, 25 μs long hollow electron beam as measured with the BGC. The working gas is a) nitrogen, b) neon, and c) argon.

The BGC is currently installed in the LHC and has been used to measure both proton and ion beam profiles. An improved version of the BGC is scheduled for installation at the EBTS in the future.

Beam Position Monitor (BPM)

At the HEL, the BPM serves to independently measure the transverse positions of the proton and electron beams using vertical and horizontal stripline electrodes [22]. Located between the sector valve and the BGC, the HEL BPM prototype at the EBTS has an outer diameter of 100 mm and inner diameter of 80 mm, with a stripline length of 400 mm and a width of 12.4 mm (Figure 11). The BPM has been designed to work with a 200 ns rise/fall time which is set by the requirements of the electron beam at the HEL.



Figure 11: 3D model of the HEL BPM prototype.

Simulations and laboratory tests have shown that the BPM can achieve a position resolution of 0.2 μm , despite a long-term drift of approximately 4 μm . The BPM was installed at the EBTS in September 2023 and conducted its first measurements with a hollow electron beam in early October. The collected data is currently under analysis.

Electron Collector

The most downstream component of the EBTS is the electron collector, depicted in Figure 12. This HEL collector prototype features an 80 mm entrance aperture and can be biased up to +5 kV relative to the cathode potential. Designed to absorb continuous beam power of up to 25 kW, it is operable in both DC and pulsed mode.

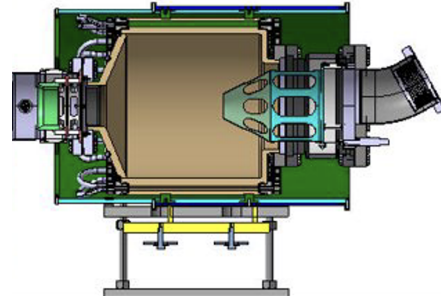


Figure 12: 3D model of the HEL collector prototype.

Utilizing this collector poses challenges due to stringent vacuum requirements and the need to minimize secondary electron emission. Its operation demands a high-voltage platform and demineralized cooling water, both of which are currently unavailable at the EBTS. Efforts are underway to provide these essential facilities.

The collector's design and simulations have been finalized, with raw materials ordered, and fabrication and assembly currently in progress. Installation of the collector at the EBTS is scheduled for 2024.

CONCLUSION

The EBTS has served as a critical testbed for prototype components essential for the HL-LHC HEL, including the electron gun, the BGC and the BPM. The collector prototype is slated for installation and testing in 2024. The EBTS is equipped with an electron gun, collector, BPM, and multiple beam profile monitors, rendering it a versatile facility for comprehensive characterization of electron guns, collectors, beam pulse modulators, and various beam instrumentation. Furthermore, its compatibility with DN-100 installation makes it an appealing resource for collaborators seeking to validate equipment for electron coolers and related applications.

ACKNOWLEDGMENTS

Funding for the EBTS was provided by High Luminosity LHC (HL-LHC) Project and Accelerator Research and Innovation for European Science and Society (ARIES) Project. The primary author would like to thank L. Yusof for valuable assistance in preparing this manuscript.

REFERENCES

- [1] ARIES, <https://aries.web.cern.ch>
- [2] O. Boine-Frankenheim and W. D. Stem, "Space charge compensation with pulsed electron lenses for intense ion beams in

- synchrotrons”, *Nucl. Instrum. Meth. A*, vol. 896, pp. 122–128, 2018. doi:10.1016/j.nima.2018.04.014
doi:10.48550/arXiv.1705.01057
- [3] S. Artikova, O. Boine-Frankenheim, O. Meusel, A. Oeftiger, D. Ondreka, K. Schulte-Urlichs and P. Spiller, “Pulsed electron lenses for space charge compensation in the FAIR synchrotrons”, *JINST*, vol. 16, no. 03, p. P03044, 2021.
doi:10.1088/1748-0221/16/03/P03044
- [4] HL-LHC, <https://hilumilhc.web.cern.ch>
- [5] S. Redaelli, R. B. Appleby, R. Bruce, O. Brüning, A. Kolehmainen, G. Ferlin, A. Foussat, M. Giovannozzi, P. Hermes and D. Mirarchi, *et al.* “Hollow electron lenses for beam collimation at the High-Luminosity Large Hadron Collider (HL-LHC)”, *JINST*, vol. 16, no. 03, p. P03042, 2021.
doi:10.1088/1748-0221/16/03/P03042
- [6] A. Rossi, D. Nikiforov, M. Arsenyeva, A. Barnyakov and A. Levichev, “Electron dynamics for high-intensity hollow electron beams”, *JINST*, vol. 16, no. 03, p. P03043, 2021.
doi:10.1088/1748-0221/16/03/P03043
- [7] HEL functional requirements and operational scenarios, CERN EDMS 277748.
- [8] S. Udrea *et al.*, “Development of a Fluorescence Based Gas Sheet Profile Monitor for Use With Electron Lenses: Optical System Design and Preparatory Experiments”, in *Proc. IBIC’17*, Grand Rapids, MI, USA, Aug. 2017, pp. 359–363.
doi:10.18429/JACoW-IBIC2017-WEPCC08
- [9] A. Salehilashkajani *et al.*, “A gas curtain beam profile monitor using beam induced fluorescence for high intensity charged particle beams”, in *Appl. Phys. Lett.*, vol. 120, no. 17, p. 174101, 2022. doi:10.1063/5.0085491
- [10] A. Salehilashkajani *et al.*, “Commissioning of the Prototype for a New Gas Curtain Beam Profile Monitor Using Beam Induced Fluorescence for HL-LHC”, in *Proc. IPAC’19*, Melbourne, Australia, May 2019, pp. 2709–2712.
doi:10.18429/JACoW-IPAC2019-WEPGW093
- [11] V. Tzoganis, and C. P. Welsch. “A non-invasive beam profile monitor for charged particle beams”, in *Appl. Phys. Lett.*, vol. 104, no. 20, p. 204104, 2014.
doi:10.1063/1.4879285
- [12] H. D. Zhang *et al.*, “A Supersonic Gas-Jet Based Beam Induced Fluorescence Prototype Monitor for Transverse Profile Determination”, in *Proc. IPAC’17*, Copenhagen, Denmark, May 2017, pp. 458–461.
doi:10.18429/JACoW-IPAC2017-MOPAB139
- [13] H. D. Zhang *et al.*, “A Supersonic Gas Jet-Based Beam Profile Monitor Using Fluorescence for HL-LHC”, in *Proc. IPAC’18*, Vancouver, Canada, Apr.-May 2018, pp. 1891–1894.
doi:10.18429/JACoW-IPAC2018-WEPAF034
- [14] A. Rossi *et al.*, “DC and pulsed electron beam test facility at CERN”, in *Proc. IPAC’23*, Venice, Italy, May 2023, pp. 1971–1974.
doi:10.18429/JACoW-IPAC2023-TUPL104
- [15] W. J. Carey and J. R. Mayes, “Marx generator design and performance”, Conference Record of the Twenty-Fifth International Power Modulator Symposium, 2002 and 2002 High-Voltage Workshop., Hollywood, CA, USA, 2002, pp. 625–628. doi:10.1109/MODSYM.2002.1189556
- [16] D. Perini, A. Kolhemainen, A. Rossi, S. Sadovich and G. Stancari, “Design of high-performance guns for the HL-LHC HEL”, *JINST*, vol. 16, no. 03, p. T03010, 2021.
doi:10.1088/1748-0221/16/03/T03010
- [17] S. Li and G. Stancari, “Characterization of an Electron Gun for Hollow Electron Beam Collimation”, Rep. FERMILAB-TM-2542-APC, 2012. doi:10.2172/1419167
- [18] E. Brevan *et al.*, “A new TV beam observation system for CERN”, Rep. CERN-AB-2005-076, CERN, Geneva, 2005. <https://cds.cern.ch/record/895159>
- [19] O. Sedlacek *et al.*, “Optical transition radiation measurements of a high intensity low energy hollow electron beam on electron beam test facility”, in *Proc. IPAC’23*, Venice, Italy, May 2023, pp. 3952–3955.
doi:10.18429/JACoW-IPAC2023-THPA002
- [20] T. Lefevre *et al.*, “A large scintillating screen for the LHC dump line”, Rep. CERN-AB-2007-023, CERN, Geneva, 2007. <https://cds.cern.ch/record/1045239>
- [21] O. Sedláček, M. Ady, A.R. Churchman, P. Forck, S. Mazzone, A. Rossi, *et al.*, “Gas Jet-Based Fluorescence Profile Monitor for Low Energy Electrons and High Energy Protons at LHC”, in *Proc. IBIC’23*, Saskatoon, Canada, Sep. 2023, pp. 316–321. doi:10.18429/JACoW-IBIC2023-WE3I01
- [22] G. Bantemits, M. G. A. Rossi, and M. Wendt, “Signal Analysis and Detection for the BPMs of the LHC Hollow Electron Lens”, in *Proc. IBIC’21*, Pohang, Korea, Sep. 2021, pp. 91–95. doi:10.18429/JACoW-IBIC2021-MOPPP22

DEVELOPMENT OF STOCHASTIC COOLING COMPONENTS FOR HIAF SPECTROMETER-RING

G.Y. Zhu^{1,†}, J.X. Wu¹, Z. Du¹, J. Yin, IMP CAS, Lanzhou, China
L.Y. Ma, Northwest Normal University, Lanzhou, China

Abstract

Stochastic cooling of the spectrometer ring (SRing) with the bandwidth of 0.6-1.2 GHz at the High Intensity Heavy-Ion Accelerator Facility (HIAF) project in China, which is used mainly for experiments with radioactive fragment beams, is applied to speed up the cooling process of a stored ion beam. In this paper, both the prototypes of coaxial notch filter with amplitude equalizer and optical notch filter with phase-stabilized optical fiber cable are built and measured for SRing stochastic cooling system. A 9 bit wide-band 360° digital adjustable phase shifter with minimum step length of 0.7° has been fabricated and tested for HIAF stochastic cooling. Meanwhile, the prototype of RF signal transmission processing units of SRing stochastic cooling are measured. Finally, the development, performance, and testing of both a Faltin prototype traveling wave structure and a novel slot-ring prototype standing wave structure based on a ceramic vacuum chamber for the HIAF SRing stochastic cooling system are discussed briefly.

INTRODUCTION

The High Intensity Heavy-Ion Accelerator Facility (HIAF) project was proposed by the Institute of Modern Physics (IMP) of the Chinese Academy of Sciences (CAS) in 2009. It will provide high intensity heavy-ion beams for nuclear physics, atomic physics, and other applications [1]. As an essential part of HIAF, the high-precision spectrometer ring (SRing) is designed to perform nuclear mass spectrometry in combination with fast beam cooling [2]. Stochastic cooling of the SRing, which is used mainly for experiments with radioactive fragment beams, plays a significant role in beam cooling and is applied to speed up the cooling process of the stored ion beam. The stochastic cooling system of SRing mainly consists of pick-ups, kickers, RF power amplifiers, and signal processing and transmission equipment, which are designed to operate with the operating bandwidth of 0.6-1.2 GHz [3]. Figure 1 shows the layout of the SRing stochastic cooling system. Notch filter, broadband phase shifter and pickup/kicker are one of the most critical devices for SRing stochastic cooling system.

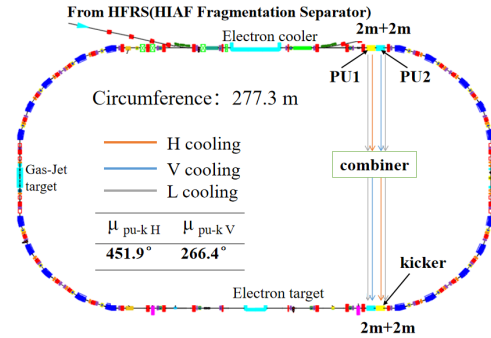


Figure 1: Layout of the stochastic cooling system on the SRing.

NOTCH FILTER

The ideal notch filter consists of an in-phase splitter, a short and a long transmission line, and a 180° microwave hybrid. The schematic drawing of an ideal notch filter is shown in Fig. 2.

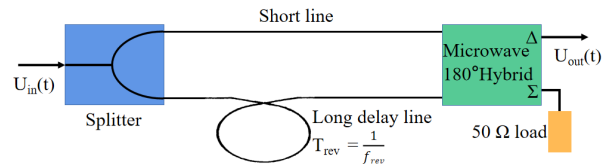


Figure 2: Schematic drawing of an ideal notch filter consisting of a splitter, a short and a long transmission line, and a “subtractor” (a microwave hybrid with a 180° phase shift in one branch).

In order to improve the notch depth of the notch filter, both the coaxial notch filter with an amplitude equalizer in the long branch and the optical notch filter with a phase-stabilized optical fiber cable are developed, performed, and measured for the SRing stochastic cooling system [4]. The coaxial notch filter with amplitude equalizer in long branch mainly consists of a power splitter, a short coaxial cable and a long coaxial cable transmission line, electrical programmable delay line, amplitude equalizer, variable attenuator, 50 Ω load and 180° microwave Hybrid, as shown in Fig. 3(a). The optical notch filter with a phase-stabilized optical fiber cable consists of RF/optical transmitter and optical/RF receiver, optical power splitter, short and long phase-stabilized optical fiber, variable optical electrical delay, variable optical attenuator, 50 Ω load and 180° microwave hybrid, as shown in Fig. 3(b). The notch depth of coaxial notch filter is also measured by VNA from 600 to 1200 MHz, the minimum and maximum notch depth are approximately 26 dB at 650 MHz and 57 dB at 800 MHz respectively. The notch depth of optical notch filter is also

[†] email address: zhuguangyu@impcas.ac.cn

measured by VNA from 600 to 1200 MHz, the minimum and maximum notch depth are approximately 40 dB at 750 MHz and 65 dB at 1050 MHz respectively.

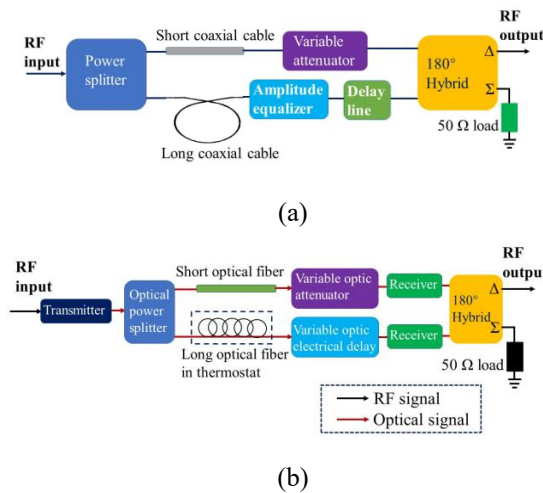


Figure 3: Schematic drawing of (a) coaxial cable notch filter with an amplitude equalizer, and (b) optical notch filter with an amplitude equalizer.

The total length of optical fiber in long branch is approximately 223 m in order to realize $1.11365 \mu\text{s}$ delay time for SRing stochastic cooling notch filter system. The frequency drift due to the change of temperature was measured using VNA, and the test results are shown in Table 1. The measurement results show that the frequency drift with phase-stabilized optical fiber from YOFC in the long branch is reduced by a factor of 8.5 at 600 MHz and a factor of 6 at 1200 MHz, compared with the normal optical fiber. The optical notch filter with phase-stabilized optical fiber prototype is built and tested, as shown in Fig. 4.

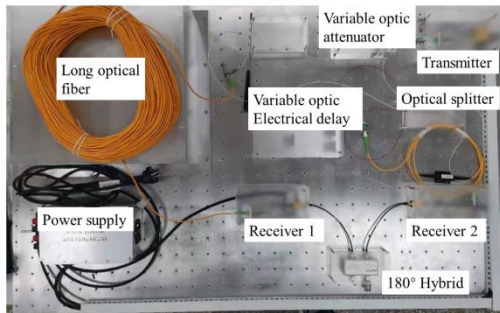


Figure 4: Photograph of optical notch filter hardware, note that the long optical fiber will be installed in the thermostat.

Table 1: Notch Frequency Drift of Two Types of Optical Fibers due to the Change of Temperature Including Both 223 m Normal and Phase-stabilized Optical Fiber in the Long Branch

Drift frequency (MHz)	Normal optical fiber (kHz/ °C)	Phase-stabilized optical fiber (kHz/ °C)
600	20.99	2.48
900	28.43	3.56
1200	39.76	6.67

BROADBAND PHASE SHIFTER

Phase shifter is one of the critical devices for both SRing stochastic cooling system, because it is essential for the correct sign of the momentum correction signal at the kicker. A digital broadband phase shifter is built with operating bandwidth from 0.15 GHz to 2 GHz consisting of a 3 dB 90° Hybrid Coupler, two 180° Microwave Hybrids, two program-controlled attenuators, two microwave switches and a 180° microwave hybrid as the combiner. The $3 \text{ dB } 90^\circ$ Hybrid Coupler, which is from Werlatone, plays a significant role for the phase shifter, and the 90° Hybrid splits the input signal into two paths with a 90° phase called the I- and Q- two way output signals. The bandwidth of the 90° Hybrid Coupler is from 0.15 GHz to 2 GHz.

The block diagram of the operating principle of the broadband phase shifter is shown in Fig. 5. The fabricated broadband digital phase shifter is shown in Fig. 6. The phase shifter provides a phase shift of $0\text{-}360^\circ$ in 512 discrete steps with 0.7° phase resolution. This phase shifter exhibits an insertion loss of $9 \pm 2 \text{ dB}$ and a RMS phase error is less than 5° in 0.15-2 GHz frequency range with a phase unbalance of less than $\pm 10^\circ$.

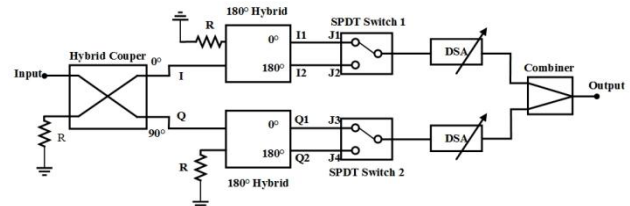


Figure 5: Block diagram of proposed method for the $0^\circ - 360^\circ$ broadband phase shifter.

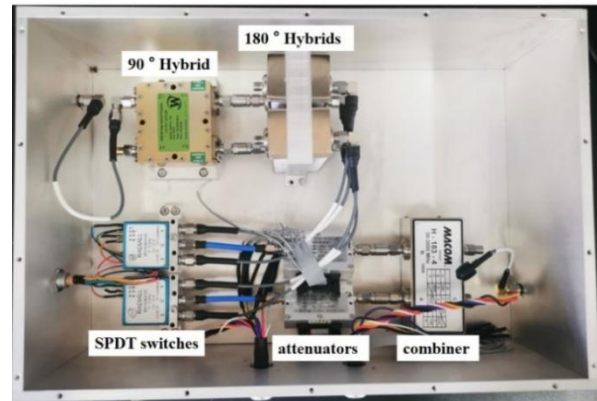


Figure 6: Photograph of the fabricated $0^\circ - 360^\circ$ broadband phase shifter.

PICKUP AND KICKER FOR SRING

The behavior of an electrode system when it functions as a pickup is intimately related to its behavior as a kicker due to the reciprocity between the kicker and pickup. In analyzing the behavior of an electrode system, it frequently proves easier to calculate its performance as a kicker, i.e., the response of the beam when the structure is powered externally, than its performance as a pickup, where a boundary-value problem must be solved, with the beam

current as a source term [5]. In this study, a power of 1 W is input into the kicker and the accelerating voltage is determined by integrating the electric field along a particle trajectory above the slots. The input power and beam voltage then yield the kicker shunt impedance, which is then converted to pickup shunt impedance, (modified by a factor of 1/4). The shunt impedance is the true efficiency of the kicker, which depends on the nature of the electrodes themselves, and not on the impedance of the input cable. The commercial simulation software ANSYS High Frequency Structure Simulation (HFSS) [6] was used for the longitudinal and transverse numerical simulations.

A Faltin prototype traveling wave structure for the HIAF SRing stochastic cooling system is developed and evaluated [3]. The Faltin electrode, which is used due to its low number of feedthroughs, robustness, and ease of manufacture, is a rectangular coaxial waveguide, with slots that couple to the beam. Figure 7 shows a photograph of a Faltin fabricated prototype for SRing. The wave in the pickup induced by the beam traveled parallel to the beam and at the same velocity, such that induction from the beam to the slotted coaxial waveguide through each slot was added constructively. Figure 8 is the result for the pickup shunt impedance from the HFSS simulation and from beam measurement with a $^{86}\text{Kr}^{30+}$ beam at energies of 476 MeV/u. There is very good agreement between the simulation and measurement results for the Faltin-type pickup shunt impedance.

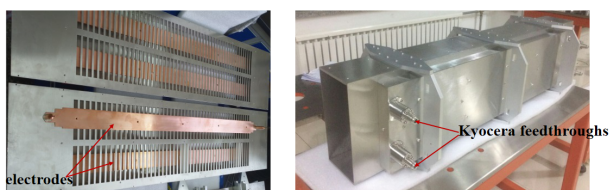


Figure 7: Photographs of a Faltin prototype structure, with eight Kyocera feed throughs. Left: before assembly, right: after assembly.

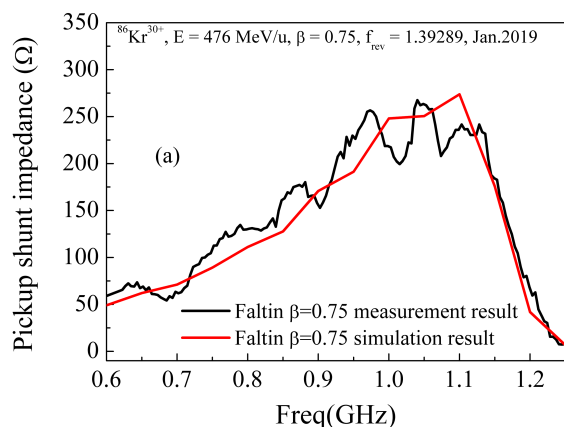


Figure 8: Faltin longitudinal pickup shunt impedance results from simulation and from beam measurement with a $^{86}\text{Kr}^{30+}$ beam energy = 476 MeV/u.

The slot-ring structure, which is a standing wave structure, was proposed originally by Lars Thorndahl and Rolf Stassen [7]. This slot-ring coupler, with a symmetric arrangement of 8 shorted electrodes gives a significantly higher longitudinal impedance than a comparable quarter-wave structure. The total image current passes the surrounding uninterrupted gap formed by two adjacent rings. The round cell is similar to a classical iris loaded linac cell, and is heavily loaded with eight 50 Ω coaxial lines to obtain the octave bandwidth. However, the disadvantages of a slot-ring structure directly installed in the vacuum tank are that it is very difficult to remove heat from a kicker when the combiner/divider board are in the vacuum rather than in the air. It also can not be used for ultra high vacuum conditions requiring a 250-300° high temperature bake-out. Finally, it is difficult to install and maintain when the slot-ring and combiner/divider board are in the vacuum tank.

A novel slot-ring prototype standing wave structure based on a ceramic vacuum chamber for the HIAF SRing stochastic cooling system are developed and evaluated [3]. Figure 9 shows a photograph of the 16 slot-ring cell structure, with a 16-way Wilkinson stripline type combiner and an 8 mm thickness ceramic vacuum chamber. Figure 10 shows a comparison of the pickup shunt impedance between the simulation result from the HFSS and the beam measurement using a $^{86}\text{Kr}^{30+}$ beam with energies of 476 MeV/u. Figure 10 shows that the pickup shunt impedance values suddenly decreased from 0.81 to 0.87 GHz, which was largely because there were some interference signal probably from cell phone signal or military radar station, and partly because alumina had 1% impurities, which could enhance adsorption and absorption of water vapor from the air, and partly because the impedance mismatch from feed throughs and adapter of cables which are not considered in the simulation.



Figure 9: Photograph of the 16 slot-ring cells structure, with 16-way Wilkinson stripline combiner-boards and an 8 mm thickness ceramic vacuum chamber.

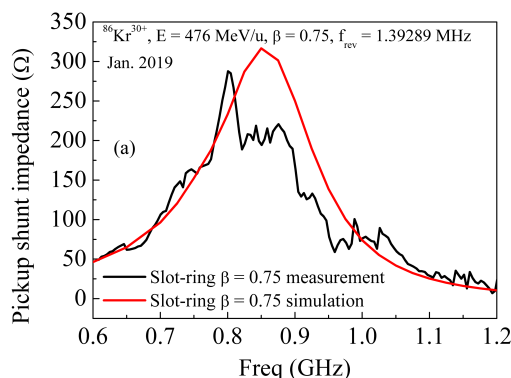


Figure 10: The slot-ring longitudinal pickup shunt impedance obtained with simulation and beam measurement: energy = 476 MeV/u.

CONCLUSION

Both a new coaxial notch filter and optical notch filter for the HIAF SRing stochastic cooling system with the operating bandwidth of 0.6 -1.2 GHz are built and evaluated. To improve the notch depth, a coaxial notch filter with amplitude equalizer in long branch is built and tested. The measurement results show the minimum and maximum notch depth are approximately 26 dB at 650 MHz and 57 dB at 800 MHz respectively. In addition, an optical notch filter with phase-stabilized optical fiber for the HIAF SRing stochastic cooling system is reported. The test results show that the minimum and maximum notch depth are approximately 40 dB at 750 MHz and 65 dB at 1050 MHz respectively, which is 14 dB larger than the value for coaxial notch filter of minimum notch depth 26 dB.

In addition, a high-resolution digital broadband phase shifter that is implemented by using the vector summation technology are built for SRing stochastic cooling. Test results show that the fabricated phase shifter has the phase resolution of 0.7°, the RMS phase error of less than 5°, the

phase unbalance less than $\pm 10^\circ$ and the amplitude flatness of less than ± 2 dB.

Finally, both a Faltin prototype traveling wave structure and a novel slot-ring prototype standing wave structure based on a ceramic vacuum chamber for the HIAF SRing stochastic cooling system are developed and manufactured. Pickup shunt impedance measurements for both the Faltin and slot-ring prototypes were found to agree well with the results of HFSS simulations, indicating that the simulation results are reliable.

ACKNOWLEDGEMENTS

The authors would like to thank Fritz Caspers and Lars Thorndahl from CERN, Rolf Stassen from Juelich, Fritz Nolden from GSI for their supports.

REFERENCES

- [1] J. C. Yang *et al.*, “High intensity heavy ion accelerator facility (HIAF) in China”, *Nucl. Instrum. Methods Phys. Res., Sect. B*, vol. 317, pp. 263–265, 2013. doi:10.1016/j.nimb.2013.08.046
- [2] B. Wu *et al.*, “The design of the spectrometer ring at the HIAF”, *Nucl. Instrum. Methods Phys. Res., Sect. A*, vol. 881, pp. 27–35, 2018. doi:10.1016/j.nima.2017.08.017
- [3] G.Y. Zhu *et al.*, “Stochastic cooling pickup/kicker developments for the high-precision spectrometer ring in the HIAF project at IMP”, *IEEE Trans. Nucl. Sci.*, vol. 68, no. 1, p. 9, 2021. doi:10.1109/TNS.2020.3038525
- [4] G.Y. Zhu *et al.*, “Stochastic cooling notch filter developments for the high-precision spectrometer ring in the high intensity heavy-ion accelerator facility project”, *Rev. Sci. Instrum.*, vol. 94, p. 093302, 2023. doi:10.1063/5.0166975
- [5] D.A. Goldberg and G.R. Lambertson, “Dynamic Devices: A Primer on Pickups and Kickers”, *AIP Conf. Proc.* 249, pp. 537–600, 1992. doi:10.1063/1.41979
- [6] <http://www.ansys.com>
- [7] R. Stassen, P. Brittner, R. Greven, H. Singer, H. Stockhorst, L. Thorndahl, “Recent developments for the HESR stochastic cooling system”, in *Proc. COOL’07*, Bad Kreuznach, Germany, Sep. 2007, paper THAP13, pp. 191-193.

NUMERICAL STUDY OF THE WIGGLER-BASED MICROBUNCHING AMPLIFIER FOR EIC*

C. Hall, RadiaSoft LLC, CO, Boulder, USA

A. Zholents[†], Argonne National Laboratory, Argonne, IL, USA

Abstract

An amplifier of microbunching instability in the electron beam employing wiggler magnets is considered. A lattice design is described. The impact of the SASE FEL resonance is analysed. A setup for macro particle tracking and a method for microbunching gain determination is presented. Calculations demonstrate feasibility of a broad band amplifier with a large gain.

INTRODUCTION

Coherent electron cooling [1] using a plasma-cascade amplifier (PCA) [2] can provide significantly faster cooling of hadrons than the conventional method of microwave stochastic cooling due to the wide bandwidth of a pickup, a kicker, and an amplifier. The PCA creates unstable plasma oscillations by varying the transverse beam size along the beam line, thus modulating the plasma frequency. An alternative approach to the amplifier is to modulate the plasma frequency by a sequence of wiggler magnets separated by weak chicanes [3]. Numerical simulations of the gain function are done using OPAL-FEL code [4] and the electron beam parameters projected for the Electron Ion Collider.

LATTICE OF THE AMPLIFIER UNIT

The basic cell of the Wiggler Enhanced Plasma Amplifier (WEPA) is composed of a wiggler and quadrupole triplet, with the triplet providing transverse matching into subsequent cells. Parameters of the wigglers used in all simulations presented here are given in Table 1.

Table 1: Wiggler Parameters

Parameter	Value	Unit
Wiggler length ℓ_w	1.188	m
Wiggler period λ_w	3.3	cm
Wiggler parameter K_w	1.5	
Wiggler peak magnetic field B_{peak}	0.487	T
Bending radius ρ	1.076	m
Wiggler magnetic gap	16.0	mm

Chicanes are placed to convert the accumulated energy modulation into additional density modulation after a set of cells. Two identical chicanes are used for convenience. We refer to a set of several wiggler and triplet cells, followed by chicanes as a single amplifier *unit*. The total length occupied by the chicanes is equal to the wiggler length such as to

* Work supported by the Director, Office of Science, of the U.S. Department of Energy under Contract No. DE-AC02-06CH11357

[†] azholents@anl.gov

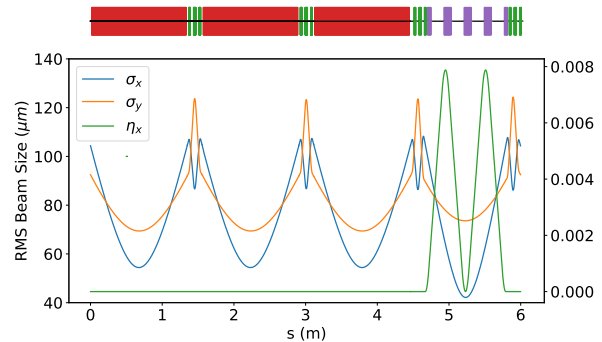


Figure 1: Lattice of a single amplifier unit with three cells followed by two chicanes. Transverse RMS beam sizes and dispersion function are shown. Locations of wigglers, triplets, and chicanes are shown at the top.

minimize a perturbation to the lattice. The basic chicane parameters are given in Table 2.

Table 2: Chicane Parameters

Parameter	Value	Unit
R_{56}	0.5×10^{-3}	m
Dipole length l_b	0.05	m
Dipole bend angle θ_b	1.96	degrees
Dipole field	0.04	T
Chicane leg L	0.18	m

Accounting for the wiggler focusing and transverse space charge effects necessitated slight modifications to the matched Twiss functions and focusing strengths of the quadrupoles comparing to a lattice in which drifts are used instead of the wigglers. To ensure that a wiggler and triplet cell is matched a numerical optimization of the initial transverse conditions of the bunch and the quadrupole strengths in the triplet was carried out with particle tracking through one cell in OPAL-FEL.

The main concerns related to use of the chicanes in the lattice are the nonlinear compression terms and coherent synchrotron radiation (CSR). Because of a small R_{56} , the weak dipoles are used and the overall impact of non-linearity and CSR is small. Indeed, the growth in energy spread in the chicane after the second amplifier unit for a bunch with peak current of 165 A and with an initial modulation wavelength of $2.88 \mu\text{m}$, where the gain in the second unit is close to 80, is around 7%. The simulations for the chicane were carried out using the particle tracking code elegant [5]. The resulting matched beam with lattice overlaid is shown for a three-cell unit in Fig. 1. For simulations involving more

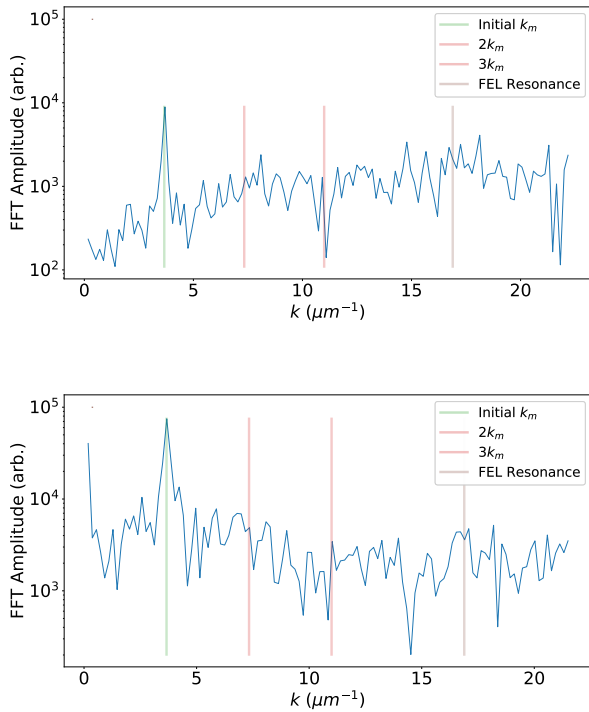


Figure 2: Peak current spectrum of a bunch initially modulated at a frequency with the wave vector $k_m = 3.67 \mu\text{m}^{-1}$ show after one wiggler (top), after three wigglers and the chicane (bottom).

than one unit the matching between units was performed with a zero-length matrix transformation.

SASE FEL RESONANCE

It was found that it is important to select the wiggler parameter $K_w = 1.5$ such that the range of the microbunching spectrum utilized in the process of hadron cooling is below the SASE FEL resonance wave vector $k_{\text{sase}} = 16.89 \mu\text{m}^{-1}$. For initial density modulation with the wavelengths nearby the FEL resonance the gain was observed to drop considerably. An additional consideration, even when the resonance lies outside the region of interest on the gain spectrum, is to ensure that the microbunching at this wave vector does not grow much beyond the noise. This is one of the reasons to divide the WEPA lattice into a set of cells with several wigglers followed by a chicane. Passage through the chicanes partially destroys the accumulated microbunching growth due to incoherent energy spread in the electron beam.

Shown in Fig. 2 are the current spectra for the bunch after the first and third wigglers. The gain between wiggler one and three of the FEL resonance is approximately 1.5. After the chicane, the amplitude of the resonance is reduced by 20 %.

SIMULATION SETUP

To study gain in a systematic fashion the longitudinal distribution of the electron bunch is prepared with a core of uniform density n_0 . Added on top of this is a small sinusoidal density modulation with amplitude of Δn . So that the density in the core is $n_C(z) = \Delta n \sin kz + n_0$ for a modulation wave vector of $k = 2\pi/\lambda$. To ameliorate the impact of space charge from the finite length of the bunch the tails of the longitudinal distribution are sampled from the error function $\text{erf}(z/\hat{z})$ where \hat{z} is typically several tens of micron long. This results in a piece-wise density function for the two tails and core. To sample from this distribution the cumulative distribution function (CDF) for this piece-wise density function is numerically calculated on a uniform grid of 10 000 points. The inverse CDF is then obtained by interpolating the inverse of the CDF grid values using a third-order spline interpolation. Samples are then drawn from a Halton sequence [6] on the unit interval and evaluated with the inverse CDF to complete the longitudinal distribution creation.

We also employ a “tail refresh” procedure whereby the tails of the bunch are cut off after each wiggler and replaced with fresh tails draw from the same erf distribution as described above. The amplitude of the distribution is matched to the edges of the core on either end to ensure that no significant jumps in the current are introduced. This procedure allows even badly distorted tails to be replaced in an automatic fashion. This allows the impact of the core from spurious space charge forces at the bunch edges to be reduced and improve the accuracy of the gain measurement.

GAIN DETERMINATION

To measure gain particles in the tails of the longitudinal distribution are cut, leaving the bunch core. The longitudinal distribution is binned, with bin size typically chosen such that the resonant frequency is outside the Nyquist limit and cannot be resolved. Determination of the gain relies on the numerical analysis of fundamental frequencies (NAFF) algorithm [7] as implemented in the `sddsnaff`¹ and `NAFFlib` [8] libraries. The NAFF algorithm, in general, begins by taking the fast Fourier transform (FFT) of the signal to find the approximate frequencies of interest. The frequencies f and their corresponding amplitudes may then be resolved to high accuracy by maximizing the Fourier integral:

$$\phi(f) = \langle \psi(t), e^{i2\pi f t} \rangle = \frac{1}{T} \int_0^T \psi(t) e^{-i2\pi f t} x(t) dt, \quad (1)$$

where $\psi(t)$ is the time domain signal of interest and $x(t)$ is a windowing function. For both `sddsnaff` and `NAFFlib` the Hanning window was used. Finally, to get the fractional modulation depth the frequency component amplitude from FFT or NAFF must be divided by the average density.

¹ <https://ops.aps.anl.gov/manuals/SDDStoolkit/SDDStoolkitsu63.html>

WEPA GAIN SIMULATION RESULTS

Base electron bunch parameters used in simulation are given in Table 3. Grid and macroparticles parameters are given in Table 4.

Table 3: Electron Beam Parameters

Parameter	Value	Unit
Beam energy, \mathcal{E}_0	157	MeV
Peak current	50, 100, 165	A
Relative energy spread, $\sigma_{\mathcal{E}}$	2×10^{-4}	
Normalized emittance, ϵ_x/ϵ_y	2.2, 2.2	μm
Average beta-function, β_x/β_y	0.75, 0.84	m
rms beam size, σ_x/σ_y	72, 77	μm

Table 4: Simulation Parameters

Parameter	Value	Unit
Domain size, L_x, L_y, L_z	1700, 1700, 90	μm
Grid dimensions, $\Delta_x, \Delta_y, \Delta_z$	10, 10, 0.0286	μm
Macroparticles, N_p	8×10^6	

Here we present the results from simulations of the microbunching amplifier with two amplification units. Each unit comprises a series of three identical wigglers joined by matching triplets. After each set of wigglers a series of two chicanes is used to convert the developed energy modulation into density modulation. Simulations use tail-refresh method and tracking through the chicane with CSR included. The chicane section was simulated in eLlegant and includes nonlinear terms in the transport and CSR.

In simulations the gain was observed to saturate after three wiggler sections. This result differs from theory, which predicts that gain should steadily increase with longer (more) wigglers. Since this saturation was consistent across simulation parameters the choice was made to use units of three wigglers for multi-unit simulations, to reduce compute time.

Figure 3 shows the microbunching gain in simulations using the electron bunch with the flat-top peak current of 165, 100, and 50 A.

CONCLUSION

Gain in density modulation has been studied through simulations using the OPAL-FEL code for the wiggler-enhanced plasma amplifier. Care was taken to control for nonphysical numerical effects and limitations in the simulation to achieve accurate determination of the gain as a function of the wavelength of initial density modulation. These results will be compared with the analytical calculations in a forthcoming publication.

REFERENCES

[1] V. N. Litvinenko and Y. S. Derbenev, “Coherent electron cooling”, *Phys. Rev. Lett.*, vol. 102, no. 11, p. 114 801, 2009.
doi:10.1103/PhysRevLett.102.114801

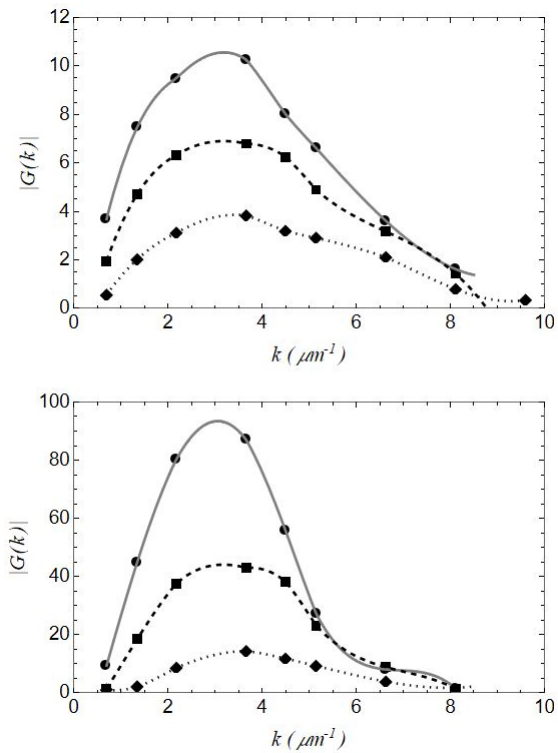


Figure 3: Gain after amplifier Unit 1 (top panel) and after amplifier Unit 2 (bottom panel) calculated using 165, 100, and 50 A peak currents. Data points are connected with solid, dashed and dotted lines for convenience.

[2] V. N. Litvinenko *et al.*, “Plasma-cascade instability”, *Phys. Rev. Accel. Beams*, vol. 24, no. 1, p. 014 402, 2021.
doi:10.1103/PhysRevAccelBeams.24.014402

[3] G. Stupakov and A. Zholents, “Wiggler Enhanced Plasma Amplifier for Coherent Electron Cooling”, in *Proc. COOL’21*, Novosibirsk, Russia, 2021, paper S803, pp. 62–65.
doi:10.18429/JACoW-COOL2021-S803

[4] A. Albà *et al.*, “Benchmarking collective effects of electron interactions in a wiggler with OPAL-FEL”, *Computer Physics Communications*, vol. 280, p. 108 475, 2022.
doi:10.1016/j.cpc.2022.108475

[5] M. Borland, “elegant: A flexible SDDS-compliant code for accelerator simulation”, Argonne National Laboratory, Rep. LS-287, 2000.

[6] M. Borland, “Modeling of the microbunching instability”, *Phys. Rev. ST Accel. Beams*, vol. 11, no. 3, p. 030 701, 2008.
doi:10.1103/PhysRevSTAB.11.030701

[7] J. Laskar, C. Froeschlé, and A. Celletti, “The measure of chaos by the numerical analysis of the fundamental frequencies. application to the standard mapping”, *Physica D: Nonlinear Phenomena*, vol. 56, no. 2-3, pp. 253–269, 1992.
doi:10.1016/0167-2789(92)90028-L

[8] S. Kostoglou, N. Karastathis, Y. Papaphilippou, D. Pellegrini, and P. Zisopoulos, “Development of computational tools for noise studies in the LHC”, in *Proc. IPAC’17*, Copenhagen, Denmark, May 2017, 2017, pp. 3807–3810.
doi:10.18429/JACoW-IPAC2017-THPAB044

SELF BUNCHING, RF BUNCHING AND COOLING OF IONS IN AN ELECTROSTATIC ION BEAM TRAP

D. Sharma^{1,*}, D. Zajfman¹, O. Heber¹, R. Ringle²

¹Department of Particle Physics and Astrophysics, Weizmann Institute of Science, Rehovot, Israel

²Department of Physics and Astronomy, Michigan State University, East Lansing, Michigan, USA

Abstract

We describe the beam dynamics in an electrostatic ion beam trap (EIBT). The ion-ion interaction plays a crucial role in governing the beam dynamics in the trap. We show that the EIBT can serve as a unique device for phase space manipulation of the ions. Three important results are presented: 1. Self-bunching of ions where the ion-ion interaction which is a repulsive Coulombic interaction provides the necessary coupling to keep the ions synchronized, 2. RF bunching of ions, where the repulsive ion-ion interaction keeps the ion bunch localized in the RF bucket and suppresses the emittance growth, 3. Auto-resonance cooling of ions, where a slice from phase space is accelerated out and cooled by evaporation.

ELECTROSTATIC ION BEAM TRAP

Electrostatic ion beam trap is a unique and versatile device to store ion beam with no mass limit [1]. A schematic is shown in Fig. 1. The ions are trapped between two sets of mirror electrodes. The motion of ions is detected by the pickup electrode placed at the center of the trap. The inner electrodes for the two mirrors are at the ground which provides a field free region in the trap. The ions dynamics in the trap are governed by the slip factor η ,

$$\eta = -\frac{2E}{f} \frac{df}{dE},$$

where f represents the oscillation frequency of the ion trapped in EIBT with energy E . The trap can be operated

in dispersive or self-bunching regime by changing the sign of the slip factor which is decided by the potential profile in the trap. An external time-dependent voltage can be applied to V_5 of the mirror electrode (see in Fig. 1). A bunch of positively charged SF_5^+ ions produced by the Even-Lavie ion source is accelerated to 4.2 keV, focused, and steered using the Einzel lens and XY deflector before being injected into the trap. The density of ions in the trapped can be monitored by adjusting the voltage on the entrance electrode V_p . The time signal obtained from the pick-up electrode is collected by a digitizer and analysed using Fourier transform to obtain the frequency distribution of the ions bunch. This trap is unique and different from the other storage rings or trap devices, since the ion density oscillates in the trap. A typical number of ions in a bunch in the field-free region is $10^5 - 10^7$. The ion density in the turning point can be $\sim 10^3$ orders higher than the field-free region. The ion-ion interaction (collisions) is important at the turning point and affects the beam dynamics in the trap. The ion-ion interaction also couples the transverse and longitudinal beam dynamics in the trap. The dynamics of ions in the trap can be simulated with a simulation technique based on particle-in-cell (2DCYLPIC). The simulation can consider the space charge effect and all the experimental results are well reproduced [2].

DISPERSION AND SELF BUNCHING

When a bunch of ions are injected in the EIBT, depending on the potential profile either it will disperse or stay localized in the trap. The dispersion and synchronization of ions in EIBT are studied very well with detail [3, 4]. A

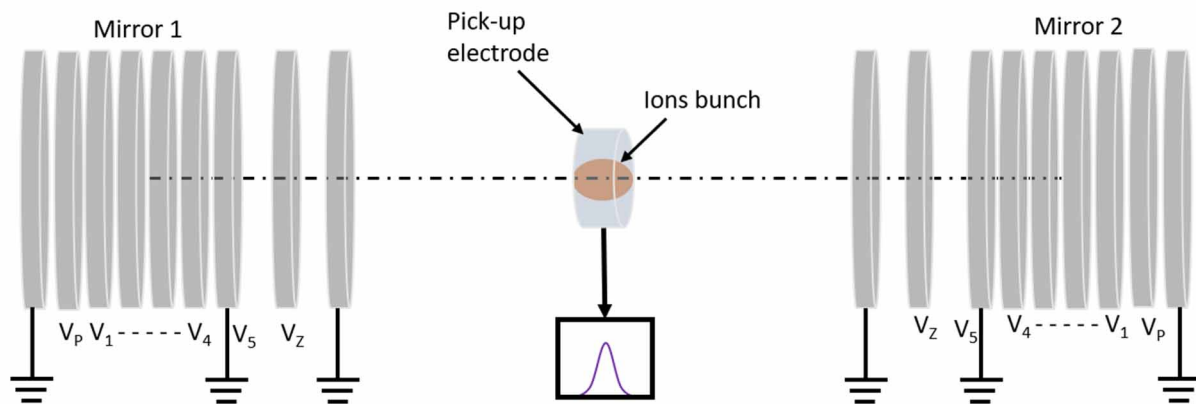


Figure 1: A schematic of electrostatic ion beam trap. The ions are trapped between two sets of mirror electrodes and the passage of ions bunch is monitored by pick-up electrode.

* deepaks4894@gmail.com

synchronization mode is: ($V_p = 5.75$ kV, $V_1 = 6.5$ kV, $V_2 = 4.875$ kV, $V_3 = 3.25$ kV, $V_4 = 1.625$ kV and $V_z = 3.4$ kV) and ($V_p = 4.05$ kV, $V_1 = 4.7$ kV, $V_2 = 4.875$ kV, $V_3 = 3.25$ kV, $V_4 = 1.625$ kV and $V_z = 4.05$ kV). When the trap is operated in the dispersive mode, the ion-ion interaction further increases the dispersion resulting in “enhanced diffusion” of ions. To keep the ions in the bunch, an external time-dependent field can be applied. This is addressed in the next section. The self-bunching of ions can be understood from the synchronization of ions in the EIBT. A non-linear interaction between two periodic systems that are oscillating with nearby frequencies results in synchronization. Inside the trap, the ions have a frequency distribution and strong ion-ion interactions in the mirror region provide the necessary coupling for synchronization. A one-dimensional analytical model for the self-bunching effect is described by Strasser *et al.* [5]. This effect is attributed to negative mass instability. A similar effect is observed in accelerators after the transition energy which results in a change in sign of slip factor.

RF BUNCHING

The most common technique to keep the ions in a bunch is RF bunching. An external time-dependent field is applied with the same frequency or high harmonics as the oscillation frequency of the ions. The synchronous particle is phase-matched (π or 0) with the external (stationary RF bucket). The high-energy ions will be decelerated and vice versa. The ions will oscillate in the longitudinal phase space around the synchronous ions and stay localized. The separatrix defines the boundary in phase space where the ions with maximum phase offset will stay in closed orbit. The oscillation frequency, commonly known as the synchrotron frequency depends on the phase offset. The oscillation frequency decreases with increased phase offset. This non-linearity results in phase space filamentation. The area occupied by the ions in phase space can be estimated by root mean square (rms) emittance. The filamentation in phase space can be estimated by the increase in rms emittance.

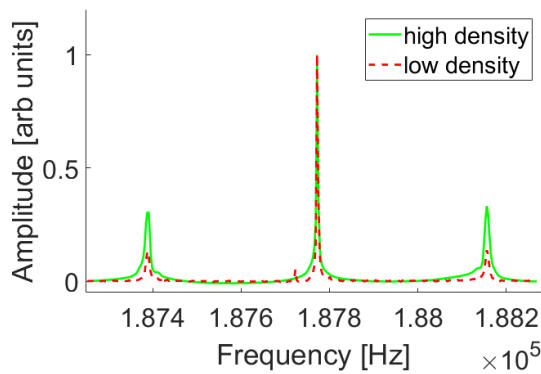


Figure 2: Experimentally observed FT spectrum for two different ion density when external RF field is applied.

When the trap is operated in dispersive mode, an external time-dependent field can be applied to one of the electrodes (V_5 in this case) for the entrance electrode.

The longitudinal motions of ions in the RF bucket result in additional side peaks in the FT spectrum obtained from the time signal from the pick-up detector [6]. If the RF bucket is uniformly filled, the height of the side peaks will be suppressed. The experimental results for RF bunching of ions in EIBT for two different ion densities are shown in Fig. 2. The relative height of side peaks is highly suppressed for low ion density resulting in a uniform distribution of ions in the RF bucket. Figure 3 shows the simulation results for relative emittance growth in the RF bucket for different ion densities. It is very counterintuitive that the emittance growth is suppressed for high ion density. The simulation results support the experimental observation.

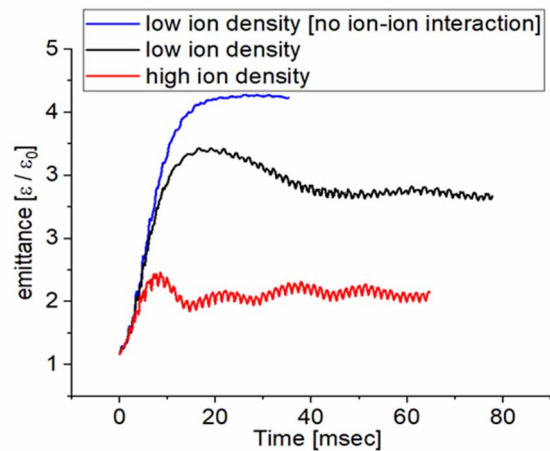


Figure 3: Emittance growth in RF bucket for different ion densities calculated from particle-in-cell (PIC) simulation.

The suppression of emittance growth for high intensity resembles the self-bunching effect in EIBT, the slip factor for the RF bucket has similar sign. A repulsive Coulombic interaction provided the necessary coupling to keep the ions localized in phase space [7].

AUTO-RESONANCE COOLING

In auto-resonance (AR), a periodic nonlinear physical system can be phase-locked with an external chirped driving force if the external force is adiabatic and exceeds a threshold value. An ion bunch injected in the trap will disperse after some time and the Schottky noise gives the initial frequency distribution of ions in the trap (black data point in Fig. 4). The spread in frequency distribution depends on the initial velocity distribution of ions in the trap determine the beam temperature. AR process has been demonstrated in an electrostatic ion beam trap where the beam temperature is reduced to well below 1 K [8].

Instead of applying a constant RF voltage, a chirped sinusoidal voltage is applied on V_5 . In this process, a slice of phase space is accelerated out from the initial distribution. Depending on the amplitude and rate of the chirp voltage, one can control the final distribution of the ions. The ions that do not satisfy the AR condition evaporate and transfer momentum for cooling.

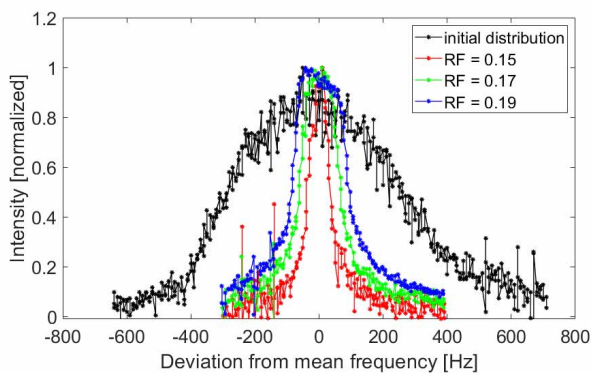


Figure 4: The frequency distribution of SF_5^+ ions in the trap. Black: the initial distribution of the ions. Red, Green, Blue: The distribution of dragged peak for different RF voltages.

Figure 4 shows the distribution of dragged peaks for different dragging voltages. The width of the frequency distribution shows the beam temperature. The sigma of the dragged peak increases linearly with an increase in dragged voltage. The amplitude increases linearly up to a certain voltage and does not change after that, showing that no more ions are lost from the dragged bunch. The dragged ion intensity shows a nonlinear dependence on the initial ion density. The ion-ion interaction strongly influences the AR process and influence the phase space density.

The distribution of the dragged peak on dragging voltage does not conform to the increase in phase space density (cooling). To demonstrate an increase in PSD, the amplitude of external voltage is decreased linearly during the AR process. For a constant sigma, the dragged peak can be increased which shows that more ions can be dragged to the same final position and velocity distribution. Different approaches can be used to show an increase in the phase space density along the AR process.

CONCLUSION

In summary, we have demonstrated the beam dynamics in an electrostatic ion beam trap. The ion density in the trap is not constant but keeps oscillating. The enhanced ion-ion interaction in the mirror region strongly influences the beam dynamics. The trap can be operated in diffusive or

self-bunching mode. The dynamics of ions under an external time-dependent field are shown. The ions bunch stays localized in the RF bucket for high ion density. The ion temperature in the trap can be reduced to less than 1 K by a novel method of auto-resonance dragging of ions. In general, EIBT can serve as a tool for phase space manipulation of ions beam at low energy.

ACKNOWLEDGEMENT

The work is supported by Israel Science Foundation Grant No. 3874/21 and US National Science Foundation Grant No. PHY-2111185. Computation resources are provided by WEXAC at Weizmann Institute of Science and High-Performance Computing Facility at Michigan State University.

REFERENCES

- [1] D. Zajfman *et al.*, “Electrostatic bottle for long time storage of fast ion beams”, *Phys. Rev. A.*, vol. 55, p. R1577, Mar. 1997. doi:10.1103/PhysRevA.55.R1577
- [2] D. Gupta *et al.*, “Particle-in-cell techniques for the study of space charge effects in an electrostatic ion beam trap”, *Phys. Rev. E.*, vol. 104, p. 065202, Dec. 2021. doi:10.1103/PhysRevE.104.065202
- [3] H. B. Pederson *et al.*, “Ion Motion Synchronization in an Ion-Trap Resonator”, *Phys. Rev. Lett.*, vol. 87, p. 055001, Jul. 2001. doi:10.1103/PhysRevLett.87.055001
- [4] H. B. Pederson *et al.*, “Diffusion and synchronization in an ion-trap resonator”, *Phys. Rev. A.*, vol. 65, p. 042704, Mar. 2002. doi:10.1103/PhysRevA.65.042704
- [5] D. Strasser *et al.*, “Negative Mass Instability for Interacting Particles in a 1D Box: Theory and Application”, *Phys. Rev. Lett.*, vol. 89, p. 283204, Dec. 2002. doi:10.1103/PhysRevLett.89.283204
- [6] D. Gupta *et al.*, “Time-dependent dynamics of radio-frequency-bunched ions in an electrostatic ion beam trap”, *Phys. Rev. E.*, vol. 107, p. 045202, Apr. 2023. doi:10.1103/PhysRevE.107.045202
- [7] D. Sharma *et al.*, “Ion-ion interaction induced non-dispersive dynamics”, submitted for publication.
- [8] R. Gangwar *et al.*, “Autoresonance Cooling of Ions in an Electrostatic Ion Beam Trap”, *Phys. Rev. Lett.*, vol. 119, p. 103202, Sep. 2017. doi:10.1103/PhysRevLett.119.103202

THEORETICAL AND SIMULATION STUDY OF DISPERSIVE ELECTRON COOLING *

H. Zhao[†], L.J. Mao, M.T. Tang, F. Ma, X.D. Yang, J.C. Yang

Institute of Modern Physics, Chinese Academy of Sciences, Lanzhou, China

Abstract

In electron cooling, the transverse cooling rate is usually smaller than the longitudinal rate, especially at high energies. By introducing dispersive cooling, it is possible to redistribute the cooling rate between longitudinal and transverse planes. Theoretically, achieving dispersive electron cooling requires an ion dispersion and a transverse gradient of longitudinal cooling force. The latter depends on many factors such as beam energy offset, transverse displacement, e-beam density distribution and space charge effect. Therefore, several methods can be employed to achieve dispersive electron cooling based on these factors. In this paper, these factors and their respective impacts on the cooling rate are discussed. Based on a linear friction force model, we propose a simple formula to numerically estimate the cooling rate redistribution effect of these methods. The analytical results are in good agreement with Monte-Carlo calculation and numerical simulation.

INTRODUCTION

In theory, dispersive cooling requires both ion beam dispersion and a transverse gradient of the longitudinal cooling force [1]. To simply explain that, we assume an off-momentum particle passing through the cooling section with a dispersion function D , and only consider the longitudinal cooling with a linear cooling force $\Delta\delta_p = -\lambda\delta_p$, the particle coordinate after cooling can be written by

$$x_{\beta 2} = x - D\delta_{p2} = x_{\beta 1} + D\lambda\delta_{p1}, \quad (1)$$

where x_{β} denotes the betatron oscillation, and x is the real coordinate which is assumed to be unchanged during passing through the cooling section. If the cooling coefficient λ is a constant, the amplitude of the betatron oscillation keeps unchanged $x_{\beta 2} = x_{\beta 1}$, which means that there is no cooling contribution from the longitudinal direction to the transverse. Otherwise, if the cooling force has a transverse gradient, for example $\lambda(x) = (M - |x|)\lambda_0$ with $M > \text{Max}[x]$, the amplitude of the oscillation turns to $x_{\beta 2} \approx (1 - \lambda_0|D\delta_{p1}|)x_{\beta 1}$. It indicates amplitude damping of the betatron motion. A schematic plot of these two processes is shown in Fig. 1, where the x -axis represents betatron oscillation under longitudinal cooling of the y -axis. It clearly shows the amplitude damping process with an appropriate longitudinal cooling force setting, i.e. dispersive cooling.

We see that the transverse gradient of the longitudinal cooling force plays a key role in dispersive electron cool-

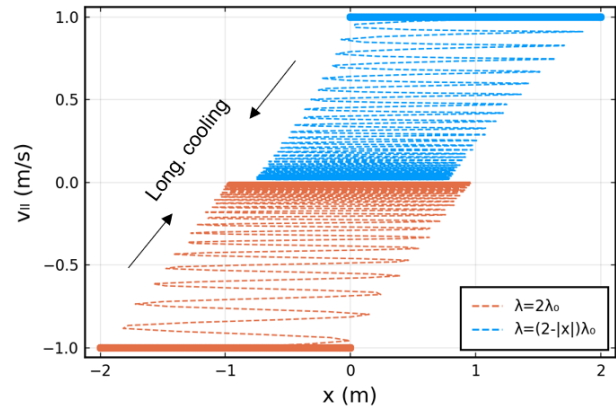


Figure 1: Comparison of the cooling process with two sets of longitudinal cooling force. It demonstrates that a dispersion and a transverse gradient of the longitudinal cooling force are necessary for dispersive cooling ($x_{\beta} = 1$ m, $D = 1$ m, $\delta_p = \pm 1$, $\lambda_0 = 0.01$).

ing. Some experimental and simulation studies have demonstrated several approaches to obtain this gradient. As indicated in Ref. [2, 3], one approach is to introduce a displacement between electron and ion beams, utilizing the parabolic velocity profile of the electrons caused by its space charge. Another method is by using an energy offset, a displacement and a transverse density gradient of the e-beam [4]. Recently, it has been demonstrated that an e-beam with Gaussian transverse distribution can naturally provide this transverse gradient, thus achieving dispersive cooling [5]. At the same time, it shows that electron dispersion is also beneficial to dispersive cooling. In this article, we conduct theoretical and simulation studies of these methods and show how they affect the cooling rate. Based on the linear cooling force model, we finally propose a simple formula to numerically estimate the cooling rate redistribution effect of these methods, and the analytical result agrees well with Monte-Carlo calculation and numerical simulation.

DISPERSIVE ELECTRON COOLING

To begin with, we assume a linear cooling force $\Delta u = -Cn_e u$ both in transverse and longitudinal directions, where n_e is the electron beam density, C is the cooling coefficient which depends on the velocity distribution of the electron beam. Consider a beam displacement x_o , an energy offset δ_o , and horizontal dispersion D of ions in the cooling section, the momentum change of a single particle after cooling can be described by $\Delta\delta \approx -C_p n_e (\delta - \delta_e - \delta_o)$, where $\delta_e = K_{sc}(x^2 + y_{\beta}^2)$ is the electron momentum deviation due

* Work supported by the National Natural Science Foundation of China

[†] hezhao@impcas.ac.cn

to space charge, and $x = x_\beta + x_o + D\delta$. Then we have

$$\Delta\delta^2 \simeq -2C_p n_e \delta^2 + 2C_p n_e \delta \delta_o + 2C_p n_e K_{sc} \delta (x^2 + y_\beta^2). \quad (2)$$

In the transverse direction, we only discuss the horizontal direction. Assume $\alpha = 0$ and ignore the betatron evolution in the cooling section, the single particle emittance is $\epsilon_x = (x - x_o - D\delta)^2 / 2\beta_x + \beta_x x'^2 / 2$, and the cooling effect can be written by

$$\Delta\epsilon_x \simeq -Dx_\beta \Delta\delta / \beta_x + \beta_x x' \Delta x', \quad (3)$$

where $\Delta x' = -C_x n_e (x' - x'_e)$, $x'_e = L_{sc} \sqrt{x^2 + y_\beta^2}$ is the drift velocity caused by the space charge and magnetic fields.

Expanding Eqs. (2)–(3) and ignoring high-order and non-correlated terms, the longitudinal and horizontal cooling effects of the ion beam can be described as

$$\begin{aligned} \langle \Delta\delta^2 \rangle &= -2C_p \langle n_e \delta^2 \rangle + 2C_p \delta_o \langle n_e \delta \rangle \\ &\quad + 2C_p K_{sc} x_o (x_o \langle n_e \delta \rangle + 2 \langle n_e x_\beta \delta \rangle + 2D \langle n_e \delta^2 \rangle) \\ \langle \Delta\epsilon \rangle &= -C_x \epsilon_0 \langle n_e \rangle + \frac{C_p D}{\beta_x} \langle n_e x_\beta \delta \rangle - \frac{C_p D \delta_o}{\beta_x} \langle n_e x_\beta \rangle \\ &\quad - \frac{C_p D K_{sc} x_o}{\beta_x} (x_o \langle n_e x_\beta \rangle + 2 \langle n_e x_\beta^2 \rangle + 2D \langle n_e x_\beta \delta \rangle), \end{aligned} \quad (4)$$

where $\langle \rangle$ denotes averaging over the ion beam phase space, $n_e(x, y, s)$ is the local density of the e-beam which depends on the position of ion particles. The equations show that energy offset, beam displacement, space charge effect as well as e-beam density are the main factors affecting the cooling rate, and that the coupling between position, momentum, and e-beam density caused by dispersion is the reason for this. The term related to drift velocity is eliminated as it has no correlation with longitudinal cooling. Based on the ion and electron beam distributions, Eq. (4) can be calculated analytically according to the law of the unconscious statistician (LOTUS) [6]. As shown in Ref. [5], the cooling rate redistribution for the e-beam with a Gaussian profile is studied. In this section, we will discuss the effect of rate redistribution for both Gaussian and uniform electron beams, while including all the mentioned factors.

We define the gain factor as the ratio of the two cooling rates with and without dispersion and other factors $k = \lambda / \lambda_0$, where $\lambda_p = \langle \Delta\delta^2 \rangle / \delta_p^2$, $\lambda_x = \langle \Delta\epsilon \rangle / \epsilon_0$ are the longitudinal and horizontal cooling rates, and δ_p , ϵ_0 are the rms momentum spread and emittance, respectively. Also, we always assume a DC e-beam, so that only transverse distribution is discussed. Using the same method in Ref. [5], several cases that can realize dispersive electron cooling are studied based on the e-beams with transverse Gaussian and uniform distributions. Moreover, a Monte-Carlo calculation based on Eq. (4) is performed and compared with the analytical formula.

Case 1: Gaussian E-Beam with Energy Offset Δ_o and Beam Displacement X_o

As Y. S. Derbenev introduced in Ref. [1, 4], dispersive electron cooling can be achieved by a longitudinal velocity

offset, a beam displacement as well as a transverse gradient of electron density. For this case, we use a Gaussian e-beam to produce the transverse density gradient

$$n_e = n_{e0} \exp\left[-\frac{(x_\beta + x_o + D\delta)^2}{2\sigma_{ex}^2} - \frac{y_\beta^2}{2\sigma_{ey}^2} - \frac{s^2}{2\sigma_{es}^2}\right]. \quad (5)$$

Furthermore, we assume that the ion beam also has a Gaussian distribution in the transverse direction. Then, Eq. (4) can be calculated and the final result of the gain factor is

$$\begin{aligned} a &= \sqrt{\sigma_{ex}^2 + \sigma_{ix}^2} \\ b &= \sqrt{\sigma_{ex}^2 + \sigma_{ix}^2 + D^2 \delta_p^2} \\ k_p &= e^{-\frac{x_o^2}{2b^2}} \left[\frac{a^3}{b^3} + \frac{a}{b^5} D^2 \delta_p^2 x_o^2 + \frac{a}{b^3} D \delta_o x_o \right] \\ k_x &= e^{-\frac{x_o^2}{2b^2}} \left[\frac{a}{b} + \frac{C_p a}{C_x b^5} D^2 \delta_p^2 (b^2 - x_o^2) - \frac{C_p a}{C_x b^3} D \delta_o x_o \right]. \end{aligned} \quad (6)$$

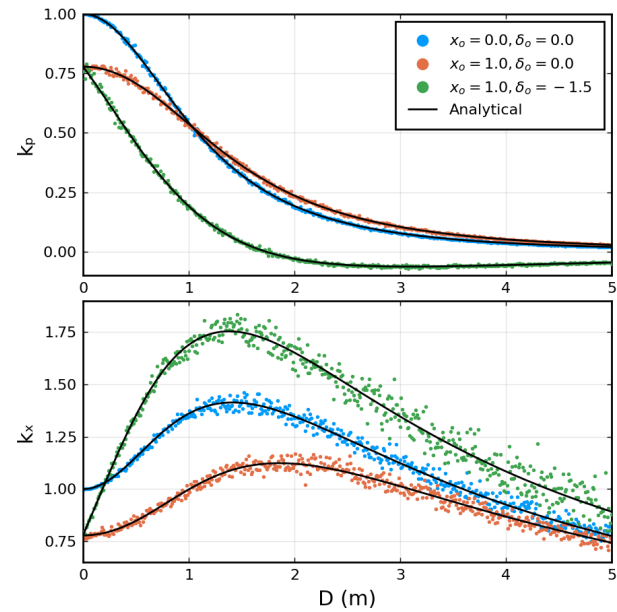


Figure 2: Monte-Carlo and analytical results of the gain factor dependence on dispersion for Case 1 with $\sigma_{ex} = 1$ m, $\sigma_{ix} = 1$ m, $\delta_p = 1$, $C_p / C_x = 2$.

Using arbitrary parameters, the dependence of the gain factors on the dispersion function under different conditions is calculated and shown in Fig. 2. The Monte-Carlo results show a good agreement with the analytical formula. We see that using dispersion alone can realize dispersive cooling and a factor of 1.4 is achieved for the horizontal cooling rate. This effect is mainly due to the Gaussian e-beam distribution, which naturally provides the transverse gradient of the longitudinal force. The details of the explanation can be found in Ref. [5]. When beam displacement is applied, it shows that the horizontal gain factor drops off and the maximum value of k_x decreases to 1.1. This is due to the fact that the displacement reduces the average cooling force on the

ion beam, which is density-dependent, thereby weakening the dispersive cooling effect as shown by the second term in the bracket of Eq. (6). Meanwhile, the third term in the bracket depends on both energy offset and beam displacement. The increase and decrease of the horizontal cooling rate can be adjusted by the product of the two values. This conclusion agrees with Ref. [1, 4]. As shown in Fig 2, the maximum value of k_x can reach 1.75 by using $x_o = 1.0$ m and $\delta_o = -1.5$, even though the beam displacement introduces a certain degradation of the horizontal cooling rate.

However, an energy mismatch between electron and ion beams may result in a circular attractor in the longitudinal phase space of the ion bunch. If the relative shift exceeds a critical value, beam heating instead of cooling may occur [7]. Therefore, the method using energy offset to realize dispersive cooling needs to be carefully calculated and evaluated in practical applications.

Case 2: Gaussian E-Beam with Space Charge K_{sc} and Beam Displacement X_o

Another method to realize dispersive cooling relies on the space charge effect of the e-beam, which in combination with a beam displacement can generate the transverse gradient of the longitudinal force [2, 3]. The radial-dependant velocity deviation in the longitudinal direction will be produced due to the space charge effect. Here we assume a parabolic velocity profile, the final result of the two gain factors is

$$\begin{aligned}
 a &= \sqrt{\sigma_{ex}^2 + \sigma_{ix}^2} \\
 b &= \sqrt{\sigma_{ex}^2 + \sigma_{ix}^2 + D^2 \delta_p^2} \\
 c &= \sqrt{\sigma_{ex}^2 - \sigma_{ix}^2 - D^2 \delta_p^2} \\
 k_p &= e^{-\frac{x_o^2}{2b^2}} \left[\frac{a^3}{b^3} + \frac{a}{b^5} D^2 \delta_p^2 x_o^2 \right. \\
 &\quad \left. - \frac{a}{b^5} D K_{sc} x_o (2\sigma_{ex}^2 b^2 - x_o^2 c^2) \right] \\
 k_x &= e^{-\frac{x_o^2}{2b^2}} \left[\frac{a}{b} + \frac{C_p a}{C_x b^5} D^2 \delta_p^2 (b^2 - x_o^2) \right. \\
 &\quad \left. + \frac{C_p a}{C_x b^5} D K_{sc} x_o (2\sigma_{ex}^2 b^2 - x_o^2 c^2) \right].
 \end{aligned} \tag{7}$$

It shows that the first and second terms in the bracket come from the Gaussian e-beam distribution, which has already been discussed above. The third term is of interest to us, and it is directly determined by the e-beam space charge and beam displacement. We see that the sign of this term also depends on the electron and ion beam parameters. Considering arbitrary parameters, a comparison between the Monte-Carlo calculation and analytical formula is shown in Fig. 3. It is clear that beam displacement and the space charge effect contribute to dispersive electron cooling. As discussed in Ref. [2, 3], an outward displacement of the e-beam is required for the increase of the horizontal cooling rate, which is consistent with our result. The equation also shows that a larger K_{sc} can improve the rate redistribution

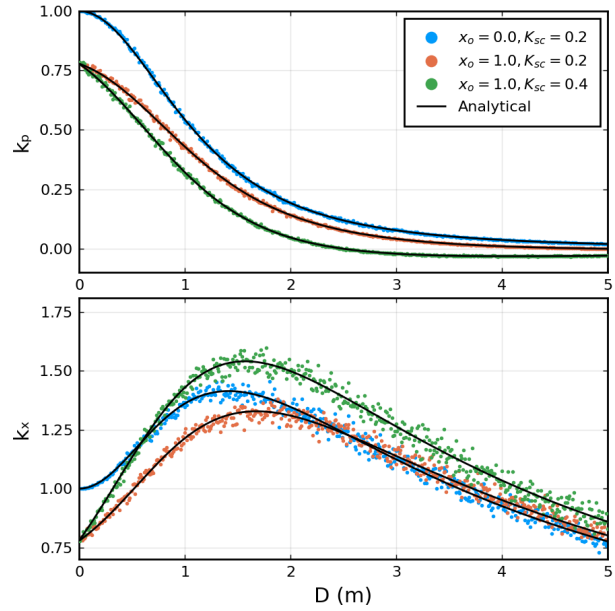


Figure 3: Monte-Carlo and analytical results of the gain factor dependence on dispersion for Case 2 with $\sigma_{ex} = 1$ m, $\sigma_{ix} = 1$ m, $\delta_p = 1$, $C_p/C_x = 2$.

effect. However, a strong space charge field is not desirable for cooling, since the transverse drift velocity and the longitudinal velocity deviation have a significant influence on the cooling process. Therefore, when studying dispersive electron cooling, the value of K_{sc} or the e-beam density should be carefully determined according to the beam energy and cooling requirements.

Case 3: Uniform E-Beam with Infinite Radius R_e , Space Charge K_{sc} , and Beam Displacement X_o

In the above, we investigated two methods that can be used to realize dispersive cooling for a Gaussian e-beam. In addition to the energy offset and space charge effect, we see that the e-beam itself also contributes to the rate redistribution effect, since the Gaussian density distribution naturally provides a transverse gradient of the longitudinal force. In fact, a uniform or hollow e-beam is much preferable for most electron coolers to avoid beam losses due to recombination, overcooling and instabilities [8,9]. Therefore, it is necessary to study the rate redistribution effect for these two e-beams. Here we only discuss the uniform e-beam.

We assume a uniform e-beam with an infinite radius that is $n_e \equiv \text{constant}$. Since there is no density gradient, the energy offset does not affect the dispersion cooling as discussed in Case 1, and the density distribution will not provide the transverse gradient of the cooling force. So, using the space charge effect of the e-beam is the only useful approach. In this case, the gain factors can be easily calculated

$$\begin{aligned}
 k_p &= 1 - 2DK_{sc}x_o \\
 k_x &= 1 + 2DK_{sc}x_o C_p/C_x.
 \end{aligned} \tag{8}$$

It shows the same conclusion that dispersive electron cooling

can be achieved by the velocity deviation caused by the e-beam space charge, combined with a beam displacement.

Case 4: Uniform E-Beam with Finite Radius R_e , Space Charge K_{sc} , and Beam Displacement X_o

For a uniform e-beam with a finite radius R_e , the density distribution is

$$n_e(r) = \begin{cases} \text{constant}, & r \leq R_e \\ 0, & r > R_e. \end{cases} \quad (9)$$

For this distribution, we can say that there is a density gradient which is created by the density difference between the inside and outside of the e-beam. Due to the betatron motion, particles with large amplitude will cross the boundary of the e-beam back and forth, thereby creating a transverse gradient of the longitudinal cooling force. As a result, a uniform e-beam itself can also be applied to achieve dispersive cooling as well as a Gaussian e-beam.

For simplicity, we only consider the space charge effect $\delta_e(r) = K_{sc}r^2$ and beam displacement. Based on the uniform density distribution (Eq. (9)), the analytical result of the gain factors is calculated as below

$$\begin{aligned} m &= \text{Erf} \left[\frac{R_e}{\sqrt{2\sigma_{ix}^2}} \right] \\ n &= \sqrt{\sigma_{ix}^2 + D^2\delta_p^2} \\ a &= \text{Erf} \left[\frac{R_e + x_o}{\sqrt{2}n} \right] + \text{Erf} \left[\frac{R_e - x_o}{\sqrt{2}n} \right] \\ b &= \frac{e^{-\frac{(R_e-x_o)^2}{2n^2}}(R_e - x_o) + e^{-\frac{(R_e+x_o)^2}{2n^2}}(R_e + x_o)}{n^3} \\ c &= \frac{e^{-\frac{(R_e+x_o)^2}{2n^2}} - e^{-\frac{(R_e-x_o)^2}{2n^2}}}{n} \\ k_p &= \frac{a}{2m} - \frac{D^2\delta_p^2 b}{\sqrt{2\pi}m} + \frac{DK_{sc}x_o}{\sqrt{2\pi}m}(2n^2b - \sqrt{2\pi}a - x_o c) \\ k_x &= \frac{a}{2m} + \frac{C_p}{C_x} \left[\frac{D^2\delta_p^2 b}{\sqrt{2\pi}m} - \frac{DK_{sc}x_o}{\sqrt{2\pi}m}(2n^2b - \sqrt{2\pi}a - x_o c) \right]. \end{aligned} \quad (10)$$

It shows that the first and second terms of the gain factor are due to the e-beam distribution, and the third term comes from the space charge effect. A comparison of different settings is shown in Fig. 4, and the Monte-Carlo results agree well with the analytical formula. We see that the rate redistribution effect strongly depends on the e-beam radius, since it directly determines how many particles can see the density gradient. If the e-beam radius is smaller than the ion beam, it is easy to realize dispersive cooling with small dispersion. Otherwise, dispersive cooling is less likely to occur unless the dispersion is large enough.

SUMMARY AND DISCUSSION

In electron cooling, transverse cooling is usually weaker than the longitudinal direction. For this reason, dispersive

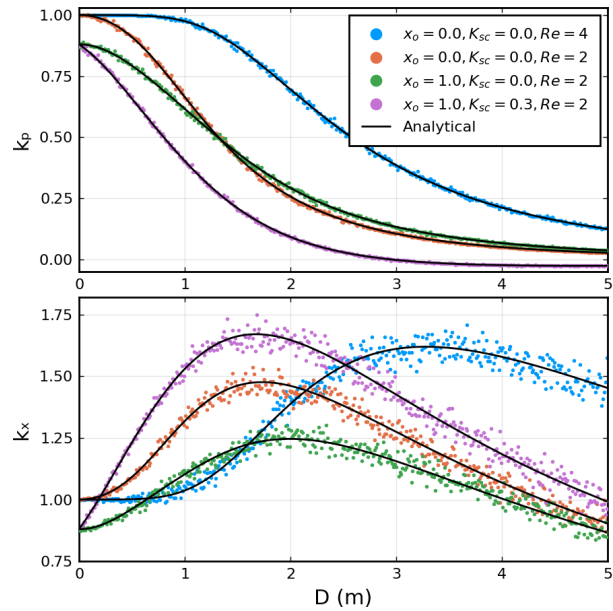


Figure 4: Monte-Carlo and analytical results of the gain factor dependence on dispersion for Case 4 with $\sigma_{ix} = 1$ m, $\delta_p = 1$, $C_p/C_x = 2$.

electron cooling is an effective scheme to redistribute the cooling rate, especially for future high-energy coolers. In this paper, we investigated several approaches that can be applied to achieve dispersive electron cooling. It is demonstrated that beam energy offset, transverse displacement, density distribution and space charge effect of e-beam all contribute to the rate redistribution in dispersive cooling. For the first time, we demonstrate that a transverse uniform e-beam with a finite radius can be applied in dispersive cooling. Based on a linear cooling force model, we present an analytical formula for numerically estimating the cooling rate redistribution effect. Moreover, a Monte-Carlo calculation and numerical simulation are also carried out, and all results show good agreement with the analytical model.

As previously discussed, the beam energy offset and displacement may affect the cooling performance and may induce some undesired effects such as circular attractor or even beam heating. So, these two approaches should be carefully calculated and evaluated in practice. Moreover, since the strong dependence of the space charge effect on beam energy, the method using the velocity deviation is only suitable for low-energy beam cooling, such as conventional electron cooling with electron energies below a few MeV. For high-energy beam cooling, such as EIC, where e-beam energy would reach tens or hundreds of MeV, the method employing beam density is much preferable. However, these factors in dispersive electron cooling have not been well explored through experiments. The influences of these factors on the cooling rate need to be further investigated. Additionally, the effects induced by the dispersion function, such as ion beam dynamics and IBS, require comprehensive exploration. It's also important to note that the dispersion function in accel-

erators is quite limited. Therefore, considering all the above points, dispersive cooling needs further extensive research in the future.

ACKNOWLEDGMENT

This work is supported by the National Natural Science Foundation of China (No. 12275323, 12275325, and 12205346).

REFERENCES

- [1] Y. Derbenev, “Optimization of HEEC of Hadron Beams in EIC”, in *Proc. EIC Hadron Cooling Workshop*, Batavia, IL, USA, October 7–8, 2019. <https://indico.fnal.gov/event/20514/contributions/58107/>
- [2] J. Bosser *et al.*, “On the optimum dispersion of a storage ring for electron cooling with high space charge”, *Nucl. Instrum. Methods Phys. Res., Sect. A*, vol. 441, no. 1–2, pp. 60–63, 2000. doi:10.1016/S0168-9002(99)01109-2
- [3] M. Beutelspacher *et al.*, “Dispersive electron cooling experiments at the heavy ion storage ring TSR”, *Nucl. Instrum. Methods Phys. Res., Sect. A*, vol. 512, no. 3, pp. 459–469, 2003. doi:10.1016/S0168-9002(03)01976-4
- [4] H. Zhang *et al.*, “Dispersive Electron Cooling for JLEIC”, Thomas Jefferson National Accelerator Facility (TJNAF), Newport News, VA, USA, Rep. JLAB-ACP-18-2719; DOE/OR/23177-4451, 2018.
- [5] H. Zhao and M. Blaskiewicz. “Rate redistribution in dispersive electron cooling”, *Phys. Rev. Accel. Beams*, vol. 24, no. 8, p. 083502, 2021. doi:10.1103/PhysRevAccelBeams.24.083502
- [6] H. Pishro-Nik, *Introduction to probability, statistics, and random processes*. Blue Bell, PA, USA: Kappa Research, LLC, 2014.
- [7] S. Seletskiy *et al.*, “Experimental studies of circular attractors in the first rf-based electron cooler”, *Phys. Rev. Accel. Beams*, vol. 26, no. 2, p. 024401, 2023. doi:10.1103/PhysRevAccelBeams.26.024401
- [8] A. Bublely *et al.*, “The Electron Gun with Variable Beam Profile for Optimization of Electron Cooling”, in *Proc. EPAC’02*, Paris, France, Jun. 2002, paper WEPRI049, pp. 1356–1358.
- [9] V. Bocharov *et al.*, “HIRFL-CSR electron cooler commissioning”, *Nucl. Instrum. Methods Phys. Res., Sect. A*, vol. 532, no. 1-2, pp. 144–149, 2004. doi:10.1016/j.nima.2004.06.041

SUSTAINING COMPETENCES FOR ELECTRON COOLING AT HESR

Kurt Aulenbacher, Thomas Beiser, Juergen Dietrich, Wolfgang Klag
Helmholtz Institute Mainz (HIM), Germany

Abstract

The HESR storage ring will be operated with a high intensity antiproton beam to serve the PANDA experiment.

Due to several reasons its completion is presently postponed which causes the issue how to keep competences required to develop and operate the electron cooler. We will present mitigation plans that will enable Helmholtz-Institut Mainz (HIM) to pursue its goals even if the present situation would last for a long time.

INTRODUCTION

The research group ACID-II at Helmholtz Institute Mainz (HIM) is aiming to resolve technical challenges related to high energy electron cooling. This is connected to a possible relativistic magnetized electron cooler for the High Energy Storage Ring HESR at FAIR. An electron kinetic energy of almost 8 MeV would be required, exceeding the voltage of the Jülich cooler [1] considerably, which is currently the cooler with the highest voltage and magnetized beam.

In cooperation with the Budker Institute for Nuclear Physics (BINP) at Novosibirsk in Russia we have proposed a modular concept based on high voltage platforms, each delivering a potential of 600 kV. The floating electric power is provided by turbogenerators which supply the solenoids and auxiliary devices such as electron source, collector-supply, or vacuum pumps. A first module was built by BINP and delivered to Mainz [2]. These modules – called platforms - are intended to be 1:1 scale size prototype for the HESR-cooler.

Since the last conference of this series all HESR related projects have been confronted with uncertainties because of cost increases and the political situation. These will probably lead to an additional delay of several years before HESR can start operation. In particular, the cooperation with most Russian institutions has been suspended and it is presently not clear when such co-operations will become possible again. This also applies to our plans to test the scalability with more than one HV-platform.

In this paper we describe the progress we have achieved since the last conference COOL'21 and try to sketch a strategy how to sustain the competences that have been gained at HIM until the timeline of the HESR becomes more predictable.

PLATFORM OPERATION

The arrangement was described in the paper covering our status at COOL'21 [2] where more details can be found. A pressure tank of 4 m inner diameter is intended to hold a stack of 600 kV high voltage platforms (Fig. 1).

Since the cooperation with BINP was suspended, no delivery of the second platform took place. This will inhibit our tests for scalability until either the cooperation is resumed, or we build the other stages from our own means. The latter is feasible but would require considerable engineering capacity. Considering the delays in the timeline of HESR it seems reasonable to postpone such decisions and restrict ourselves to operation of the first 600 kV platform. We will operate the gas-expansion turbines for power generation with dry nitrogen at the beginning. An input pressure of 3 bar can be generated by our screw compressor with a mass-throughput that suffices to drive at least two turbines. It was considered most favourable to use a closed Nitrogen circuit, i.e., feeding the exhaust gas of the turbines back to the compressor, the input and the exhaust flanges can be seen in Fig. 2. In first tests it turned out that stable operation of the system, e.g., when changing the load on the turbine, was difficult to achieve.

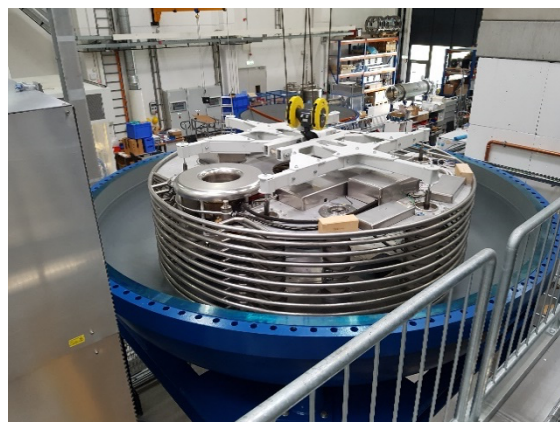


Figure 1: Lower part of HV tank at HIM with first platform installed. Inner diameter of tank is 4 meters.

In cooperation with Prof. Wirsum from the Institute for turbo electric power generation at RWTH Aachen a thorough analysis of the pneumatic circuit was completed [3]. The reasons for the instabilities were identified and countermeasures proposed. The modifications were delayed by the supply chain problems that occurred during 2022, for instance by a very long delivery time for regulation valves. However, the modifications were finalized in spring 2023 and stable operation of a turbine in the closed cycle configuration was achieved. As a next step we will connect the already installed turbine on the 600 kV platform to the circuit. In this configuration the gas supply line is made from insulating material and integrated into the platform. Later, HV-tests will start, with the goal to reach 600 kV operation. This step will be challenging because the support from the designers of the platform at BINP is presently missing. To have stable HV-conditions on the platform, the supply lines and the turbine will be exposed to a moderate overpressure

† aulenbac@uni-mainz.de

in the HV-tank, which will be generated by filling the tank with nitrogen at 2-3 bar. We expect to finalize these experiments within the next two years.



Figure 2: “Big-Blue-Bubble” HV tank with several ports in the bottom flange. Besides the input/output port for the cooler beam, the bottom flange also comprises input/output ports for the gas flow.

MEDIUM TERM STRATEGY

The experiments described in the last section will be performed with the available resources at HIM. From the R&D point of view, further developments are well defined and have been described in [2]. In the same paper, several alternatives how to use our competences and installations have been sketched. These projects can be related to R&D in particle physics as well as for applied science. They can allow us sustaining the special competences needed for the cooling device until the present period of uncertainty concerning the HESR-experiments is over. There are two different areas in which continuity must be maintained. Besides the expertise in handling the HV-modules, it is our experience in handling and diagnosing the high beam currents needed for magnetized cooling, see also the contribution by Thomas Beiser in these proceedings [4].

The most promising recent development where these competences can be used is a medical application. We have been asked to contribute to such a project where a similar beam current and energy as in our HESR-device is needed. This project is pursued by a collaboration of German national research centres and universities. It deals with generating a spatially modulated X-ray field for cancer therapy. Promising results of such radiation fields have been obtained at the ESRF-synchrotron, but clinical application requires to miniaturize the accelerator system needed. It turns out that a so called “Line focus X-ray tube (LFXT)” could achieve this [5]. The line focus on the anode with dimensions of approximately 0.05*15 mm is adapted to make optimum use of a linear X-ray collimator grid. A device suitable to be used in cancer treatment will have to operate at a beam energy of 600 keV with a beam current of about 2 Ampere. This is accidentally a similar parameter region as in the cooler-prototype. For the LFXT, we have

already designed and build a prototype gun for 300 kV, 300 mA which is currently being commissioned at TU-Munich [6]. Such an X-ray tube fulfils the desire to have a compact device that fits into a hospital, see Fig. 3.

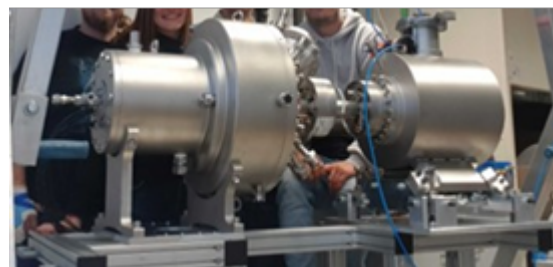


Figure 3: 300 kV, 0.3 Ampere prototype of the Line Focus X-ray Tube (LFXT-1). Tube length is about 1.5 m. Electron gun and focusing system (right half of vacuum vessel) have been built by us [6]. The system uses conventional HV-Isolators and HV-power-supplies to accelerate the beam.

One may note that there are differences between the Cooler- and the LFXT-prototype. First, the LFXT does not use energy recuperation. It dumps the full beam power on the anode, albeit only for a period of a few seconds which is enough to create the X-ray dose needed for treatment. Therefore, it relies on stored electrical energy, not on continuous power flow as in the cooler case. Second, it is not necessary to have a big HV-tank for only 600 kV. On the other hand, even if the turbines and the “big-blue-bubble”-tank would not be used it is evident that the aforementioned competences fit very well to this project.

CONCLUSION

Our group will continue to develop important components for a possible electron cooler at HESR/PANDA. After a successful test of a turbogenerator in closed circuit last summer we will continue with an installation of the turbine at our high voltage platform with the goal to demonstrate operation of the system under 600 kV. If the situation concerning the future of the HESR-experiment remains unclear, it is possible to maintain the competences by bridging even a long-lasting time gap by applied physics research for X-ray tubes which need beam powers comparable to those at needed for HESR-Antiproton-cooling. This project can be handled in parallel to the ongoing cooler-activities since additional funding and personnel may become available.

REFERENCES

- [1] V.B. Reva *et al.*, “Experimental Observation of Longitudinal Electron Cooling of DC and Bunched Proton Beam at 2425 MeV/c at COSY”, in *Proc. COOL'15*, Newport News, VA, USA, Sep.-Oct. 2015, paper MOXAUD02, pp. 10-14.
- [2] K. Aulenbacher *et al.*, “Scalable HV-Modules for a Magnetized Relativistic Electron Cooler”, in *Proc. COOL'21*, Novosibirsk, Russia, Sep. 2021, pp. 31-32.
doi:10.18429/JACoW-COOL2021-S501

- [3] R. Wirsum, Konzeptpapier – Potentialfreie Stromversorgung mit Turbogenerator (Mainz, 2021, unpublished)
- [4] Th Beiser *et al.*, “Investigation of Ion Trapping and Beam-Induced Fluorescence at the Electron Cooler Test-Bench at HIM”, presented at COOL’23, Montreux, Switzerland, Oct. 2023, paper THPOSRP13, this conference.
- [5] J. Winter *et al.*, “Clinical Microbeam Radiation Therapy with a Compact Source: Specifications of the Line-Focus X-Ray Tube”, *Phys. Imaging Radiat. Oncol.*, vol. 14, pp. 74-81, 2020. doi:10.1016/j.phro.2020.05.010
- [6] Ch. Matejcek *et al.*, “A Novel Electron Source for a Compact X-Ray Tube for Microbeamradiotherapy with Very High Dose Rates, *Physica Med., EJMP*, 102532, 2023. doi:10.1016/j.ejmp.2023.102532

STATUS OF E-COOLING CHARACTERISATION AT 100 keV IN ELENA

D. Gamba*, F. Asvesta, P. Kruyt¹, L. Ponce, and G. Russo
 CERN, 1211 Geneva, Switzerland
¹ also at Goethe University, Frankfurt, Germany

Abstract

The Extra Low ENergy Antiproton ring (ELENA) ring at CERN was commissioned in 2018 and has been in regular production operation since 2021. ELENA uses e-cooling for cooling antiproton (pbar) beams on two plateaus at 653 keV and 100 keV kinetic energy. The first cooling is necessary to allow for efficient deceleration of the 5.3 MeV pbar beam coming from the Antiproton Decelerator (AD), while the second cooling is used to define the quality of the bunches before extraction. The experience accumulated so far shows that cooling at 653 keV is sufficient to ensure good deceleration efficiency, while cooling at 100 keV might not be enough to provide the design transverse beam emittances at extraction. In this paper, we document the present ELENA e-cooling performance at 100 keV, the typical optimisation procedure used during setup, and we investigate possible limitations of the present system.

INTRODUCTION

The ELENA ring is part of the Antimatter Factory at CERN, which is a unique facility that provides pbar beams for low energy antimatter physics [1, 2]. Pbars are produced in the AD target area by sending a 26.4 GeV/c proton beam on an iridium-based target. The emerging pbars at 3.575 GeV/c are guided and collected into the AD ring which cools and decelerates them down to 5.3 MeV kinetic energy. They are then transferred to the ELENA ring which further decelerates and cools them down to 100 keV kinetic energy. Here, four bunches are produced and distributed to up to four experiments at the same time. An overall parameter to assess the antimatter factory performance is the number of pbars delivered to the users as a function of protons sent on target. This is shown in Fig. 1, in which about four weeks of data from 2022 is compared to an equivalent period in 2023. Continuous optimisation of the AD target area and transport allows to regularly reach a pbar yield of 3×10^{-6} pbar injected in AD per proton delivered on target. Proton intensity from the CERN injectors was increased during 2022 and 2023 runs in steps from about 1.4×10^{13} to about 1.7×10^{13} . This, together with improved deceleration efficiency, allowed to increase the number of pbars to more than 5×10^7 injected in AD and more than 4×10^7 in ELENA. Each user requesting beam is now typically receiving 9×10^6 pbar, which is about a factor of 2 higher than the design value.

In the following sections, an update on the ELENA cycle and its hardware will be outlined followed by the latest measurements of e-cooling characterisation with emphasis on the extraction plateau at 100 keV.

* davide.gamba@cern.ch

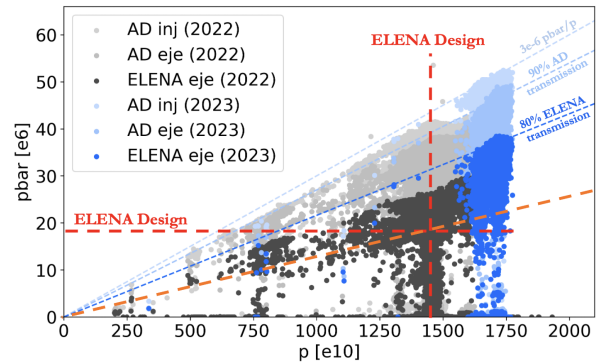


Figure 1: Antiproton intensity as a function of protons on AD target. Pbars measured at AD injection, ELENA injection and ELENA extraction are indicated from lighter to darker colors. Shades of black and blue indicate 2022 and 2023 data, respectively. Proton on target and ELENA extraction design parameters are also indicated in dashed red.

ELENA CYCLE AND INSTRUMENTATION

The ELENA magnetic cycle and available instrumentation are basically unchanged with respect to what is reported in [3]. On top of the regular operation with pbar, ELENA can still be operated with H^- from its local source [4, 5], which continues to be an essential asset for machine setup.

The typical magnetic cycle, basically identical for both pbar and H^- operation, is shown in Fig. 2. During H^- operation the beam is injected at the lowest plateau at 100 keV, it is accelerated to pbar injection energy (5.3 MeV), and then it follows the nominal deceleration cycle as for the pbar. The lifetime of H^- beam is of the order of 5 s, mainly driven by the average ring pressure level which settled at about 1×10^{-11} mbar, while no sizable lifetime degradation via interaction with the electron beam of the e-cooler has been observed so far.

Due to the sizeable H^- beam intensity reduction after deceleration, a second injection at the beginning of the last e-cooling plateau is performed, so to obtain H^- beams at extraction of comparable intensities to the pbar ones.

The ELENA e-cooler [6] was commissioned in 2018 [7], and so far did not require any modifications nor major maintenance. Its main parameters are summarised in Table 1. Since e-cooler parameters cannot be quickly changed between H^- and pbar cycles operation, and hence the electron velocity is fixed, the H^- momentum at the different plateaus is adjusted to match the pbar revolution frequency.

The main instrumentation for e-cooling setup and adjustment remains the Schottky signal, which in ELENA is obtained by combining the signal of several Beam Position

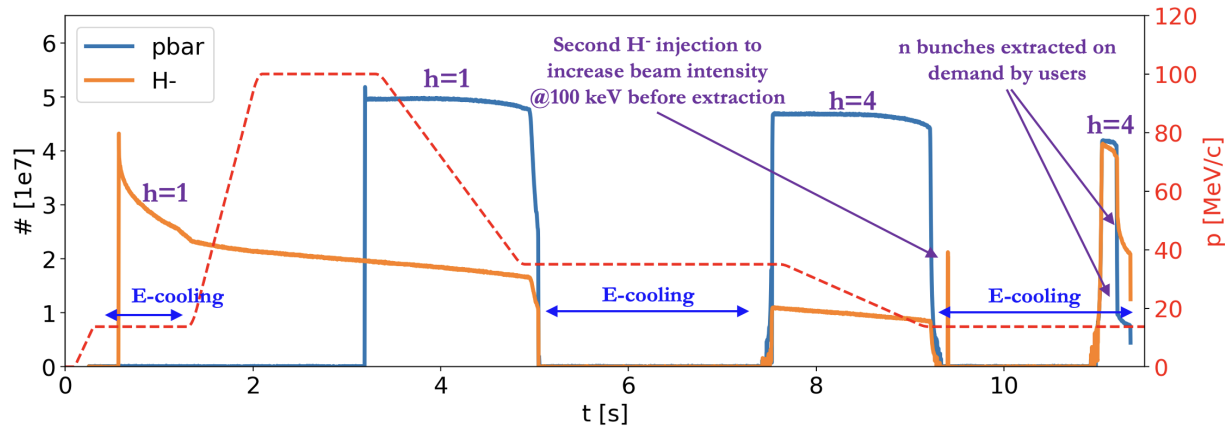


Figure 2: H^- (orange) and $pbar$ (blue) beam intensity along a typical ELENA cycle (dashed red). Intensity signal is visible only when the beam is bunched. Key points and observations are highlighted.

Monitor (BPM) pickups [8]. A typical spectrogram obtained by this system along the 100 keV plateau with H^- is shown in Fig. 3. To be noted the second H^- injection at about 9.4 s from the start of the cycle, which is longitudinally cooled in a few hundred ms, and the start of the RF at about 11.8 s, where synchrotron side-bands show up.

The main instrument for transverse beam profile measurements in the ELENA ring is based on a scraper blade [9, 10], which measures the secondary emission from losses induced by the moving blade progressively approaching the beam closed orbit. Characterisation of this instrument is ongoing [11], however, it remains of limited use due to the observed fast cooling time with respect to the typical measurement time of a few hundred ms. Moreover, if for $pbar$ one can obtain clean loss signals, the measurement of H^- based on in-vacuum microchannel plates (MCPs) is more sensitive to noise and difficult to interpret.

A monitor to measure neutral hydrogen atoms escaping the ELENA ring is installed on the e-cooler straight section. Its interpretation is also being studied [12], but this system is not yet used for e-cooling setup and operation.

Transverse e-cooling characterisation at 100 keV is typically done by profiting of the semi-intercepting micro-

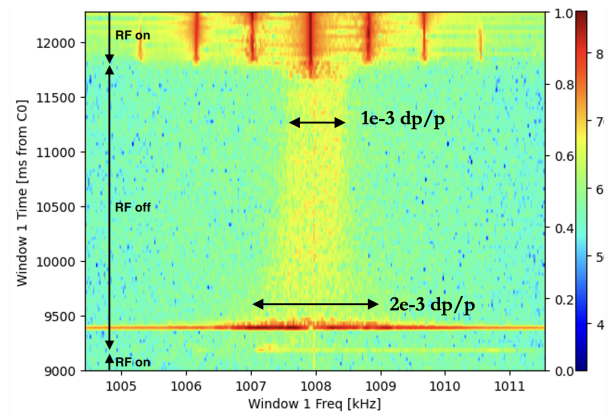


Figure 3: Spectrogram of the Schottky signal measured along the 100 keV extraction plateau in ELENA with H^- beams.

wire monitors, also called Secondary Emission Monitors (SEMs) [13], installed in the ELENA-extraction transfer lines. Using several of those monitors inserted into the beam path allows to perform a multi-profile Twiss measurement, as shown for example in Fig. 4. This method is regularly used to monitor extracted beam performance. Approximately 10% of beam intensity is lost during the passage in each SEM monitor inserted into the beam. Therefore, several monitors can be inserted in the beam line only during dedicated machine development times, while typically a single monitor is used to log the beam profile stability or for parasitic machine development with H^- .

Effort is being put into producing a simulation framework [14] based on the Parkhomchuk model [15] of e-cooling to allow for modelling the expected cooling performance for different machine configurations. For example, Fig. 5 shows a preliminary study to estimate of the impact of the e-cooler magnetic field imperfection on the cooling time in ELENA at 100 keV neglecting heating effects. To be noted that the ELENA e-cooler magnetic field imperfection is somewhere below 5×10^{-3} (Table 1), hence some degra-

Table 1: ELENA E-Cooler Main Parameters

Parameter	ELENA	
$Pbar p$ [MeV/c]	35	13.7
$Pbar E_k$ [MeV]	0.635	0.1
$e^- E_k$ [keV]	0.355	0.055
β_{rel}	0.037	0.015
I_{e^-} [mA]	5	1
Cooler L [m]	1	
Ring L [m]	30.41	
Gun B [G]	up to 1000	
Drift B [G]	100	
Drift B_{\perp}/B_{\parallel}	$< 5 \times 10^{-3}$	
e^- beam r [mm]	8 to 25	

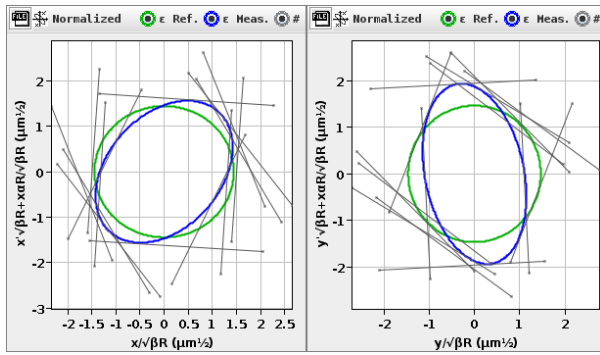


Figure 4: Horizontal (left) and vertical (right) transverse Twiss measurement (blue) compared to the nominal TWISS ellipse (green) in normalised phase space. Gray lines correspond to beam sizes measured by several SEM's along the LNE00 transfer line.

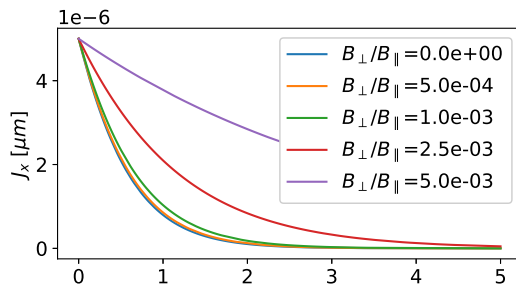


Figure 5: Simulated time evolution of horizontal action of a single particle representing the beam envelope for different e-cooler magnetic field quality: perfect magnetic field (blue), $B_{\perp}/B_{\parallel} = 5 \times 10^{-4}$ (orange), 1×10^{-3} (green), 2.5×10^{-3} (red), and 5×10^{-3} (purple).

ation of the cooling time with respect to an ideal magnetic field is to be expected. The cooling time should be of the order of a second, which is indeed compatible with what observed so far.

EXTRACTED BEAM CHARACTERISATION

The beam is re-bunched before extraction at harmonic four while e-cooling is kept on, hence bunched-beam cooling is performed for reaching minimum energy spread and bunch length. The intensity of the extracted bunches is much above the design value of 4.5×10^6 , see Fig. 1. With the present machine working point, it was observed that e-cooler currents above 1 mA result in beam losses when the bunch length reaches a minimum of about 150 ns Full Width Half Maximum (FWHM). Hence, the e-cooler is typically set to deliver about 0.5 mA on the 100 keV plateau, such to ensure that no or minimum beam losses are produced during bunched-beam cooling. The obtained bunch length is close to the ELENA design value [16], but some users prefer to have even shorter bunches and 100 ns-long FWHM bunches are obtained by performing bunch rotation just before extrac-

tion. The corresponding bunch rms momentum spread is less than 1×10^{-3} , while, for bunches without bunch rotation, it is less than 5×10^{-4} .

The transverse cooling setup and optimisation are mainly done by monitoring the size of the extracted beam. This can be performed without re-bunching the beam before extraction in order to decouple the coasting beam e-cooling performance from effects linked to the re-bunching and/or from the bunched-beam cooling before extraction. In this case, all the beam is extracted towards a transfer line. The horizontal sweep of the particles extracted during the rise time of the extraction kicker (less than $1 \mu\text{s}$) does not seem to be sizeable compared to the total particle stream length of $7 \mu\text{s}$, which corresponds to the ring revolution period.

Figure 6 shows an example optimisation of the angle between e^{-} trajectory and, in this case, H^{-} orbit inside the e-cooler: while the e^{-} beam trajectory is not changed, the H^{-} beam closed-orbit angle inside the e-cooler is varied over consecutive cycles using four correctors in the e-cooler straight section. The beam size in the ELENA extraction is measured on a SEM grid after each cycle, and the H^{-} orbit that minimises the beam size is chosen as optimum.

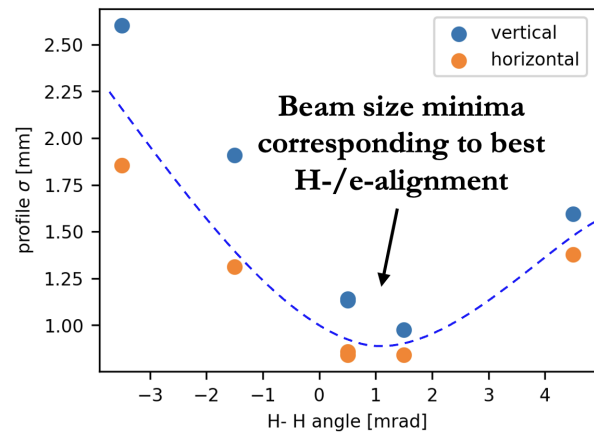


Figure 6: Horizontal (orange) and Vertical (blue) beam size measured on a SEM grid in the ELENA extraction line as a function of the H^{-} closed orbit angle in the e-cooler. The dashed blue line only serves to guide the eyes.

In a similar way, the minimum length of the e-cooling plateau can be found by varying cycle-to-cycle beam extraction time, as shown in Fig. 7. In this measurement, one can see that the extracted beam size flattens out after about 1.5 s from the second H^{-} beam injection, which is performed at $t = 9.4$ s into the cycle (See Fig. 2).

Our future plan is to perform these kind of measurements in a more systematic way and to compare the obtained results between H^{-} and pbars, as well as with simulations. To be noted that these methods do not allow to evaluate the cooling performance of the tails of the transverse beam distribution, because they are not easily detectable by the SEM profile monitor. This kind of analysis will need to be done using

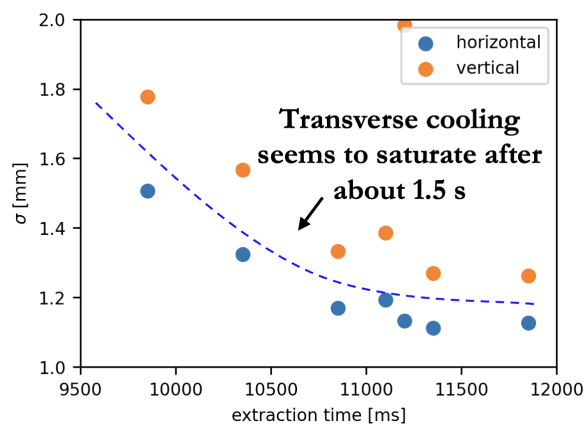


Figure 7: Horizontal (orange) and Vertical (blue) beam size measured on a SEM grid in the ELENA extraction line as a function of extraction beam time. The dashed blue line only serves to guide the eyes.

scrapers inside the ring, which is also the subject of future studies.

RECENT DEVELOPMENT

Despite having good control of the e-cooler setup, the measured transverse emittances of the extracted bunched beams are about a factor of two higher than the design values. Most users do not seem to be strongly affected by the larger beam size, but investigations are ongoing to see if this limitation could be overcome.

Previous observations have already shown that the extracted beam emittance is dependent on the beam intensity [3]. This observation, together with the beam losses observed when reaching even shorter bunches with aggressive bunched-beam cooling, suggests a space-charge-driven effect.

The tune spread due to direct space charge for a Gaussian beam can be computed using the approach described in [17]. Assuming a bunch of 1×10^7 pbars, 150 ns FWHM bunch length, $2 \mu\text{m}$ rms geometric transverse emittances and the nominal ELENA optics [18], one obtains the tune footprint shown in Fig. 8, which correspond to a maximum tune spread of about 0.1. To be noted that the tune footprint for the bunched beam crosses several third-order resonances. For a coasting beam, and assuming 4×10^7 pbars, the tune spread drops to about 0.01, and no resonances are crossed. The present working hypothesis is that the beam interacts with a not-corrected third-order resonance during and after the bunching process takes place, and this leads to emittance growth and eventually beam losses.

Tune scans have been performed to investigate this hypothesis. Figure 9 shows an example of such a measurement. The beam, after cooling, is re-bunched as usual and kept in the machine for about 1 s. This is presently the only way to have a measurement of beam intensity inside the ring. In order to subtract the natural loss of H^- due to vacuum interaction, an

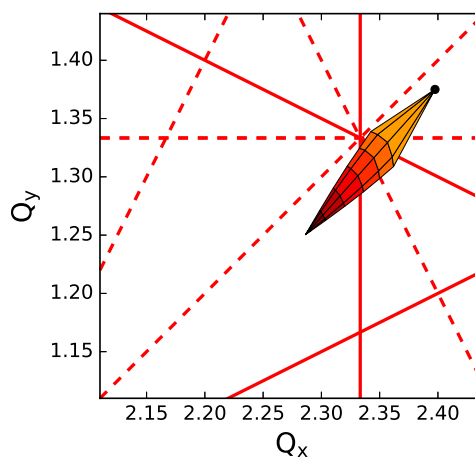


Figure 8: Tune footprint due to space charge for a typical bunch at ELENA extraction energy for the present working point ($Q_x = 2.3975$, $Q_y = 1.375$). Normal (solid) and skew (dashed) resonance up to the third order are also shown.

exponential compensation of the measured beam intensity is applied assuming a lifetime of 5.5 s. While the beam is bunched, the machine working point is moved linearly over time, and the loss rate as a function of the working point is logged. By performing such a measurement starting also from different vertical working points, one obtains the map shown in Fig. 10. This preliminary measurement suggests that a strong third-order resonance ($Q_x = 2.33$) is indeed present, and it cannot be approached without encountering considerable beam losses. Other beam-loss mechanisms at higher horizontal tunes seem to be also present. So far no scans of the working point at a lower vertical tune have been performed. More detailed measurements are envisaged to extend the explored parameter space and to better understand the observed beam losses.

From the tune diagram in Fig. 8 one might desire to move the working point below the third-order resonances. A first attempt to do so before re-bunching was unsuccessful (all

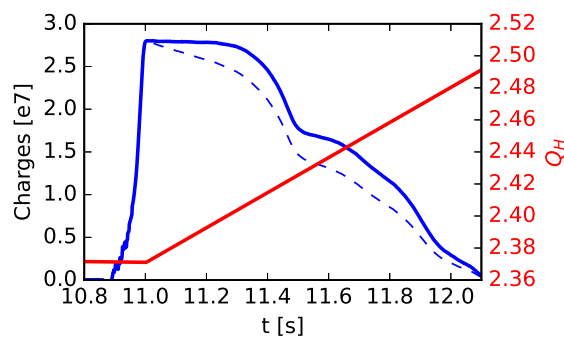


Figure 9: Raw (dashed blue) and lifetime-compensated (solid blue) intensity measurement of an H^- beam during and after recapture at 100 keV. At the end of the recapture process ($t = 11$ s), the set horizontal tune (red) is varied linearly.

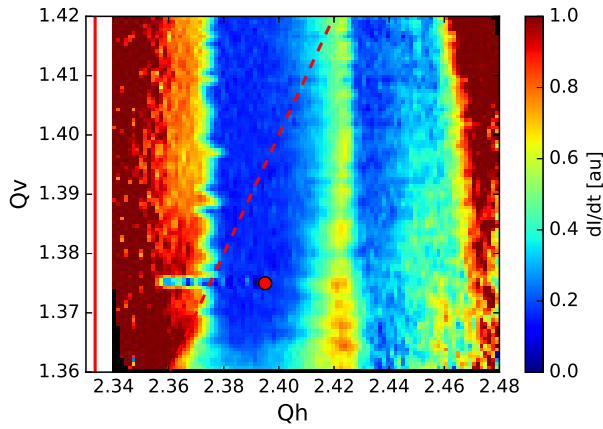


Figure 10: Beam intensity loss rate as a function of working point measured with several horizontal tune scan measurements with H^- beam. The nominal working point used as the start for all measurements is shown as a red dot. The horizontal third-order resonance (solid red) and the second-order coupling resonance (dashed red) are also shown.

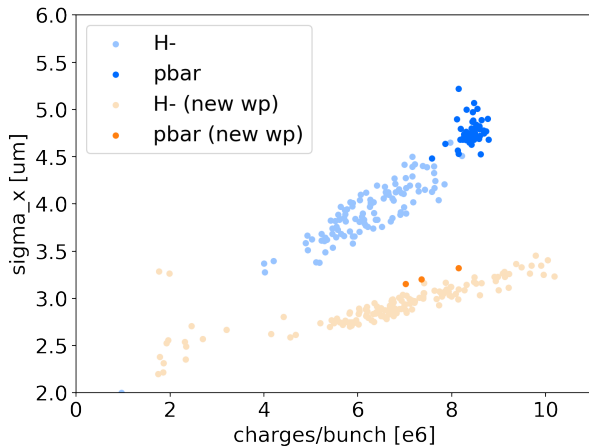


Figure 11: Measured horizontal beam size as a function of bunch intensity measured on a single SEM in the ELENA extraction line for the old (blue) and new (orange) machine working point using H^- (light) and pbars (dark).

beam was lost), hence an attempt was made by modifying the working point of the whole ELENA cycle. Empirically, it was found that by setting the tunes at about $Q_x = 2.30$ and $Q_y = 1.32$ the machine could be operated without major losses along the whole cycle both for H^- and pbar beams. Figure 11 shows a comparison of the beam size measured in the ELENA transfer line over consecutive cycles with the previous and new working points. Note that pbar cycle intensities are typically more stable than the H^- ones, as the latter suffers from a known shot-to-shot intensity instability of the ELENA H^- source. This is useful to naturally show the dependency of extracted beam size/emittance on intensity. It was only possible to collect data from three pbar cycles with the new working point, as this measurement was done during physics time and not in a dedicated machine development slot. Nevertheless, it is interesting to observe

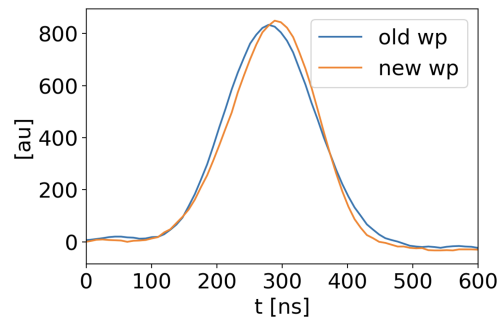


Figure 12: Longitudinal pbar bunch profile measured by a longitudinal profile monitor in ELENA extraction line for the old (blue) and new (orange) working point for two pbar cycles with intensities of about 8×10^6 pbars/bunch.

how the pbar cycles overlap well with the trend shown by the H^- cycles, demonstrating the good equivalence between the two particles/cycles. The significantly reduced beam size is evident. The bunch length obtained with the two working points is comparable, as shown in Fig. 12, hence the difference in transverse beam size cannot be due to reduced line density of the bunch.

The difference in beam size could also be explained by beta beating due to the change of working point, but independent measurements using several SEM monitors, not shown here, suggest that emittances have indeed been reduced by about a factor of two. Additional investigations are necessary to confirm this preliminary result, and possibly further improve the working point and hence the emittances of the beams delivered to the users.

CONCLUSION

The Antimatter Factory at CERN and especially the ELENA ring have demonstrated to reliably achieve the design beam performance, except for transverse beam emittance. The availability of H^- beam is fundamental for machine setup and in particular for e-cooling studies. No degradation of the H^- beam lifetime with e-cooling has been observed and the cooling performance seems to be equivalent between pbar and H^- beams.

Work is continuously ongoing to better characterise the beam instrumentation and hence better control the beam and further improve the beam quality. For example, the preliminary studies presented in this paper pave the way towards the possibility of achieving the design transverse beam emittances despite the much higher beam intensity compared to the design.

Effort is also being put into developing e-cooling simulation tools that will hopefully allow for the exploration of fundamental e-cooling physics processes, for example, the impact of transverse field quality on the cooling time.

ACKNOWLEDGEMENTS

The authors acknowledge the CERN Beam Instrumentation colleagues in charge of the CERN e-coolers and the

AD/ELENA operation crew for their invaluable support and dedication.

REFERENCES

- [1] M. Hori and J. Walz, “Physics at CERN’s Antiproton Decelerator”, *Prog. Part. Nucl. Phys.*, vol. 72, pp. 206–253, Sep. 2013. doi:10.1016/j.pnpnp.2013.02.004
- [2] C. Carli *et al.*, “ELENA: Bright Perspectives for Low Energy Antiproton Physics”, *Nucl. Phys. News*, vol. 32, no. 3, pp. 21–27, 2022. doi:10.1080/10619127.2022.2100646
- [3] D. Gamba, L. Bojtár, C. Carli, B. Dupuy, A. Frassier, L.V. Jørgensen, *et al.*, “AD/ELENA Electron Cooling Experience During and after CERNs Long Shutdown (LS2)”, in *Proc. COOL’21*, Novosibirsk, Russia, Nov. 2021, pp. 36–41. doi:10.18429/JACoW-COOL2021-S503
- [4] A. Megía-Macías, R. Gebel and B. Lefort, “The ion source for the commissioning of ELENA ring”, in *Proc. ICIS’2017*, Geneva, Switzerland, Oct. 2017, vol. 2011, no. 1, p. 090014. doi:10.1063/1.5053395
- [5] D. Gamba *et al.*, “Operational experience with the ELENA ion source”, in *AIP Conf. Proc. NIBS 2020*, Online, Sep. 2020, vol. 2373, no. 1, p. 040005. doi:10.1063/5.0057535
- [6] G. Tranquille *et al.*, “The ELENA Electron Cooler”, in *Proc. IPAC’16*, Busan, Korea, May 2016, pp. 1236–1238. doi:10.18429/JACoW-IPAC2016-TUPMR006
- [7] G. Tranquille, J. Cenede, S. Deschamps, A. Frassier, and L.V. Jørgensen, “Commissioning the ELENA Electron Cooler”, presented at COOL’19, Novosibirsk, Russia, Sep. 2019, paper TUPS12, unpublished.
- [8] O. Marqversen and S. Jensen, “Schottky Signal From Distributed Orbit Pick-Ups”, in *Proc. IBIC’21*, Pohang, Korea, Sep. 2021, pp. 366–369. doi:10.18429/JACoW-IBIC2021-WEPP04
- [9] P. Grandemange, “Preliminary simulation with Geant4 for the AD scraper renovation”, CERN, Geneva, Switzerland, Oct. 2016.
- [10] J. R. Hunt, “Beam Quality Characterisation and the Optimisation of Next Generation Antimatter Facilities”, Ph.D. Thesis, U. Liverpool, United Kingdom, 2019.
- [11] G. Russo, B. Dupuy, D. Gamba and L. Ponce, “Transverse emittance reconstruction along the cycle of the CERN Antiproton Decelerator”, presented at HB’23, Geneva, Switzerland, Oct. 2023, paper THC1C1, unpublished.
- [12] G. Tranquille *et al.*, “H0 Diagnostics for the ELENA Electron Cooler”, presented at COOL’23, Montreux, Switzerland, Oct. 2023, paper THPOSRP09, this conference.
- [13] M. Hori, “Photocathode Microwire Monitor for Nondestructive and Highly Sensitive Spatial Profile Measurements of Ultraviolet, X-Ray, and Charged Particle Beams”, *Rev. Sci. Instrum.*, vol. 76, no. 11, p. 113303, 2005. doi:10.1063/1.2130931
- [14] P. Kruyt, G. Franchetti, and D. Gamba, “Advancements and Applications of Cooling Simulation Tools: A Focus on Xsuite”, presented at COOL’23, Montreux, Switzerland, Oct. 2023, paper THPOSRP02, this conference.
- [15] V. V. Parkhomchuk, “New insights in the theory of electron cooling”, *Nucl. Instr. Meth.*, vol. 441, no. 1, pp. 9–17, 2000. doi:10.1016/S0168-9002(99)01100-6
- [16] V. Chohan (ed.) *et al.*, “Extra Low ENergy Antiproton (ELENA) ring and its Transfer Lines: Design Report”, CERN, Geneva, Switzerland, Rep. CERN-2014-002, Jan. 2014.
- [17] F. Asvesta and H. Bartosik, “Resonance Driving Terms From Space Charge Potential”, CERN, Geneva, Switzerland, Rep. CERN-ACC-NOTE-2019-0046, Oct 2019.
- [18] D. Gamba *et al.*, “ELENA Commissioning”, in *Proc. NAPAC’19*, Lansing, MI, USA, Sep. 2019, pp. 626–631. doi:10.18429/JACoW-NAPAC2019-WEYBB1

INFLUENCES OF THE LONGITUDINAL SHIFT OF THE ELECTRON BUNCH TO THE LONGITUDINAL COOLING RATE*

G. Wang[†], A. Fedotov, D. Kayran

Collider-Accelerator Department, Brookhaven National Laboratory, Upton, NY, USA

Abstract

As two major techniques of cooling a bunched hadron beam in a storage ring, both coherent electron cooling and rf-based traditional electron cooling involve overlapping the cooling electron bunches with the circulating ion bunch. A longitudinal offset of a cooling electron bunch with respect to the ion bunch centre is often introduced, either to cool a single ion bunch with multiple electron bunches or to cool the ions with large synchrotron amplitude more efficiently, i.e. painting. In this work, we derive how the cooling rate is affected by such a longitudinal offset. We use the EIC pre-cooler as an example to study how different overlapping pattern of the cooling electron bunches, e.g. the number of the cooling electron bunches and their longitudinal positions, affect the evolution of the circulating hadron bunches.

INTRODUCTION

Cooling hadrons with a bunched electron beam often involves overlapping one hadron bunch with multiple electron bunches so that the cooling rate can be increased. Examples for such cooling systems include the Low Energy RHIC electron Cooling (LEReC) system [1] and the pre-cooler designed for the Electron Ion Collider (EIC) [2]. Due to the variation of the ions' longitudinal density and their synchrotron oscillations, electrons sitting at different location along the ion bunch have different contributions to the cooling process. It is important to evaluate how the cooling performance changes with the locations of cooling electron bunches with respect to the hadron bunch so that they can be optimized to achieve more efficient cooling. Another example for cooling the hadron bunch with the longitudinally shifted electron bunches is cooling with painting. Since the cooling rate is usually more efficient for hadrons with small synchrotron oscillation amplitudes, the longitudinal profile of the hadron bunch can deviate from Gaussian and a dense core may form after being cooled for some time, which may lead to single bunch instability and degradation of beam lifetime due to large space charge tune shift. One way to counteract the non-uniformity of the cooling rate is to modulate slowly the longitudinal locations of the electron bunches, i.e. painting. Evaluating the cooling rate in the presence of painting also requires calculation of how the cooling rate depends on the longitudinal offset of the electron bunch.

In this work, we derived an analytical formula to calculate the cooling rate as a function of the ion's synchrotron oscillation amplitude with the cooling electron bunch longitudinally shifted away from the ion bunch centre.

* Work supported by Brookhaven Science Associates, LLC under Contract No. DE-SC0012704 with the U.S. Department of Energy.

[†] gawang@bnl.gov

AVERAGING THE COOLING RATE OVER SYNCHROTRON OSCILLATION

We consider a hadron circulating in a storage ring. Due to the energy kick in the RF cavities, the ion carries out synchrotron oscillation as shown in Fig. 1.

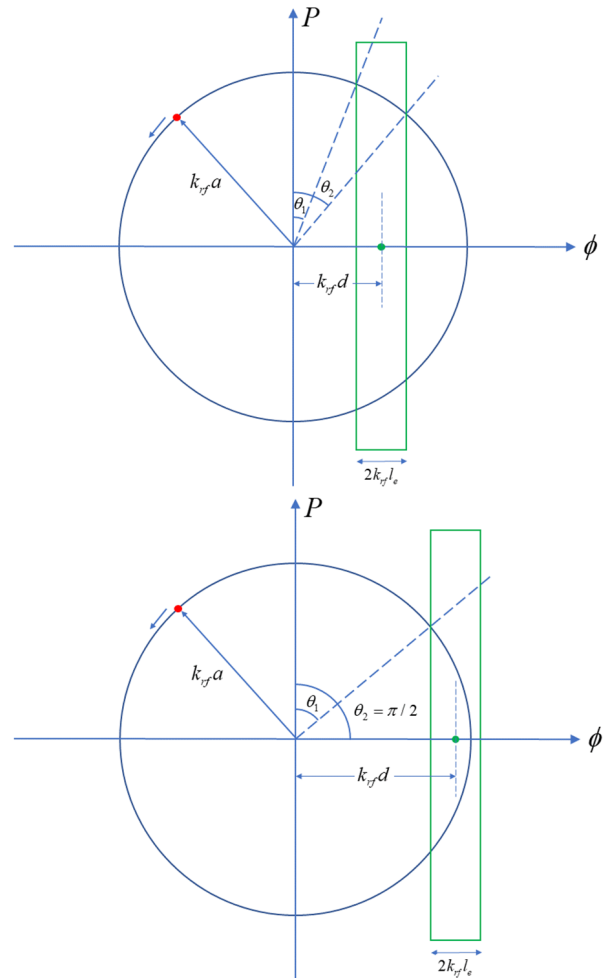


Figure 1: Illustration of the longitudinal cooling of an ion with synchrotron oscillation amplitude $\phi r f_{max}$ and a cooling electron bunch with bunch length of $2l_e$ and offset of d . The red dot represents the ion and the green box represents the region in the ion's longitudinal phase space covered by the cooling electron bunch, i.e. the ion is overlapping with the electrons when it gets into the box. The green dot represents the centre of the electron bunch. The abscissa is the RF phase of the ion and the ordinate is the normalized energy deviation.

Figure 1 shows two cases of the ion conducting synchrotron oscillation in its phase space with the abscissa and

ordinate axis defined as

$$P \equiv -h \frac{|\eta| \Delta p}{v_s p}, \quad (1)$$

and

$$\phi \equiv \omega_{rf} \tau, \quad (2)$$

where h is the harmonic number of the RF cavity, η is the phase slipping factor, v_s is the synchrotron tune, $\Delta p/p$ is the relative momentum deviation of the ion, ω_{rf} is the angular frequency of the RF cavity and τ is the arriving time of the ion. If we use the action-angle variables, (I, w) , defined as

$$P = \sqrt{2I} \cos w \quad (3)$$

and

$$\phi = \sqrt{2I} \sin w \quad (4)$$

For every turn that an ion passing through the electrons, the reduction of its action is

$$\Delta I_c = \frac{1}{2} \Delta (P^2 + \phi^2) = P \Delta P_c, \quad (5)$$

where

$$\Delta P_c = \frac{h|\eta|}{v_s \gamma} \Delta \delta \gamma_c, \quad (6)$$

and $\Delta \delta \gamma_c$ is the one turn energy kick due to cooling which is proportional to the energy deviation of the ion, $\delta \gamma = \gamma \Delta p / p$, through the following equation

$$\Delta \delta \gamma_c = -\zeta_0 T_{rev} \delta \gamma \quad (7)$$

with ζ_0 being the local cooling rate. Eq. (7) can be rewritten as

$$\Delta P_c = -\zeta_0 T_{rev} P \quad (8)$$

and inserting Eq. (8) into Eq. (5) yields

$$\Delta I_c = -\zeta_0 T_{rev} P^2 = -2I \zeta_0 T_{rev} \cos^2 w. \quad (9)$$

For an ion with oscillation amplitude of

$$\phi_{\max} = \sqrt{2I} = \omega_{rf} a,$$

its cooling rate is obtained by averaging Eq. (9) over one synchrotron oscillation period, i.e.

$$\zeta(I) = -\frac{1}{I} \left\langle \frac{\Delta I_c}{T_{rev}} \right\rangle_{T_s} = \zeta_0 \bar{\zeta}(I), \quad (10)$$

with

$$\bar{\zeta}(I) = \frac{4}{2\pi} \int_{\theta_1}^{\theta_2} \cos^2 w dw = \frac{1}{\pi} \int_{\theta_1}^{\theta_2} (\cos(2w) + 1) dw, \quad (11)$$

$$= \frac{\theta_2 - \theta_1}{\pi} + \frac{1}{2\pi} \cos(\theta_1 + \theta_2) \sin(\theta_2 - \theta_1)$$

$$\theta_1 = \arcsin\left(\frac{d - l_e}{a}\right), \quad (12)$$

and

$$\theta_2 = \arcsin\left(\frac{d + l_e}{a}\right). \quad (13)$$

As shown in Fig. 1 (bottom), if $d + l_e > a$, Eq. (10) and (11) are still valid if one take $\theta_2 = \pi/2$. Similarly, if $d - l_e > a$, one need to take $\theta_1 = \theta_2 = \pi/2$ and consequently,

the cooling rate is zero since the ion with amplitude $\omega_{rf} a$ will never see the electrons. From the above analysis, we obtained the expression for the cooling rate to an ion with synchrotron oscillation amplitude of $\phi_{rf_{max}}$ and electron bunch with offset of $d > 0$ (it is obvious that the cooling rate for $d < 0$ is identical with that for the case of electrons with offset of $-d > 0$) and half bunch length of l_e , as the following:

$$\zeta(I) = \zeta_0 \left\{ \frac{\theta_2 - \theta_1}{\pi} + \frac{1}{2\pi} \cos(\theta_1 + \theta_2) \sin(\theta_2 - \theta_1) \right\}, \quad (14)$$

with

$$\theta_1 = \begin{cases} \arcsin\left(\frac{d - l_e}{a}\right), & \text{for } a \geq |d - l_e| \\ \frac{\pi}{2} \text{sgn}(d - l_e), & \text{for } a < |d - l_e| \end{cases}, \quad (15)$$

and

$$\theta_2 = \begin{cases} \arcsin\left(\frac{d + l_e}{a}\right), & \text{for } a \geq d + l_e \\ \frac{\pi}{2}, & \text{for } a < d + l_e \end{cases}. \quad (16)$$

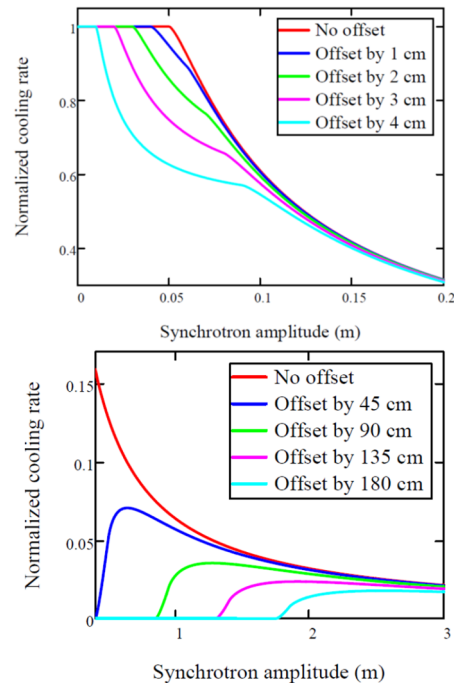


Figure 2: Normalized cooling rate for an electron bunch with various offsets. The abscissa is the synchrotron oscillation amplitude of the ion being cooled and the ordinate is the cooling rate as calculated from Eq. (14) in units of ζ_0 , i.e. the local cooling rate as defined in Eq. (7). The half electron bunch length is $l_e = 5$ cm for these plots.

In the absence of the offset of the electron bunch, $d = 0$ and $\theta_1 = -\theta_2 = -\arcsin(l_e/a)$, Eq. (14) reduces to the results derived in Ref. [3]. Figure 2 shows how the cooling rate depends on the synchrotron oscillation amplitude for various offsets of the electron bunch, with the half electron bunch length, $l_e = 5$ cm. It is worth noting that introducing

a longitudinal offset of the electron bunch will not increase the cooling rate for the ions with large synchrotron oscillation amplitude and consequently, cooling with painting will decrease cooling rate for all the ions, as shown in Fig. 2.

AN EXAMPLE: PRE-COOLER FOR EIC

To achieve the initial proton beam parameters in the hadron storage ring (HSR), a pre-cooler will be built to cool the proton beam at energy of $\gamma = 25.4$. The designed RMS bunch length for the cooling electrons is 5 cm and that for the proton beam is 70 cm. In the cooling section, a proton bunch overlaps with multiple electron bunches so that the desired cooling performance can be obtained. Since the ratio between the repetition frequency of the electron beam and that of the proton beam is not an integer, different proton bunch overlaps with the electron bunches differently in the cooling section. Two typical cases of the overlapping patterns are shown in Fig. 3, which corresponds to the proton bunch in the 0th bucket and that in the 80th bucket. The dependence of the cooling rate on the synchrotron oscillation amplitude is shown in Fig. 4, for a proton in the 0th bucket (red) and that in the 80th bucket (blue).

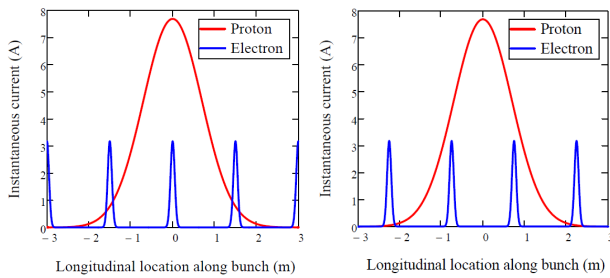


Figure 3: Overlapping of the electron bunches with the ion bunch in the 0th bucket (Left) and in the 80th bucket (Right). The electron bunches locate at $s = 0$ m, ± 1.5 m for the ion bunch in the 0th bucket (Left) and $s = \pm 0.75$ m, ± 2.25 m for the ion bunch in the 80th bucket (Right).

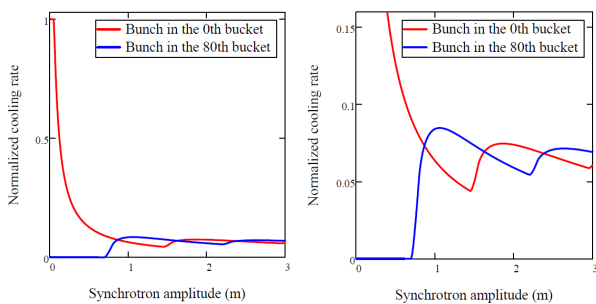


Figure 4: Normalized longitudinal cooling rate as a function of the synchrotron oscillation amplitude of an ion in the 0th bucket (red) and in the 80th bucket (blue) as shown in Fig. 3.

Figure 5 shows the profiles of the ion bunch in the 0th bucket (red), the 40th bucket (green) and the 80th bucket (blue) after 40 minutes of cooling, which suggests that the

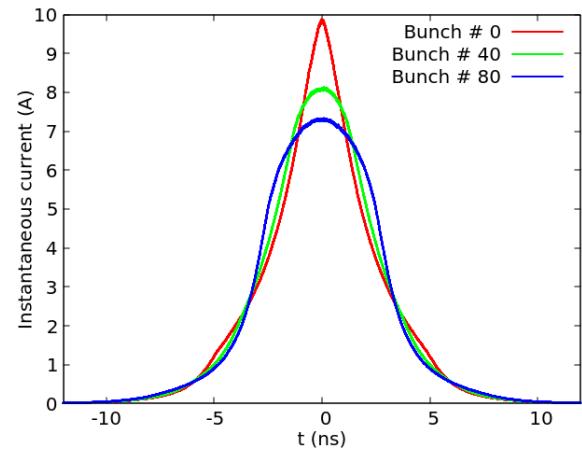


Figure 5: The proton bunch profiles after 40 minutes of cooling.

peak current of the ion bunches varies along the bunch train as a result of different overlapping patterns with the cooling electron bunches. One way to avoid the bunch-to-bunch variations is to paint the electron bunches slowly with respect to the ion bunches. If the painting is done uniformly with time, all proton bunches will be cooled identically and hence will have the same longitudinal profile.

SUMMARY

Assuming the cooling rate is independent of the location within the electron bunch, we derived an expression to calculate how the average cooling rate of an ion depends on its synchrotron oscillation amplitude when the cooling electron bunch is longitudinally shifted with respect to the ion bunch. We found that shifting the electron bunch away from the centre of the ion bunch will not increase the cooling rate for the ions with large synchrotron oscillation amplitude and hence painting will reduce the cooling rate for all ions in the bunch.

We have applied the results to study how the proton bunches in different rf bucket of the EIC will be cooled in the pre-cooler and found that their longitudinal profiles will be significantly different since every proton bunch in the train overlaps with the electron bunches differently. The variation of the proton bunch profile along the bunch train can be eliminated if a uniform painting of the cooling electron bunches is introduced.

REFERENCES

- [1] A. Fedotov *et al.*, “Experimental demonstration of hadron beam cooling using radio-frequency accelerated electron bunches”, *Phys. Rev. Lett.*, vol. 124, p. 084801, 2020. doi:10.1103/PhysRevLett.124.084801
- [2] A. Fedotov *et al.*, “Low-Energy Cooling for Electron Ion Collider”, Report No. EIC-HDR-TN-012, 2020.
- [3] G. Wang, “Evolution of ion bunch profile in the presence of longitudinal coherent electron cooling”, *Phys. Rev. Accel. Beams*, vol. 22, p. 111002, 2019. doi:10.1103/PhysRevAccelBeams.22.111002

ADVANCEMENTS AND APPLICATIONS OF COOLING SIMULATION TOOLS: A FOCUS ON Xsuite

P. Kruyt*¹, D. Gamba, G. Franchetti^{1,2,3}

CERN, Geneva, Switzerland

¹also at Goethe University, Frankfurt, Germany

²also at GSI, Darmstadt, Germany

³also at HFHF, Frankfurt am Main, Germany

Abstract

This paper presents recent advancements in cooling simulation tools in Xsuite, which is a new particle accelerator simulation code developed at CERN. An electron cooling module, based on the Parkhomchuk model, has been implemented and benchmarked against Betacool using parameters of the LEIR e-cooler at CERN. Additionally, a laser cooling module has been implemented, capable of simulating various laser pulse types, including Fourier-limited and continuous wave lasers. This module is applied to the Super Proton Synchrotron (SPS) with the aim of simulating the Gamma Factory proof-of-principle experiment (PoP) at CERN. First results are presented.

INTRODUCTION

The goal of this paper is to present the electron cooling and the laser cooling module of Xsuite and their respective advantages compared to other tracking codes. Xsuite is a collection of Python packages for multi-particle simulations for particle accelerators. It has been under development at CERN since 2021 and it has the capability to run on both CPUs and GPUs [1]. As for electron cooling, two currently available codes that also incorporate the Parkhomchuk model of electron cooling [2, 3] are Betacool [4, 5] and JSPEC (JLab Simulation Package for Electron Cooling) [6, 7]. The main advantage that Xsuite provides over Betacool is that it is under active development, whereas Betacool is no longer active. In comparison to JSPEC, Xsuite offers GPU capability and offers a wide variety of features beyond electron cooling, including synchrotron radiation, beam-beam effects, electron cloud, etc.

As for laser cooling, the Xsuite module is the first publicly available code that simulates laser cooling in particle accelerators with a great level of detail. While Betacool does offer laser cooling capabilities, it does not have an elaborate excitation scheme like Xsuite. The main goal of the new Xsuite module is to provide tools for simulating the beam cooling in the Gamma Factory [8–12], which is part of the Physics Beyond Colliders (PBC) study at CERN that aims to generate intense beams of scattered photons. Before the implementation of the Gamma Factory in the Large Hadron Collider (LHC), a proof-of-principle (PoP) experiment is intended to be carried out in the Super Proton Synchrotron

(SPS). The laser cooling module of Xsuite will be a key tool in simulating these two cases.

ELECTRON COOLING

This work is an expansion of the electron cooling simulation tools developed by N. Biancacci and A. Latina, which were initially used for simulating the impact of IBS on low-intensity cooled beams in LEIR [13, 14]. The electron cooling module of Xsuite has been benchmarked with BETA-COOL for the CERN accelerator LEIR (Low Energy Ion Ring) [15]. The benchmark compares the implementation of the Parkhomchuk model in both codes. The first part of the benchmark is done by comparing the time evolution of the emittance. The second part compares the cooling force as a function of the velocity difference between the circulating beam particles and the electrons. The electron cooler parameters are displayed in Table 1. The blue curve in Fig. 1, labeled as SC=0, represents the emittance comparison for a lead coasting beam in LEIR at 18 GeV/c. Here, SC=0 indicates that the space charge effect of the electron beam is inactive. The cooling force comparison is displayed in Fig. 2. The benchmark shows that Xsuite and Betacool produce compatible results for the time evolution of the emittance as well as for the cooling force as a function of the velocity difference. Additionally, the same benchmark was successfully performed for coasting beams in ELENA at 35 MeV/c [16], utilizing the electron cooler parameters provided in [17, 18]. Lastly, the module proved valuable in clarifying the magnetic field straightness requirements for the new AD electron cooler [19].

Table 1: LEIR Electron Cooling Simulation Parameters [20]

Parameter	Value
Electron beam radius	25 mm
Cooler length	3 m
Magnetic field strength	0.07 T
Transverse temperature	10 meV
Longitudinal temperature	1 meV
Current	0.6 A
β_x/β_y in the cooler	5/5 m

Initially, the benchmark between Xsuite and Betacool failed when the electron beam space charge was included. The Xsuite module incorporates two components of the electron beam space charge. Firstly, it incorporates an energy

* pieter.martin.kruyt@cern.ch

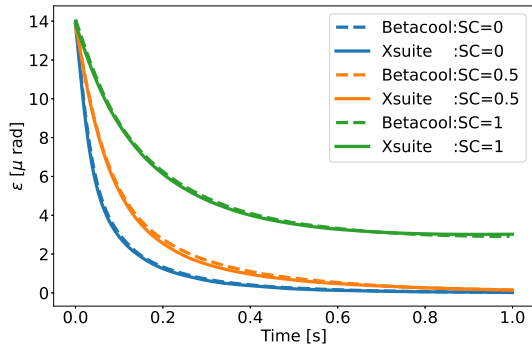


Figure 1: Comparison of cooling performance between the Parkhomchuk model in Xsuite and Betacool in LEIR at 18 GeV/c. The graph shows the time evolution of the transverse horizontal emittance. The value of SC indicates the magnitude of the space charge effects of the electron beam, where 0 indicates no space charge effects and 1 indicates the theoretical space charge of the electron beam, with no neutralisation from rest gas ions or similar.

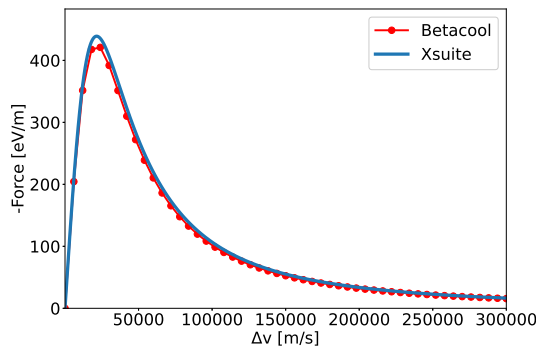


Figure 2: Comparison of longitudinal cooling force between the Parkhomchuk model in Xsuite and Betacool for a lead beam in LEIR at 18 GeV/c. The dependence of the longitudinal component of the cooling force on the relative velocity difference is displayed.

offset based on the location of the electron along the electron beam radius, assuming a uniform electron distribution with hard edges. Secondly, a collective rotation of the electron beam is implemented. Both these aspects of the electron beam space charge are described in [21]. The discrepancy between the two codes was eventually resolved by rectifying two minor bugs in the Betacool code and by disabling an undocumented and unclear effect that is implemented in Betacool only. After implementing these three changes, the cooling rates with space charge effects are in agreement, as can be seen in Fig. 1. The undocumented effect implemented in Betacool acts on the local electron temperature due to the electron beam rotation, but no reference for this effect was found. This remains to be investigated.

LASER COOLING

In addition to the electron cooler, a laser cooling module is also being developed in Xsuite. Laser cooling is a

well-established technique for cooling atoms in traps, and it is recently also being explored experimentally in synchrotrons [22, 23]. First, lasers excite atoms, causing them to emit photons in a random direction, which on average reduces momentum in the direction of the incoming laser pulse. To narrow the momentum spread, laser cooling leverages on the narrow bandwidth of lasers and the large Doppler shift of the laser frequency when colliding head-on with charged atoms circulating in the storage ring. By carefully adjusting the laser frequency, it is possible to selectively interact with high-energy particles only, while leaving low-energy particles unaffected.

The laser cooling module is currently capable of using two different types of laser pulses: a Fourier-limited pulse and a continuous wave laser. Here, the focus will be on the continuous wave laser. The laser cooling process consists of two parts: excitation and spontaneous emission. The model that is being used for the excitation will be discussed first and then the model of spontaneous emission.

Excitation

The governing equations for this scenario are the optical Bloch equations with damping, which are described in [24, 25]. The excitation probability can be obtained by finding the steady-state solution of the population of the excited state. A graphical representation of this solution is shown in Fig. 3, which depends on three parameters:

1. Γ is the decay rate of the excited state.
2. $\Delta = \omega_l - \omega_0$ is the detuning, which is the difference between the frequency of the laser light and the frequency corresponding to the transition to the excitation state.
3. Ω_R is the Rabi frequency, which quantifies the laser-ion coupling strength.

Each particle in the beam will correspond to a different position in the excitation map, based on its parameters. In particular, the detuning is different for each particle because all the ions have different energies and momenta, which means that they experience a different laser frequency due to a different Doppler shift. The laser cooling module of Xsuite computes Ω_R , Γ , and Δ for every particle crossing the laser cooler element and employs the excitation map shown in Fig. 3 to assign it an excitation probability.

Spontaneous Emission

The current model for spontaneous emission remains consistent across various laser pulse types. Firstly, when an ion becomes excited, it loses energy because of the quasi head-on collision with the photon. Secondly, the ion will emit a photon in a random direction, which causes it to gain or lose energy based on the outcome of the random event. Lastly, a Lorentz transformation is applied to transform from the co-moving frame of the ion to the lab frame. The whole emission process is assumed to be instantaneous, which is a valid approximation, for example, for the ions considered in the Gamma Factory proof of principle experiment: Li-like $^{208}_{82}\text{Pb}^{79+}$, with an excited-state lifetime of 76.6 ps [26],

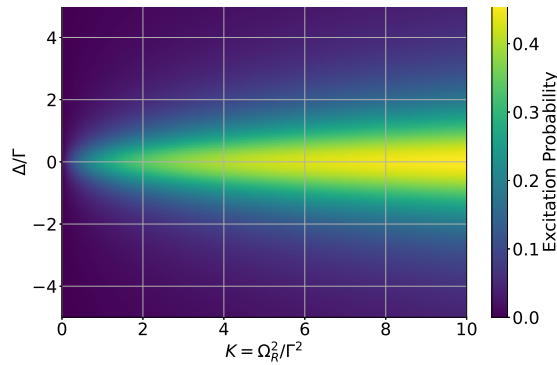


Figure 3: Steady-state solution for excited state population vs. detuning-to-decay rate ratio (vertical axis) and saturation parameter $K = \Omega_R^2/\Gamma^2$ (horizontal axis). Color indicates the ratio of the number of excited ions to the total number of ions.

which is much shorter than the SPS revolution period, which is 23 μs [27].

Laser Cooling Results

Preliminary simulations have already been performed by A. Petrenko for the Gamma Factory proof-of-principle experiment in the SPS [28, 29]. The difference between his simulations and the ones in this paper is the type of laser that is used. The simulations in this paper make use of a CW-laser, whereas the previous results were performed with a Fourier-limited pulse. Aside from that, the same simulation parameters were used, which are provided in Table 2. The current simulation utilized coasting beams and did not account for heating effects like Intra-beam scattering (IBS) and beam space charge. The primary focus of the analysis was the time evolution of the number of excited particles, as depicted in Fig. 4. This plot also illustrates the evolution of the RMS momentum spread. It is noteworthy that both the number of excited particles and the RMS momentum spread decrease together. Indeed, the simulation parameters were tuned such that only particles with a large $\Delta p/p$ experience momentum reduction through interaction with the laser cooler. As the high-momentum particles have their momentum reduced, the excitation process diminishes, ultimately halting the cooling process, as no ions with a matching momentum are left in the beam. This is confirmed by looking at the momentum distribution at the start and end of the simulation, which is shown in Fig. 5. Particles with large $\Delta p/p$ have indeed experienced momentum reduction, and there is an accumulation of particles with a momentum offset of $\Delta p/p = 3 \times 10^{-4}$. The absence of heating effects in the simulation exacerbates this accumulation.

CONCLUSIONS

An electron cooling module based on the Parkhomchuk model was developed in Xsuite and successfully benchmarked against Betacool. During the benchmarking process, two minor bugs were found in the electron beam space charge

Table 2: Gamma Factory PoP Simulation Parameters

Ion excited freq. ω_0	3.5×10^{17}	s^{-1}
Excited time τ [26]	76.6×10^{-12}	s
Fractional $\Delta p/p$	3.0×10^{-4}	
Relativistic γ	96.3	
Excited decay Γ	1.31×10^{10}	s^{-1}
$K = \Omega_R^2/\Gamma^2$	7.17 ± 0.01	

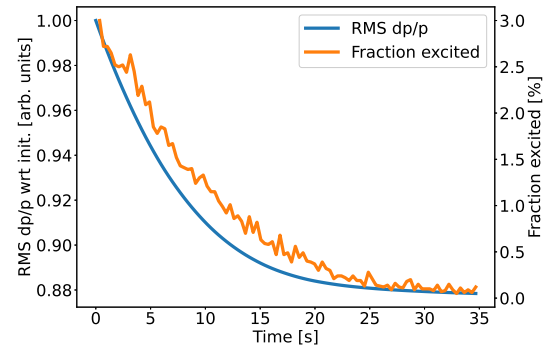


Figure 4: Time evolution of RMS $\Delta p/p$ and the fraction of excited particles in the accelerator. Left vertical axis: RMS $\Delta p/p$ relative to the initial value ($\Delta p/p = 3 \times 10^{-4}$). Right vertical axis: Fraction of excited particles. Horizontal axis: Elapsed time.

module of Betacool and these have been fixed. An undocumented effect of the electron beam space charge rotation of the transverse temperature of the electrons was found in the Betacool implementation, which still needs to be understood. The version of Betacool with these changes can be found in [30]. The electron cooling module of Xsuite will form a powerful tool with the possibility to include effects such as IBS and space charge, and thus will be a comprehensive tool for simulating all machines with electron coolers at CERN. A laser cooling module was also developed in Xsuite, which has the capability of using different laser pulses, including

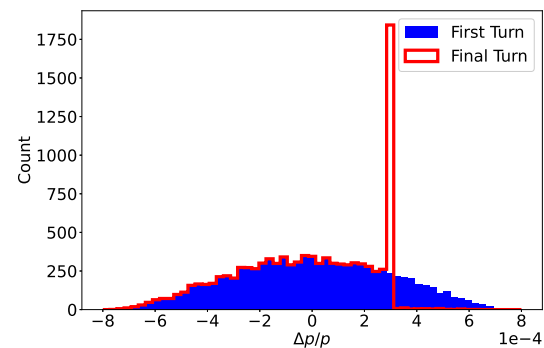


Figure 5: Comparison of histograms for $\Delta p/p$ at the first and final turn of the beam in the simulation. The blue histogram represents the first turn, while the red histogram represents the distribution of $\Delta p/p$ at the end of the simulation.

Fourier-limited and continuous wave lasers. The module is still under testing. First results show that the physics of the process is captured by the implementation. The next aim is the simulation of the SPS PoP experiment.

ACKNOWLEDGEMENTS

Firstly, the authors thank N. Biancacci and A. Latina for sharing their e-cooling simulation tools for LEIR. Secondly, the authors express their gratitude to A. Petrenko for pioneering and generously sharing his tools for simulating laser cooling with a Fourier-limited laser pulse. Furthermore, this work is supported by the Physics Beyond Colliders Study Group. Lastly, this work is partially supported by the European Union's Horizon 2020 Research and Innovation programme under Grant Agreement No. 101004730 (iFAST).

REFERENCES

- [1] Xsuite, <https://github.com/xsuite>
- [2] V.V. Parkhomchuk and Aleksandr N. Skriskii, "Electron cooling: 35 years of development", *Physics-Uspexhi*, vol. 43, no. 5, pp. 433–452, May 2000. doi:10.1070/pu2000v043n
- [3] V. V. Parkhomchuk, "New insights in the theory of electron cooling", *Nucl. Instrum. Methods Phys. Res. A*, vol. 441, no. 1, pp. 9–17, Feb. 2000. doi:10.1016/S0168-9002(99)01100-6
- [4] Igor Meshkov, A.O. Sidorin, Aleksandr Smirnov, and G. Trubnikov, "Physics guide of BETACOOOL code Version 1.1", 2006.
- [5] I.N. Meshkov, A.O. Sidorin, A.V. Smirnov, E.M. Syresin, G.V. Trubnikov, and P.R. Zenkevich, "Simulation of Electron Cooling Process in Storage Rings Using BETACOOOL Program", in *Proc. Beam Cool. Relat. Top.*, Bad Honnef, Germany, 2001.
- [6] H. Zhang, S. V. Benson, M. W. Bruker, and Y. Zhang, "JSPEC - A Simulation Program for IBS and Electron Cooling", in *Proc. IPAC'21*, Campinas, Brazil, May 2021, pp. 49–52. doi:10.18429/JACoW-IPAC2021-MOPAB004
- [7] H. Zhang, S. Benson, M.W. Bruker, Y. Zhang, *et al.*, "Jspec: A Program for IBS and Electron Cooling Simulation", Thomas Jefferson National Accelerator Facility (TJ-NAF), Newport News, VA, Tech. Rep., 2021.
- [8] M.W. Krasny, "The Gamma Factory proposal for CERN", Tech. Rep., CERN, 2015. doi:10.48550/arXiv.1511.07794
- [9] M.W. Krasny *et al.*, "Gamma Factory Proof-of-Principle Experiment", CERN, Geneva, Rep. CERN-SPSC-2019-031, SPSC-I-253, 2019.
- [10] J. Jaeckel, M. Lamont, and C. Vallée, "The quest for new physics with the physics beyond colliders programme", *Nat. Phys.*, vol. 16, p. 393, 2020. doi:10.1038/s41567-020-0838-4
- [11] D. Budker *et al.*, "Atomic physics studies at the Gamma Factory at CERN", *Ann. Phys.*, vol. 532, p. 2000204, 2020. doi:10.1002/andp.202000204

- [12] Junlan Jin *et al.*, "Excitation and probing of low-energy nuclear states at high-energy storage rings", *Phys. Rev. Res.*, vol. 5, no. 2, p. 23134, 2023. doi:10.1103/PhysRevResearch.5.023134
- [13] Impact of IBS on low intensity cooled beam in LEIR, https://indico.cern.ch/event/1139824/contributions/4788863/attachments/2411719/4127031/Impact_IBS_low_intensity_21032022_NB.pdf
- [14] Update on Electron Cooling tests with RF-Track and PyHT, https://indico.cern.ch/event/904424/contributions/3806029/attachments/2016378/3370302/UpdateElectronCoolingTests_07042020_NB.pdf
- [15] G. Tranquille, "Specification of a new electron cooler for the low energy ion accumulator ring, LEIR", *Nucl. Instrum. Methods Sect. A*, vol. 532, pp. 399–402, 2004. doi:10.1016/j.nima.2004.06.072
- [16] C. Carli *et al.*, "ELENA Commissioning and Status", in *Proc. IPAC'21*, Campinas, Brazil, May 2021, pp. 598–601. doi:10.18429/JACoW-IPAC2021-MOPAB177
- [17] G. Tranquille, A. Frassier, and L. Joergensen, "The ELENA electron cooler: parameter choice and expected performance", Tech. Rep., 2013.
- [18] D. Gamba, L. Bojtár, C. Carli, B. Dupuy, A. Frassier, L.V. Jørgensen, *et al.*, "AD/ELENA Electron Cooling Experience During and after CERNs Long Shutdown (LS2)", in *Proc. COOL'21*, Novosibirsk, Russia, Nov. 2021, pp. 36–41. doi:10.18429/JACoW-COOL2021-S503
- [19] D. Gamba *et al.*, "Specifications for a new electron cooler of the antiproton decelerator at CERN", in *Proc. IPAC'23*, Venice, Italy, May 2023, pp. 2241-2244. doi:10.18429/JACoW-IPAC2023-TUPM027
- [20] Agnieszka Borucka, Davide Gamba, and Andrea Latina, "Benchmark of e-cooling simulations with RF-Track", CERN, Geneva, Switzerland, Rep. CERN-ACC-NOTE-2021-0031, 2021.
- [21] H. Poth, "Electron cooling: Theory, experiment, application", *Phys. Rep.*, vol. 196, no. 3, pp. 135–297, 1990. doi:10.1016/0370-1573(90)90040-9
- [22] U. Schramm *et al.*, "Laser Cooling of Relativistic Heavy Ion Beams", in *Proc. of the 2005 Part. Accel. Conf.*, 2005, pp. 401–403, doi:10.1109/PAC.2005.1590446
- [23] D. Winters *et al.*, "Laser Cooling of Relativistic Heavy Ion Beams for FAIR", *Physica Scripta*, vol. 2015, no. T166, p. 014048, 2015, doi:10.1088/0031-8949/2015/T166/014048
- [24] Marcis Auzinsh, Dmitry Budker, and Simon Rochester, *Optically polarized atoms: understanding light-atom interactions*. Oxford University Press, 2010.
- [25] Harold J. Metcalf and Peter der Straten, *Laser cooling and trapping*. Springer Science & Business Media, 1999.
- [26] W.R. Johnson, Z.W. Liu, and J. Sapirstein, "Transition rates for lithium-like ions, sodium-like ions, and neutral alkali-metal atoms", *At. Data Nucl. Data Tables*, vol. 64, no. 2, pp. 279–300, 1996. doi:10.1006/adnd.1996.0024

- [27] F. J. Galindo Guarch *et al.*, “A new beam synchronous processing architecture with a fixed frequency processing clock”, *Nucl. Instrum. Methods Phys. Res. A*, vol. 988, p. 164894, 2021. doi:10.1016/j.nima.2020.164894
- [28] M.W. Krasny, A. Martens, and Y. Dutheil, “Gamma Factory proof-of-principle experiment”, 2020.
- [29] F. Zimmermann, *et al.*, “Summary of ARIES WP6 APEC & iFAST WP5.2 PAF joint Brainstorming & Strategy Workshop (BSW22)”, 2022. doi:10.5281/zenodo.7071937
- [30] Betacool, <https://github.com/dgamba/betacool>

INFLUENCES OF BEAM PARAMETERS ON THE INTERACTION BETWEEN ION AND ELECTRON BEAMS

V. A. Britten*, O. Meusel, H. Podlech¹, A. Schempp

Institute of Applied Physics (IAP), Goethe-University, Frankfurt am Main, Germany

¹ also at Helmholtz Research Academy Hesse for FAIR (HFHF), Frankfurt, Germany

Abstract

Electrons can be confined as a static column or as a comoving beam for applications in accelerator physics. Depending on the configuration of the electrons, they can cool [1], compensate [2] or even focus [3] the ion beam. In the case of an electron beam, the parameters must be chosen correctly to obtain the desired effects. The influences of these beam parameters on the interaction between the ion and electron beam are investigated in numerical simulations by using a particle-in-cell code [4]. The understanding of the different interaction mechanisms will allow an even better matching of the beams to each other for the intended application. With additional suitable beam diagnostics, it will be possible to draw conclusions about the interaction of the superimposed beams in order to evaluate the quality of the settings and, if necessary, to correct them.

SIMULATION SETTINGS

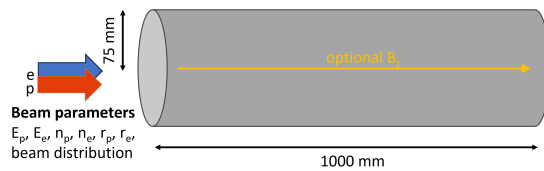


Figure 1: Schematic layout of the simulation setup.

To investigate the influence of the initial beam parameters, simulations were performed by using the particle-in-cell code Bender [4]. A proton beam is superimposed with an electron beam (Fig. 1). The simulation volume is bounded by a beam tube with a radius of 75 mm and a length of 1000 mm. In each simulation, the initial kinetic energies are set to $E_{\text{kin,protons}} = 50$ keV and $E_{\text{kin,electrons}} = 27.23$ eV so that the velocities of the beams are the same ($v_e = v_p$). The resulting transit time is $\tau = 323$ ns. The beams start with the same radius ($r_e = r_p = 15$ mm). In the simulations, in which the mean density is varied to study the influence of the initial density, the initial distribution is chosen the same. In addition, a longitudinal homogenous magnetic field of $B = 3$ mT is used in some simulations.

Table 1: Initial Beam Parameters

beam particles	E_{kin}	r	distribution
protons	50 keV	15 mm	Gaussian/KV
electrons	27.23 eV	15 mm	KV

* britten@iap.uni-frankfurt.de

DENSITY INFLUENCE

In order to investigate only the influence of a density difference, all other initial beam parameters were left constant in each simulation (see Table 1), while the mean density was varied. A KV distribution was chosen as an initial distribution for the electron and proton beam to ensure linear space charge fields.

Without a Longitudinal Magnetic Field

To allow undisturbed particle interactions, simulations were first performed without a longitudinal magnetic field for different cases. First, the same density for both beams was simulated as a reference. Then, different densities were chosen: $n_e < n_p$ and $n_e > n_p$.

Case $n_e < n_p$: When the density of the protons is greater than the density of the electrons, the electrons, as they move in the z -direction, begin to oscillate radially around the beam axis, creating focal points of increased density (similar to Fig. 2). This leads to strong non-linear fields, so that a redistribution of both beams can be observed. The kurtosis of the proton beam grows from an initial value of 2 to 2.3 for the case $5n_e = n_p$ and to over 2.4 for the case $1.5n_e = n_p$ (Fig. 3b) while the kurtosis of the electrons (Fig. 3e) increases right at the beginning and oscillates around the value 2.4. This oscillation decreases in the course of the simulation. This redistribution of particles in the beam causes an emittance growth of both beams (Figs. 3a and 3d). Another important effect is the energy shift, which also occurs at different densities. The greater the density difference, the greater the energy shift, which can be seen in Figs. 4 and 5.

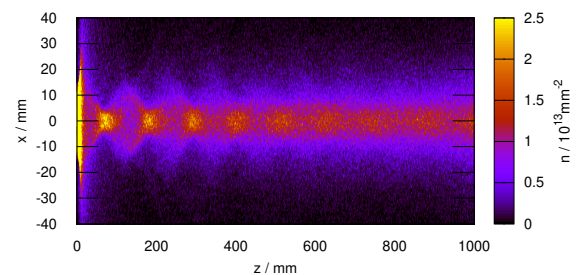


Figure 2: x - z -plane of the electron density distribution for $n_e > n_p$. The electron slice is seen at the beginning, which is a result of the high space charge forces. The following oscillation of the electrons is similar to the oscillation of the electrons in the case $n_e < n_p$.

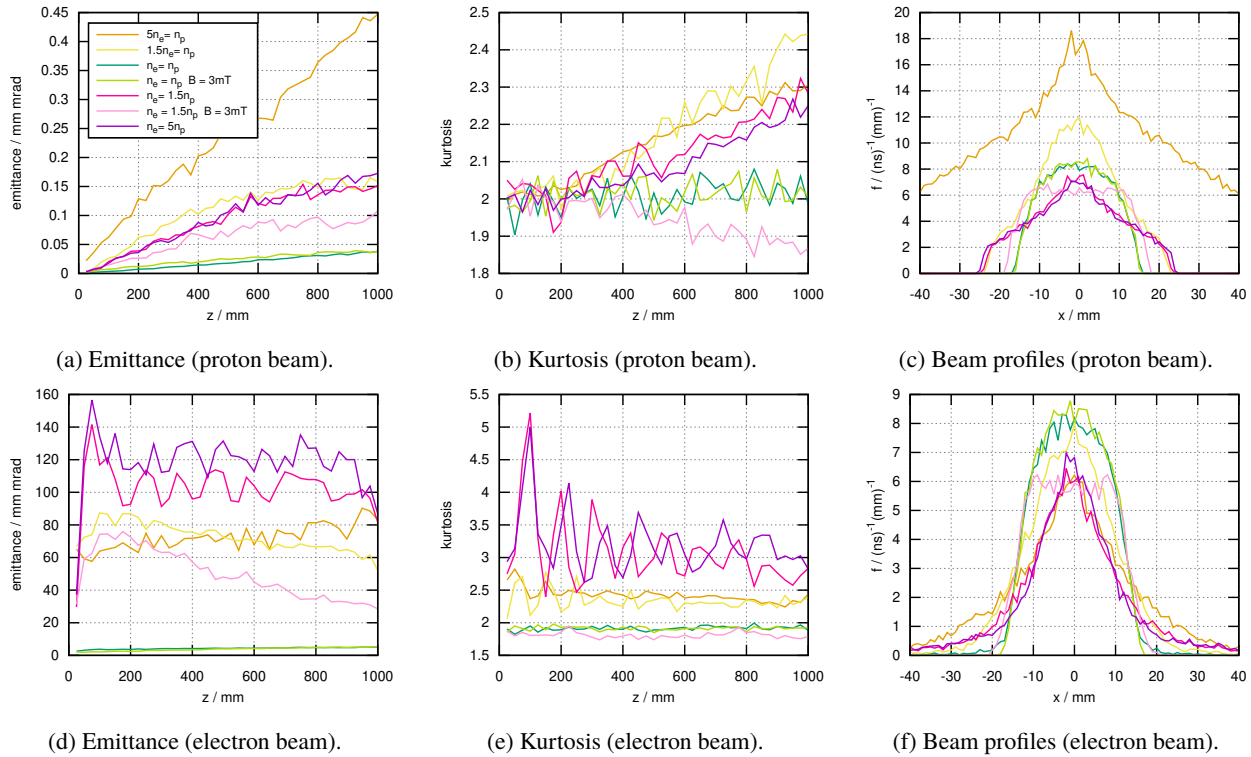


Figure 3: Comparison of emittance $\epsilon_{rms, norm} = \beta\gamma\sqrt{\langle x^2 \rangle \langle x'^2 \rangle - \langle xx' \rangle^2}$, kurtosis $V_x = \frac{\langle x^4 \rangle}{\langle x^2 \rangle^2}$ and beam profiles for the cases $n_e < n_p$, $n_e = n_p$, and $n_e > n_p$. Density differences lead to emittance growth, kurtosis change and related distribution change. A magnetic field reduces the emittance growth and leads to lower kurtosis.

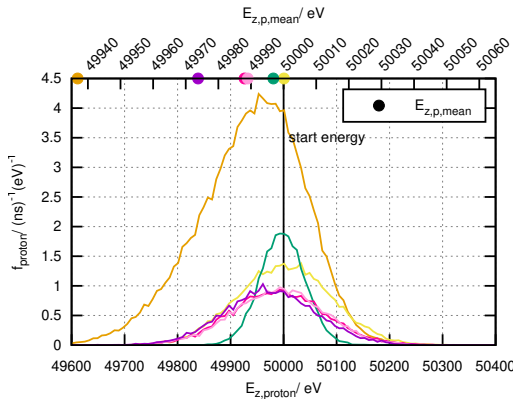


Figure 4: Kinetic energy distribution of the proton beam at $z = 1000$ mm with energy shift due to density difference.

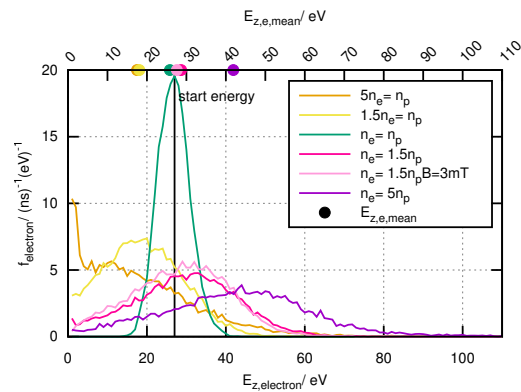


Figure 5: Kinetic energy distribution of the electron beam at $z = 1000$ mm with energy shift due to density difference.

Case $n_e > n_p$: All cases with initial $n_e > n_p$ result in $n_e < n_p$, because the space charge forces and the strong mobility of the electrons at the beginning of the simulation volume leads to a strong divergence and accumulation of the electrons in an electron slice ($E_z = 0$ eV), which reduces the following density of the electrons. In Fig. 2, the electron slice can be seen at small x values. Similar to the simulation for $n_e < n_p$ there is an oscillation of the electrons around the beam center (Fig. 2), the emittance grows, a redistribution takes place with an increasing kurtosis and an energy shift can also be observed (Fig. 3).

With a Longitudinal Magnetic Field

The simulation for $n_e = 1.5n_p$ was carried out with an additional longitudinal magnetic field. A longitudinal magnetic field is needed to avoid radial losses of electrons and to preserve the electron density. This reduces the electron slice at the beginning. This electron accumulation does not disappear completely, because the electrons, which diverged strongly without magnetic field, still have this tendency, but are held in the beam by the magnetic field and gyrate. Nevertheless, they have changed their longitudinal velocity into transversal velocity, so that they still form an electron slice

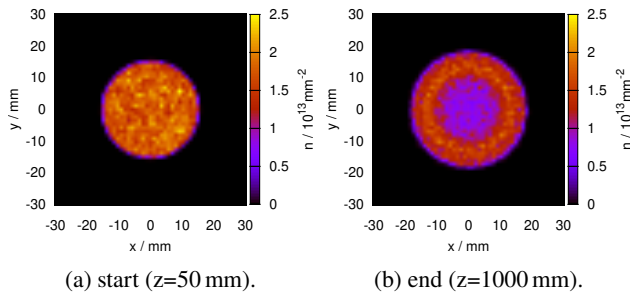


Figure 6: x-y-plane with the density distribution of the proton beam. The proton beam adapts to the distribution of the electron beam (hollow beam distribution).

with a well-defined radius at the beginning. The electrons in the beam directly form a slight hollow beam due to the magnetic field. This distribution remains through the whole simulation volume which can be observed by the value of the kurtosis, which is less than 2 (Fig. 3d). Because of the magnetic field, the mobility of the electrons decreases, so that the protons are radially more mobile than the electrons. The protons therefore adapt to the electrons in order to reach a state of equilibrium. At the end, the proton beam also reaches a hollow distribution (Figs. 6 and 3b). Compared to the case without a magnetic field, the additional magnetic field reduces the emittance growth (Fig. 3a). The emittance of the electrons increases globally but decreases after the initial rise (Fig. 3d). Anyhow the magnetic field does not change the already existing energy shift (Figs. 4 and 5).

DISTRIBUTION INFLUENCE

To study the distribution influence, the superposed beams have the same initial parameters as in the density influence simulations except that the distributions differ. The proton beam starts with a Gaussian distribution and the electron beam with a KV distribution. Simulations were performed without and with a longitudinal magnetic field (Fig. 7). With

a magnetic field, the electron beam is kept approximately in its initial distribution, so that the proton beam reaches the KV distribution faster than without a magnetic field (Fig. 7b). The emittance growth of the electron beam reaches in both cases a maximum, but in the case with magnetic field the emittance decreases along the z-direction. In contrast, the emittance growth of the proton beam is higher in the case with magnetic field (Fig. 7a).

CONCLUSION

These investigations clearly show the influence of a density or a distribution difference. Depending on the application these influences can be disadvantageous or even advantageous. If an ion beam is to be preserved as cool as possible or even to be cooled by its interaction with the electron beam, emittance growth is by no means beneficial. An unwanted energy shift or distribution change can cause problems in the following accelerator system. Thus, it is important to choose the initial beam parameters accordingly. In a previous publication [5] the influence of the radius was already presented. In these simulations it is evident that to avoid non-linear field forces and to preserve the distribution, the electron beam radius must always be larger than the ion beam. The simulations presented in this publication show the requirement of the same density and distribution for the superposed beams if an emittance growth, an energy shift or a change of the distribution is undesired.

Nevertheless, a difference in the density distributions can also be useful. Since a magnetic field is always required for the electrons, the adapting of the ion beam to the electron beam can be used to intentionally change the distribution of the ion beam, either to obtain a different distribution or to improve the present distribution.

With more detailed investigation, in simulations as well as in experiments, it should also be possible to draw conclusions about the interaction of the beams by using the beam diagnostics of the electron beam, in order to make adjustments to the system if necessary.

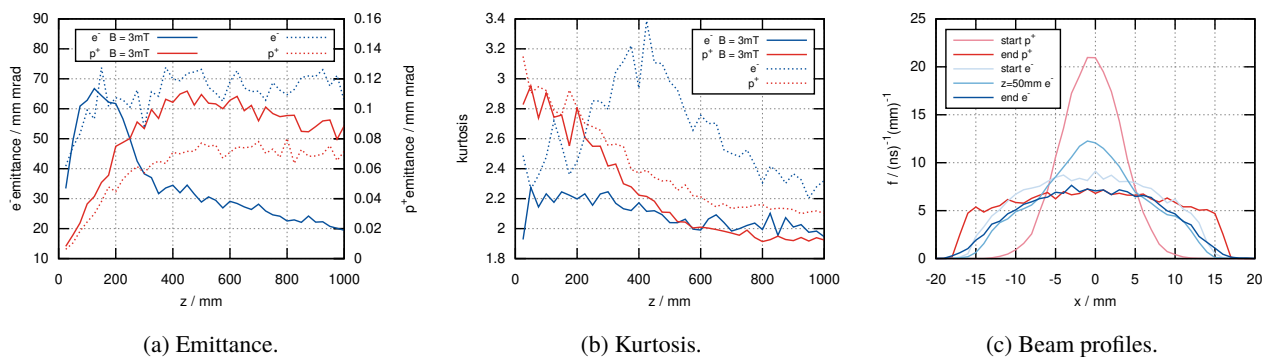


Figure 7: Emittance $\epsilon_{rms, norm} = \beta \gamma \sqrt{\langle x^2 \rangle \langle x'^2 \rangle - \langle x x' \rangle^2}$, kurtosis $V_x = \frac{\langle x^4 \rangle}{\langle x^2 \rangle^2}$ and beam profiles of the simulation results to study the distribution influence. With a magnetic field, the electron beam approximately keeps its KV distribution. The proton beam thus reaches the KV distribution faster than without a magnetic field.

REFERENCES

- [1] G. I. Budker *et al.*, “Experimental studies of electron cooling”, *Part. Accel.*, vol. 7, p. 197–211, 1976.
- [2] V. Shiltsev, “Electron lenses: historical overview and outlook”, *JINST*, vol. 16, p. P03039, 2021.
doi:10.1088/1748-0221/16/03/P03039
- [3] D. Gabor, “A Space-Charge Lens for the Focusing of Ion Beams”, *Nature*, vol. 160, p. 89-90, 1947.
doi:10.1038/160089b0
- [4] D. Noll, M. Droba, O. Meusel, U. Ratzinger, K. Schulte, and C. Wiesner, “The Particle-in-Cell Code Bender and Its Application to Non-Relativistic Beam Transport”, in *Proc. HB’14*, East Lansing, MI, USA, Nov. 2014, paper WEO4LR02, pp. 304–308.
- [5] V. A. Britten, M. Droba, O. Meusel, H. Podlech, A. Schempp, and K. Schulte, “The Interaction Between Electrons and Ions in Comoving and Static Electron Columns”, in *Proc. COOL’17*, Bonn, Germany, Sep. 2017, pp. 47–49.
doi:10.18429/JACoW-COOL2017-TUP11

EXPLICIT EXPRESSIONS FOR NON-MAGNETIZED BUNCHED ELECTRON COOLING*

S. Seletskiy[†], A. Fedotov, Brookhaven National Laboratory, Upton, Long Island, NY, USA

Abstract

Recent success of Low Energy RHIC Electron Cooler (LEReC) leads the way in development of high energy electron coolers based on non-magnetized electron bunches accelerated by RF cavities. In this paper we derive explicit formulas for the friction force and the cooling rates in non-magnetized electron coolers in the presence of redistribution of cooling decrements. We further consider several particular cases reducing the general expressions to simple analytic formulas useful for optimization of coolers' parameters.

INTRODUCTION

Redistribution of cooling between longitudinal and transverse directions [1] requires two conditions. The first one is a coupling between the longitudinal and transverse (in this paper we will consider the horizontal one) motion of an ion. This is created by the ions' dispersion in the cooling section (CS). The second condition is dependence of the longitudinal friction force on the horizontal position of an ion in the cooling section, i.e. the longitudinal component of the cooling force must have the transverse gradient. A robust way to create the required gradient (which will be the focus of this paper) is to introduce the electron beam dispersion in the CS.

In the following section we will derive the explicit expressions for the dynamical friction force in the presence of electron dispersion. Next, we will show how introduction of ion dispersion results in $x - z$ redistribution of the cooling rates. Finally, we will apply the obtained formulas to several "asymptotic" cases.

DYNAMICAL FRICTION FORCE

The general expression for the dynamical friction force in non-magnetized cooling is:

$$\vec{F} = -\frac{4\pi N_e e^4 Z_i^2}{m_e} \int \Lambda_C \frac{\vec{v}_i - \vec{v}_e}{|\vec{v}_i - \vec{v}_e|^3} f_e(r_e, v_e) d^3 v_e, \quad (1)$$

where N_e is the number of electrons per bunch, e and m_e are an electron's charge and mass, Z_i is an ion's charge number, v_e and v_i are electron and ion velocities, Λ_C is a Coulomb logarithm, which is a weak function of velocity and can be taken out of integral, and $f_e(r_e, v_e)$ is the electrons 6-D distribution function.

Assuming Gaussian electron distribution, in the presence of electron dispersion (D_e) in the cooling section and using

$x - D_e \delta_e$ for horizontal electron coordinate (here $\delta_e = \frac{v_{ze}}{\beta c}$), one can write f_e in the form $f_e = \rho_e f_{ve}$, where

$$\rho_e = \frac{1}{\gamma(2\pi)^{3/2} \sigma_{1xe} \sigma_{ye} \sigma_{ze}} \exp\left(-\frac{x^2}{2\sigma_{1xe}^2} - \frac{y^2}{2\sigma_{ye}^2} - \frac{z^2}{2\sigma_{ze}^2}\right), \quad (2)$$

$$f_{ve} = \frac{1}{\gamma(2\pi)^{3/2} \sigma_{vxe} \sigma_{vye} \sigma_{1vze}} \times \exp\left(-\frac{v_{xe}^2}{2\sigma_{vxe}^2} - \frac{v_{ye}^2}{2\sigma_{vye}^2} - \frac{(v_{ze} - \mu)^2}{2\sigma_{1vze}^2}\right), \quad (3)$$

with $\sigma_{1xe} = \sqrt{\sigma_{xe}^2 + D_e^2 \sigma_{\delta_e}^2}$, $\sigma_{1vze} = \sigma_{vze} \frac{\sigma_{xe}}{\sqrt{\sigma_{xe}^2 + D_e^2 \sigma_{\delta_e}^2}}$ and

$$\mu = x \sigma_{vze} \frac{D_e \sigma_{\delta_e}}{\sigma_{xe}^2 + D_e^2 \sigma_{\delta_e}^2}.$$

Now, we can rewrite Eq. (1) as:

$$\vec{F} = -C_0 \rho_e \int \frac{\vec{v}_i - \vec{v}_e}{|\vec{v}_i - \vec{v}_e|^3} f_{ve} d^3 v_e, \quad (4)$$

where $C_0 = \frac{4\pi N_e e^4 Z_i^2}{m_e} \Lambda_C$. We further introduce an effective potential in the velocity-space:

$$U = C_0 \rho_e \int \frac{f_{ve}}{|\vec{v}_i - \vec{v}_e|} d^3 v_e. \quad (5)$$

Noticing that components of the friction force can be presented by $F_{x,y,z} = \partial U / \partial v_{xi,yi,zi}$, one can reduce Eq. (4) to 1-D integrals [2, 3]. For the sake of clarity, we will consider the case of $\sigma_{vxe} = \sigma_{vye} \equiv \sigma_{v\perp e}$ (for detailed derivations and more general cases see [2-4]).

After some algebraic manipulations we get Binney's formulas [5] for friction force components:

$$F_{x,y} = -C_1 \rho_e v_{xi,yi} \int_0^\infty g_\perp(q) dq$$

$$F_z = -C_1 \rho_e (v_{zi} - \mu) \int_0^\infty g_z(q) dq$$

$$g_\perp(q) = \frac{E(q)}{\sigma_{v\perp e}^2 (1+q)^2 \sqrt{\sigma_{v\perp e}^2 q + \sigma_{1vze}^2}}, \quad (6)$$

$$g_z = \frac{E(q)}{(1+q)(\sigma_{v\perp e}^2 q + \sigma_{1vze}^2)^{3/2}}$$

$$E(q) = \exp\left[-\frac{v_{xi}^2 + v_{yi}^2}{2\sigma_{v\perp e}^2 (1+q)} - \frac{(v_{zi} - \mu)^2}{2(\sigma_{v\perp e}^2 q + \sigma_{1vze}^2)}\right]$$

where $C_1 = 2\sqrt{2\pi} N_e r_e^2 m_e c^4 Z_i^2 \Lambda_C$.

To simplify final expressions we will further consider an approximation of small amplitudes ($v_i < \sigma_{ve}$). Then, one can analytically take integrals in Eq. (6). Switching to laboratory frame values $\sigma_{\delta_e} = \frac{\sigma_{vze}}{\beta c}$ and $\sigma_{\theta_e} = \frac{\sigma_{v\perp e}}{\gamma \beta c}$, we get:

$$F_x = -C_2 \rho_e h v_{xi} \Phi\left(\frac{\sigma_{\delta_e}}{\gamma \sigma_{\theta_e} h}\right)$$

$$F_z = -2C_2 \rho_e h (v_{zi} - K x_i) \left[1 - \Phi\left(\frac{\sigma_{\delta_e}}{\gamma \sigma_{\theta_e} h}\right)\right], \quad (7)$$

where $C_2 = \frac{2\sqrt{2\pi} N_e r_e^2 m_e c^4 Z_i^2 \Lambda_C}{\gamma^2 \beta^3 \sigma_{\theta_e}^2 \sigma_{\delta_e}}$, $h = \frac{\sqrt{\sigma_{xe}^2 + D_e^2 \sigma_{\delta_e}^2}}{\sigma_{xe}}$ and parameter

$K = \beta c \frac{D_e \sigma_{\delta_e}}{\sigma_{xe}^2 + D_e^2 \sigma_{\delta_e}^2}$. The function Φ is given by:

*Work supported by Brookhaven Science Associates, LLC under Contract No. DE-SC0012704 with the U.S. Department of Energy

[†] seletskiy@bnl.gov

$$\Phi(d) = \begin{cases} \frac{d}{1-d^2} \left(\frac{\arccos(d)}{\sqrt{1-d^2}} - d \right), & d < 1 \\ \frac{2}{3}, & d = 1 \\ \frac{d}{d^2-1} \left(\frac{\log(d-\sqrt{d^2-1})}{\sqrt{d^2-1}} + d \right), & d > 1 \end{cases} \quad (8)$$

The plot in Fig. 1 shows that Φ is a rather strong function of the ratio of electrons effective longitudinal and transverse velocity spreads in the range most relevant to bunched electron cooling.

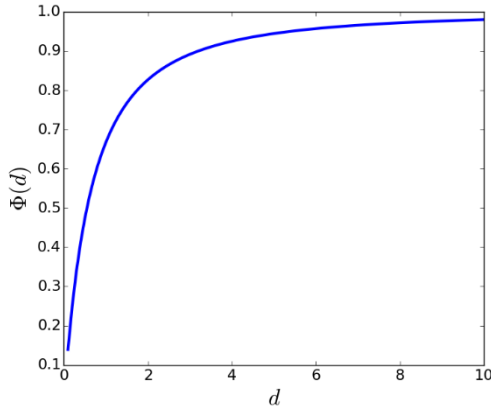


Figure 1: Function Φ .

COOLING REDISTRIBUTION

It follows from Eqs. (7) and (8) that on a single pass through the cooling section changes in an ion's angle ($\Delta x'_i$) and relative momentum ($\Delta \delta_i$) are given by:

$$\begin{aligned} \Delta x'_i &= c_0 \rho_e h x'_{iCS} \Phi \left(\frac{\sigma_{\delta e} 1}{\gamma \sigma_{\theta e} h} \right) \\ \Delta \delta_i &= 2c_0 \rho_e h (\delta_{iCS} - k x_{iCS}) \left[1 - \Phi \left(\frac{\sigma_{\delta e} 1}{\gamma \sigma_{\theta e} h} \right) \right] \end{aligned} \quad (9)$$

where $c_0 = \frac{C_2 L_{CS}}{\gamma^2 \beta A_i m_p}$, $k = \frac{K}{\beta c}$, L_{CS} is the length of the cooling section, A_i is an ion's atomic number and x_{iCS} , x'_{iCS} , δ_{iCS} are ion's position, angle and relative momentum in the cooling section.

Denoting ion's parameters upstream and downstream of the cooling section with indexes 0 and 1 respectively and noticing that $x_{iCS} = x_{i0} + D_i \delta_{i0}$ and $x_{i1} = x_{iCS} - D_i (\delta_{i0} + \Delta \delta_i)$, we get $\Delta x_i = -D_i \Delta \delta_i$. Combining this with Eq. (9) we obtain:

$$\begin{aligned} \Delta x_i &= 2c_0 \rho_{e1} h \left[1 - \Phi \left(\frac{\sigma_{\delta e} 1}{\gamma \sigma_{\theta e} h} \right) \right] D_i (\delta_{i0} - k(x_{i0} + D_i \delta_{i0})) \\ \Delta x'_i &= -c_0 \rho_{e1} h \Phi \left(\frac{\sigma_{\delta e} 1}{\gamma \sigma_{\theta e} h} \right) x'_{i0} \\ \Delta \delta_i &= -2c_0 \rho_{e1} h \left[1 - \Phi \left(\frac{\sigma_{\delta e} 1}{\gamma \sigma_{\theta e} h} \right) \right] (\delta_{i0} - k(x_{i0} + D_i \delta_{i0})), \end{aligned} \quad (10)$$

where the electrons density "probed" by an ion is:

$$\rho_e = \frac{1}{\gamma (2\pi)^{3/2} \sigma_{1xe} \sigma_{ye} \sigma_{ze}} \exp \left(-\frac{(x_{i0} + D_i \delta_{i0})^2}{2\sigma_{1xe}^2} - \frac{y_{i0}^2}{2\sigma_{ye}^2} - \frac{z_{i0}^2}{2\sigma_{ze}^2} \right). \quad (11)$$

We introduce horizontal and longitudinal actions of an ion, assuming that in the CS $\alpha_x = 0$:

$$\begin{aligned} J_x &= \frac{1}{2} \left(\frac{x_i^2}{\beta_x} + \beta_x x_i'^2 \right) \\ J_z &= \frac{1}{2} \left(\frac{z_i^2}{\beta_z} + \beta_z \delta_i^2 \right) \end{aligned}, \quad (12)$$

where $\beta_z \equiv \sigma_{zi}/\sigma_{\delta i}$.

The change in actions on a single pass through the CS is:

$$\begin{aligned} \Delta J_x &\approx \frac{x_{i0} \Delta x_i}{\beta_x} + \beta_x x'_{i0} \Delta x'_i \\ \Delta J_z &\approx \beta_z \delta_{i0} \Delta \delta_i \end{aligned} \quad (13)$$

Finally, the change of i-bunch emittances over a single pass through the cooling section can be found as:

$$\begin{aligned} \Delta \varepsilon_x &= \int_{-\infty}^{\infty} \dots \int_{-\infty}^{\infty} f_i \Delta J_x dx_i \dots d\delta_i \\ \Delta \varepsilon_z &= \int_{-\infty}^{\infty} \dots \int_{-\infty}^{\infty} f_i \Delta J_z dx_i \dots d\delta_i \end{aligned} \quad (14)$$

We assume the 6-D Gaussian distribution of ions:

$$f_i = \frac{\exp \left(-\frac{x^2}{2\sigma_{xi}^2} - \frac{y^2}{2\sigma_{yi}^2} - \frac{z^2}{2\sigma_{zi}^2} - \frac{x'^2}{2\sigma_{\theta xi}^2} - \frac{y'^2}{2\sigma_{\theta yi}^2} - \frac{\delta^2}{2\sigma_{\delta i}^2} \right)}{(2\pi)^3 \sigma_{xi} \sigma_{yi} \sigma_{zi} \sigma_{\theta xi} \sigma_{\theta yi} \sigma_{\delta i}} \quad (15)$$

Noticing that the cooling rate is $\lambda = \frac{1}{T_{rev}} \frac{\Delta \varepsilon}{\varepsilon}$, where T_{rev} is a revolution period in the ion storage ring, we get from Eqs. (10)-(15):

$$\begin{aligned} \lambda_x &= -P \left(c_x + c_z \frac{D_i^2 \sigma_{\delta i}^2 + D_e D_i \sigma_{\delta e}^2}{D_i^2 \sigma_{\delta i}^2 + \sigma_{xi}^2 + D_e^2 \sigma_{\delta e}^2 + \sigma_{xe}^2} \right) \\ \lambda_z &= -P \left(c_x - c_z \frac{D_i^2 \sigma_{\delta i}^2 + D_e D_i \sigma_{\delta e}^2}{D_i^2 \sigma_{\delta i}^2 + \sigma_{xi}^2 + D_e^2 \sigma_{\delta e}^2 + \sigma_{xe}^2} \right) \\ c_x &= \frac{N_e r_e^2 Z_i^2 m_e c \Lambda_C \eta}{\pi \gamma^4 \beta^3 A_i m_p \sigma_{\theta e}^2 \sigma_{\delta e}} \Phi \left(\frac{\sigma_{\delta e}}{\gamma \sigma_{\theta e}} \frac{\sigma_{xe}}{\sqrt{D_e^2 \sigma_{\delta e}^2 + \sigma_{xe}^2}} \right) \\ c_z &= 2 \frac{N_e r_e^2 Z_i^2 m_e c \Lambda_C \eta}{\pi \gamma^4 \beta^3 A_i m_p \sigma_{\theta e}^2 \sigma_{\delta e}} \left[1 - \Phi \left(\frac{\sigma_{\delta e}}{\gamma \sigma_{\theta e}} \frac{\sigma_{xe}}{\sqrt{D_e^2 \sigma_{\delta e}^2 + \sigma_{xe}^2}} \right) \right] \\ P &= \frac{\sqrt{D_e^2 \sigma_{\delta e}^2 + \sigma_{xe}^2}}{\sigma_{xe} \sqrt{D_i^2 \sigma_{\delta i}^2 + \sigma_{xi}^2 + D_e^2 \sigma_{\delta e}^2 + \sigma_{xe}^2} \sqrt{\sigma_{xe}^2 + \sigma_{xi}^2} \sqrt{\sigma_{ye}^2 + \sigma_{zi}^2}} \end{aligned} \quad (16)$$

where duty factor $\eta = L_{CS}/C_{ring}$ and C_{ring} is the storage ring circumference.

Equations (16) give the explicit expressions for redistribution of cooling rates between longitudinal and horizontal direction in presence of electron and ion dispersions in the cooling section. The equations take into account nonuniformity of e-bunch density distribution. Therefore, even with $D_e = 0$ some redistribution is present (non-zero term $D_i^2 \sigma_{\delta i}^2$ in the numerator of the redistribution coefficient in the two first equations).

It is important to stress that coefficients c_x and c_z are themselves functions of D_e . Hence, generally speaking, one cannot simply calculate the "undisturbed" cooling rates ($\lambda_{x0}, \lambda_{z0}$) and plug them into simple redistribution equations of the form $\lambda_x = \lambda_{x0} + r \lambda_{z0}$; $\lambda_x = \lambda_{x0} - r \lambda_{z0}$. To the best of our knowledge, this fact was ignored in the previous works dedicated to studies of cooling redistribution.

SPECIAL CASES

Absence of Redistribution ($D_e = D_i = 0$)

We first consider the simplest case of $D_e = D_i = 0$, which allows us to compare the derived formulas to two well-known asymptotic cases. Zeroing the terms containing dispersion in the friction force equation (7) and using the peak electron density in the beam frame n_e , we get:

$$\begin{aligned} F_{x,y} &= -2\sqrt{2}n_e r_e^2 m_e c^4 Z_i^2 \Lambda_C \frac{v_{xi,yi}}{\sigma_{v\perp e}^2 \sigma_{vze}} \Phi\left(\frac{\sigma_{vze}}{\sigma_{v\perp e}}\right) \\ F_z &= -4\sqrt{2}n_e r_e^2 m_e c^4 Z_i^2 \Lambda_C \frac{v_{zi}}{\sigma_{v\perp e}^2 \sigma_{vze}} \left[1 - \Phi\left(\frac{\sigma_{vze}}{\sigma_{v\perp e}}\right)\right] \end{aligned} \quad (17)$$

For the case of spherically symmetric velocity distribution ($\sigma_{vze} = \sigma_{v\perp e} \equiv \sigma_{ve}$) $\Phi(1) = 2/3$ and we get:

$$F_{x,y} = F_z = -\frac{4\sqrt{2}\pi n_e r_e^2 m_e c^4 Z_i^2 \Lambda_C}{3 \sigma_{ve}^3} v_{xi,yi,zi} \quad (18)$$

For the case of $\sigma_{vze} \ll \sigma_{v\perp e}$, which is typical for the coolers utilizing DC electron beam, $\lim_{d \rightarrow 0} \Phi(d) = \frac{\pi d}{2}$. Then, from Eq. (17) we get:

$$\begin{aligned} F_{x,y} &= -\pi\sqrt{2}\pi \frac{n_e r_e^2 m_e c^4 Z_i^2 \Lambda_C}{\sigma_{v\perp e}^3} v_{xi,yi} \\ F_z &= -4\sqrt{2}\pi \frac{n_e r_e^2 m_e c^4 Z_i^2 \Lambda_C}{\sigma_{v\perp e}^2 \sigma_{vze}} v_{zi} \end{aligned} \quad (19)$$

Both equations (18) and (19) coincide with the expressions derived in [1].

Zero Electron Dispersion ($D_e = 0$)

For the case of $D_e = 0$ the redistribution is caused by a nonuniformity of the electron density only (as was discussed above), and Eq. (16) becomes:

$$\begin{aligned} \lambda_x &= -P_0 \left(c_{x0} + c_{z0} \frac{D_i^2 \sigma_{\delta i}^2}{D_i^2 \sigma_{\delta i}^2 + \sigma_{xi}^2 + \sigma_{xe}^2} \right) \\ \lambda_z &= -P_0 \left(c_{x0} - c_{z0} \frac{D_i^2 \sigma_{\delta i}^2}{D_i^2 \sigma_{\delta i}^2 + \sigma_{xi}^2 + \sigma_{xe}^2} \right) \\ c_{x0} &= \frac{N_e r_e^2 Z_i^2 m_e c \Lambda_C \eta}{\pi \gamma^4 \beta^3 A_i m_p \sigma_{\theta e}^2 \sigma_{\delta e}} \Phi\left(\frac{\sigma_{\delta e}}{\gamma \sigma_{\theta e}}\right) \\ c_{z0} &= 2 \frac{N_e r_e^2 Z_i^2 m_e c \Lambda_C \eta}{\pi \gamma^4 \beta^3 A_i m_p \sigma_{\theta e}^2 \sigma_{\delta e}} \left[1 - \Phi\left(\frac{\sigma_{\delta e}}{\gamma \sigma_{\theta e}}\right)\right] \\ P_0 &= \frac{1}{\sqrt{D_i^2 \sigma_{\delta i}^2 + \sigma_{xi}^2 + \sigma_{xe}^2} \sqrt{\sigma_{xe}^2 + \sigma_{xi}^2} \sqrt{\sigma_{ye}^2 + \sigma_{zi}^2}} \end{aligned} \quad (20)$$

Redistribution formulas similar to Eq. (20) were first derived in [6], although, without specifying the explicit expressions for c_{x0} , c_{z0} .

Uniform Electron Density

The case of a uniform electron density can be obtained from Eq. (16) by assuming $\sigma_{xi}^2 + D_i^2 \sigma_{\delta i}^2 \ll \sigma_{xe}^2 + D_e^2 \sigma_{\delta e}^2$, $\sigma_{yi} \ll \sigma_{ye}$, $\sigma_{zi} \ll \sigma_{ze}$. Then, we get:

$$\begin{aligned} \lambda_x &= \lambda_{x1} + \frac{D_i D_e \sigma_{\delta e}^2}{\sigma_{xe}^2 + D_e^2 \sigma_{\delta e}^2} \lambda_{z1} \\ \lambda_z &= \lambda_{z1} - \frac{D_i D_e \sigma_{\delta e}^2}{\sigma_{xe}^2 + D_e^2 \sigma_{\delta e}^2} \lambda_{x1} \\ \lambda_{x1} &= c_1 \Phi\left(\frac{\sigma_{\delta e}}{\gamma \sigma_{\theta e}} \frac{\sigma_x}{\sqrt{\sigma_{xe}^2 + D_e^2 \sigma_{\delta e}^2}}\right) \\ \lambda_{z1} &= 2c_1 \left[1 - \Phi\left(\frac{\sigma_{\delta e}}{\gamma \sigma_{\theta e}} \frac{\sigma_x}{\sqrt{\sigma_{xe}^2 + D_e^2 \sigma_{\delta e}^2}}\right)\right] \\ c_1 &= \frac{N_e r_e^2 Z_i^2 m_e c \Lambda_C \eta}{\pi \gamma^4 \beta^3 A_i m_p \sigma_{xe} \sigma_{ye} \sigma_{ze} \sigma_{\theta e}^2 \sigma_{\delta e}} \end{aligned} \quad (21)$$

The first two formulas in Eq. (21) are well-known (see [1, 7] for example). Yet, the previous works ignored dependence of λ_{x1} and λ_{z1} on D_e , which is important for accurate calculation of the redistributed cooling rates.

CONCLUSION

We derived explicit formulas (Eq. (16)) for redistribution of the cooling rates in non-magnetized electron coolers. The derived expressions take into account both the redistribution due to electron and ion dispersions in the cooling section and a nonuniform transverse density of the electron bunch.

The derived equations show that introduction of electron dispersion changes the cooling rates from their ‘‘unperturbed’’ values and that it is the ‘‘new’’, ‘‘perturbed’’ rates that get redistributed.

The equations shown in this paper allow for accurate calculation of the redistributed cooling rates.

REFERENCES

- [1] Ya.S. Derbenev, ‘‘Theory of Electron Cooling’’, TJNAF, Newport News, USA, Dr. Thesis, 1978.
<https://arxiv.org/abs/1703.09735>
- [2] S. Seletskiy, A. Fedotov, BNL-220641-2020-TECH, 2020.
- [3] S. Seletskiy, A. Fedotov, BNL-222963-2022-TECH, 2022.
<https://arxiv.org/pdf/2205.00051v2.pdf>
- [4] S. Seletskiy, BNL-223860-2023-TECH, 2023.
- [5] J. Binney, ‘‘Dynamical Friction in Aspherical Clusters’’, Mon. Not. R. Astr. Soc., vol.181, no. 4, pp. 735-746, 1977.
- [6] H. Zhao and M. Blaskiewicz, ‘‘Rate Redistribution in Dispersive Electron Cooling’’, *Phys. Rev. Accel. Beams*, vol. 24, p. 083502, 2021.
doi:10.1103/PhysRevAccelBeams.24.083502
- [7] M. Blaskiewicz, BNL-210932-2019-TECH, 2019.

A TEST BENCH FOR CHARACTERIZING ELECTRON COOLER COMPONENTS AT UP TO -80 kVDC

G. Khatri*, J. Cenede, A. Frassier, G. Tranquille
CERN, Geneva, Switzerland

Abstract

During the upcoming Long Shutdown 3 (LS3), the electron cooler of CERN's Antiproton Decelerator (AD) will be replaced by a new electron cooler. Present electron cooler is operating at the maximum energy of about 27 keV. However, the new electron cooler will have electron collector and electron gun with the possibility of operating at up to 68 keV electron energy. To characterize the gun and the collector at this higher energy, a test bench has been built and put in operation. The test bench is equipped with a drift solenoid of 1.5 m length operating at 600 Gauss, a Faraday cage with high voltage platform that can be biased up to -80 kVDC. First element of the new AD electron cooler, the electron collector, is presently being tested at the test bench. In this poster we describe in detail the main elements of the test stand, give some highlights of the ongoing tests with the new collector and future plans.

INTRODUCTION

Electron cooling of charged particle beams, originally proposed by G. Budker in 1966 [1], allows to improve quality of the beam by reducing its emittance. The AD electron cooler was originally built for Initial Cooling Experiment (ICE) at CERN [2] and subsequently modified for use in the Low Energy Antiproton Ring (LEAR) [3] and then in AD [4]. Parts of the cooler are more than 40 years old and lack spares. Therefore decision was made to build a new electron cooler to replace the existing one [5].

Scope of this work is to develop, test and characterize electron gun and collector for the new cooler that can work at least at 2.4 Amp / 27 keV and possibly at higher power. For this purpose a dedicated test bench was put in place. In the section following, a detailed description of the test bench is given. And then some preliminary results of the new collector/gun tests are presented.

TEST BENCH

Figure 1 shows main elements and layout of the test bench. It is a linear test bench, having no bending magnets but only a straight solenoid between the electron gun and the collector. As shown in Fig. 2, the gun is located inside the solenoid at a uniform axial field of 600 Gauss, while the collector is situated at the end of solenoid. At the entrance of the collector a magnetic coil is used to compress the transverse electron beam size, and thus maximising collector efficiency. The high voltage platform consists of a Faraday cage enclosing a 3-phase isolation transformer and two 19"

racks on isolation leg posts. The secondary windings of the transformer are floating at the cathode potential provided by an -80 kV power supply that is situated outside the Faraday cage (on ground potential). The high voltage potentials, as illustrated in Fig. 3, are referenced to the cathode by placing the relevant power supplies on the racks inside the Faraday cage. The magnet power supplies are located on the racks at ground potential.

The necessary low vacuum pressure is achieved with the help of turbomolecular pump, titanium-sublimation pump and an ion pump. Due to being more than 20 years old, the achieved vacuum with these pumps is not great. A vacuum bakeout at 150 °C helped remove water and improved overall vacuum and thus electron beam transport. The pressure between the gun and collector in the drift region is estimated to be between 5×10^{-6} and 5×10^{-7} mbar.

The test bench is equipped with safety interlock system that prevents damage to the equipment and allows safe operation for the users. A LabVIEW and python based hybrid control system allows remote control and monitoring of all the power supplies as well as vacuum pressure readout and have logical dependencies on the safety interlock system.

TESTS OF THE NEW COLLECTOR

The original design of the collector underwent a few iterative refinements to mitigate issues related high voltage sparks (e.g. triple junction) in the vacuum before it was able to hold the 30 kV DC bias. However several challenging issues came up before further tests could be done and are described below. Note that the new collector was tested using existing electron gun from AD that operated at nominal beam of 2.4 A and 27 keV.

Observation of Magnetron Discharge

When the magnetic field of 600 Gauss was switched on along with the high voltage, regular and reproducible spikes in the vacuum pressure readout were seen, see Fig. 4. These were understood as magnetron discharges. A surface at relatively negative electric potential would emit an electron which, under crossed electric and magnetic field, would then take a helical path as it accelerates. By collision with the residual gas in the vacuum, it creates secondary electrons and eventually an avalanche. This process repeats when the residual gas replenish in the location of discharge. As this happens, the vacuum is conditioned (by high voltage) and thus the time interval between two consecutive vacuum spikes increases. The solution for getting rid of these discharges was to do a vacuum chamber bakeout. Due to risk of breaking ceramic insulators in the gun and collector, the

* gunn.khatri@cern.ch

Content from this work may be used under the terms of the CC-BY-4.0 licence (© 2023). Any distribution of this work must maintain attribution to the author(s), title of the work, publisher, and DOI

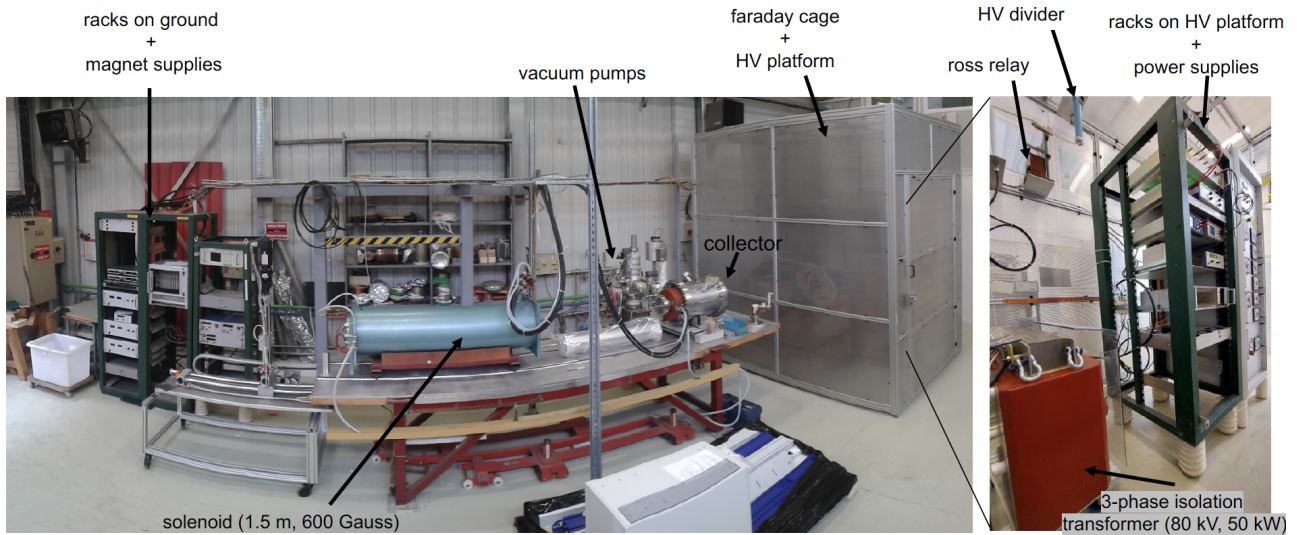


Figure 1: Test bench layout and main elements.

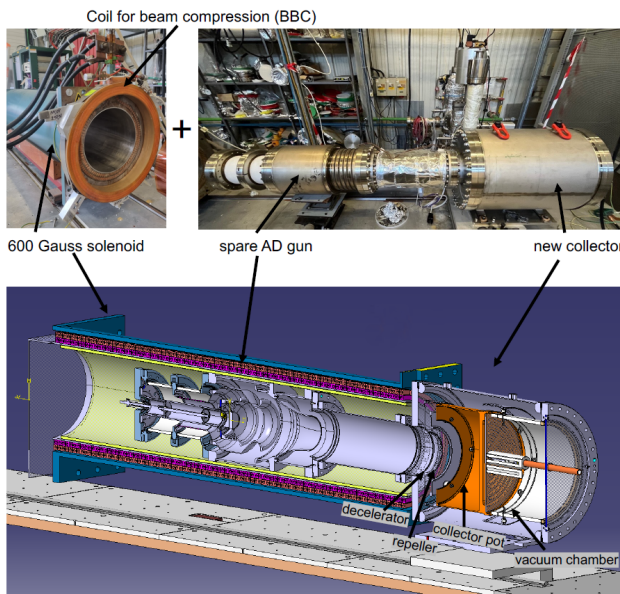


Figure 2: Experimental setup: top of the figure shows photos of the magnets, gun and collector whereas the bottom shows cut-view of the setup drawing.

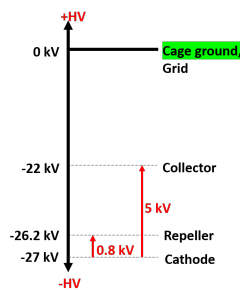


Figure 3: High voltage biasing scheme.

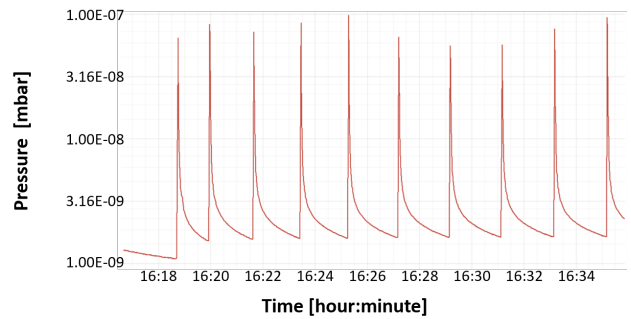


Figure 4: Vacuum gauge readout. The spikes seen are due to magnetron discharge - the time interval between two consecutive peaks is getting longer as more spikes occur.

bakeout was limited to 150 °C. The bakeout helped suppress the magnetron discharges. This allowed to shoot electron beam into the collector.

Beam Compression at the Collector Entrance

Above 100 mA DC electron beam, the electron losses were seen going up with the increase in the beam current. At the point, the collector was placed right against the end of the drift solenoid. Simulation shown that the electron beam was expanding partially hit the entrance electrode in the collector. An additional magnetic coil (“compression coil”) was placed between the drift solenoid and the collector that allowed beam compression and thus reduction in the electron losses. Figure 5 shows simulation of the electron beam transport from the gun to the collector with and without this compression coil.

TESTS OF THE NEW GUN

A prototype electron gun for the new electron cooler was recently built, having purpose of only testing and validating the geometry, it was made with low-cost and low-precision,

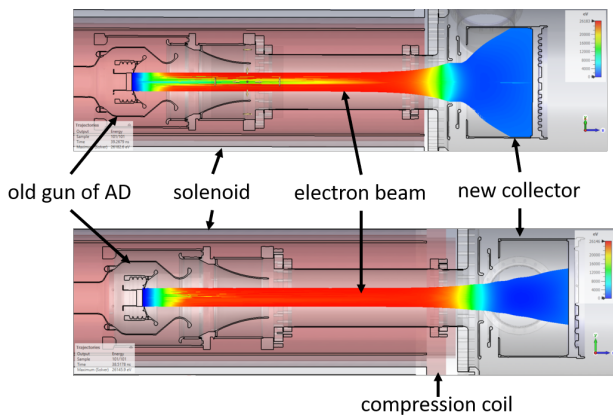


Figure 5: Electron beam transport from gun to collector simulated in CST Particle studio. Top image shows the case without the compression coil and bottom with the coil.

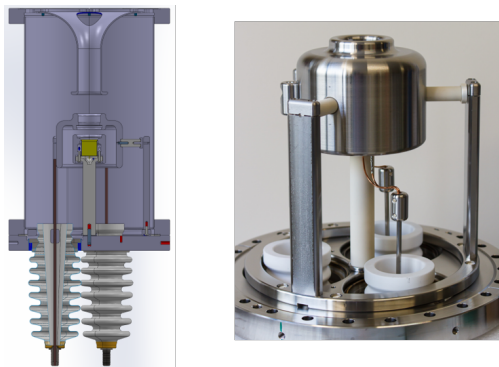


Figure 6: The new electron gun: left image shows a CAD model and right image shows gun assembly without the vacuum chamber.

see Fig. 6. The gun design was originally proposed by [6], and adopted in this work with minor changes in the electrode shape for easier manufacturing. The cathode was heated to nominal temperature of 1000 °C and left hot for few weeks, no sign of damage to the ceramic insulators was observed. A preliminary test with electron beam extraction was demonstrated.

RESULTS

A 1.75 A DC electron beam transport from the old gun to the new collector was demonstrated for 72 hours. During this test, collector cooling water had a 15 °C temperature increase. The objective is to reach the minimum of 2.4 A but due to aging of the cathode in the old gun, it was not possible. Tests will resume with a new cathode early 2024. Figure 7 shows important results from the collector tests - basically minimising the electron losses (in other word maximizing collector efficiency).

As discussed above, one of these is the compression coil need at the entrance of the collector helps greatly in the reduction of the electron losses. Second is the effect of vacuum quality on the electron beam. Higher the beam intensity, the

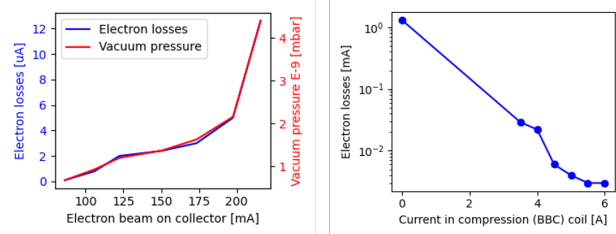


Figure 7: Electron losses and their relation with (a) ESD (left plot) and (b) compression coil current (right plot).

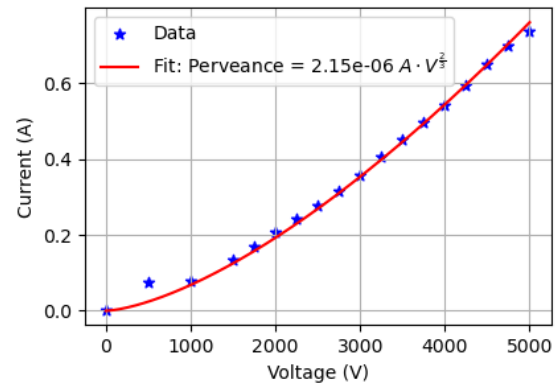


Figure 8: Preliminary results of measured perveance with the new electron gun.

more out-gassing in the collector due to Electron Stimulated Desorption (ESD). The electron beam interacts with the residual gas and causes electron losses.

Electron beam was extracted from the prototype gun, the preliminary results are shown in Fig. 8. The perveance measured here agrees with the simulated design values of $2.2 \times 10^{-6} \text{ A} \cdot \text{V}^{2/3}$ and hence the gun geometry is validated.

CONCLUSION

A fully operational test bench dedicated for testing high power electron gun and collectors is presented. Further improvements and upgrades of the test bench, in terms of computer control system and vacuum setup, are underway.

The collector tests so far show optimistic results and not far from full validation at nominal beam of 2.4 A / 27 keV. If time permits, one can optimise the collector operational settings by separating the deceleration electrode from the main cup and biasing them separately. Plan is to add a stronger magnetic compression coil to compress the beam at the entrance of the collector which will help trap secondary electrons and reduce back reflected electrons. And finally do a vacuum bake-out of the collector to at least 250 °C to check that it will not break the copper-ceramic brazing during operation.

Preliminary results of the new electron gun shows agreement with the design value of the perveance. However fur-

ther tests are necessary, mainly with the expansion solenoid at 2.4 A / 27 keV and possibly at higher power.

ACKNOWLEDGEMENTS

The authors would like to thank A. Pikin and F. Wenander for helpful discussion in understanding the test bench results, D. Steyaert and Y. Coutron for the design of the new collector and CERN AD-CONS project members for their collaboration.

REFERENCES

[1] G. I. Budker *et al.*, “Experiments on cooling by electrons”, *Soviet Atomic Energy*, vol. 40, pp. 50–54, 1976.

- [2] F. Krienen, “Initial Cooling Experiments (ICE) at CERN” in *Proc. 11th International Conference on High-Energy Accelerators*, CERN, Geneva, Switzerland, July 1980, pp.781-793.
- [3] H. Poth *et al.*, “First Results of Electron Cooling Experiments at LEAR”, *Zeitschrift für Physik*, vol. A332, 1987.
- [4] G. Tranquille, “40 Years of Electron Cooling at CERN”, in *Proc. IPAC’18*, Vancouver, Canada, Apr.-May 2018, pp. 69–72. doi:10.18429/JACoW-IPAC2018-MOZGBF3
- [5] M. Lamont *et al.*, “AD e-cooler Consolidation Strategy”, presented at the 259th IEFC meeting, CERN, Geneva, Switzerland, Dec. 2019, unpublished
- [6] A. Pikin *et al.*, “Simulation of electron guns for electron cooler”, presented at CERN internal meeting on 10 Jan. 2019. <https://indico.cern.ch/event/774322/>

The shorter free space delay is used as a continuous 0-0.5 ns delay, the excess 0.2 ns is used to compensate for splicing errors and temperature dependence of a step delay. The attenuator acts as a normal attenuator and as an insertion loss equalizer for both the free space and step delays.

DELAY EQUALISATION

The optical fibers in step delay can be cut with 1 mm (or ~5 ps) accuracy on the best average, so the absolute delay error for 8-bit delay could exceed 40 ps. The other source of delay error is the temperature dependence of the optical fiber. Typical single-mode fibers provide a thermal coefficient of delay of about 40 ps/km/K, so for OPDM with 128 ns of total delay, the temperature drift is about 1 ps/K. To make the delay as linear as possible, both errors are compensated by the precise motorized free space delay line. For each step of the step delay, the OPDMs were measured multiple times in a thermostat at a range of temperatures from 10 °C to 40 °C, then the temperature points were averaged and extrapolated to provide calibration data for each step of the fiber step delay (Fig. 3).

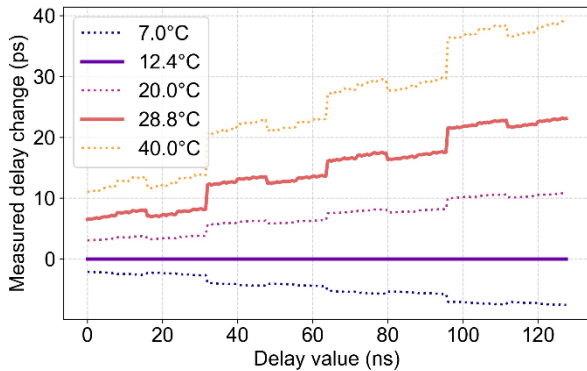


Figure 3: Delay change due to temperature for each step of step delay relative to 12.4 °C, real measurements (solid) and extrapolated values (dotted).

OPDM has a temperature feedback loop, which measures the temperature at a specified intervals and applies the correction according to the calibration data. The overall accuracy of the OPDM depends on the range. For a short range of 0-0.5 ps, the delay is set only with the motorized free space delay line, and the accuracy is defined by the precision of its motor, which is ~0.01 ps in the worst case. For larger delay ranges the accuracy is mostly limited by the initial measurement and calibration accuracy and averages to about 0.05 ps (Fig. 4).

INSERTION LOSS EQUALIZATION

The optical switches that form the delay bits have slight insertion loss variations, and the switches also have different insertion losses for different paths. Thus, the total insertion loss can change significantly for a single delay step. In addition to the switches, the insertion loss of the short free space delay varies significantly within its delay range. To compensate for the overall insertion loss variation, the OPDM was measured at each step of both the free space and step delay, and this measurement data is used to

compensate for the variation at each delay change of the OPDM with an integrated optical attenuator. The resulting total insertion loss variation is ultimately less than 0.1 dB:

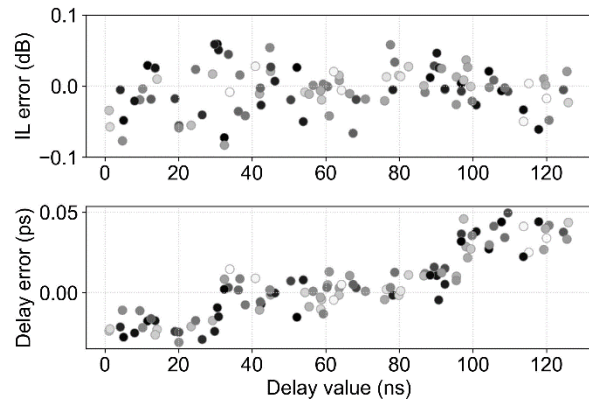


Figure 4: Measured OPDM insertion loss (IL) and delay errors. This is the result of a “stress test” where the temperature inside the thermostat was gradually changed from ~7 °C to ~40 °C within 12 hours, and the delay errors were measured for randomly selected delay values. The marker colours indicate the measured temperature from lowest (black) to highest (white).

OPERATION AT COSY

A total of seven OPDM delays were produced – one prototype unit with a ns total range of 64 and six units for the stochastic cooling systems of the HESR. The HESR accelerator was developed by the Institute for Nuclear Physics (IKP) at FZ Jülich, and its systems, including stochastic cooling, were installed at the COSY accelerator at FZ Jülich for testing. Thus, four of the manufactured delays were used at the COSY for tests in 2021-2023 (Fig. 5).

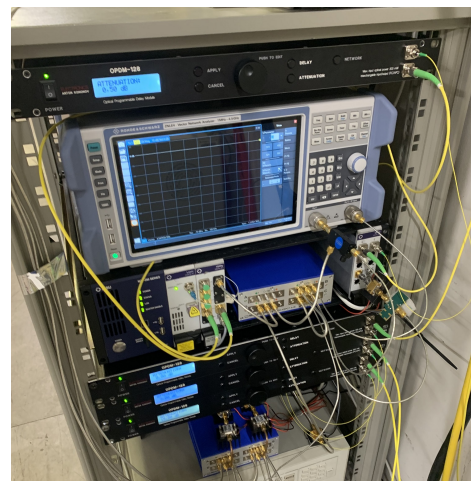


Figure 5: Four optical delays during operation in the stochastic cooling system of COSY, delays were used in vertical, horizontal and longitudinal cooling systems and in an optical comb filter.

During the test period the developed delays proved to be reliable and accurate. In fact, the delay variation due to daily temperature changes was negligible for operation during the experiments, making the whole setup simpler and more robust.

Content from this work may be used under the terms of the CC-BY-4.0 licence (© 2023). Any distribution of this work must maintain attribution to the author(s), title of the work, publisher, and DOI

CONCLUSION

The main parameters of the developed optical delay lines are summarized in Table 1.

Table 1: OPDM Main Parameters

Delay range	0 to 128 ns
Delay resolution	± 0.001 ps
Delay accuracy <0.5 ns	± 0.01 ps
Delay accuracy >0.5 ns	± 0.05 ps
Latency (insertion delay)	<14 ns
Insertion loss	<5.5 dB
Insertion loss variation	± 0.1 dB
Operating temperature	10 °C to 40 °C

The developed optical delay lines are compact, reliable and provide highly accurate results within the specified temperature range. The extensive tests at COSY have shown that the use of these delays simplifies and improves the setup of stochastic cooling systems and eliminates the need for periodic fine-tuning of the systems over long periods of operation due to daily temperature changes.

REFERENCES

- [1] R. Stassen, B. Breitzkreutz, N. Shurkhno, H. Stockhorst, and L. Thorndahl, “The HESR Stochastic Cooling System, Design, Construction and Test Experiments in COSY”, in *Proc. COOL'17*, Bonn, Germany, Sep. 2017, pp. 89-93. doi:10.18429/JACoW-COOL2017-THA11
- [2] I. Kadenko *et al.*, “An optical comb filter for the stochastic cooling system at the Nuclotron accelerator”, *Phys. Part. Nucl. Lett.*, vol. 11, no. 5, pp. 705-707, 2014. doi:10.1134/S1547477114050148
- [3] M. Bousonville *et al.*, “New Phase Stable Optical Fibre”, in *Proc. BIW'12*, Newport News, VA, USA, Apr. 2012, paper MOPG033, pp. 101-103.

H0 DIAGNOSTICS FOR THE ELENA ELECTRON COOLER

G. Tranquille[†], CERN, Geneva, Switzerland

Abstract

In addition to antiprotons, the ELENA ring at CERN can also inject protons and H⁻ ions from a dedicated ion source located close to the ring. These particles offer the possibility for extra diagnostics for detailed investigations into the cooling process at the very low energy of the ELENA ring. To this effect a monitor was installed downstream of the electron cooler to measure the recombination of protons with the cooling electrons. Although protons have never been used in ELENA, H⁻ ions are routinely used to setup and optimise the ring. The installed device is now used to monitor the stripping of the H⁻ ions on the residual gas and in the presence of electrons generated by the cooler, providing some insight on the evolution of the beam size during the deceleration cycle and the performance of the electron cooler on the two cooling plateaus.

INTRODUCTION

During the cooling process the centre of mass energy difference becomes very small and ions can capture an electron by radiative or di-electronic recombination. In the next bending magnet, their trajectory becomes very different from that of the circulating ions. For proton beams, neutral hydrogen atoms are formed and travel straight towards a detector.

The formation rate is related to the effective temperature of the electrons and is given by:

$$R_H = N_p \eta \alpha_r n_e \gamma^{-2}$$

where η is the ratio of cooling length to ring circumference, N_p the number of stored ions, n_e the electron current density and α_r the recombination coefficient [1]. Hence the measurement of this rate provides important information on the apparent temperature of the electron beam in the region defined by the overlap with the ions and the possible misalignment of both beams as the highest down-charge rate corresponds to the best matching of electron cooling. Direct measurement of the cooling time and the equilibrium emittances can also be estimated by observing the neutral beam profile.

In ELENA [2] a dedicated H⁻ linac, operating at an energy of 100 keV allows the machine to be operated with H⁻ ions or protons when it is not sending antiprotons to the experiments. Unfortunately, proton mode of operation has never been tested due to the complexity of changing the magnetic polarity of the ELENA ring resulting in a lengthy setting up. Moreover, after such a change, the machine performance in antiproton mode would need much time to recover because of the hysteresis of the magnets.

DETECTOR SETUP

To measure the neutral hydrogen beam profile a detector was installed in the vacuum extension of the 90° bending

magnet approximately 6.3 m downstream from the electron cooler. The beam profiler consists of a chevron mounted micro-channel plate (MCP) coupled to a P43 phosphor screen. The H0 atoms that are created travel straight towards the monitor and as they hit the MCP surface, electrons are produced and are amplified in the MCP before they are accelerated onto the phosphor screen. The image of the phosphor screen is acquired by a Raspberry Pi4 computer using the Pi HQ camera mount with interchangeable lenses (see Fig. 1) [3].

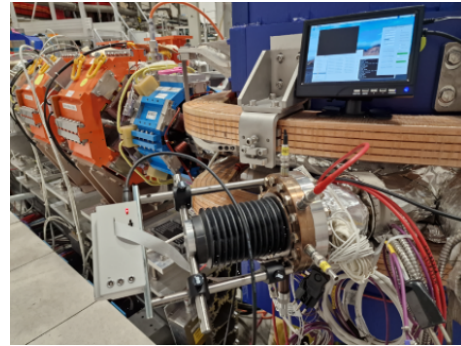


Figure 1: H0 beam monitor in the magnet extension.

Controls and Data Acquisition (DAQ)

The high voltage for the MCP and P43 screen is provided by an iSeg THQ dual channel power supply. A Python script controls the voltage ramp that is applied to the MCP and screen. Camera control is also performed via a Python script which enables the user to adjust the camera settings (resolution, exposure etc.) and to select the acquisition mode (see Fig. 2). Continuous, single/multi frame and video capture are available and can be triggered synchronously with events in the ELENA magnetic cycle.

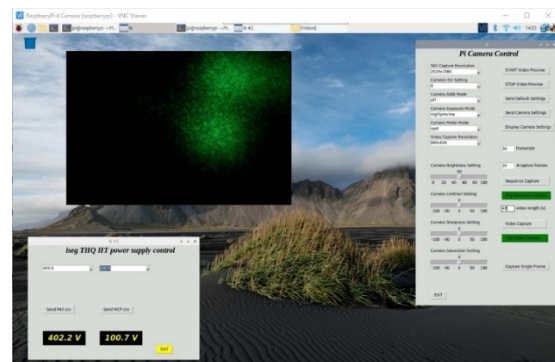


Figure 2: Raspberry Pi controls and DAQ setup.

Calibration

The 12.3-megapixel CCD camera allows single image capture resolutions up to 4056x3040 pixels and a maximum video resolution of 1920x1080 pixels (1080p). A transparent target was mounted on the window and the images at the available video resolutions were acquired to

[†] email Gerard.tranquille@cern.ch
 THPOSRP09

determine the spatial resolution for the different lens/resolution combinations (Table 1).

In video mode, the preferred acquisition mode, to keep an acquisition rate of 30 Hz, a lower resolution of 880x600 was chosen as the best compromise.

Table 1: Lens / Video Resolution Combinations

Resolution	FUJINON 25mm	RPI 6mm
640x480	39 $\mu\text{m}/\text{px}$	110 $\mu\text{m}/\text{px}$
880x600	22 $\mu\text{m}/\text{px}$	64 $\mu\text{m}/\text{px}$
1280x720	18 $\mu\text{m}/\text{px}$	
1600x900	15 $\mu\text{m}/\text{px}$	
1920x1080	12 $\mu\text{m}/\text{px}$	

The MCP gain was calibrated by recording the integral of the H0 signal at the end of the first injection plateau as a function of the MCP voltage. To avoid signal saturation, a voltage of 1400 V was selected, giving a gain of approximately 10^5 .

DATA ANALYSIS

Image Analysis

Single images captured by the camera system can be analysed to measure the neutral beam size at a particular time in the ELENA cycle. The raw data is first smoothed using a Savitzky-Golay filter which calculates a polynomial fit of successive data windows based on polynomial degree and window size. A Gaussian fit is then applied to the filtered data and the beam parameters are calculated and displayed with the fitted curve (see Fig. 3). One can also “zoom” into a zone of interest for a selective fitting in which the image consists of multiple beams as shown in Fig. 4.

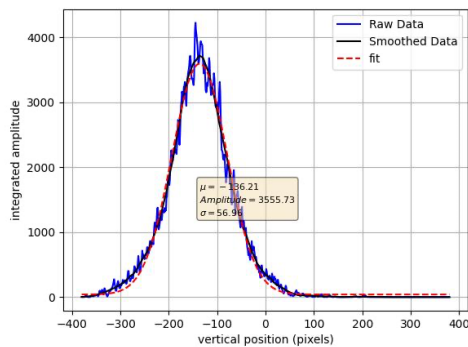


Figure 3: Example of a fitted vertical beam profile.

Frame-by-Frame Analysis

To measure properties of the beam profiles acquired by the video capture, a python script was developed to perform a frame-by-frame analysis. For each selected frame the beam parameters are evaluated using the same methods described above. The data is stored in a text file for further post-processing.

Full Video Signal Analysis

In addition to the frame-by-frame method, the complete video can be analysed to display the H0 formation rate and the estimated beam sizes for the full acquisition time. The drawback with this method is that the measured beam sizes are influenced by the distortions to the beam spots seen during the cycle as the “zoom” option is not implemented in this analysis method.

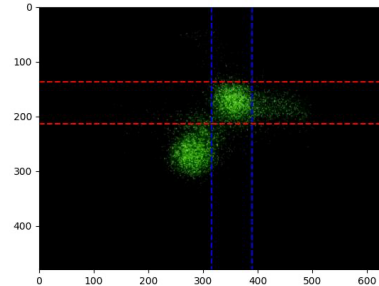


Figure 4: Selective fitting of the beam profile.

RESULTS

H0 Formation With and Without Electrons

The first series of measurements consisted in observing the effect of the electron beam of the cooler on the stripping of the circulating H⁺ beam. From Fig. 5 it is clearly seen that the H0 formation rate, due to the stripping of the loosely bound H⁺ electron, is greatly enhanced in the presence of the cooler electron beam. The blue trace shows the H0 rate when the electrons are present only on the lower cooling plateau (100 keV, after 8.6 s). With electrons also present on the first cooling plateau (red trace) one sees a significant increase in the H0 rate. However, without a measurement of the circulating beam intensity one cannot confirm that the beam lifetime [4] is affected by the increase in the stripping rate. Bunched beam intensity measurements at the start and end of each cooling plateau are available but do not have the required accuracy to determine the beam lifetime.

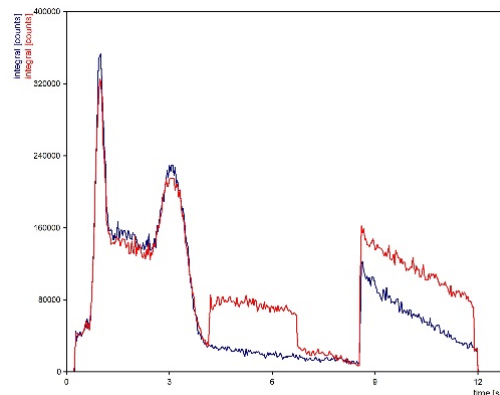


Figure 5: Total H0 signal measured for a full ELENA cycle with electrons (red) and without electrons (blue).

Beam Size Measurements at 648 keV

Using the frame-by-frame method we were able to plot the evolution of the neutral beam size with the electron cooler switched on and off. At 648 keV the analysis is somewhat difficult due to the presence of two beams after deceleration from 5.3 MeV. First indications from the video seem to indicate that only the upper right beamlet sees the cooler electrons. However, if both beamlets are analysed separately one sees that they both behave in a similar way when electrons are present.

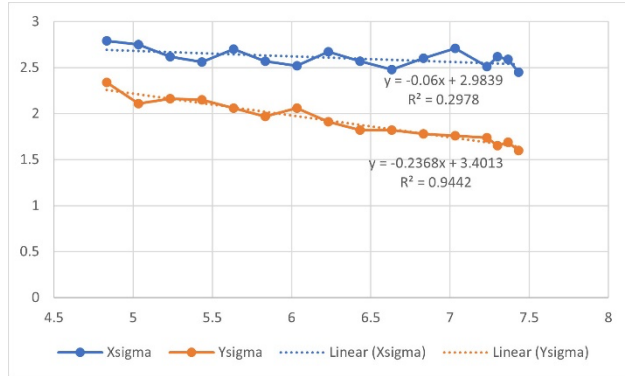


Figure 6: Horizontal (blue) and vertical (orange) beam size evolution with cooling on the first cooling plateau.

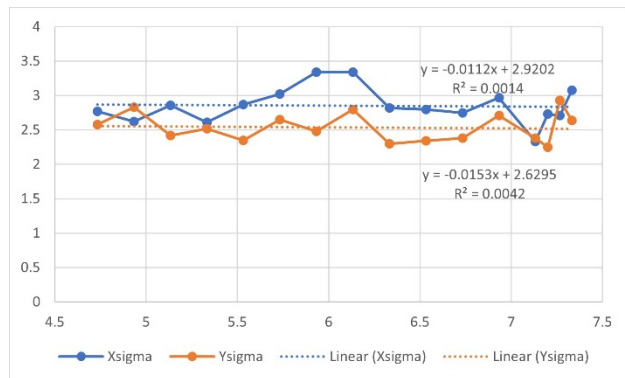


Figure 7: Horizontal (blue) and vertical (orange) beam size evolution without cooling on the first cooling plateau.

Figure 6 shows the horizontal (blue) and vertical (orange) beam size (1σ) evolution under electron cooling as a function of time. Figure 7 shows the same but this time without any cooling electrons. In the horizontal plane no cooling is observed whilst in the vertical plane the beam size reduction is only marginal. Another indication that the beam is not cooled is the variation of the profile amplitude which decreases over time in the same manner, with or without cooling.

Beam Size Measurements at 100 keV

At the low energy plateau of 100 keV the situation is somewhat different as can be seen in Figs. 8 and 9. On this plateau a new beam is injected as the intensity of the decelerated beam is too low to be of any use. The amplitude of the fitted profiles (orange) indicates an increase in particle beam density, but the change in beam size (blue) seems to indicate the contrary. The sudden decrease of the horizontal

beam size after injection is probably due to particle loss and not cooling. Throughout the plateau the beam size remains constant, again indicating that the circulating beam is not cooled.

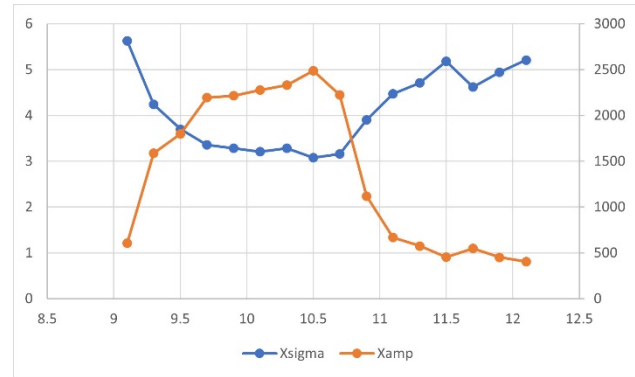


Figure 8: Horizontal beam size (blue) and Gaussian fit amplitude during the second cooling plateau.

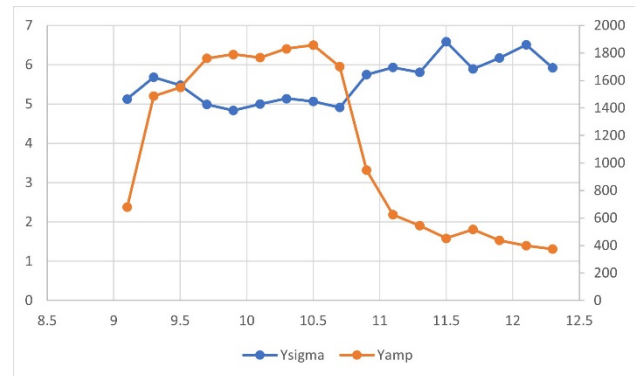


Figure 9: Verticalal beam size (blue) and Gaussian fit amplitude during the second cooling plateau.

CONCLUSION AND OUTLOOK

The neutral beam profile monitor in ELENA has been optimised to capture the effect of H⁻ beam stripping due to residual gas interactions or the presence of electrons from the cooler.

The measurements so far do not show clear signs of beam cooling but there is a need to disentangle the effect of residual gas stripping, which occurs over the full length of the straight section, from the stripping from the cooler electrons, which takes place over only 1 metre. Moreover, the two-beam structure that is observed over most of the cycle also hinders the proper evaluation of the beam size and the source of this perturbation needs to be fully understood.

For future measurements we will investigate the effect of the circulating beam position and intensity as well as the electron beam current on the H0 profile. A correlation with the profile measured with the beam scrapers will also be necessary to confirm the observed two-beam structure.

The use of protons in ELENA should also be envisaged as a wealth of information can be obtained and will allow us to optimise the cooling of antiprotons more efficiently.

REFERENCES

- [1] L. Spitzer, *Physics of Fully Ionised Gases*. New York, NY, USA: Interscience, 1956.
- [2] C. Carli *et al.*, “ELENA Commissioning and Status”, in *Proc. IPAC’21*, Campinas, Brazil, May 2021, pp. 598-601. doi:10.18429/JACoW-IPAC2021-MOPAB177
- [3] Raspberry Pi Org., <https://www.raspberrypi.com/>
- [4] D. Allen *et al.*, “H⁻ beam lifetime measurements at 10 MeV in LEAR”, CERN, Geneva, Switzerland, Rep. CERN-88-34, Sep. 1988.

DEVELOPMENT OF A FIELD EMISSION ELECTRON GUN FOR LOW ENERGY ELECTRON COOLING

E.-S. Welker¹, J.Cenede, B. Galante², G.A. Tranquille*, CERN, Geneva, Switzerland

¹ also at Technische Universität Wien, Vienna, Austria

² at Paul-Scherrer-Institut, Zürich, Switzerland

Abstract

The use of carbon nanotubes (CNT) as a cold electron source for a low energy electron cooler has been studied in detail. To fully characterise different CNT arrays (conditioning process, emitted current, lifetime) and to investigate the optimum electrical configuration of the source to be used in an electron gun, a cold cathode test bench (CCTB) has been set up. From the measurements performed on the CCTB, an electron gun has been designed, constructed and is being tested to measure the properties of an electron gun using a larger (4 cm diameter) CNT array as the source. The CCTB has been modified to incorporate a beam transport system as well as the relevant diagnostics needed to perform the experiments. The results will be compared to the CST Particle Studio simulations and will be used to optimise the design for use in the ELENA low energy electron cooler.

INTRODUCTION

In ELENA (Extra Low Energy Antiproton Ring), electron cooling is fundamental to reduce the emittance blow-up of the antiproton beam so that a focused and bright beam can be delivered to the experiments [1]. Presently, the electron gun relies on thermionic emission, where a tungsten-doped barium oxide (BaO) source is heated to 1200 °C. However, this imposes several limitations on the transverse beam energy and the required magnet system. A cold emission-based electron gun might overcome these constraints, as field emission relies solely on high electric fields to both generate and control the electron beam.

Carbon Nanotubes (CNTs) are considered among the most promising materials for this purpose, and their feasibility as field emitters has been studied. Previous research [2] established CNT cathodes as viable candidates for the use in the electron cooler of ELENA. Still, there remains a crucial research gap in determining their optimal characteristics (maximal current density, lifetime, etc.). Bridging this gap is fundamental for advancing the development of a more efficient electron gun system in ELENA, especially in light of the requirements of future particle accelerators.

EXPERIMENTAL SET-UP

The gun assembly was installed in a vacuum tank to enable an Ultra-High Vacuum (UHV) environment and mounted on a specifically constructed Cold-Cathode-Test-Bench 2 (CCBT2).

* gerard.tranquille@cern.com

Gun Description

The CNT-based gun prototype (see Fig. 1) is comprised of a sample holder with a 4 cm x 4 cm hollow well to place the CNT-Sample. Vertically aligned Carbon Nanotube (VCNT) arrays have been shown to have the most optimal emission properties for our purposes [2]. The VCNTs were grown on silicon plates by using chemical vapor deposition. The gun also features two finely conductive grids, made out of a highly n-doped silicon wafer with a mesh pattern (15 μm square holes with 3 μm walls). The first grid acts as an extracting anode by developing a local electric field, while the second grid is used to decelerate the beam. For insulation between the elements and to limit the beam size, two MACOR® rings are employed. The final component is an aluminium ring with a triangular-shaped cross-section, essential for maintaining straight field lines and keeping the transverse energy of the emitted beam low.

Einzel-Lenses

Given the considerable drift distance between sample and detector, an Einzel-Lens system (comprised of three cylindrical and symmetric electrodes) is used to transport and focus the beam onto an imaging screen. The configuration of voltages determines the fringe fields and thus how the particles will be deflected and focused - without significantly changing their kinetic energy. Typically, the outer electrodes share a common electrical potential, while the central electrode is held at a different potential. It was decided to use the lenses in the acceleration-deceleration mode, as this mode is preferable for longer focal lengths due to the minimized spherical and chromatic image aberration [3].

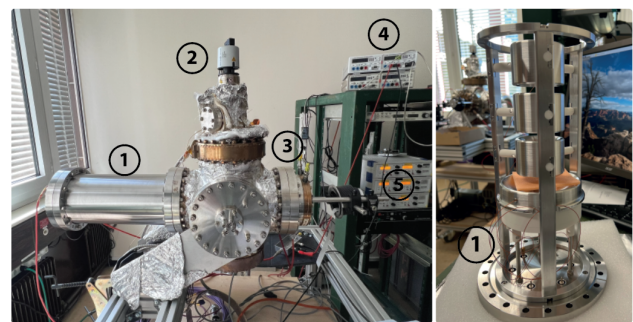


Figure 1: Left: Cold-Cathode-Test-Bench 2: ① Vacuum tank with gun assembly ② Pfeiffer Vacuum Dual Gauge ③PHOTONICS Ion Beam Profiler HM6012 Multimeter ⑤ ISEG HV Power Supply, Right: CNT-based gun assembly.

Test-Bench Set Up CCTB2

The Cold-Cathode-Test-Bench 2 (see Fig. 1) encompasses the gun assembly installed in a vacuum tank, mounted on a 6-way cross, where three flanges are dedicated for the Edwards Vacuum Pump, a Pfeiffer TPG 362 Dual Gauge and a PHOTONIS Ion Beam Profiler (IBP). The Test-Bench can be used in two different configurations: by replacing the first grid with a copper plate serving as a Faraday Cup, the samples current can be read out by a HAMEG HM8012 Multimeter. Secondly, electron beam profile measurements can be made with the modified IBP, mounted 33 cm downstream of the gun assembly. It utilizes a Microchannel Plate (MCP) coupled to a phosphor screen, and a high resolution camera, to amplify and capture even very dim ion beam events.

In the CCTB2, the electron beam is transported from the main electron source to the IBP. Three potentials are responsible for this transport: the sample holder (fixed at -355 V), the first grid (variable - depending on distance and desired electric field), and the center Einzel-Lens (also variable). All other conducting components are grounded. These gradients result in a beam that allows the energy required for ELENA operation (355 eV).

SIMULATION SET-UP

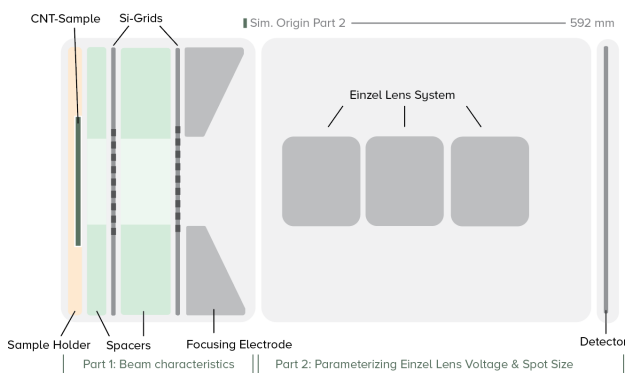


Figure 2: Schematic model for CST simulation with simplified gun components.

Due to the rectangular grids, cylindrical symmetry is disrupted, and therefore 3-dimensional simulations are imperative. All simulations were performed in CST Studio Suite[®](CST) (see Fig. 2) [4].

Firstly, a simplified model of the gun was constructed directly in CST, and therefore retaining parametric control for possible subsequent optimization. The grid consist of $\sim 4.9 \times 10^6$ holes and introduced several constrictions into the simulations. For example, CST is unable import the CAD-model of the grid, as it couldn't recognize it as a solid, preventing the simulation of a full-sized gun.

Furthermore, to maintain accuracy, each $3 \mu\text{m}$ thick wall necessitates a minimum of 2 mesh cells to ensure precise particle tracking. However, the number of mesh cells is correlated to the simulation time and is inherently constrained by the available computing power.

In considerations of these limitations, the electron gun was simulated at 1%, 2%, and 3% of its actual size. Each simulation was again divided in two parts to further reduce the number of mesh cells. The first part covers the electron source. The resulting beam was exported and reimported into the second part, which encompassed the beam transport through the three Einzel-Lenses. This approach allows to preserve simulation precision. In all simulations, beam position monitors are set perpendicular to the beam, enabling the tracking of beam parameters, such as beam divergence Θ , emittance ϵ , beam radius r and mean beam energy \bar{E} .

Beam Characterization

In the first simulation section, the beam starting from the CNT-Sample Holder until the end of the Grounded Electrode was simulated. A field-induced emission model was used and the following parameters were set based on previous studies [2]: the initial kinetic energy $E = 0.1$ eV, two Fowler-Nordheim equation related material specific constants $a = 3.1537 \times 10^{-11}$ and $b = 7.5793 \times 10^6$, and the angle spread $\alpha = 89^\circ$. The potentials were set according to the requirements: the sample holder is fixed to -355 V while second grid is at ground potential. The extracting grid voltage was scaled with the same factor as the gun size (100%: 1 kV \rightarrow 1%: 10 V, 2%: 20 V, 3%: 30 V) in order have comparable electric fields. Both the grid thickness and the CNT sample thickness retained their real sizes.

Local mesh properties, including a step width in x, y, and z of $1.2 \mu\text{m}$ at and near the grid, were carefully selected to maintain the previously mentioned precision without excessively extending the simulation time. It's worth noting that the 3% gun simulation had already reached 417×10^6 mesh cells.

Beam Transport and Spot Size

The objective of the second set of simulations was to investigate the beam dynamics of the Einzel-Lenses and their focusing properties. In almost all cases, the focal length of Einzel-Lens systems cannot be solved numerically and only computed analytically, thus making a simulation approach necessary. The three cylindrical lenses were modelled with their original size, and the corresponding beam interfaces obtained for each size were imported. This step serves as a representation of how a scaled CNT sample would behave in the actual test bench setup and was essential to allow comparison of the focusing behaviour.

Beam Transport Firstly, the voltage applied to the to the center lens (V_{center}) was varied, to observe changes in the electron trajectories. Negative values were dismissed, as they would lead to recoil. A range of nine values for parameterization was chosen between 0 V and 3000 V. To archive precision, a finer mesh was employed near the lenses (step size of 0.4 mm).

Spot Size Based on these results, the next objective was to optimize the spot size at the approximate detector

distance, which is located ~ 592 mm downstream after the Grounded Electrode. The maximum beam radius is limited to approximately 22 mm due to the size of the IBP phosphor screen. CSTs internal optimization tool allowed to fine tune V_{center} . A single goal was defined: to minimize the result of the post-processing template "x at 2nd y-Minimum of the Envelope" to a value of 592 mm. Specifically, the algorithm "Trust Region Framework" was employed, suitable for refining solutions in the vicinity of an initial guess within a defined region. The lower and upper bounds were set to 80% and 120% of the initial guess.

In addition, we sought to generally validate the simulation results to ensure that our simulation setup accurately represents the physical system.

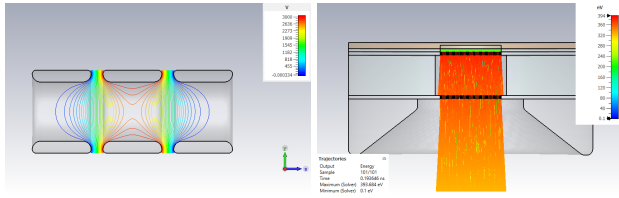


Figure 3: Left: Equipotential lines of fringe fields in lens system. Right: Electron trajectories near the CNT-Sample.

RESULTS AND DISCUSSION

Beam Characteristics

Table 1 summarizes the obtained beam parameters directly after the Grounded Electrode. The trajectories of the beam passing the two grids in the first simulation part can be seen in Fig. 3 (right). We observed that the beam energy is simulation-size-independent, while the beam radius increased with the size, as expected. The emittance is directly proportional to the size as well. Controversially, the beam divergence for the 1% simulation is significantly larger than anticipated. This could be due to CSTs internal calculation of the beam properties and requires further investigation into the software specific formulas.

Table 1: Beam Parameters After Grounded Electrode

Simulation Scale	1%	2%	3%
Θ [mrad]	0.4414	0.2696	0.2095
ϵ_x [mm · rad]	0.0031	0.0039	0.0043
r [mm]	0.2095	0.3653	0.5394
\bar{E} [eV]	339.050	338.036	338.913

Beam Transport and Spot Size

The simulations revealed that the mean electron beam energy remains consistent both before and after its passage through the lens system, aligning with theoretical expectations. This is true for all three simulation sizes.

In Fig. 4 (Bottom), the correlation of the focusing length and the applied voltage is clearly visible. We observed that

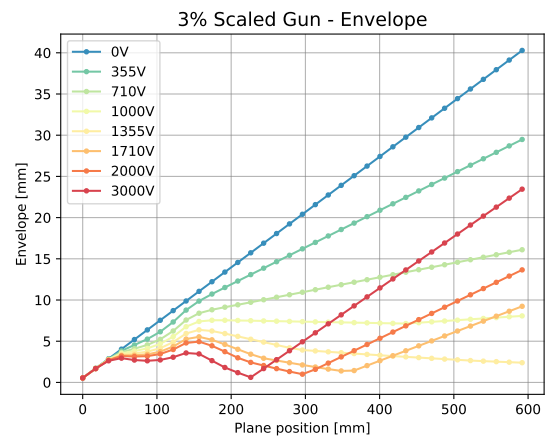
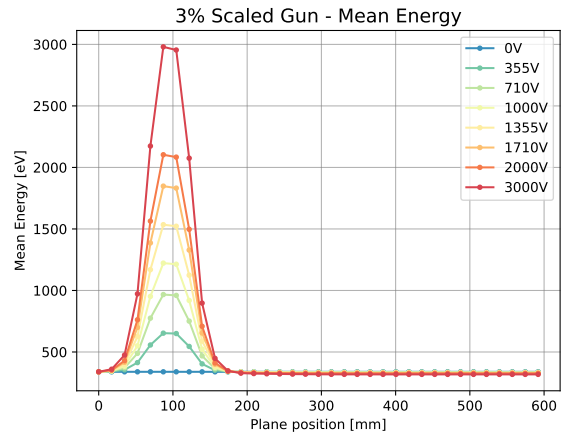


Figure 4: Selected simulation results for the beam passing the Einzel-Lenses for different center lens voltages V_{center} . Top: Mean Energy; Bottom: Envelope.

below a voltage of 1 kV, there was no significant focusing effect, primarily due to the insufficient electric field strength. However, beyond this threshold, increasing voltage results in a reduced focal length and a higher lens refraction power, as expected. The steep angles after the focus point are caused by the high initial beam divergence and result in spot sizes significantly larger than expected.

It was established that the optimal voltage setting for minimizing the beam radius at the detector distance is ~ 1355 V, for all three simulations.

CONCLUSION

The electron beam was modelled based on a field emission model and the focusing properties of a system of Einzel-Lenses were shown. The comparatively high beam divergence after passing the two grids warrants further investigation into the simulation approach. Our future research will focus on refining our simulation modelling techniques and eventually validate the data with experimental results of the CCBT2. We intent to manufacture new CNT-Samples in different sizes and measure the beam characteristics to improve the gun prototype and identify any potential challenges.

ACKNOWLEDGEMENTS

The authors wish to thank W. Devauchelle for modelling the grid in CATIA.

REFERENCES

- [1] G. Tranquille, A. Frassier, and L. V. Joergensen, “The ELENA Electron Cooler: Parameter Choice and Expected Performance,” in *Proc. COOL'13*, Muerren, Switzerland, Jun. 2013, pp. 133–135.
<https://jacow.org/COOL2013/papers/WEPP016.pdf>
- [2] B. Galante, “Characterization studies of carbon nanotubes as cold electron field emitters for electron cooling applications in the Extra Low ENergy Antiproton (ELENA) ring at CERN”, Ph.D. thesis, Phys. Dept., The University of Liverpool, Liverpool, L69 3BX, United Kingdom, 2023.
- [3] H. Liebl, *Applied Charged Particle Optics*, Heidelberg, Germany Springer-Verlag, 2008.
- [4] CST Studio Suite,
<https://www.3ds.com/products-services/simulia/products/cst-studio-suite/>

INVESTIGATION OF ION TRAPPING AND BEAM-INDUCED FLUORESCENCE AT THE ELECTRON COOLER TEST-BENCH AT HIM*

T. Beiser^{†1}, K. Aulenbacher¹, J. Dietrich, Helmholtz-Institute Mainz, Germany
 and GSI Helmholtzzentrum für Schwerionenforschung, Darmstadt, Germany
¹also at Johannes Gutenberg-University, Mainz, Germany

Abstract

Beam-current dependent and wavelength-resolved studies of the beam-induced fluorescence at the electron cooler test-bench recorded with a low-noise, cooled sCMOS-camera, will be presented. As a new feature, a high-voltage switch was utilized for beam interruptions, counteracting ion trapping.

BEAM-INDUCED FLUORESCENCE AT THE ELECTRON COOLER TEST BENCH AT HIM

The test bench uses an energy-recovery setup to produce an electron beam [1] with up to 1 A of 30 keV electrons for 3 kW of wall power (see Figure 1). Beam-induced fluorescence (BIF) was observed in the residual gas of the beam pipe at 3×10^{-10} mbar (see Figure 2). Most measurements were taken with 18 keV electrons and a current of 550 mA to limit the X-Ray exposure of the cooled, low-noise sCMOS camera. Images were acquired over 30 s, with a 400–550 nm bandpass filter to limit the black-body background generated by the thermionic cathode [2]. The resulting profiles were averaged over 500 pixel rows (see Figure 3).

The observed data showed an intensity increase of the BIF over time, plateauing after 3-5 minutes. This was noticeable even after normalizing for the change in pressure, a result of the collector heating induced by the dumped electrons. Taking this into account and measuring the BIF for a number of beam currents from 0 to 550 mA, a overproportional correlation of the integrated signal intensity with the beam current became evident (see Figure 4). This suggested the trapping of photon-emitting ions.

ION TRAPPING IN THE ELECTRON BEAM

Residual gas particles are ionized by the electron beam along its path. To explain the trapping mechanism, the DC electron beam of the test-bench can be approximated as a cylindrical homogeneous charge distribution. The grounded, small apertures of the anode and the deceleration optics along the beam path shape the beam potential and facilitate longitudinal trapping (see Figure 5), as long as the momentum transfer is small enough. A simple model was derived to explain the shape of the BIF. The measured BIF photons are most likely emitted by trapped ions that get excited by

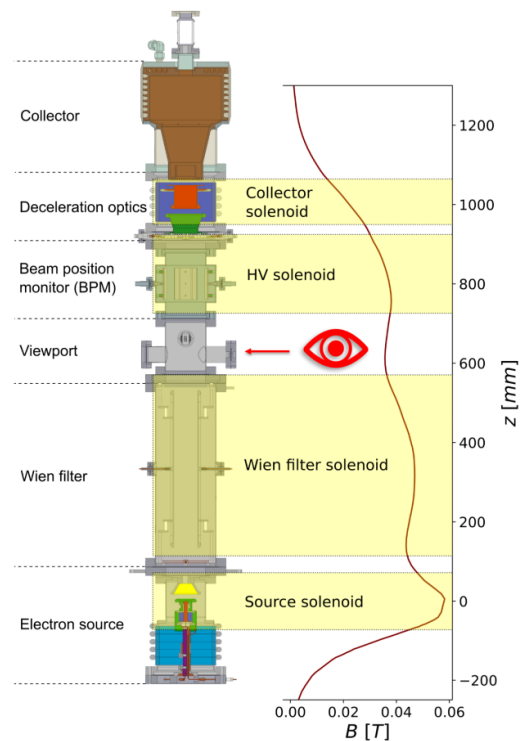


Figure 1: Schematic of the test bench with the simulated solenoid field-strength along the beam path.

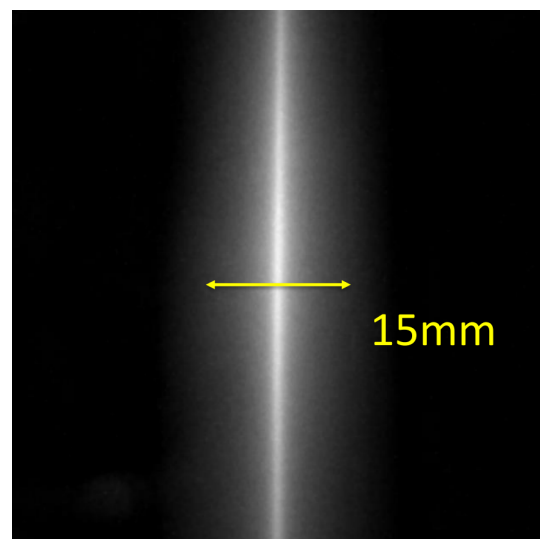


Figure 2: Image of BIF produced by a 30 keV, 1 A electron beam with indicated width.

* Work supported by the German Federal Ministry of Education and Research (BMBF Verbundforschung) 05P18UMRB1

[†] thbeiser@uni-mainz.de

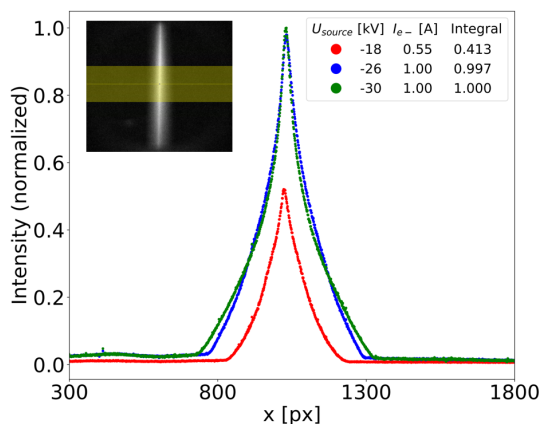


Figure 3: Averaged profiles of BIF for several parameters. (Averaged region indicated in yellow).

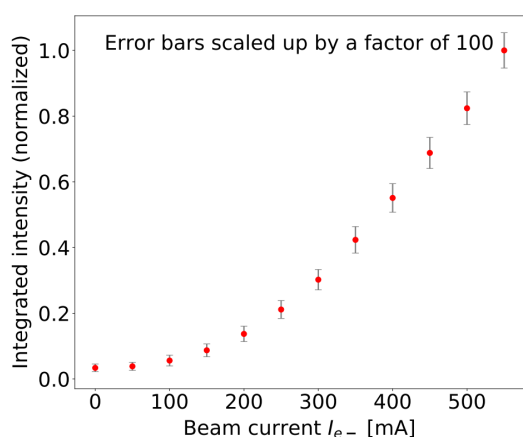


Figure 4: Integrated intensity of BIF profiles correlated with the electron beam current.

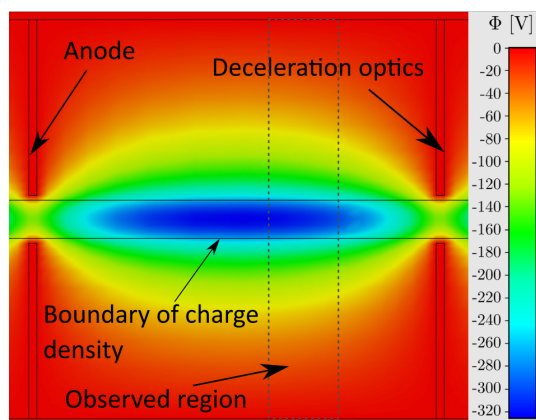


Figure 5: CST-simulated, simplified model of the test-bench and the potential of a homogeneous charge distribution (on the center plane).

the electron beam repeatedly. Particles do not interact with each other and do not change the electrostatic potential of the beam. Their motion is harmonic inside the potential, i.e. the oscillation period is independent from the starting position. The fact that all particles produced outside a given

radius reach this radius at the same time may be taken into account by having a density distribution

$$\sigma(r) = e^{-r}/r. \quad (1)$$

This resembles a Laplace distribution. This model for the charge density of the ions diverges at $r = 0$, but this is also the point where the assumptions made about the ions break down.

Introduction of an amplitude parameter a , which is due to the fact that the observed signal is a projection of the ion distribution and a transition $r = \tilde{r} + \Delta r$ (with $\Delta r \ll r$) to avoid division by zero,

$$f_{fit} = \frac{a}{2\phi} \exp\left[-\frac{|\tilde{r} + \Delta r + \ln(|\tilde{r} + \Delta r|) - \theta|}{\phi}\right], \quad (2)$$

with the location parameter θ and the scale parameter $\phi > 0$, can be fitted to the observed data (see Figure 6). Consequently, the position of the center of charge could be identified, and through the sharp transition of the signal into the background, the border of the electron beam was observed.

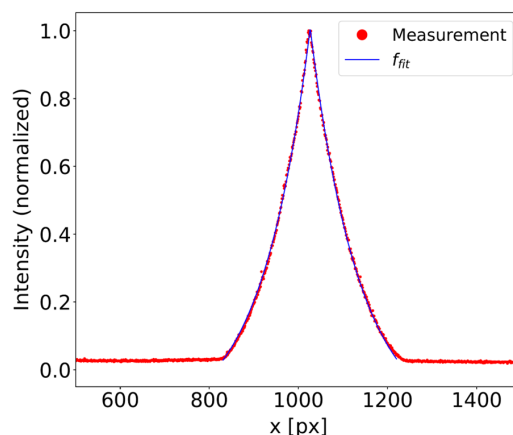


Figure 6: BIF profile of a 550 mA electron beam and the derived fit function.

ION CLEARING THROUGH BEAM INTERRUPTIONS

Following an experiment at the Recycler Electron Cooler at Fermilab a fast HV-switch was implemented at the Pierce electrode of the test-bench to interrupt the beam with 15 Hz [3]. Pulsing the electron beam in this way resulted in a decrease of BIF photons (see Figure 7). It takes about 4 ms to switch the electron beam off completely, because of the capacitive load of the Pierce electrode. The reduction in the number trapped ions was previously only indirectly observed via the cooling power of the beam (at Fermilab). Further measurements with different interruption frequencies were conducted to maximize the duty cycle of the electron beam while minimizing the number of trapped ions (see Figure 8).

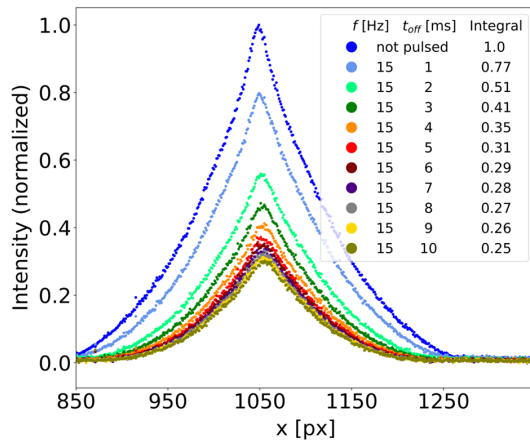


Figure 7: BIF profiles for a pulsed electron beam compared to a DC beam.

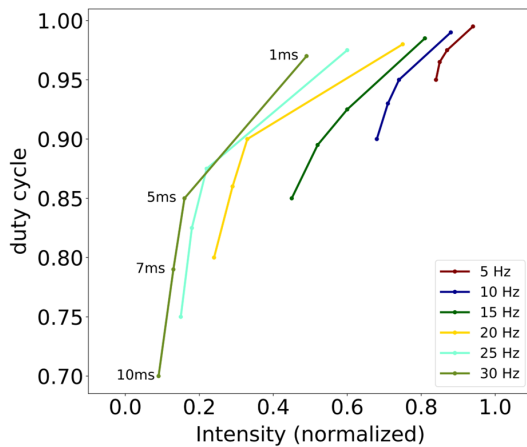


Figure 8: Duty cycle for several pulsing frequencies and switch-off durations.

SPECTRALLY-RESOLVED BIF

The test-bench has similarities to an EBIT (Electron Beam Ion Trap). In such devices a background of Barium is often detected during optical measurements, caused by the widely used Barium dispenser cathodes [4]. A comparable Ba dispenser cathode is installed at the test-bench. The H_2 spectral lines, expected in a baked out ultra-high vacuum vessel like the test-bench, are not present. Considering the partial pressure of Barium that develops in the beam region due to evaporation according to the manufacturer ($p_{Ba} = 1.37 \times 10^{-10}$ mbar), which is higher than typical for H_2 in such a vacuum vessel ($p_{H_2} = 5.64 \times 10^{-11}$ mbar) and the corresponding electron-impact ionization cross-section of Barium that is about 5 times higher than the one of H_2 ($\sigma(H_2) = 0.02 \text{ \AA}^2$) at the given energy, the data could potentially be explained by different charge states of Barium.

The charge density of the electron beam is relatively low compared to an EBIT, so it is not certain if they are present (see Figure 9).

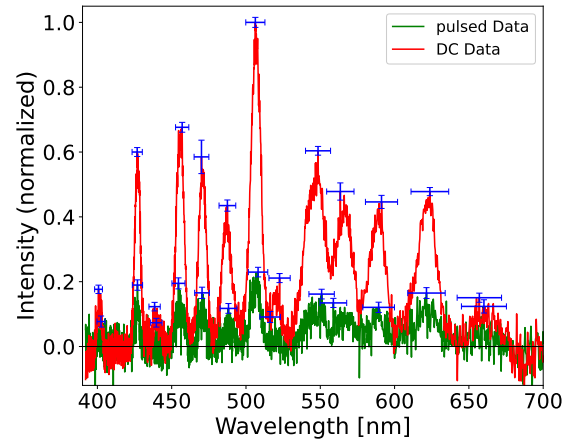


Figure 9: Spectrally-resolved measurements comparing DC and pulsed beams (at 15 Hz, integrated over a 550 mA electron beam switched on for 10 h each).

CONCLUSION

We observed beam-induced fluorescence (BIF) emitted by continuously excited ions, which were created and trapped by the electron beam itself. These photons allowed us to locate the center and the borders of the electron beam. Ion clearing through beam interruptions was directly measured with the BIF. The obtained BIF spectrum suggested that the Barium evaporating from the dispenser cathode installed at the test-bench might be a source of particles ionized by the electron beam.

REFERENCES

- [1] M.W. Bruker *et al.*, “Secondary electron measurements at the HIM electron cooler test set-up”, *Nucl. Instrum. Methods Phys. Res., Sect. A*, vol. 872, pp.169–173, 2017. doi:10.1016/j.nima.2017.08.025
- [2] Th. Beiser, K. Aulenbacher, and J. Dietrich, “Observation of Beam Induced Fluorescence (BIF) at the Electron Cooler Test Bench at Helmholtz-Institut Mainz (HIM)”, in *Proc. COOL’21*, Novosibirsk, Russia, Nov. 2021, pp. 33–35. doi:10.18429/JACoW-COOL2021-S502
- [3] A. V. Shemyakin, L. R. Prost, and G. W. Saewert, “Effect of Secondary Ions on the Electron Beam Optics in the Recycler Electron Cooler”, in *Proc. IPAC’10*, Kyoto, Japan, May 2010, paper MOPD075, pp. 867–869.
- [4] R. E. Marrs, “Milestones in EBIT Spectroscopy and Why it Almost Didn’t Work”, *Canadian Journal of Physics*, vol. 86, 2007. https://www.osti.gov/biblio/942051

JSPEC: A PROGRAM FOR IBS AND ELECTRON COOLING SIMULATION*

H. Zhang[†], Y. Zhang, S.V. Benson, M.W. Bruker
Thomas Jefferson National Accelerator Facility, Newport News, VA, United States

Abstract

JSPEC (JLab Simulation Package on Electron Cooling) is an open-source C++ program developed at Jefferson Lab to simulate the evolution of the ion beam under the intrabeam scattering effect and/or the electron cooling effect. JSPEC includes various models of the ion beam, the electron beam, and the friction force, aiming to reflect the latest advances in the field and to provide a useful tool to the community. JSPEC has been benchmarked against other cooling simulation codes and experimental data. It has been used to support the cooler design for JLEIC, an earlier JLab design for the Electron-Ion Collider. A Python wrapper of the C++ code, pyJSPEC, for Python 3.x environment has also been developed and released. It allows users to run JSPEC simulations in a Python environment and makes it possible for JSPEC to collaborate with other accelerator and beam modeling programs, as well as plentiful Python tools in data visualization, optimization, machine learning, *etc.* A Fortran interface is being developed, aiming at seamless call of JSPEC functions in Fortran. In this report, we introduce the features of JSPEC, with a focus on the latest development, and demonstrate how to use JSPEC, pyJSPEC, and the FORTRAN interface with sample codes.

INTRODUCTION

Intrabeam scattering (IBS) [1] is an effect that may reduce the quality of a high-intensity beam and impair the luminosity of a collider. Electron cooling [2] is an experimentally proven leading method to reduce the ion beam emittance and it is often used to mitigate the IBS effect. JSPEC (JLab Simulation Package on Electron Cooling) is an open-source program [3] developed at Jefferson Lab, which simulates the evolution of the ion beam under the influence of both IBS and electron cooling effects. Originally developed to support the Electron Ion Collider (EIC) design at Jefferson Lab [4], our goal is now to provide a convenient toolkit for the IBS and electron cooling effect simulation to the wider accelerator community. JSPEC includes the most frequently used formulas for the friction forces and variant models of electron/ion beams. The main code is developed in C++ with emphasis on both the validity of the physical models and the efficiency of computation. Most modules in JSPEC supports parallel computing in shared-memory structure using OPENMP. A Python wrapper, pyJSPEC, gives users access to most JSPEC functions in Python 3.x environment allowing JSPEC to work collaboratively with other simulation tools that have a Python interface [5, 6]. Many legacy codes, developed in

Fortran, remain widely used in accelerator modelling. In response to this, we are developing a Fortran interface for JSPEC. Our goal is to allow JSPEC functions to be seamlessly called within Fortran, facilitating the modelling of the electron cooling effect in those codes.

FEATURES

The basic feature of JSPEC is to calculate the emittance growth rate of the ion beam under the IBS and/or the electron cooling effect. The rate at time t is defined as $r_i(t) = \frac{1}{\epsilon_i(t)} \frac{d\epsilon_i(t)}{dt}$, where $i = x, y, s$, representing the horizontal, vertical, and longitudinal direction, and ϵ_i is the emittance in the respective direction. For the IBS rate, JSPEC provides the Martini model [7], the original Bjorken-Mtingwa model [8] calculated by Nagaitsev's method [9], and the complete Bjorken-Mtingwa model with vertical dispersion and non-relativistic terms included [10]. The electron cooling rate is calculated statistically on a group of sample ions, each receiving a *kick* by the friction force. The rate is calculated as the relative change of the emittance per unit time before and after the kick. JSPEC provides several formulas [11-14] for both the non-magnetized and the magnetized friction force. Using different formulas in the transverse and the longitudinal direction is allowed.

JSPEC also simulates the evolution of the ion beam under the IBS effect and/or the electron cooling effect. The RMS dynamic model represents the ion beam by its macroscopic parameters, *i.e.* the emittances, the momentum spread, and the bunch length (for a bunched beam), calculates the instant expansion rate r at a time t and updates the parameters using $\epsilon_i(t + \Delta t) = \epsilon_i(t) \exp(r_i \Delta t)$ for the time step Δt . The particle model applies kicks due to IBS and electron cooling to sample ions and moves them by a random phase advance for the betatron and synchrotron oscillation in Δt . The turn-by-turn model is similar to the particle model but the betatron and synchrotron motion is modeled by a linear transfer matrix and the simulation is carried out in a turn-by-turn manner.

Recently we have added two new features [15]. One is to treat the cooler as a lengthy element. Previously, JSPEC used a thin lens model for the cooler. The electron beam is assumed constant during the cooling process. In the new model, we cut the cooler into n slices. For ions, each slice works as a drift. The position of an ion changes but the velocity does not when moving through a slice. In the middle of the slice, the ion get a kick due to cooling. For cooling simulations, it is not necessary to consider the motion of individual electrons but rather the properties of the electron beam as a whole. For non-magnetized beam, we calculate the Twiss function β and α at different locations and then

* Work supported by the U.S. Department of Energy, Office of Science, Office of Nuclear Physics under contract DE-AC05-06OR23177.

[†] hezhang@jlab.org

compute the new bunch size, density function, and velocity distribution function. In magnetized cooling, electrons always travel a helical trajectory along the magnetic line. The "matched" β function is constant in the cooler, resulting in a constant bunch size and the elimination of α function. Therefore, the electron beam can still be considered constant in the cooler for magnetized cooling. The other new feature allows the introduction of electron beam horizontal dispersion for non-magnetized cooling, which affects the distribution of cooling between the longitudinal direction and the transverse direction. Due to the dispersion, the density function and the velocity distribution function of the electron beam deviate from the original distribution [16]. JSPEC performs 3D numerical integration using the new distribution function to calculate the friction force. A numerical model without the assumption of initial Gaussian distribution is also developed, based on the arbitrary electron beam model [15] in JSPEC. However, additional testing is needed to better understand the numerical properties of this model.

BENCHMARK

JSPEC has been benchmarked with BETACOOOL [11] for various scenarios. The two programs agree well. For the typical simulations we have done for the EIC project, a significant improvement of efficiency has been achieved even without using multiprocessing in JSPEC. Parallel computation will further improve the efficiency.

We also compared JSPEC simulations with experimental data, obtained from the collaboration of Jefferson Lab in the U.S. and Institute of Modern Physics in China from 2016 to 2019 [17]. Figure 1 shows the cooling of the $^{86}\text{Kr}^{25+}$ beam with an energy of 5 MeV/nucleon using electron pulses with a length varying from 600 ns to 1000 ns. A longer pulse length means a longer overlap between the two beams and a stronger cooling, which is observed through the larger slope of the plots. The solid lines in the plot are the results from the simulation using the turn-by-turn model. The dots are experimental data. In all the cases, the simulation agrees with the experiment reasonably well.

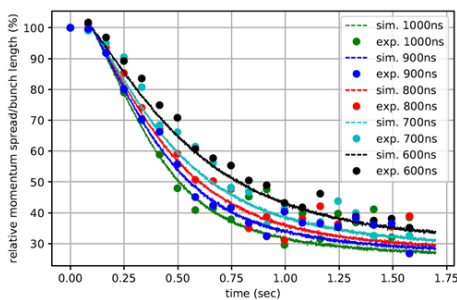


Figure 1: Cooling the $^{86}\text{Kr}^{25+}$ beam using pulsed electron beam, simulation (solid lines) and experiments (dots).

USER INTERFACE

JSPEC has been tested on both Windows and Linux systems. It can be run from the command line by typing the executable file name followed by the input file name.

The JSPEC input file is in plain text format. It is composed of a few sections as shown in Fig. 2. Most sections are used to define the elements or to set up models for the effects under study. In these sections, we set values to the keywords, which describe an element or represent parameters of a model/formula. In the last section (section_run), the elements are created and the simulation is carried out. A valid input must include the above two types of sections. There are two optional sections: section_scratch and section_comment. We can define variables and perform simple calculations in section_scratch. The variables can be used in the following sections. In section_comment, we can write a long note that is not suitable for inline comments. For more useful examples, we suggest that the readers check out the *github* repository [3].

```
section_ion #define the ion beam
    charge_number = 1
    mass = 938.272
    kinetic_energy = 3e4
    ...
section_ring #define the ring
    ...
section_cooler #define the cooler
    ...
section_scratch
    m = 938.272
    ke = 3e4
    gamma_ion = ke/m + 1
section_e_beam #use gamma_ion above
    gamma = gamma_ion
    ...
section_ibs #set up IBS calculation
    model = bm
    log_c = 24
    coupling = 0
section_ecool
    ...
section_simulation
    ...
section_run
    create_ion_beam
    create_ring
    create_e_beam
    create_cooler
    run_simulation
```

Figure 2: Structure of JSPEC input.

PYTHON INTERFACE

Python is one of the most popular programming languages in use today. Those who work with Python benefit from a vast array of libraries in data processing, optimization, machine learning, *etc.* pyJSPEC serves as the Python interface for JSPEC, and it has been developed using Pybind11 [18]. pyJSPEC is a library for Python 3.x. Once imported, users can access most functions offered by JSPEC. The Python wrapper enables JSPEC to integrate seamlessly with the rich set of Python libraries, as well as with other accelerator modeling programs that offer Python support. For instance, one could utilize an evolutionary optimizer in conjunction with JSPEC to optimize cooling performance [6]. Figure 3 shows an example on calculating the expansion rate due to both the electron cooling and the IBS effect and carrying out a dynamic simulation using the particle model. The code is easy to understand. Since

JSPEC is object-oriented, one first needs to create an element. Once the element is established, one can call its member functions to set up the element's properties or to conduct specific calculations or simulations.

```

1 import jspec
2 # create the ion beam
3 ...
4 ...
5 p_beam = jspec.Beam(n_charge, n_mass,
6     ke, ex, ey, dp, ds, np)
7
8 # create the ring
9 lat = jspec.Lattice("lattice.tfs")
10 ring = jspec.Ring(lat, p_beam)
11
12 # create the cooler
13 ...
14 cooler = jspec.Cooler(length, section_number,
15     magnetic_field, twiss_beta, twiss_beta,
16     dx, dy)
17
18 # create electron bunch
19 ...
20 e_beam = jspec.GaussianBunch(ne, sigma_x,
21     sigma_y, sigma_z)
22 e_beam.set_gamma(gamma)
23 e_beam.set_tpr(0.5, 0.1)
24
25 # calculate electron cooling rate
26 force_solver = jspec.ForcePark()
27 n_sample = 40000
28 ecool_solver = jspec.ECool()
29 rate = ecool_solver.rate(force_solver, p_beam,
30     n_sample, cooler, e_beam, ring)
31
32 # calculate IBS rate
33 ibs_solver = jspec.IBSSolver_BM(log_c)
34 rate = ibs_solver.rate(lat, p_beam)
35
36 # create proton samples
37 p_samples = jspec.Ions_MonteCarlo(n_sample)
38 p_samples.set_twiss(cooler)
39 p_samples.create_samples(p_beam)
40
41 # run simulation
42 ...
43 simulator = jspec.ParticleModel(time, n_step)
44 simulator.set_ibs(True)
45 simulator.set_ecool(True)
46 simulator.run(p_beam, p_samples, cooler,
47     e_beam, ring, ibs_solver, ecool_solver,
48     force_solver)

```

Figure 3: pyJSPEC sample code.

FORTRAN INTERFACE

In modern proposed colliders like the EIC, high-density ion beams achieve unparalleled luminosity. This introduces the necessity to simulate the IBS effect and electron cooling in conjunction with other collective effects, such as the space charge effect, CSR effect, and more. While the simulation of these collective effects is beyond the purview of JSPEC, there are robust tools available in other accelerator modeling programs. Several legacy programs, developed in FORTRAN, remain in widespread use. These programs, such as BMAD [19], are well-benchmarked, meticulously documented, and furnish many reliable models. Integrating JSPEC with these legacy programs will significantly enhance our capabilities in electron cooling simulation. This realization prompted us to develop a FORTRAN interface for JSPEC. We hope to seamlessly invoke JSPEC functions within FORTRAN. Although this initiative is

still underway, we have already ported the majority of data types from JSPEC into FORTRAN, validating that our ultimate objective is feasible. Figure 4 offers a sample code that demonstrates the computation of the cooling rate on a proton beam using JSPEC in FORTRAN.

```

1 program main
2   use jspec
3   use iso_c_binding
4   implicit none
5
6   type(Beam) :: my_beam
7   type(Lattice) :: my_lattice
8   type(Ring) :: my_ring
9   type(Cooler) :: my_cooler
10  type(FrictionForceSolver) :: my_force_solver
11  type(EBeam) :: my_ebeam
12  type(ECoolRate) :: rate_ec
13  real(8) :: rx, ry, rs
14
15  ! Define variables
16  integer(c_int) :: charge = 1
17  real(c_double) :: mass = 938.272
18  ...
19
20  ! Create ion beam
21  my_beam = create_beam(charge, mass, ke, &
22      ex, ey, dp, ds, np)
23
24  ! Create the lattice from some file
25  my_lattice = create_lattice("lattice.txt")
26
27  ! Create a ring
28  my_ring = create_ring(my_lattice, my_beam)
29
30  ! Create a cooler
31  my_cooler = create_cooler(length, n_section, &
32      mag_field, twiss_beta, twiss_beta)
33
34  ! Create friction force solver
35  my_force_solver = create_force_solver(PARKHOMCHUK)
36
37  ! Create electron beam with Gaussian distribution
38  my_ebeam = create_gaussian_bunch(ne, sigma_x, &
39      sigma_y, ds)
40  call ebeam_set_gamma(my_ebeam, gamma)
41  call ebeam_set_temperature(my_ebeam, tmp_tr, tmp_l)
42
43  ! Calculate the cooling rate rx, ry, rs
44  rate_ec = create_ecool_rate_calculator()
45  call ecool_rate(rate_ec, my_force_solver, &
46      my_beam, n_sample, my_cooler, &
47      my_ebeam, my_ring, rx, ry, rs)
48 end program main

```

Figure 4: FORTRAN interface sample code.

SUMMARY

JSPEC is an open-source program for IBS and electron cooling simulations developed at Jefferson Lab. The source code, manuals, and examples are provided [3]. A Python wrapper, pyJSPEC, has been developed and most functions from JSPEC has been ported to Python 3.x environment. pyJSPEC enables us to tap into the vast array of Python libraries for cooling scheme design and study. Additionally, a FORTRAN interface is under development. This interface aims to make JSPEC functions accessible in FORTRAN, allowing for the simulation of electron cooling in conjunction with other collective effects.

ACKNOWLEDGMENT

This material is based upon work supported by the U.S. Department of Energy, Office of Science, Office of Nuclear Physics under contract DE-AC05-06OR23177.

REFERENCES

- [1] A. Piwinski, "Intra-beam-scattering", in *Proc. 9th Int. Conf. on High Energy Accelerators*, Stanford, CA, USA, May 1974, pp. 405-409. doi: 10.5170/CERN-1992-001.226
- [2] Ya. Derbenev, "Theory of electron cooling", arXiv:1703.09735. doi:10.18429/10.48550/arXiv.1703.09735
- [3] JSPEC, <https://github.com/zhanghe9704/electroncooling/>
- [4] S. Abeyratne *et al.*, "MEIC Design Summary", arXiv:1504.07961. doi:10.48550/arXiv.1504.07961
- [5] pyJSPEC, <https://github.com/zhanghe9704/jspec2-python/>
- [6] H. Zhang *et al.*, "pyJSPEC – A Python module for IBS and electron cooling", in *Proc. 5th North American Particle Accelerator Conf. (NAPAC2022)*, Albuquerque, NM, USA, Aug. 2022, pp. 672-674. doi: 10.18429/JACoW-NAPAC2022-WEPA24
- [7] M. Martini, "Intrabeam scattering in the ACOL-AA machines," Rep. CERN-PS-8-4-9-AA, CERN, 1984.
- [8] J. Bjorken and S. Mtingwa, "Intrabeam scattering," *Part. Accel.* 13, pp. 115-143, 1982.
- [9] S. Nagaitsev, "Intrabeam scattering formulas for fast numerical evaluation," *Phys. Rev. ST Accel. Beams*, vol. 8, p. 064403, 2005. doi: 10.1103/PhysRevSTAB.8.064403
- [10] F. Zimmermann, "Intrabeam scattering with non-ultrarelativistic corrections and vertical dispersion for MAD-X," Rep. CERN-AB-2006-002, CERN, 2005.
- [11] I. Meshkov *et al.*, "BETACool physics guide", Joint Institute for Nuclear Research, Dubna, Russian Federation, 2007.
- [12] I. Meshkov, "Electron cooling: status and perspectives," *Phys. Part. Nucl.*, vol. 25, pp. 631-661, 1994.
- [13] V. Parkhomchuk, "New insights in the theory of electron cooling," *Nucl. Instrum. Methods Phys. Res., Sect. A*, vol. 441, pp. 9-17, 2000. doi: 10.1016/S0168-9002(99)01100-6
- [14] Y. Derbenev and A. Skrinsky, "The effect of an accompanying magnetic field on electron cooling," *Part. Accel.*, vol 8, pp. 235-243, 1978.
- [15] H. Zhang *et al.*, "Latest updates on JSPEC – an IBS and electron cooling simulation program", in *Proc. 14th International Particle Accelerator Conf. (IPAC2023)*, Venice, Italy, May. 2023, pp. 2253-2256. doi:10.18429/JACoW-IPAC2023-TUPM030
- [16] M. Blaskiewicz., "Dispersion and electron cooling", Brookhaven National Lab, Upton, NY, USA, Rep. BNL-210932-2019-TECH, 2019.
- [17] M. Bruker *et al.*, "Demonstration of electron cooling using a pulsed beam from an electrostatic electron cooler," *Phys. Rev. Accel. Beams*, vol. 24, p. 012801, 2021. doi: 10.1103/PhysRevAccelBeams.24.012801
- [18] Pybind11, <https://pybind11.readthedocs.io>
- [19] BMAD, <https://www.classe.cornell.edu/bmad/>

INFLUENCE OF ENERGY SHIFT OF ELECTRON BEAM ON THE ELECTRON COOLING AT EicC*

X. D. Yang[†], Institute of Modern Physics, CAS, Lanzhou, China

Abstract

The cooling process of 20 GeV proton beam was simulated in the case of different energy shift of electron beam. The changes of horizontal emittance and longitudinal momentum spread of proton beam with time was presented. The different performances in horizontal and longitudinal direction were observed comparing with the traditional low energy electron cooling. The final emittance and minimum momentum spread was demonstrated in the different parameters configuration. In order to achieve expected cooling requirements, the energy shift of electron beam should be paid enough attention in the case of high energy electron cooling, especially considering a RF accelerator as electron cooling device.

INTRODUCTION

The basic requirement of electron cooling is that the longitudinal average velocity of the electron beam is equal to that of the ion beam. In order to ensure the desired cooling effect, the energy of the electron beam should be set precisely and accurate matching of longitudinal velocity of the ion beam [1, 2].

The deviation of electron beam energy from the optimal value reflects two requirements. On the one hand, the energy of an electron beam needs to be measured accurately in the electron cooling commissioning and operation. On the other hand, in order to meet the parameters required for cooling, the energy stability and energy spread of the electron beam are required in the design and manufacture of electronic cooling devices.

In future projects, electron cooling plays an important role. It is a necessary means to obtain high brightness and long lifetime ion beams. The performance of electron cooling is related to many parameters, such as ion beam, electron beam, storage ring, electron cooling device, etc. The energy shift of the electron beam is an important indicator. The effects of energy shift of electron beam on the transverse and longitudinal cooling processes should be simulated previously. In particular, the effect on longitudinal cooling, the simulation results have reference value for the design and operation of electron cooling devices in the future.

The electron cooling time not only depends on the lattice parameters of the storage ring, the Betatron function, dispersion of the cooling section, such as energy, initial emittance and momentum spread of proton beam, but also on the construction parameters of electron cooling device, the strength of magnetic field, the parallelism of magnetic field in the cooling section, the effective cooling length, and the parameters of electron beam, such as radius, density and

temperature of electron beam. These parameters are determined by the storage ring and the technology limitation, on the other hand, they are influenced and restricted each other.

The performance of electron cooling is not only related to the ion beam parameters of the storage ring, but also related to the electron beam parameters of the electron cooling device. The important parameters of the electron beam are the transverse and longitudinal temperature of the electron beam.

The electron cooling process of 20 GeV proton beam in EicC was simulated in cases of variety of parameters in the previous studies [3, 4], the longitudinal temperature of the electron beam was not involved in the simulations. The energy shift of the electron beam was not taken into account.

During the optimization of electron cooling process, the average velocity of an electron and an ion is required to be equal. In the case of the given distribution of the ion beam, the energy spread of the ion beam is about the same order of magnitude comparing with the electron beam.

The energy shift of the electron beam is a very important parameter in the electron cooling process, especially in high-energy electron cooling [5, 6]. And the energy shift of the electron beam determines the final parameters of the proton beam after electron cooling, so the effect of energy shift of electron beam on electron cooling is necessary.

The RF accelerator is the option for high-energy electron cooling [7, 8]. The electron beam generated by the RF accelerator has a large energy spread. The necessary measures are needed to reduce the energy spread of the electron beam.

From the experience and experimental results from LEReC BNL [9-11], the longitudinal temperature of the electron beam should be paid enough attention in the case of high energy electron cooling.

The influence of electron beam energy shift on electron cooling process should be investigated. It is useful to understand the requirements for electron cooling, and provide the guidance for design parameters of high energy electronic cooling.

MOTIVATION

In order to get the required brightness in the future EicC project, not only does it require an intense proton beam, but also it requires a small emittance and momentum spread. Electron cooling can increase the density of phase space and improve the quality of proton beam, Electron cooling plays an important role.

In the second phase of EicC, the energy of proton will upgrade to 60~100 GeV, and the energy of electron beam will increase to 5~10 GeV, the luminosity will expect to achieve 1×10^{35} .

* Work supported by NSFC No. 12275325, 12275323, 12205346.

[†] email address yangxd@impcas.ac.cn.

With this parameter, conventional electrostatic cooling device cannot meet the requirements. The radio-frequency accelerator system must be used. There are requirements for the quality of electron beams generated by RF accelerator systems in the transverse and longitudinal both directions. The emittance and energy spread of the electron beam are two important parameters.

In this paper, the transverse and longitudinal cooling of a proton beam were simulated with the help of simulation program. The image of the cooling process was obtained. The main parameters of the electron beam were proposed.

ELECTRON COOLING SIMULATION

A typical transverse cooling process were illustrated in Fig. 1. The normalized horizontal emittance was plotted in the case of the energy shift of electron beam in the order of magnitude of 10^{-3} . The proton beam was not cooled in the longitudinal direction. As one can see, the transverse cooling present different behaviour at the different energy shift of electron beam.

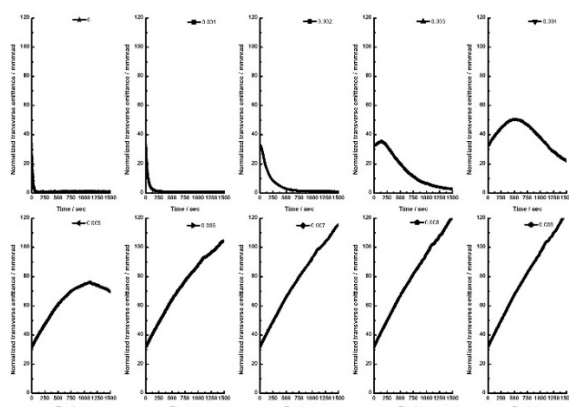


Figure 1: The normalized emittance as a function of the time in the case of different shift of electron energy.

The longitudinal cooling process was presented in Fig. 2. The momentum spread of proton beam was plotted in the case of the energy shift of electron beam in the order of magnitude of 10^{-4} .

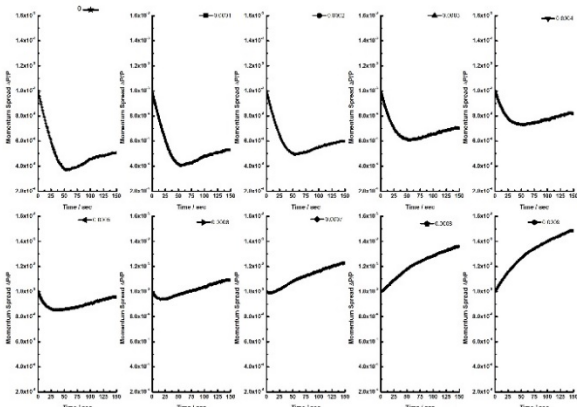


Figure 2: The momentum spread as a function of the time in the case of different shift of electron energy.

As mentioned in the previous paragraph, the proton beam was cooled down in the transverse direction. The longitudinal cooling process was different from the transverse one. During the initial cooling, the momentum spread drop rapidly, and then get to the minimum. And then the momentum spread start to grow. It bounce back from the bottom. The proton beam was not cooled when the energy shift of electron beam bigger than a certain value.

In this parameter configuration, the transverse cooling behaved differently from longitudinal cooling. The transverse emittance decreased exponentially. It was not a standard exponential function of decay or increase in the longitudinal direction. There was a deviation in the fitting process.

In order to compare the simulation results, the same calculation time was used.

In the longitudinal direction, due to the cooling happened firstly and then scattering happened later. So only the cooling part was fitted. The longitudinal cooling time was replaced by the time when the momentum spread reach its minimum.

RESULTS AND DISCUSSION

The transverse cooling time as a function of the shift of electron energy was demonstrated in Fig. 3. The transverse cooling time became longer with the increasing of the energy shift of the electron beam.

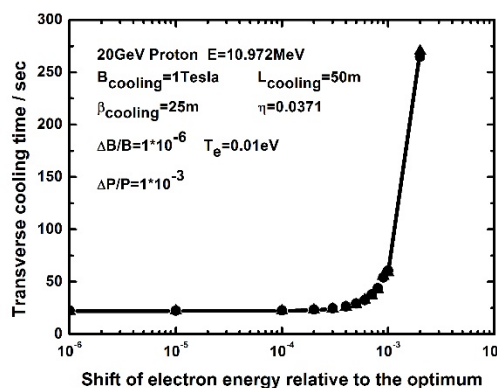


Figure 3: The transverse cooling time as a function of the shift of electron energy.

The minimum normalized emittance as a function of the shift of electron energy was illustrated in the Fig. 4. The minimum normalized emittance became bigger with the increasing of the energy shift of the electron beam.

The time approaching minimum momentum spread as a function of the shift of electron energy was demonstrated in Fig. 5. The time to reach the minimum value was almost the same. It did not change with the energy shift of the electron beam.

The minimum momentum spread as a function of the shift of electron energy was illustrated in Fig. 6. The minimum momentum spread became bigger with the increasing of the energy shift of the electron beam.

From these simulation results, the transverse and longitudinal cooling time and the minimum emittance and momentum spread were analysed. The longitudinal temperature of the electron beam has influenced the final transverse emittance and longitudinal momentum spread of the proton beam.

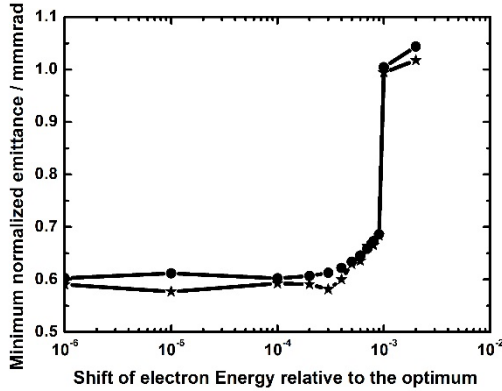


Figure 4: The minimum normalized emittance as a function of the shift of electron energy.

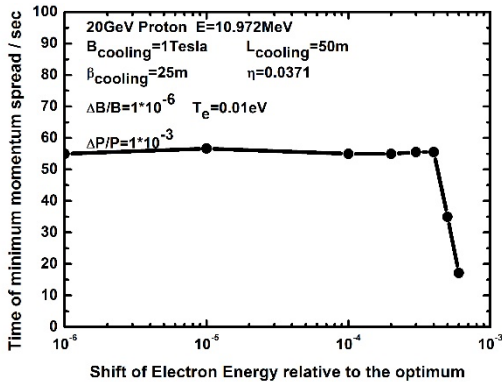


Figure 5: The time approaching minimum momentum spread as a function of the shift of electron energy.

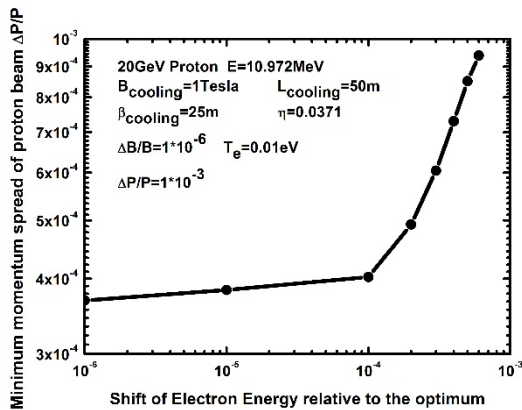


Figure 6: The minimum momentum spread as a function of the shift of electron energy.

When the energy shift of the electron beam was bigger than a certain value, the proton beam cannot be cooled in both transverse and longitudinal directions.

When the energy shift of the electron beam was smaller than another value, the proton beam can be cooled in the transverse direction, but not be cooled in the longitudinal direction.

When the energy shift of the electron beam was smaller than the third value, the proton beam can be cooled in both transverse and longitudinal directions.

In the case of high energy electron cooling, the longitudinal velocity of the electron beam was much greater than the transverse velocity. In the cooling simulation calculations, the same time interval was used for both transverse and longitudinal. Proton beams travelled at different path lengths during the same time interval in the transverse and longitudinal directions. The electron beam has about the same size in the transverse and longitudinal directions. There may be the cause of the unexpected results in the simulations.

By the way, the cooling forces vary with the absolute value of velocity difference, not relative value.

SUMMARY

The longitudinal cooling behaviour is different from the transverse one. After the balance is achieved in the transverse direction, the emittance remain unchanged. But the longitudinal momentum spread shrink rapidly at the beginning and then bounces back from the bottom.

If the proton beam was expected to be cooled in the transverse direction, the energy shift of electron beam must be smaller than $2 \cdot 10^{-3}$.

To achieve longitudinal cooling, the energy shift of electron beam has to be smaller than $5 \cdot 10^{-4}$.

The longitudinal cooling force is not enough to counteract the longitudinal scattering effect in the different cooling period.

The electron beam produced by the traditional electrostatic accelerator has a smaller energy spread. The electron beam generated by the RF accelerator has a larger spread of energy. In high energy electron cooling, the energy spread of electron beam is an important parameter to be concerned.

ACKNOWLEDGEMENTS

The author would like to thank Prof. V. Parkhomchuk for him to provide the simulation code SIMCOOL and useful guidance in the simulation during this work.

REFERENCES

- [1] S. Seletskiy *et al.*, "Absolute Energy Measurement of the LEReC Electron Beam", in *Proc. NAPAC'16*, Chicago, IL, USA, Oct. 2016, pp. 1033-1035.
doi: 10.18429/JACoW-NAPAC2016-WEPOB62
- [2] S. Seletskiy, M. Blaskiewicz, A. Drees, *et al.* "Accurate setting of electron energy for demonstration of first hadron beam cooling with rf-accelerated electron bunches", *Phys. Rev. Accel. Beams*, vol. 22, p. 111004, 2019.
doi: 10.1103/PhysRevAccelBeams.22.111004

- [3] X. D. Yang, “Simulation of electron cooling and IBS at EicC”, in *Proc. COOL'19*, Novosibirsk, Russia, Sep. pp. 77-79. doi:10.18429/JACoW-COOL2019-TUPS01
- [4] X. D. Yang, “Simulation of transverse electron cooling and IBS of 20 GeV proton beam at EicC”, in *Proc. COOL'21*, Novosibirsk, Russia, Nov. 2021, pp. 70-73. doi:10.18429/JACoW-COOL2021-P1002
- [5] D. Kayran, Z. Altinbas, D. Bruno, *et al.* “First results from commissioning of low energy RHIC electron cooler (LEREC)”, in *Proc. IPAC2019*, Melbourne, Australia, May 2019, pp.769-772. doi:10.18429/JACoW-IPAC2019-MOPRB085
- [6] D. Kayran, Z. Altinbas, D. Bruno, *et al.* “Commissioning of the electron accelerator LEReC for bunched beam cooling”, in *Proc. of NAPAC'19*, Lansing, MI, USA, Sep. 2019, pp. 330-334. doi:10.18429/JACoW-NAPAC2019-TUZBA1
- [7] A.V. Fedotov, S. Belomestnykh, I. Ben-Zvi, *et al.* “Bunched beam electron cooler for low-energy RHIC operation”, in *Proc. PAC'13*, Pasadena, CA, USA, Sep.-Oct. 2013, pp. 363-365.
- [8] A.V. Fedotov, M. Blaskiewicz, W. Fischer, *et al.* “Accelerator physics design requirements and challenges of RF based electron cooler LEReC”, in *Proc. NAPAC'16*, Chicago, IL, USA, Oct. 2016, pp.867-869.
- [9] A.V. Fedotov, Z. Altinbas, M. Blaskiewicz, *et al.* “First electron cooling of hardron beams using bunched electron beam”, in *Proc. NAPAC'19*, Lansing, MI, USA, Sep. 2019, pp.957-960. doi:10.18429/JACoW-NAPAC2019-THZBA5
- [10] A. V. Fedotov, Z. Altinbas, S. Belomestnykh, *et al.* “Experimental Demonstration of Hadron Beam Cooling Using Radio-Frequency Accelerated Electron Bunches”, *Phys. Rev. Lett.*, vol. 124, p. 084801, 2020. doi:10.1103/PhysRevLett.124.084801
- [11] A. V. Fedotov, W. Fischer, X. Gu, *et al.* “Electron cooling of colliding ion beam in RHIC: status and perspectives”, in *Proc. COOL2021*, Novosibirsk, Russia, Nov. 2021, pp. 42-47. doi:10.18429/JACoW-COOL2021-S601

DEVELOPMENT OF AN ERL FOR COHERENT ELECTRON COOLING AT THE ELECTRON-ION COLLIDER

K. Deitrick*, S. Benson, Thomas Jefferson National Accelerator Facility, Newport News, VA, USA
J. Conway, B. Dunham, R. Eichhorn, C. Gulliford, V. Kostroun,
C. Mayes, K. Smolenski, N. Taylor, Xelera Research LLC, Ithaca, NY, USA
W. Bergan, A. Fedotov, D. Kayran, E. Wang, D. Xu, Brookhaven National Lab, Upton, NY, USA
N. Wang, Cornell University, Ithaca, NY, USA

Abstract

The Electron-Ion Collider (EIC) is currently under development to be built at Brookhaven National Lab and requires cooling during collisions in order to preserve the quality of the hadron beam despite degradation due to intra-beam scattering and beam-beam effect. An Energy Recovery Linac (ERL) is being designed to deliver the necessary electron beam for Coherent electron Cooling (CeC) of the hadron beam, with an electron bunch charge of 1 nC and an average current of 100 mA; two modes of operation are being developed for 150 and 55 MeV electrons, corresponding to 275 and 100 GeV protons. The injector of this Strong Hadron Cooler ERL (SHC-ERL) is shared with the Precooler ERL, which cools lower energy proton beams via bunched beam cooling, as used in the Low Energy RHIC electron Cooling (LEReC). This paper reviews the current state of the design.

INTRODUCTION

The Electron-Ion Collider (EIC) is a partnership project between Brookhaven National Lab (BNL) and Thomas Jefferson National Accelerator Facility (TJNAF) to be constructed at BNL, using much of the existing infrastructure of the Relativistic Heavy Ion Collider (RHIC); a layout of the EIC is shown in Fig. 1. Collisions occur between the hadrons in the Hadron Storage Ring (HSR) and the electrons supplied by the Electron Storage Ring (ESR); in order to maintain a high average polarization of the ESR, bunches are frequently replaced using the Rapid Cycling Synchrotron (RCS). While most of the magnets for the HSR are repurposed RHIC magnets, already installed in the existing tunnel, both the ESR and RCS will have to be installed. In the current scope of the EIC, only one interaction region (IR) is supported, sited at the current IR6 of RHIC; however, it is highly desired that a second IR may be supported at IR8 in the future, and design efforts support that eventuality [1].

In order to achieve the design emittances of the hadron beam, a two-stage cooling system is necessary. First, hadron beams are injected into the HSR and cooled to the target emittances. After the target emittances are achieved, the HSR is ramped to the collision energy, and the hadron beam is cooled during collision in order to maintain the beam emittances; preserving the design emittances is critical to achieve the desired luminosity of the EIC. The electron cooler which provides cooling to the hadron beam is located in IR2 [1].

* kirstend@jlab.org

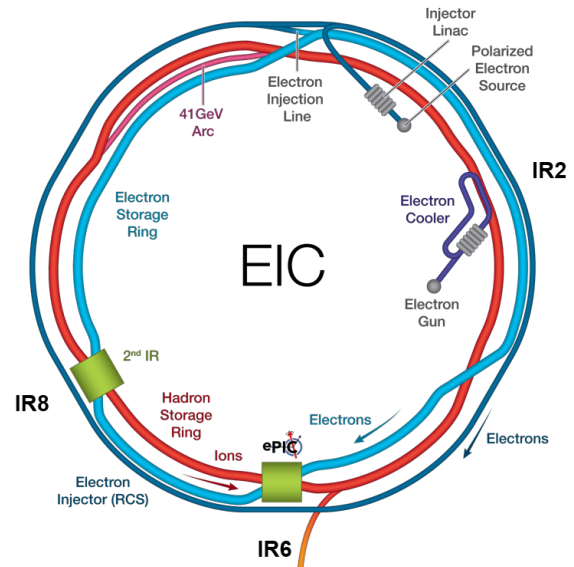


Figure 1: The current layout of a portion of the Electron-Ion Collider (EIC). The Hadron Storage Ring (HSR), Electron Storage Ring (ESR), and the Rapid Cycling Synchrotron (RCS) labels are color-coded to their respective rings; the current and proposed IRs are shown at IR6 and IR8, with the electron cooler in IR2.

COOLING MECHANISMS

The two cooling stages use different cooling mechanisms in order to cool the hadron beam. The Pre-cooler, which cools during injection, uses non-magnetized bunched beam cooling, which is the mechanism currently used in Low Energy RHIC electron Cooling (LEReC) [2, 3]. In this scheme, three electron bunches at an energy of 13 MeV are used to cool each hadron bunch, which has an energy of 24 GeV.

The Strong Hadron Cooler (SHC), which cools during collision, uses Coherent electron Cooling (CeC) where the electron beam detects the hadron distribution, amplifies the imprinted distribution, and feeds back on the hadron beam to reduce the emittance of the hadron beam [4]. The cooling section of the SHC can be separated into three sections for each of these actions - modulator, amplifier, and kicker, respectively. The type of CeC to be used is microbunched electron cooling (MBEC), where chicanes and space charge provide the necessary amplification. While the EIC is intended to operate over a range of proton energies, only the 275 and

Table 1: The electron beam parameters and cooling mechanism for the three proton beam energies. The electron beam longitudinal distribution is assumed to be a superGaussian of order $\sim 2-4$, and the bunched beam cooling assumes 3 electron bunches with a charge of 1.33 nC each for each hadron bunch.

Proton Energy	100 GeV	275 GeV	24 GeV
Gamma	106.6	293.1	25.58
Bunch charge (nC)		1	1.33
Avg. current (mA)		98.5	98.5
<i>rms</i> bunch length (mm)	9	7	40
Slice energy spread $dp/p(10^{-4})$	0.6-1.5	0.4-0.8	5
Norm. trans. emit. (mm-mrad)		2.8	1.5

100 GeV proton beams are currently being considered to cool by Strong Hadron Cooling, corresponding to electron beam energies of 150 and 55 MeV, respectively [5-7]. A summary table of select electron beam parameters in the cooling section for both stages is shown in Table 1.

Given the significant electron beam power required by both cooling schemes, an energy recovery linac (ERL) is required - the operational power necessary to produce the desired electron beams with a linac is prohibitive. Instead of designing two separate ERLs, one for each stage of cooling, the two ERLs have a common injector, and the beam is directed to either the Pre-Cooler or SHC transport afterwards; additionally, the return line is shared. A conceptual layout (not to scale) of the cooling complex is shown in Fig. 2.

STRONG HADRON COOLER ERL

Xelera Research had previously developed a complete model of the SHC-ERL, without the incorporated Pre-Cooler ERL, working with colleagues at BNL and TJNAF (Jefferson Lab). With the decision to incorporate the Pre-Cooler ERL in the summer of 2022 and a change in the target electron beam parameters in the cooling section, the design had to be updated. One of the design aspects is that IR2 already contains the HSR, the ESR, and the RCS, making the geometry challenging [8].

The main sections of the SHC-ERL, in beamline order, are the injector (IN), the merger (MG), the pre-cooler linac (PL), the bunch compressor (BC), the main linac (LA), transport to the cooler section (HM), the cooler section (modulator, amplifier, and kicker), the first turnaround (TA), the return line, and the second turnaround (TB) - after which, the beam begins energy recovery; the high power beam dump for the SHC-ERL is located after the main linac.

In the current design, the injector consists of a DC gun, two 197 MHz quarter-wave cavities, and a 591 MHz single cell cavity to help linearize the longitudinal distribution. The pre-cooler linac consists of two 197 MHz quarter-wave

cavities, two 591 MHz single cell cavities, and another two 197 MHz quarter-wave cavities. The main linac consists of eight 591 MHz five-cell cavities, with four 1773 MHz five-cell cavities placed in the center.

When pre-cooling was incorporated into the SHC, this resulted in a longer electron bunch out of the injector and introduced the necessity of bunching the beam before the main linac. However, due to the location of the bunch compressor, the beam is at different energies through the compressor depending on if it is accelerating or decelerating. Consequently, the bunch compressor has two lines - a low-energy line for the accelerating bunch and a high-energy line for the decelerating bunch; both lines are required to have the same time of flight.

An initial design has been completed for the 55 MeV SHC-ERL, with the optics shown in Fig. 3. The main simulation program used is *Tao* and the *Bmad* library [9], while the low energy, space-charge dominated sections are modeled with General Particle Tracer (GPT) and Impact-T. For improved cooling behaviors, the longitudinal distribution is a superGaussian of order $\sim 2-4$ to approximate a top hat, as opposed to a more typical Gaussian distribution [8].

In Table 1, the required slice energy spread of the electron beam is a range - if the slice energy spread falls outside of this range, the desired cooling is not achieved. With the current injector design, the simulated slice energy spread is too small. We will use a laser heater after the main linac to increase the slice energy spread [10].

PRE-COOLER ERL

The main sections of the Pre-cooler ERL, in beamline order, are the injector, the merger, the pre-cooler linac, the dogleg to exit the SHC-ERL, transport to the cooler, the cooler section, the first turn around, the return line, and the second turnaround - after which, the beam begins energy recovery; the high power beam dump for the Pre-cooler ERL is located after the pre-cooler linac.

The design of the pre-cooler transport between the pre-cooler linac and the cooling section is ongoing. Because the electron beam has both a high bunch charge and relatively low energy, the challenge of transporting the bunch from the pre-cooler linac to the cooling section while preserving the emittance is non-trivial.

Presently, no cooling solution exists for 41 GeV protons; the current concept is to add an additional cryomodule to the pre-cooler linac to increase the electron beam energy to 22 MeV, and use bunched beam cooling with the pre-cooler at this higher energy. Consequently, we have included enough space after the pre-cooler linac to add an additional cryomodule.

CONCLUSION

An initial closed design for the 55 MeV SHC-ERL has been completed, and no show stoppers have been identified; the completion of a closed design for the 150 MeV SHC-ERL is expected in the near future. Efforts will continue

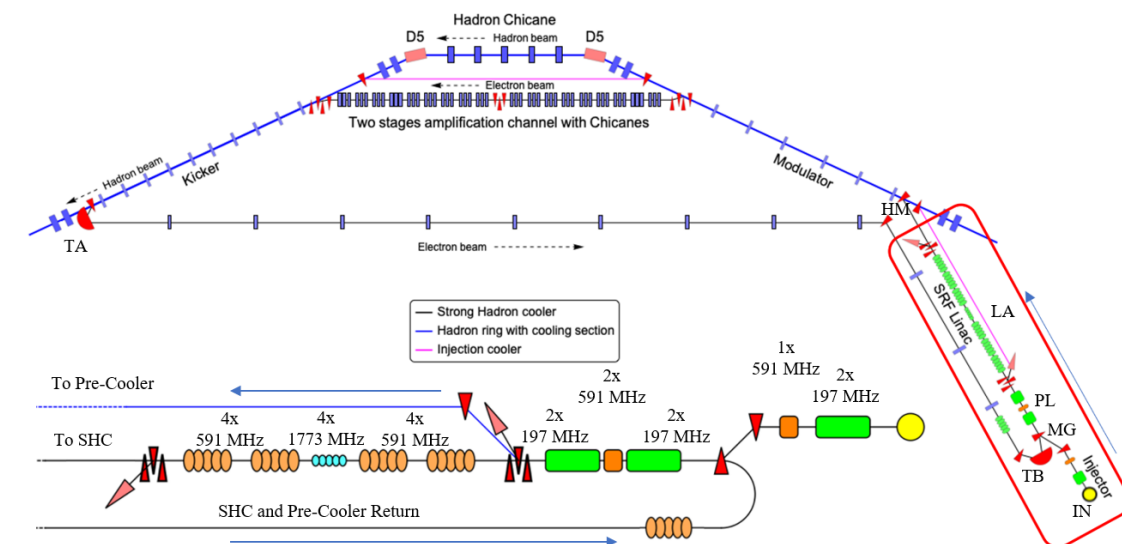


Figure 2: (Top) A conceptual layout of the cooling complex in IR2. At the bottom right, the shared injector and pre-cooler linac separate into two distinct transport lines to the HSR (shown at the top), one for the Pre-cooler and one for the SHC. Both lines merge with the HSR, demerging to take different paths in the center to bypass the hadron chicane, before both once again merge with the hadron line. A common return line is used in both paradigms to demerge with the HSR and return to energy recover. The red box indicates the area on this figure that is shown at greater size below the legend box. (Bottom) A conceptual layout of a portion of the two ERL coolers corresponding to the red box in the top diagram. Represented is the injector, followed by the merger, the pre-cooler linac, the extraction to the pre-cooler transport to the cooler for the pre-cooler (top line) and the bunch compressor for the SHC, the main linac of the SHC, the SHC dump, SHC transport to the cooler (center line) and the shared return line from the cooler (bottom line).

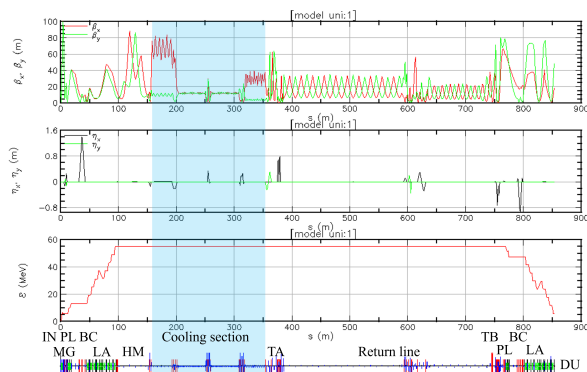


Figure 3: The preliminary design of the 55 MeV electron cooler. Shown are the beta functions in meters (top), dispersion in meters (center), and beam energy (bottom), all as a function of s in meters. Below the three plots is the component layout, with the various sections labeled.

to mature the design while accommodating the design constraints required by the incorporation of the Pre-Cooler ERL and performing additional studies of the SHC-ERL beam dynamics and collective effects.

ACKNOWLEDGEMENTS

This work is supported by Jefferson Science Associates, LLC under U.S. DOE Contract DE-AC05-06OR23177 and Brookhaven Science Associates, LLC, Contract DE-

SC0012704, while Xelera was supported by the U.S. DOE Small Business Innovation Research (SBIR) Phase II program under Federal Grant Number DE-SC0020514 during earlier stages of this work.

REFERENCES

- [1] C. Montag *et al.*, “Design status of the Electron-Ion Collider”, in *Proc. IPAC’23*, Venice, Italy, May 2023, pp. 136-139. doi: 10.18429/JACoW-IPAC2023-MOPA049
- [2] A.V. Fedotov *et al.*, “Accelerator Physics Design Requirements and Challenges of RF Based Electron Cooler LEReC”, in *Proc. NAPAC2016*, Chicago, IL, USA, Oct. 2016, paper WEA4C005, pp. 867–869. doi: 10.18429/JACoW-NAPAC2016-WEA4C005
- [3] A.V. Fedotov *et al.*, “Experience and Challenges with Electron Cooling of Colliding Ion Beams in RHIC”, in *Proc. NAPAC’22*, Albuquerque, NM, USA, Aug. 2022, pp. 325–328. doi: 10.18429/JACoW-NAPAC2022-TUZD5
- [4] V.N. Litvinenko and Y.S. Derbenev, “Coherent electron cooling”, *Phys. Rev. Lett.*, vol. 102, p. 114801, 2009. doi: 10.1103/PhysRevLett.102.114801
- [5] E. Wang *et al.*, “The Accelerator Design Progress for EIC Strong Hadron Cooling”, in *Proc. IPAC’21*, Campinas, SP, Brazil, May 2021, pp. 1424–1427. doi: 10.18429/JACoW-IPAC2021-TUPAB036
- [6] E. Wang *et al.*, “Electron Ion Collider Strong Hadron Cooling Injector and ERL”, in *Proc. LINAC’22*, Liverpool, UK, Aug.-Sep. 2022, pp. 7–12. doi: 10.18429/JACoW-LINAC2022-M02AA04

- [7] W.F. Bergan *et al.*, “Design of an MBEC Cooler for the EIC”, in *Proc. IPAC’21*, Campinas, SP, Brazil, May 2021, pp. 1819–1822.
doi:10.18429/JACoW-IPAC2021-TUPAB179
- [8] C. Gulliford *et al.*, “Design and optimization of an ERL for cooling EIC hadron beams”, in *Proc. IPAC’23*, Venice, Italy, May 2023, pp. 73-76.
doi:10.18429/JACoW-IPAC2023-MOPA016
- [9] D. Sagan, “Bmad: A relativistic charged particle simulation library”, *Nuc. Instrum. Methods Phys. Res., Sect. A*, vol. 558, no. 1, pp. 356–359, 2006.
doi:10.1016/j.nima.2005.11.001
- [10] Z. Huang *et al.*, “Measurements of the linac coherent light source laser heater and its impact on the x-ray free-electron laser performance”, *Phys. Rev. ST Accel. Beams*, vol. 13, no. 2, p. 020703, 2010.
doi:10.1103/PhysRevSTAB.13.020703

SIMULATION STUDY OF A MULTI-STAGE RECTILINEAR CHANNEL FOR MUON COOLING

R. H. Zhu^{1*}, J. C. Yang, H. Zhao

Institute of Modern Physics, Chinese Academy of Sciences, Lanzhou, China

C. T. Rogers, Rutherford Appleton Laboratory, Didcot, United Kingdom

¹also at University of Chinese Academy of Sciences, Beijing, China

Abstract

The muon collider has the potential to be a powerful tool for the exploration of frontiers in particle physics. In order to reach the high luminosity, the 6D emittance of the muon beam needs to be reduced by several orders of magnitude. Ionization cooling, which has recently been demonstrated in 4D by the Muon Ionization Cooling Experiment (MICE), is a promising cooling method for the muon beam. In the future, muon production and 6D ionization cooling experiments are planned at the High Intensity Accelerator Facility (HIAF) at the Institute of Modern Physics, Chinese Academy of Sciences (IMP, CAS). In this paper, a multi-stage rectilinear 6D ionization cooling channel is developed and the cooling simulation results using G4Beamline are presented, indicating good performance for muon beams with large emittance. This work serves as a good starting point for future research at HIAF.

INTRODUCITON

Electron (e+e-) colliders have many advantages over hadron colliders mainly because they produce much cleaner and simpler collision events, allowing physicists to analyze the resulting particles more easily. However, the multi-TeV collision energy is hard to achieve for (e+e-) colliders due to the small mass of the electron which will lead to the significant radiative energy loss. Muons have much larger mass compared with electrons which makes them almost not affected by the synchrotron radiation. Meanwhile, muons also have electron like nature, thus it seems wiser and more cost effective to choose muon colliders for high-energy physics study [1].

One technical challenge for the muon collider is that the muon beam emittance from the pion decay is too large which significantly exceeds the acceptance of the downstream accelerator parts and a dedicated cooling channel is needed to shrink the beam volume space [2]. A conceptual rectilinear cooling channel containing 12 stages has been designed during the MAP (muon accelerator program) project. Its basic idea is using stronger focus for the later stage to achieve better transverse cooling and tilting the solenoid coils to generate dispersion for longitudinal cooling. However, tilting the solenoid might have technical issues. So, using extra dipole magnet for dispersion generation might be a better choice. Here we present a multi-stage rectilinear cooling channel design with additional dipole magnets which shows

a better cooling performance compared with the design of previous studies and this conceptual design of rectilinear cooling channel would be a preparation work for the muon cooling experiments at HIAF [3] in the future, as shown in Fig. 1.

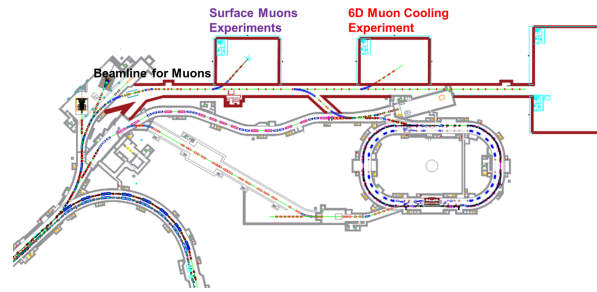


Figure 1: Muon Experiments Planned at HIAF.

DESCRIPTION OF RECTILINEAR COOLING LATTICE DESIGN

Formulas of Ionization Cooling

Ionization cooling involves muon beams losing both transverse and longitudinal momentum by the ionization of the atoms in the absorber material. The longitudinal momentum will get compensated in the RF cavities and the transverse momentum will not. Thus the momentum of the muons is more parallel and the emittance is reduced. The emittance evolution neglecting energy straggling is described as [4]:

$$\frac{d\epsilon_n}{ds} = -\frac{1}{\beta^2} \frac{dE_\mu}{ds} \frac{\epsilon_n}{E_\mu} + \frac{1}{\beta^3} \frac{\beta_T (13.6 \text{ MeV})^2}{2E_\mu m_\mu c^2 L_R} \quad (1)$$

where ϵ_n is the normalized transverse emittance, E_μ is the muon beam energy in GeV, m_μ is the muon mass, β is the muon particle velocity, c is the speed of light, β_T is the transverse beta value, dE_μ/ds is the energy loss per unit length and L_R is the radiation length of absorber material. The first part of this equation can be regarded as cooling term and the second heating term. The equilibrium transverse emittance is defined when dE_μ/ds in Eq.(1) is 0 [4]:

$$\epsilon_{n,eq} = \frac{\beta_T (13.6 \text{ MeV})^2}{2\beta m_\mu c^2 L_R \left| \frac{dE_\mu}{ds} \right|} \quad (2)$$

It can be easily seen from the Eq. (2) that, to reach a lower equilibrium transverse emittance, the focusing at the

* zhuruihu@impcas.ac.cn

absorber should be tight (smaller transverse beta value) and the absorber material should have a large product of L_R and $|\frac{dE_\mu}{ds}|$ (e.g., liquid hydrogen and lithium hydride).

For the longitudinal ionization cooling, dispersion is needed at the absorber and a wedge-shaped absorber can be used. The dispersion will spread the beam transversely so that particles with higher momentum go through a thicker part of the absorber and lose more energy leading to the reduction of the longitudinal emittance.

Optics Design of Rectilinear Cooling Lattice

Transverse beta value, dynamic aperture and dispersion are three important factors in rectilinear cooling channel design. Transverse beta value represents the focusing strength of the solenoid and evolves as [5]:

$$2\beta_T\beta_T'' - \beta_T'^2 + 4\beta_T^2k^2 - 4(1 + L^2) = 0 \quad (3)$$

where L is the normalized canonical angular momentum and k is the solenoid focusing strength,

$$k = \frac{qcB_z(z, r = 0)}{2p_z} \quad (4)$$

Assuming $L = 0$, one can solve Eq.(3) periodically to obtain the beta values in the rectilinear cooling channel. Phase advance is defined as:

$$\phi = \int \frac{1}{\beta_T} dz \quad (5)$$

Phase advance is closely related to the dynamical aperture and it must avoid the resonance which can cause serious particle loss.

The dispersion is important for the longitudinal cooling and can be obtained from the difference of closed orbit in different energies as:

$$D_x = \frac{\delta x}{\delta p} \quad (6)$$

where δx is the difference of the closed orbit relative to the reference particle and δp is the difference of the z -momentum relative to the reference particle.

Once the transverse beta value, dynamic aperture and dispersion are decided, then one can start the cooling simulation by choosing the suitable RF and wedge parameters.

Layout of Rectilinear Cooling Lattice

The basic lattice layout of one cell used in this paper is shown in Fig. 2 which closely follows Stratakis design [6] but using the additional dipole magnets for the longitudinal cooling as tilting the solenoids might have some technical issues.

The whole cooling channel consists of 5 stages and each stage includes repeated cells. The cell length will gradually reduce for stronger focusing at the wedge absorber in order to achieve smaller emittance. Main parameters of the cooling cell in each stage are listed in Table 1. Fringe field of dipole magnets is considered as well and for now a simple quadratic

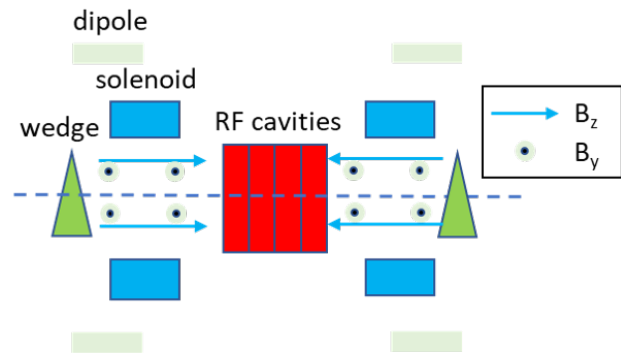


Figure 2: Layout of One Cooling Cell.

function is used to describe the fringe. The absorber material in all stages is liquid hydrogen (LH_2) and 100 μm Be safety window is used.

ANALYSIS OF SIMULATION RESULTS

As can be seen from Table 1, the transverse beta value drops gradually from 35 cm to 10 cm. The reason for choosing a large beta value at the early stage is to keep the dynamic aperture high. The on-axis length of the wedge absorber is always close to the beta value at the position of the wedge (3~5 cm longer). During the simulation, we also find that some high mean z -momentum (~ 220 MeV) of the beam will cause very bad cooling performance, so it's crucial to keep the mean z -momentum at a reasonable range (200~210 MeV) and this can be done by changing the length of the wedge absorber. The dispersion and wedge apex angle influence the longitudinal cooling greatly and their values are decided empirically trying to reach a best balance between longitudinal cooling and transverse heating. Meanwhile, the RF settings also matter especially the RF phase which can not be too large otherwise instability in beam longitudinal motion will occur.

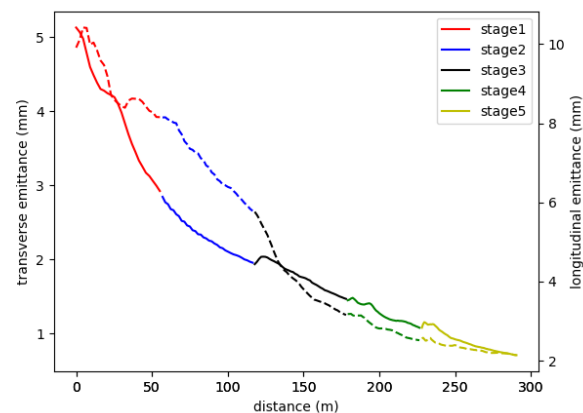


Figure 3: Emittance Evolution in the Cooling Channel (solid line: transverse emittance, dashed line: longitudinal emittance).

Table 1: Parameters of Cooling Cells in Each Stage

	Stage 1	Stage 2	Stage 3	Stage 4	Stage 5
Cell length (m)	2.3	1.8	1.4	1.1	0.8
$B_{z,max}$ (T)	3.1	4.1	4.8	6.2	8.8
β_T (cm)	35	30	20	15	10
B_y (T)	0.3	0.375	0.425	0.45	0.35
Dispersion (cm)	5	5	4.5	2.5	1.8
On-axis wedge length (cm)	37	32	24	20	12
Wedge apex angle	110°	120°	115°	110°	120°
RF frequency (MHz)	325	325	325	325	650
RF #	6	6	6	4	4
RF length (cm)	22	17.7	12	14.6	11.6
RF gradient (MV/m)	22	21.4	24.3	22.9	21.1
RF phase	27.7°	29.8°	27.9°	32°	28.3°

Similar to the previous study, we use the beam after bunch merging as the input instead of an idea Gaussian distribution. G4Beamline-3.08 [7] is adopted as the simulation tool and the reference particle is allowed to lose energy in the absorber and affected by the electromagnetic field so it travels with the whole beam. G4Beamline is based on Geant4 so it has all physics libraries of Geant4 and we choose the QGSP_BERT_EMX which includes all relevant process between the muons and the wedge material.

The emittance evolution and the initial and final beam distribution are plotted in Fig. 3 and Fig. 4. The emittance and transmission at the end of each stage are listed in Table 2. After passing through the rectilinear cooling channel which is about 290 m long, both the transverse and longitudinal emittance of initial muon beam get substantial reduction (transverse: 5.13 to 0.71 mm, longitudinal: 9.91 to 2.14 mm) with an overall transmission of 57.5 % including decay. There is a sudden rise in transverse and longitudinal emittance at the junction between two different stages which can be explained by the mismatching of the beta value and the rise can be limited by a soft reduction of beta value for each stage. Compared with the cooling performance at the end of stage 5 (transverse emittance: 0.68 mm, longitudinal emittance: 2.97 mm) from Ref. [6], we find the design of this paper has a smaller longitudinal emittance and a slightly larger transverse emittance and the length of the channel is reduced by 46 m.

Table 2: Emittance and Transmission at the End of Each Stage

	ϵ_T (mm)	ϵ_L (mm)	ϵ_{6D} (mm ³)	T (%)
Initial	5.13	9.91	260	
Stage 1	2.92	8.16	71.6	87.1
Stage 2	1.96	5.78	22.6	91.2
Stage 3	1.47	3.16	7.12	88
Stage 4	1.08	2.52	3.11	92.2
Stage 5	0.71	2.14	1.14	89.2

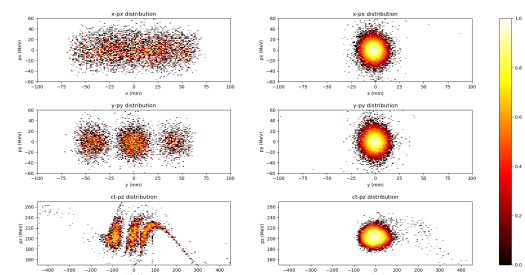


Figure 4: Beam Distribution at the Start and End of Cooling Channel (left column: start, right column: end).

CONCLUSION AND OUTLOOK

The 6D muon cooling scheme is essential for a muon collider. We have presented a 5-stage rectilinear cooling channel design with additional dipole magnets which shows a better performance than previous study. In the future, we will extend the cooling channel to more stages and check the limit of the cooling emittance. Meanwhile, we will explore the collective effects (e.g., space charge, short-range wakefield) in muon cooling by adding new modules in G4Beamline.

ACKNOWLEDGEMENTS

The authors would like to thank J. S. Berg, E. Fol and many other people from IMCC working groups for lots of fruitful discussions.

REFERENCES

- [1] C. Accettura *et al.*, “Towards a Muon Collider”, *arXiv preprint*, 2023. doi:10.48550/arXiv.2303.08533
- [2] M. Bogomilov *et al.*, “Demonstration of cooling by the Muon Ionization Cooling Experiment”, *Nature*, vol. 578, pp. 53–59, 2020. doi:10.1038/s41586-020-1958-9
- [3] J. C. Yang, *et al.*, “High Intensity heavy ion Accelerator Facility (HIAF) in China”, *Nucl. Instrum. Meth. B*, vol. 317, pp. 263–265, 2013. doi:10.1016/j.nimb.2013.08.046

- [4] D. Neuffer, “Introduction to muon cooling”, *Nucl. Instrum. Meth. A*, vol. 532, no. 1, pp. 26–31, 2004.
doi:10.1016/j.nima.2004.06.051
- [5] G. Franchetti, “Linear beam optics in solenoidal channels”, *Phys. Rev. ST Accel. Beams*, vol. 4, p. 074001, 2004.
doi:10.1103/PhysRevSTAB.4.074001
- [6] D. Stratakis and R. B. Palmer, “Rectilinear six-dimensional ionization cooling channel for a muon collider: A theoretical and numerical study”, *Phys. Rev. ST Accel. Beams*, vol. 18, p. 031003, 2015. doi:10.1103/PhysRevSTAB.18.031003
- [7] T. J. Roberts and D. M. Kaplan, “G4Beamline Simulation Program for Matter-dominated Beamlines”, in *Proc. PAC’07*, Albuquerque, NM, USA, Jun. 2007, paper THPAN103, pp. 3468–3470. doi:10.1109/PAC.2007.4440461

Content from this work may be used under the terms of the CC-BY-4.0 licence (© 2023). Any distribution of this work must maintain attribution to the author(s), title of the work, publisher, and DOI

BEAM MEASUREMENTS OF A PALMER PICK-UP FOR THE COLLECTOR RING OF FAIR

C. Peschke*, R. Böhm, C. Dimopoulou, S. Wunderlich, C. Zhang, GSI, Darmstadt, Germany

Abstract

The stochastic cooling system of the Collector Ring (CR) of the future FAIR facility will have three pick-up (PU) tanks and two kicker tanks. For the pre-cooling of very hot RIBs, a pick-up tank with eight Faltin-type structures for Palmer-cooling has been constructed by GSI. The structures have been designed using High-Frequency Structure Simulator (HFSS).

The Palmer PU tank has been tested with $\beta = 0.83$ proton beams at the Cooler Synchrotron (COSY) of the FZJ. This publication presents the results of measurements with beam and compare them with simulations (HFSS and Microwave Studio).

The pick-up operates at room temperature. But it has artificial cold loads instead of normal terminators. The results of the noise temperature measurements are also be presented.

PALMER PICK-UP

For very hot rare isotope beams, the distance from the slotline pick-ups to the kickers is too large. The undesired mixing prevents cooling. Therefore a Palmer pick-up with smaller distance to the kicker permits an high acceptance for the start of the cooling cycle.

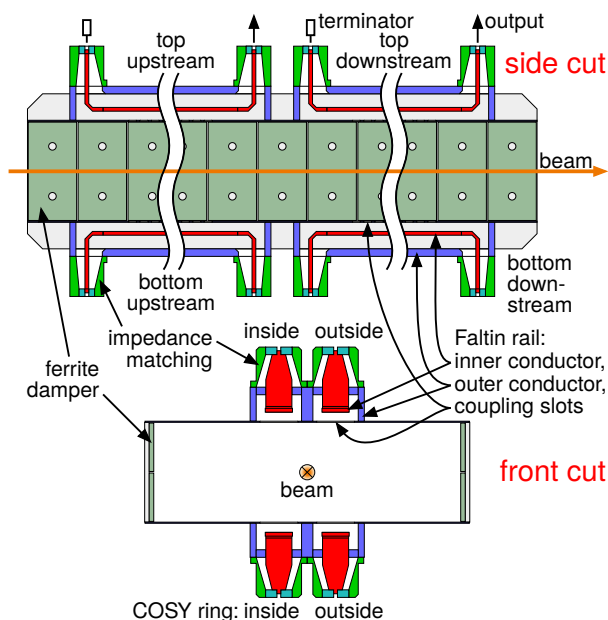


Figure 1: Layout of the Palmer pick-up tank.

Figure 1 shows the schematic layout inside the palmer pick-up tank. It uses Faltin type structures for coupling and

* C.Peschke@gsi.de

has been developed using HFSS FEM field calculation program [1]. Faltin rails show an high dispersion. To archive an octave bandwidth the four long rails of the Palmer arrangement, the rails are divided into identical upstream and downstream parts. A lot of ferrite material (Ferroxcube 4S60) has been installed to damp undesired wave modes. The dampers are on the side walls, far from the coupling slots, to avoid reduction of the shunt impedance.

MEASUREMENT SETUP

To verify the design performance, the CR Palmer pick-up tank has been installed in the COSY ring, as shown in Fig. 2. We have used stored proton beams for our experiment. The beams were weakly bunched to allow the beam position monitors (BPM) to work. Table 1 shows the parameters typically used here.

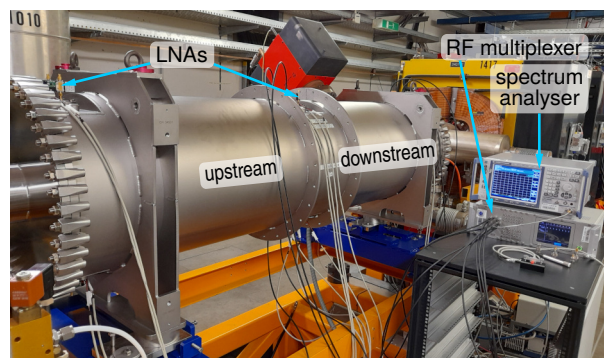


Figure 2: CR Palmer pick-up tank installed in COSY ring.

Table 1: Typical Beam Parameters

velocity factor	$\beta = 0.830$
number of protons (measured for each run)	$N = 1.7 \cdot 10^{10}$
beam dimensions	$\Delta x = 5.3 \text{ mm}$ $\Delta y = 3.9 \text{ mm}$
dispersion at Palmer-PU	$D = 0 \text{ m}$
RMS momentum spread	$\Delta p/p = 2.2 \cdot 10^{-4}$

For the measurements, the tank has been equipped with all eight Faltin rails and the low noise amplifiers (LNAs), but without the subsequent Palmer signal processing. Figure 3 shows a block diagram of the measurement setup.

To prevent additional noise from cable damping, the low noise amplifiers (LNAs) were installed directly on the vacuum feedthroughs. The LNAs at the outputs of the Faltin rails were used as normal amplifiers for the Schottky signals.

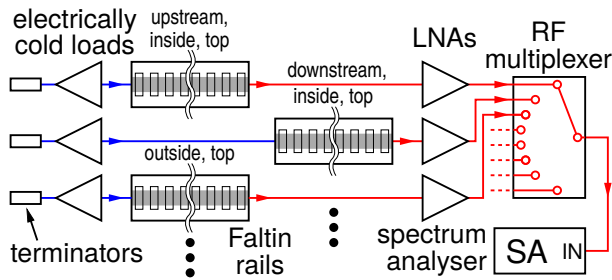


Figure 3: Measurement setup.

The inputs of the Faltin rails have to be terminated, normally by resistors. Instead of this, we have terminated it by inputs of additional LNAs. The noise power density dP/df of a normal resistor as terminator is the product of the Boltzmann constant k_B and the absolute temperature T . Due to the second law of thermodynamics this is true for passive devices. An active circuit can behave like a noise source with different noise power density. Due to the internal negative feedback, the input of an LNA can behave like a noise source with much lower noise power density [2]. The installed LNAs (Miteq AFS3-01000200-07-10P-GW-APM) have a specified noise figure $NF \leq 0.7$ dB. The measured values are 0.4 to 0.65 dB in the frequency range 1 to 2 GHz. This corresponds to a noise temperature of 28 to 47 K.

A remote controlled RF multiplexer selects measurement signal from the main control room. The spectrum analyzer (Rohde & Schwarz FSV) is also remote controlled.

MEASUREMENT AND DATA ANALYSIS

We have tested the pick-up with different beam positions and some β -variations. For each beam setup and each Faltin rail we have recorded 220 spectrum sweeps with center frequencies from 0.3 to 2.3 GHz at harmonics of revolution frequency. Table 2 shows the parameters.

Table 2: Spectrum Analyzer Parameters

sweep span	1.5 MHz
points	1001
resolution bandwidth	10 Hz
video bandwidth	20 Hz
detector	RMS

The raw data are a composition of characteristics of the pick-up and measurement setup. We have removed the errors from the frequency depending damping and gain of most RF components. Errors due to reflections are not considered.

The gain curves of the LNAs have been measured for each individual device. For the cable from the amplifiers to the RF multiplexer (3 m Suhner SX04272D-02) we have considered a measured attenuation curve of a typical cable. For the cable from RF multiplexer to spectrum analyzer (50 cm Semi-Flex .141) we have assumed the attenuation curve from data sheet. For the transmission path of the multiplexer together with both cables we have measured the attenuation at 1 GHz using

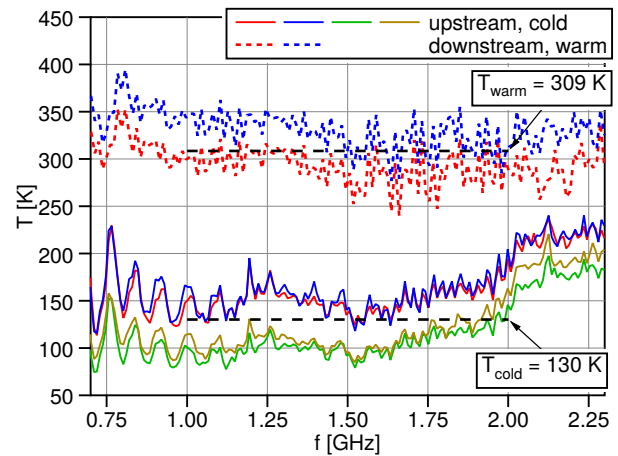


Figure 4: Noise temperatures.

a power meter (Rohde & Schwarz NRX with test generator option NRX-B1 and power sensor NRP18S).

The power per point values from the spectrum analyzer have been translated into spectral power densities. The filter response of spectrum analyzer has been checked with the test generator. The power density curves are a composition of noise and Schottky signals.

To get the frequency dependent noise temperature we have calculated the mean spectral power density without the main and side peaks of Schottky signal. Divided by k_B this is the temperature of a normal resistive terminator at the input of a noise free amplifier. This means, the noise of the LNA at output is included in the calculated noise temperature.

For the shunt impedance calculation we have subtracted the mean noise around each harmonic. The integral over the main and side peaks gives the line power P_{line} . The longitudinal shunt impedance $R_{||}$ in circuit convention for N protons (q_e) circulating with revolution frequency f_{rev} is

$$R_{||} = \frac{P_{line}}{2 \cdot N \cdot (q_e \cdot f_{rev})^2}. \quad (1)$$

ELECTRODYNAMIC FEM CALCULATION

We have made simulations using MicroWave Studio (MWS). The pick-up has been simulated as kicker in time domain with subsequent FFT. For arbitrary beam positions we used the full geometry. The model includes the impedance matching cones but not the ferrite dampers. For cross checking we also have made a simple quarter structure HFSS calculation in frequency domain without the matching cones.

RESULTS

To test the efficiency of the artificial cold terminators, we had installed LNAs at the inputs of the four upstream Faltin rails and normal passive terminators at the two top side downstream rails. The rails at the bottom side had a problem which could not be fixed quickly. Figure 4 shows the results of these measurements.

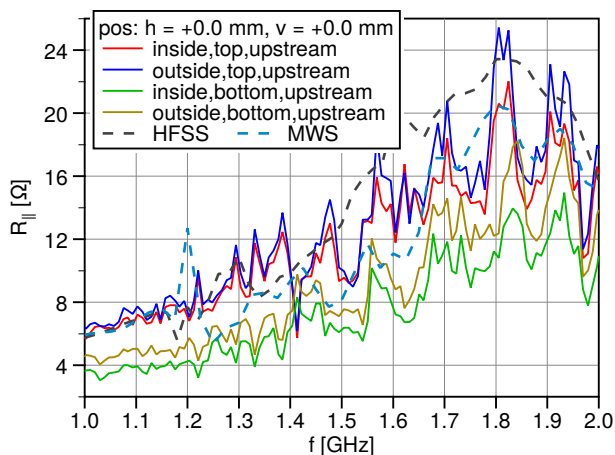


Figure 5: Shunt impedance with beam on axis.

The mean noise temperature of the four artificial cold rails in our frequency range is 130 K. This has been achieved with all components at room temperature. The contribution of the LNAs at the inputs and outputs is approximately between 56 to 94 K. The remaining noise is from losses of the Faltn rails, matching, and feedthroughs. As expected, the normally terminated rails have a noise temperature above the room temperature.

To test the pick-up and to verify the calculations, we have made single rail measurements with different beam positions and β -variations. All values are longitudinal pick-up shunt impedances in circuit convention. The shunt impedance values of the whole tank would be 8 times these values. The Palmer mode is not part of this publication. Figure 5 shows the measurements with beam on axis compared with HFSS and MWS calculations. There is a good agreement with MWS and a reasonable agreement with the simpler HFSS calculation. No electrical adjustments has been done. Therefore, a beam on mechanical axis is not exactly on electrical axis.

Figure 6 shows the results for some of the measurements with beam off axis. The measurements also have a good agreement with MWS. Finally, Fig. 7 shows results from β variation. From the point of magnitude, the PU is still usable for these β values, but phase could not be measured.

CONCLUSION

The CR Palmer pick-up for FAIR has been tested successfully in the COSY at the FZJ. The presented measurement results show a good agreement with simulations. The active artificial cold loads work as expected.

ACKNOWLEDGEMENT

The authors thank the COSY team for the good prepared and smooth-running beam time, and especially Nikolay Shurkhno for his helpful and agile data acquisition software.

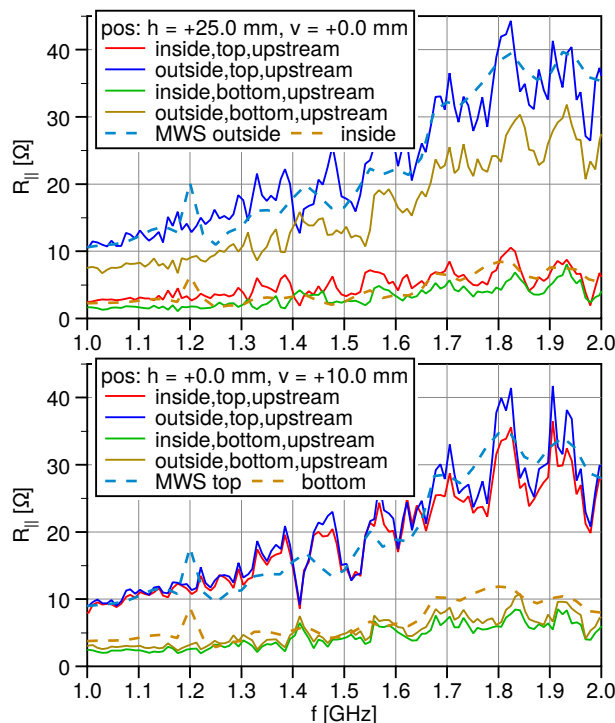


Figure 6: Shunt impedance with beam off axis.

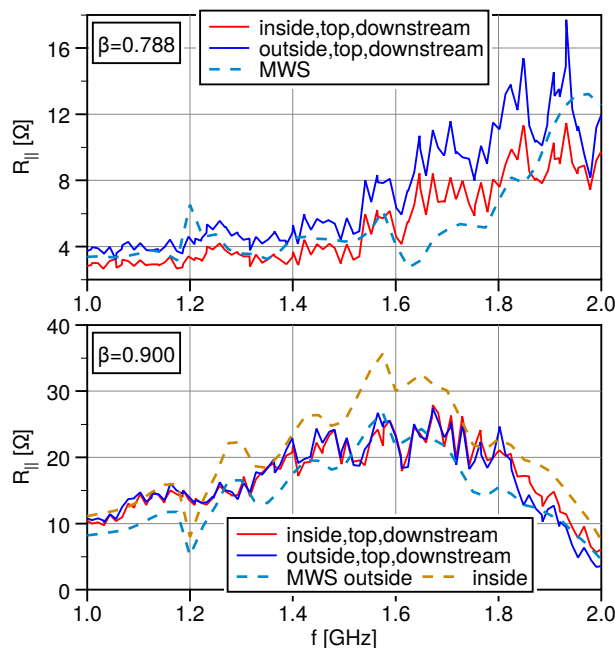


Figure 7: Shunt impedance with β variation.

REFERENCES

- [1] D. Barker, C. Dimopoulou, C. Peschke, and L. Thorndahl, "Design of the Palmer Pickup for Stochastic Pre-Cooling of Hot Rare Isotopes at the CR", in *Proc. COOL'15*, Newport News, VA, USA, Sep.-Oct. 2015, paper FRWAUD03, pp. 175–178.
- [2] R. H. Frater and D.R. Williams, "An Active 'Cold' Noise Source", *IEEE Trans. Microwave Theory Tech.*, vol. 29, no. 4, pp. 344–347, 1981. doi:10.1109/TMTT.1981.1130355

HOW TO ADJUST STOCHASTIC COOLING SYSTEMS

N. Shurkhno[†], GSI, Darmstadt, Germany

Abstract

The paper summarizes techniques and algorithms for adjustment of stochastic cooling systems, that have been developed and tested at the COSY accelerator facility (FZ Jülich, Germany). An overall goal was to automate typical time-consuming manual adjustment routines. As a result, a set of algorithms based on a theoretical description of the stochastic cooling process has been developed, which allows accurate and fast automatic adjustment of main system's parameters. The methods have been elaborated and used at COSY during development and testing of stochastic cooling systems for HESR and are planned for further use at the FAIR accelerator complex (GSI, Germany). The methods are quite universal and can be applied or adapted to any similar system.

INTRODUCTION

In a broad sense, an adjustment of a stochastic cooling system is bringing its broadband frequency response to its instantaneous optimum, so that it would provide the fastest cooling at a given moment of time. From a hardware point of view, common parameters for adjustment are system gain and delay and optionally a comb filter if it is used. System gain and delay control the amplitude and phase slope of the system frequency response respectively. The developed adjustment techniques for both gain and delay are based on calculating the system transfer function from open loop measurements and using it in Focker-Planck or single particle equations to obtain the optimum values, while the comb filter is adjusted iteratively. The system delay and comb filter adjustment algorithms are fully automatic, accurate and robust, providing adjustment time ~ 1 s or less, whereas previous manual adjustment could easily take hours. System gain adjustment on the other hand, is more subtle within the developed approach, allowing simple adjustment only in special cases (negligible hardware noise and IBS, non-resonant BTF), while generally requiring additional measurements and elaboration. The adjustment techniques have been developed and tested at the COSY accelerator facility (FZ Jülich, Germany) as a part of the HESR stochastic cooling systems development (GSI, Germany) [1].

SYSTEM TRANSFER FUNCTION

System transfer function can be estimated or directly calculated from open-loop measurements (OLM), which is a common technique for studying beam and system transfer functions [2, 3]. Open-loop measurements are made by opening the cooling loop to feed the signal from the vector network analyzer in and out (Fig. 1).

To get a broadband frequency response open-loop measurements should be performed at the full system bandwidth. This is done by measuring multiple single Schottky bands in the passband (single band OLM) or by performing

single broadband measurement with VNA sweep points set to the centers of Schottky bands or betatron sidebands (broadband OLM). The single band OLM is very flexible and reliable, it may require some additional processing (e.g., smoothing and correlation with measured particle distribution function). On the other hand, broadband OLM is a single measurement and therefore much faster, but it may produce false results, since it measures only a single point within the Schottky band, which can be influenced, e.g., by a resonance. Also, a combination of methods can be used for cross-checking in an automated setup, preserving measurement speed and identifying possible problems at the same time.

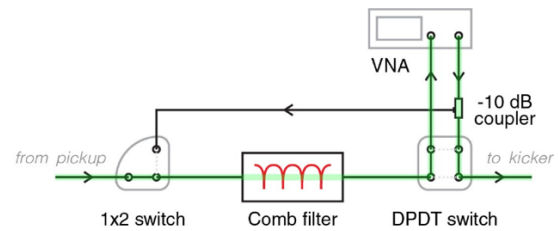


Figure 1: Layout for OLM (green) and comb filter adjustment. To open and close the loop a transfer (DPDT) switch is used, providing the lowest possible insertion delay.

Open-loop measurements produce direct product of beam and system transfer functions, so the latter can be obtained by substituting the BTF in the equation $G(f) = OLM(f)/BTF(f)$, where $G(f)$ and $BTF(f)$ are system and beam transfer functions respectively, f – measurement frequency. Analytical formulas for beam transfer functions are well known and can be found for example in [3, 4].

The overall calculation is reasonably tolerable to measurement uncertainties (beam intensity, particle distribution function, resonances, etc.), since further calculations do not require high accuracy of the system transfer function, as will be discussed later.

The obtained system transfer function is used then for calculating the optimum gain and delay with Fokker-Planck and/or single particle equation in the following form [5]:

$$\frac{dx}{dt} = F(x, t) + \frac{D(x, t)}{x}, \quad (1)$$

where $F(x, t)$ and $D(x, t)$ are drift and diffusion terms (or cooling and heating terms), x is a parameter being cooled.

Single particle equations are often sufficient since we are mostly interested in instantaneous values and not in the cooling evolution.

SYSTEM DELAY ADJUSTMENT

The system delay synchronizes the correction signal with the measured particles. It defines the phase slope of the system transfer function, so a common approach to setting the system delay is to flatten the phase of the OLM and then fine-tune. The delay corresponding to the flattened

phase of the OLM is a good starting point, not an optimum. The frequency response of the system is non-linear, so it is necessary to correlate the phase flatness with the amplitude, which is done then by fine-tuning.

The cooling force F in Eq. (1) is actually based on such a correlation, so it can be used to calculate the optimum delay immediately without fine-tuning. For both longitudinal and transverse cooling forces the following dependence can be written [4]:

$$F \sim f_p \cdot \text{Re} \sum_n \frac{G}{1 - G \cdot \text{BTF}} e^{i2\pi n f_p T_{pk}(f_p)},$$

where f_p – particle frequency, n – harmonic number, T_{pk} – pickup to kicker travel time for particle f_p .

We need to find a delay that will bring a proper zero of the cooling force to a center. Since we are only interested in the positions of the zeros, constant coefficients can be omitted. The actual amplitude is also not needed, only the proportionality, so instead of substituting the real BTF functions, we consider only their amplitude dependence $1/n$. After substitution of the OLM, expansion of T_{pk} and simplification, we obtain the final equation for the cooling force, from which the optimum delay can be easily found:

$$F' = f_p \cdot \text{Re} \sum_n n \cdot \text{OLM} \cdot e^{-i2\pi n f_p T_{pk} \frac{\eta_{pk} f_p - f_0}{\eta f_0}}, \quad (2)$$

where η, η_{pk} – full and pickup to kicker slip-factors.

When the comb filter is used, the open-loop measurements are made with filter's long path opened, so Eq. (2) must be multiplied by the transfer function a comb filter [4], which is also discussed further.

As an example, Fig. 2 shows actual open-loop measurements with calculated optimum and “flat phase” delays, and Fig. 3 shows the corresponding cooling forces, calculated with Eq. (2). The “flat phase” delay is ~ 40.3 ps higher than the optimum resulting in significantly slower cooling.

The developed method for calculating the system delay is universal and proved to be robust and accurate, the adjustment time depends only on the duration of the open-loop measurements and takes up to 1 s when adjusted from scratch, and ~ 100 -200 ms if only fine-tuning needed.

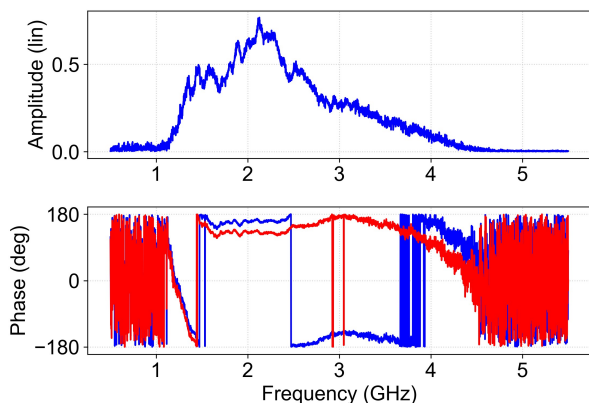


Figure 2: Amplitude and phase of vertical OLM for optimum delay (blue) and flattened phase (red).

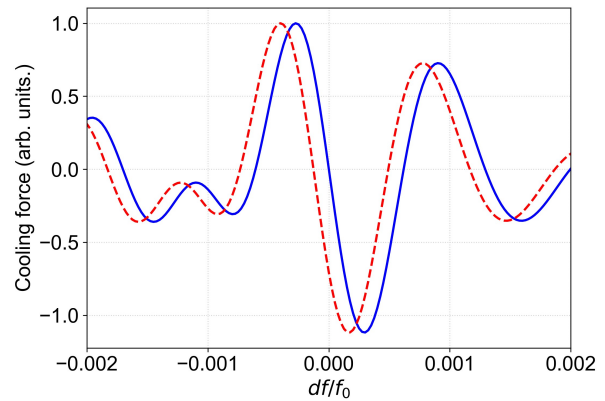


Figure 3: Cooling force calculated with Eq. (2) for optimum delay (blue) and delay, that flattens the phase (red), which differs by ~ 40 ps.

SYSTEM GAIN ADJUSTMENT

The system gain controls the cooling rate and final equilibrium state of the parameter being cooled by balancing the cooling and heating forces. The higher the gain, the faster the cooling and the higher the noise in the system, resulting in a worse final equilibrium state, and vice versa. Thus, we can distinguish the *optimum gain* g_{opt} , which provides fastest instantaneous cooling rate, but worse final state, and the *equilibrium gain* g_{eq} , which provides the smallest final equilibrium, but slower cooling.

The optimum gain is a function of the instantaneous beam state (particle distribution function or betatron amplitudes), and therefore it changes during cooling until the equilibrium gain is reached. Thus, the general strategy for stochastic cooling is to calculate or measure the optimum and equilibrium gains, and then continuously or stepwise change the gain from optimum to equilibrium during cooling. In this way the beam is cooled to the smallest possible final state at the fastest rate (Fig. 4). An optimum time dependence for system gain change from g_{opt} to g_{eq} can be calculated from Fokker-Planck or single particle equations.

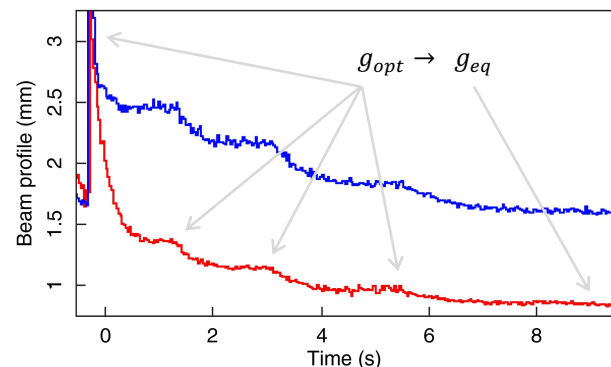


Figure 4: Horizontal (blue) and vertical (red) beam profiles during transverse cooling with stepped gain changing. Each step the gain is reduced by ~ 3 dB.

In many cases, however, it is not necessary or possible to change the gain. It is not necessary to reach the best final equilibrium state, e.g., when the only goal is to counteract heating due to IBS, internal target, or various accelerator

imperfections. The gain is also often limited by the power amplifiers, so g_{opt} or even g_{eq} are not reachable. In all such cases, gain setting is based on the specific task.

Gain calculation and adjustment. The optimum gain can be found from Eq. (1) by calculating the gain value that maximizes the right part. This single particle rate equation is typically calculated for the rms particle, but it can be used for a particle in the core or in the tail of the distribution depending on the goal. The equilibrium gain for betatron cooling in general can also be found from Eq. (1) by calculating the gain that gives the smallest final state x_∞ in steady state ($dx/dt = 0$). During longitudinal cooling the particle distribution evolves, so the Fokker-Planck equation should be used to find the asymptotic equilibrium distribution [3].

Having a simple numerical solution, the task is complicated in real applications because the diffusion coefficient cannot be measured directly. The diffusion is the sum of two components – diffusion due to the Schottky noise D_{Sch} , which is straightforward to calculate, and diffusion due to amplifier and thermal noises D_{th} [3, 4]:

$$D_{th} = \frac{1}{2} f_0^2 k (T_{pu} + T_{amp}) Z_0 \sum_n \left| \frac{G_{cl}}{Z_p} \right|^2,$$

where k – Boltzmann constant, T_{pu} – pick-up temperature, T_{amp} – amplifier noise temperature, Z_p – pick-up transfer function, Z_p – line impedance, $G_{cl} = G/(1 - G \cdot BTF)$.

The temperatures and especially the pick-up transfer function in D_{th} are very tricky to measure for calculations. In some cases, D_{th} is negligible, e.g., when the beam current is high enough, but in general it should be estimated from measurements of cooling times or final equilibrium states. For these measurements we are not interested in either the real noise values or the actual pick-up frequency response, we can replace coefficients and pickup transfer function by the constant average value $\overline{D_{th}}$ and substitute it into Fokker-Planck equation or Eq. (1):

$$\frac{dx}{dt} = F + \frac{D_{Sch}}{x} + \frac{\overline{D_{th}}}{x} \sum_n |G_{cl}|^2.$$

This equation can be used to calculate $\overline{D_{th}}$ after measuring the initial cooling rate at a given system gain. Alternatively or in addition, $\overline{D_{th}}$ can be calculated in the steady state equations after measuring the final equilibrium state. For a more accurate estimate both calculations can be performed at different gains and averaged.

The cooling time in the vicinity of the optimum gain doesn't change much with respect to the gain change within a safety margin of around a few dB (Fig. 5), so the resulting accuracy for adjustment of 1 dB is typically sufficient. This makes the calculations quite tolerant of measurement errors.

The experiments at COSY were carried out with H⁺ and D⁺, where the IBS effect is negligible. But for heavy ions the diffusion due to the IBS should be added. Since it does

not depend on the gain, as a first estimate it could be treated as a constant and calculated in the same way as $\overline{D_{th}}$.

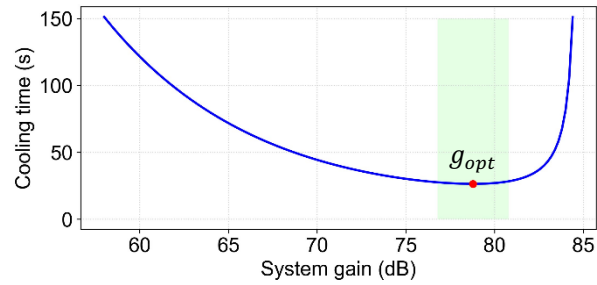


Figure 5: Cooling time as a function of system gain. The safety margin around optimum gain (green) is ± 2 dB, resulting in $\sim 5\%$ slower cooling.

COMB FILTER ADJUSTMENT

A feedforward comb filter [6] is used for longitudinal stochastic cooling (filter method), it can also be used for example in the transverse cooling to filter out the longitudinal signal. The frequency response of such a comb filter represents amplitude notches with phase inverse at each harmonic of the revolution frequency within the filter's passband. There are two main parameters adjusted in the filter – frequency and depth of notches. The notch frequency should be equal to the revolution frequency and is adjusted by setting a delay between filter paths to the revolution period. Notch depth is adjusted by equalizing attenuation in both paths, the deeper the notches (broadband average) the better.

The notch frequency is adjusted iteratively by measuring the current frequency and subsequent delay correction. The notch depth is also adjusted iteratively by varying the attenuation and using a binary search to find the optimum value for a given accuracy. Comb filter adjustment is much simpler than system delay and gain adjustments because it is done without the beam, and the algorithm can be fine-tuned on a test bench. In the end, filter adjustment is fully automatic and fast, taking a few seconds to adjust from scratch and less than a second to fine-tune.

In the operational stochastic cooling system, a simple loop is added for remote filter tuning, as shown in Fig. 1.

Due to dispersion and mismatch in the filter components [7], both the depths and positions of the notches vary within the passband. Therefore, for filter cooling, the distributions of notch positions and depths should be measured and used in the system delay and gain calculations.

SUMMARY

The developed techniques for system gain, system delay, and comb filter adjustments significantly simplified, improved, and sped up the setup of the stochastic cooling systems at COSY. Full adjustment can be done automatically in a few seconds or less if only fine-tuning is required. While the system gain adjustment may require some adaptation to a specific setup and goal, the techniques for the system delay and comb filter adjustments are sufficiently universal to be applied to any similar system.

REFERENCES

- [1] R. Stassen, B. Breikreutz, N. Shurkhno, H. Stockhorst, and L. Thorndahl, “The HESR Stochastic Cooling System, Design, Construction and Test Experiments in COSY”, in *Proc. COOL'17*, Bonn, Germany, Sep. 2017, pp. 89-93. doi:10.18429/JACoW-COOL2017-THA11
- [2] J. Borer *et al.*, “Information from beam response to longitudinal and transverse excitation”, *IEEE Trans. on Nucl. Sci.*, vol. NS-26, no. 3, pp. 3405-3408, June 1979.
- [3] D. Möhl, *Stochastic cooling of particle beams*. Lecture notes in physics, Springer-Verlag Berlin Heidelberg, 2013.
- [4] H. Stockhorst, T. Katayama, and R. Maier, *Beam cooling at COSY and HESR. Theory and simulation – Part 1 Theory*, Forschungszentrum Jülich GmbH, 2016.
- [5] N. Shurkhno, “Stochastic Cooling as Wiener Process”, in *Proc. COOL'17*, Bonn, Germany, Sep. 2017, pp. 37-39. doi:10.18429/JACoW-COOL2017-TUP06
- [6] I. Kadenko *et al.*, “An optical comb filter for the stochastic cooling system at the Nuclotron accelerator”, *Physics of Particles and Nuclei Letters*, vol. 11, no. 5, pp. 705-707, 2014. doi:10.1134/S1547477114050148
- [7] N. Shurkhno and R. Stassen, “Algorithmic control of stochastic cooling systems”, presented at COOL'17, Germany, Sep. 2017, paper THA13, unpublished.

EXPERIENCE WITH BEAM TRANSFER FUNCTION MEASUREMENTS FOR SETTING-UP THE STOCHASTIC COOLING SYSTEM IN THE CERN ANTI-PROTON DECELERATOR (AD)

S. Rey*, W. Höfle†, W. Bastos, F. Caspers, B. Dupuy, D. Gamba, R. Louwse
 CERN, Geneva, Switzerland

Abstract

Beam transfer function measurements have regularly been used to set-up the adjustable parameters for stochastic cooling systems. We report on the automation of these measurements at CERN that permit efficient set-up of the cooling loops in the anti-proton decelerator (AD) and enables insight into the bandwidth (nominal frequency range of 850 MHz to 1.7 GHz) of the overall system for the longitudinal, horizontal and vertical cooling at the two different beam momenta of 2 GeV/c and 3.57 GeV/c. Additionally, data collected during machine development sessions can be used to identify areas of improvement and will be indispensable in defining the planned path for consolidation and upgrade of the system. For example, it allows the comparison of the bandwidth with the computed shunt impedance of the currently used kickers. The unwanted crosstalk between the three different planes of cooling is also evaluated and will help to define improvements in the system for the future.

INTRODUCTION

Stochastic cooling is currently used in the CERN Anti-proton Decelerator (AD) at two different beam momenta of 2 GeV/c and 3.57 GeV/c [1]. Anti-protons are routinely decelerated since 1999 [2] and since the start-up after long-shutdown 2 (LS2) exclusively provided for further deceleration to the new ELENA decelerator [3]. The transfer momentum to Elena is 100 MeV/c with electron cooling used at two further momentum plateaus in AD at 300 MeV/c and 100 MeV/c.

In the framework of increasing the efficiency and set-up time of the stochastic cooling system in AD it was highly desirable to conceive an automated beam transfer function measurement that could go beyond the normal setting-up, but also be used for diagnosis during the run, and to probe the efficacy and available bandwidth of the existing systems that operate in all three planes at the two beam momenta. The data collected during such measurements helps to define upgrades required in view of future operation, also possibly with the stochastic cooling used at a lower momenta.

OVERVIEW OF AD STOCHASTIC COOLING SYSTEM AND BEAMS

The stochastic cooling system in AD comprises four elements in the ring: horizontal pick-up UHM 3107, horizontal kicker KHM 0307, vertical pick-up UVM 3207 and vertical

kicker KVM 0407 [1]. The longitudinal cooling is obtained using the same pick-ups and kickers in their common mode combining both signals from the horizontal and vertical pick-ups and splitting on the back-end the signal to feed both the horizontal and vertical kickers through notch filters.

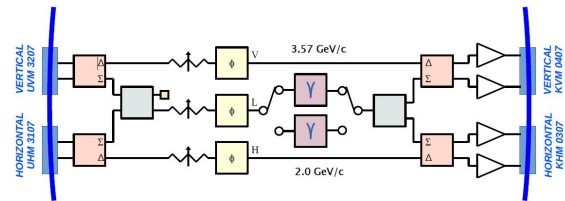


Figure 1: AD Stochastic Cooling Overview.

Layout and Optics for Stochastic Cooling at 2 GeV/c and 3.57 GeV/c

The two pairs of pick-up and and kicker are installed in locations opposing each other in the ring. For a ring circumference of 182.433 m the beam orbit length between pick-up to kicker and kicker to pick-up amounts to between 91.21 m to 91.22 m in length rounded to centimeters for nominal momentum. For the two cooling plateaus (2 GeV/c and

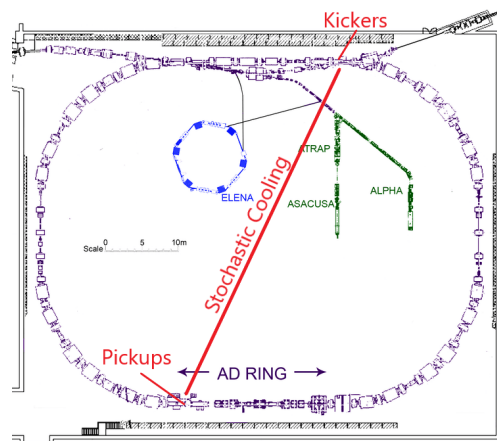


Figure 2: AD Stochastic Cooling.

3.57 GeV/c) the beam β equals 0.90532 and 0.96724, respectively, giving time of flights of ~ 336.1 ns and ~ 314.6 ns. The time of flight difference of ~ 21.5 ns must be properly compensated when switching between the two plateaus. Implementation of the switching is by means of RF relays controlled by a PLC system and with the total delay difference split into several parts located along the signal chain. The pick-ups have only one feed-through per side with internal delays being adjusted for 3.57 GeV/c, while the kicker

* stephane.franck.rey@cern.ch

† wolfgang.hofle@cern.ch

has individual feed-throughs for the twelve amplifiers per side permitting a better adjustment of the delay difference between the two different plateaus.

Table 1 shows the values for the transverse tune and phase advances from pick-up to kicker. Phase advances deviate by

Table 1: Optics Parameters Transverse Cooling in AD

horizontal tune Q_H	5.385
Phase advance from H pickup to H kicker	256°
vertical tune Q_V	5.369
Phase advance from V pickup to V kicker	283°

less than 20° from the optimum value for transverse cooling. In an open loop beam transfer measurement this deviation will be visible in a Nyquist plot as a rotation of the circles corresponding to the lower and upper betatron side bands in the opposite sense [4].

Optical Delay Line Notch Filter

The notch filter is actually a comb filter structure as given in Figure 3. The output signal of such a structure in time

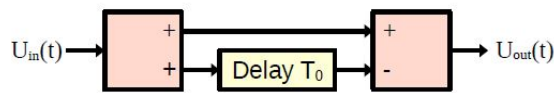


Figure 3: Comb filter principle.

domain is given by:

$$U_{out}(t) = \frac{1}{2} (U_{in}(t) - U_{in}(t - T_0)) \quad (1)$$

A Fourier transform performed on equation (1), modified to take into the account attenuation difference of long and short branch, gives the following transfer function:

$$H(\omega) = \frac{1}{1+a} (1 - a \cdot e^{-j2\pi\omega/\omega_0}) \quad (2)$$

where a characterizes the additional attenuation factor of

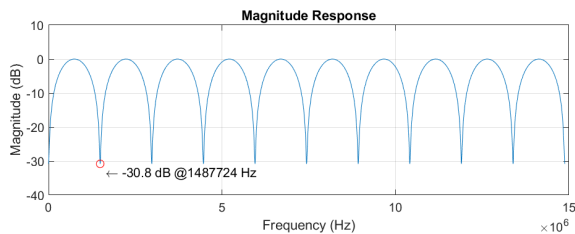


Figure 4: Simulated Comb filter magnitude @ 2.0 GeV/c.

the long branch with respect to the short branch. The notch depth in dB is $20 \log_{10}((1-a)/(1+a))$. Figures 4 & 5 show ideal magnitude and phase for a filter with no delay in the short branch. The principle of periodic filters for stochastic cooling was invented at CERN [5] and has worked well for decades using coaxial cables. The search for greater cooling performances has led to test an optical notch filter prototype on the 3.57 GeV/c [6] similar to current usage

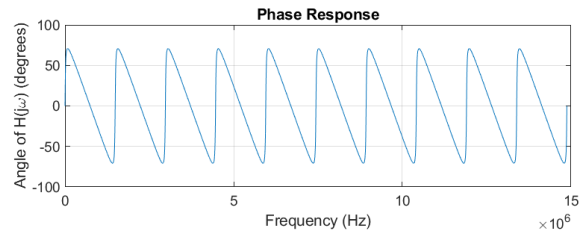


Figure 5: Simulated Comb filter phase @ 2.0 GeV/c.

in other accelerators. Replacing the RF devices by optical devices has enabled us to reduce the size of the system and the prototype now in use at CERN has shown not only greater performances but a greater robustness and ease for maintenance and diagnosis as well.

Subsequently, an industrial version has been studied and built where all the optical devices are inside a temperature stabilized enclosure as shown in Figure 6. The long branch is made of a fixed 120 m fiber and additional short patch fibers to approach the nominal target length. An optical delay line is then used to fine tune the notch frequency.

The long fiber is wound on an aluminium reel which is heated to a stable temperature within $\pm 0.02^\circ\text{C}$. The reel acts as well as a heater for the whole enclosure and provides thus a good temperature stability for all the other less critical optical elements. The steady state temperature is kept at 40 degrees with no active cooling. Steady state temperature is reached after a few hours.

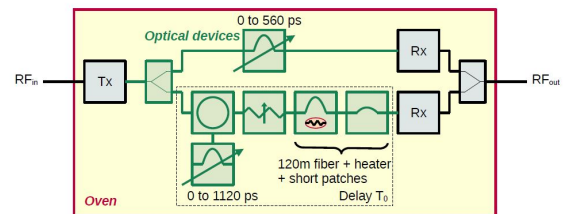


Figure 6: New optical notch filter synoptic.

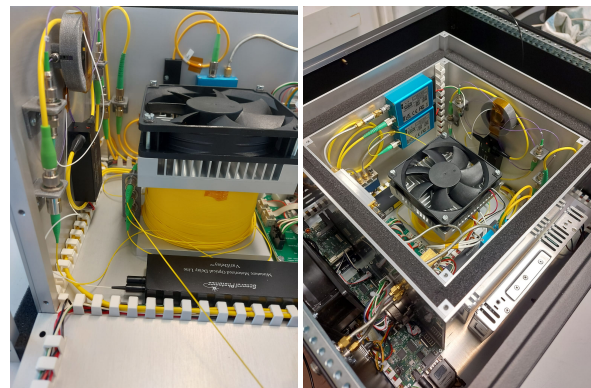


Figure 7: New optical notch filter.

SET-UP FOR MEASURING BTFS

Beam Transfer Functions (BTFs) are performed using a Vector Network Analyzer (VNA). A transmission measurement S21 is performed in open loop for the targeted plane using a swept frequency covering a few revolution harmonics. The signal from the VNA feeds power amplifiers and the beam response is recovered with signals from the pick-ups. A number of relays are remotely controlled in a predefined sequence. BTFs are measured in several (typical 11) intervals distributed over the frequency range of 800 MHz to 1.8 GHz. With three planes to measure and two plateaus this gives a total of 66 BTFs needed for a reasonable set-up and check of the stochastic cooling system. The BTFs are

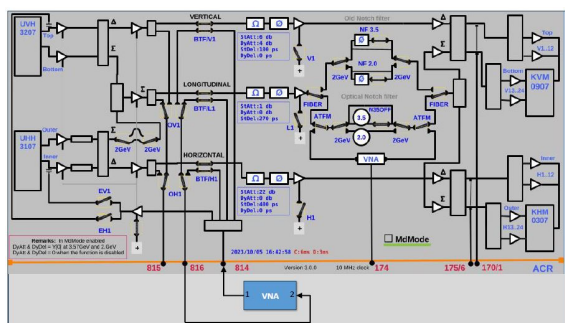


Figure 8: BTF measurements setup.

conducted during the annual machine commissioning and periodically throughout the year whenever modifications or maintenance have been performed. Previously, this process required two full days of work.

A suite of software tools, called the ‘BTF toolbox,’ has been developed to automate these measurements and analysis. With this automation, a full plateau can now be achieved in 15 minutes instead of a day. This not only offers a more efficient way of saving data and performing analysis but also allows for quicker measurements. As a result, more measurements can be performed in the same time-frame, making it possible to adjust certain parameters. This has improved the understanding of setting-up stochastic cooling and has helped in identifying lingering errors.

The automation process involves sweeping frequency in steps across the bandwidth. For each frequency step, a span of 3 MHz is captured using 1600 points. RF relays are then controlled to calibrate the VNA, eliminating the effects of the cables’ length from the VNA to the measurement points.

After calibration, the relays are adjusted to set the machine to the desired plane. In the longitudinal plane, the notch filter is turned off by opening the long branch with a relay. As the VNA sends a signal to the kicker, it disturbs the beam which tends to blow-up. Before starting any new measurement in the sequence, the tool controls the relays to reactivate the cooling.



Figure 9: BTF toolbox analysis.

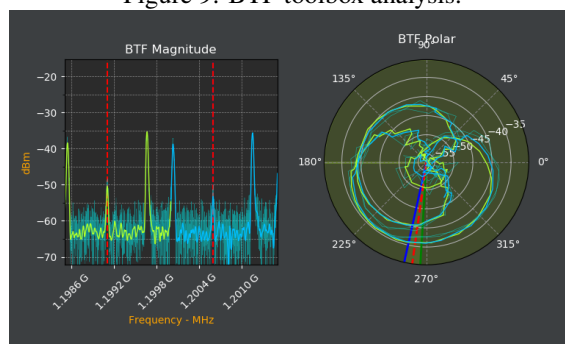


Figure 10: 1.2 GHz vertical response @ 2 GeV/c showing betatron side bands and unwanted response at harmonics of the revolution frequency due to beam offsets.

CONCLUSIONS

The Beam Transfer Function toolbox has enabled to reduce the measurement time and increase the number of analysis iterations and machine adjustments. Phase and delay errors could be identified in the longitudinal plane at 2 GeV/c and corrected. Thanks to the improved cooling at 2 GeV/c it has provided an overall transmission increase of 4% and it has been identified a potential reduction of the AD decelerating cycle time. In addition it enables to reduce significantly the yearly commissioning time after the machine end of year technical stop. This ends into more anti-protons available for physics experiments.

ACKNOWLEDGEMENT

The authors would like to thank their colleagues from SY-RF, BE-OP, TE-VSC, EN-CV for continued support in the operation and maintenance.

REFERENCES

- [1] F. Caspers and C. Carli, “Stochastic Cooling at the CERN Antiproton Decelerator”, in *Proc. EPAC2000*, Vienna, Austria, 2000, pp. 2014–2016.
- [2] P. Belochitskii *et al.*, “Commissioning and First Operation of the Antiproton Decelerator AD”, in *Proc. PAC’01*, Chicago, Ill., USA, June 2001, pp. 580–584.

- [3] L. Ponce, L. Bojtár, C. Carli, B. Dupuy, Y. Dutheil, P. Freyermuth, *et al.*, “ELENA - From Commissioning to Operation”, in *Proc. IPAC’22*, Bangkok, Thailand, Jun. 2022, pp. 2391–2394. doi:10.18429/JACoW-IPAC2022-THOXGD1
- [4] H. Stockhorst, T. Katayama, R. Maier, “Beam cooling at COSY and HESR, Part 1 Theory”, *Schlüsseltechnologien*, Volume 120, ISBN 978-3-95806-127-9, Forschungszentrum Jülich, Jülich, 2016. <https://juser.fz-juelich.de/record/807739>
- [5] L. Thorndahl, G. Carron, “Stochastic cooling of momentum spread by filter techniques”, CERN-ISR-RF-78-12, CERN, Geneva, Switzerland, 1978.
- [6] F. Caspers *et al.*, “First Operation for Stochastic Cooling of p-Bars in the CERN AD using Optical Delay Notch Filter and Plans for 2021 Operation”, 12th Workshop on Beam cooling and Related Topics, in *proc. of COOL’19*, Novosibirsk, September 2019. doi:10.18429/JACoW-COOL2019-MOY01

KICKER FOR THE CR STOCHASTIC COOLING SYSTEM BASED ON HESR SLOT-RING COUPLERS

R. Stassen†, R. Greven, H. Schneider, J. Wolters, Forschungszentrum Jülich, Jülich, Germany
B. Breitzkreutz, GSI Helmholtzzentrum für Schwerionenforschung GmbH, Darmstadt, Germany

Abstract

A ‘light’ version of the HESR stochastic cooling system was already successfully tested in the Cooler Synchrotron COSY. There the stochastic cooling system was operated together with the original PANDA cluster jet target from University Münster. The system layout includes all components as planned for the HESR like low noise amplifier, switchable delay-lines and optical notch-filter. The robust slot-ring design has been proven. Hence it was decided to use this concept for the CR kicker as well. Therefore, the parameters need to be adapted for the CR cooling system. However, the significantly higher RF power requires a new water cooling concept. First simulations and measurements show that using heat pipes could be a possible solution. At COOL’23 main parameter as well as the promising results achieved at COSY will be presented.

STOCHASTIC COOLING SYSTEM OF HESR

The HESR is the planned High Energy Storage Ring (1.5 - 15 GeV/c) for antiprotons at the FAIR facility (Facility for Antiprotons and Ion Research) in Darmstadt (GSI) [1]. One of the key systems at the HESR will be the stochastic cooling. It is not only essential to enhance the beam quality for the experiments but is also indispensable for the accumulation of antiprotons in HESR [2]. The system is based on dedicated structures. Each beam-surrounding slot of these so-called slot-ring couplers covers the whole image current without a reduction of the HESR aperture [3, 4].

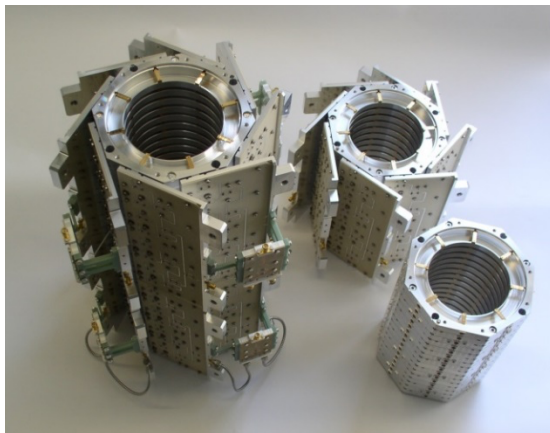


Figure 1: Stacks of slot ring couplers with and without 16:1 combiner-boards and two stacks mounted together including 2:1 combiner with heat-trap.

Each resonant ring structure is heavily loaded with eight 50Ω electrodes for a broad-band operation. The rings are screwed together to a self-supporting structure in stacks of 16 rings. Four of these stacks will build the spindle for one tank. Figure 1 shows these stacks; one without combiner, one with combiner board and a combination of two stacks including additional 2:1 combiner especially designed to minimize the heat flow to the 16:1 combiners. The structures can be used for all cooling directions simultaneously. No complicate plunging system is needed.

A ‘light’ cooling version with one original pickup (PU) and kicker (KI) tank of the HESR was installed in COSY. The system layout includes all components as planned for the HESR like low noise amplifiers, switchable delay-lines, optical notch-filter and - of course - the high power amplifier. The inner structure of the pickup was cooled down to less than 20 K within 10 h. Although the tank is not bakeable, the vacuum reached already $1 \cdot 10^{-10}$ mbar. The HESR needs fast transmission-lines between PU and KI. Beside air-filled coax-lines, optical hollow fibre-lines are very attractive [5]. Three of such 50 m long fibres were installed in COSY and used during the cooling experiments. See Fig. 2 below.

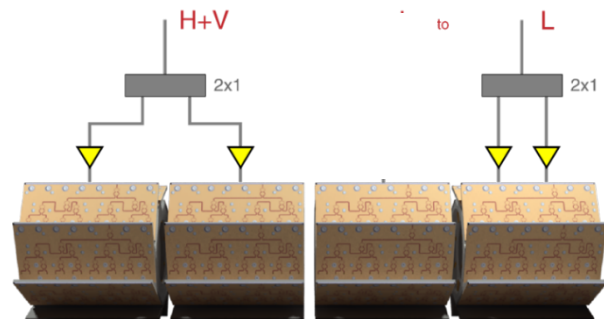


Figure 2: HESR Kicker arrangement at COSY.

The kicker tank was equipped with six custom-made HESR 100 W power amplifier based on gallium nitride (GaN) transistors. Although GaN is not as linear as Gallium Arsenide (GaAs), it is meanwhile the first choice of broadband power amplifier in the GHz region. The kicker is used for all three cooling planes. Two groups of the HESR kicker are for both transverse planes and one group with two amplifiers for longitudinal cooling.

PANDA TARGET MEETS HESR STOCHASTIC COOLING SYSTEM IN COSY

The HESR originally has been optimized for the PANDA experiment (antiProton ANihilation at DArmstadt). The PANDA collaboration comprises more than 500 scientists coming from 20 countries. Their research is dedicated to fundamental physics research covering topics such as

†r.stassen@fz-juelich.de

strong and weak interaction, exotic states of matter, and the structure of hadrons. One big contributor is IKP-1 of FZJ. In order to record as much information as possible from the antiproton - proton collisions a versatile detector is being built that allows precise track reconstruction, energy and momentum measurements, and efficient identification of charged particles. One of the required targets is being built by scientists at the Münster University [6]. This cluster target has been installed and successfully commissioned in COSY during summer 2018. The PANDA cluster target reached densities in the order of $1E15$ atoms/cm². Such high target densities leads to fast energy loss and emittance growth of the beam. Almost all particles were lost during the 5-minute cycle.

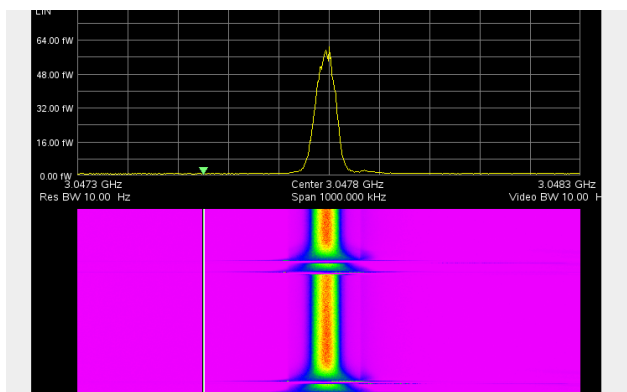


Figure 3: Schottky signal of 1500th harmonic with stochastic cooling, barrier bucket and target.

Even with the ‘light’ version of the HESR cooling system, cooling was demonstrated in all three directions. Each direction could be cooled by a factor of 3 to 4 without target.

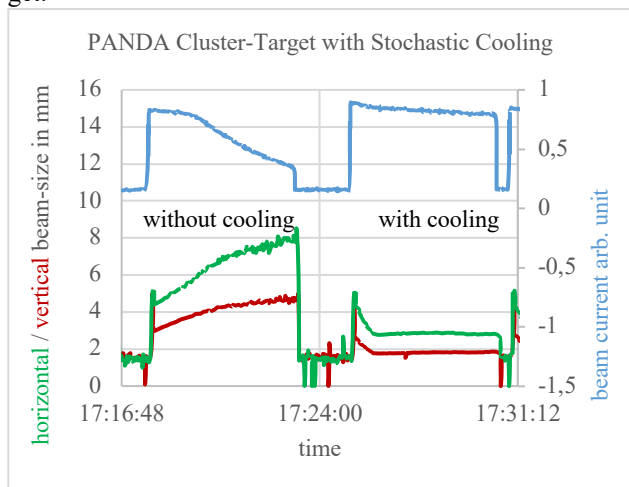


Figure 4: Beam current and beam size with (right) and without stochastic cooling (left).

With longitudinal cooling and target, a fast cooling was observed at the beginning of the cycle. The momentum spread was decreased by a factor of 2 and a very stable equilibrium was observed for the rest of the 5-minute cycle (Fig. 3).

Energy loss and beam broadening in the cluster target could be compensated efficiently. In Fig. 4 the beam current (=intensity), and the horizontal together with the vertical beam size are displayed evolving in time. The first cycle is without cooling, the second one with stochastic cooling on. The cycle time was 5 minutes.

Beam losses were significantly reduced. Transverse cooling not only compensates for beam size growth by the target, it was able to reduce the equilibrium emittance even by factor 2 in both planes.

CR KICKER DESIGN

The stochastic cooling system of Collector Ring (CR) is used to fast reduce the phase space of hot rare isotope beams (RIBs) and antiproton beams [7]. Both operation modes are designed for fixed particle velocities, i.e. 0.83 times the speed of light for RIBs (corresponds to a kinetic energy of 740 MeV/u) and 0.97 times for antiprotons (3 GeV/c). Since stochastic cooling is more sensitive to heavy particles, the kicker is optimized for the latter. The robust slot-ring design of the HESR has been proven. Hence it was decided to use this concept for the CR kicker as well. Therefore, the parameters need to be adapted for the CR cooling system. The aperture was increased to 140 mm while the operating frequency was changed to 1 - 2 GHz.

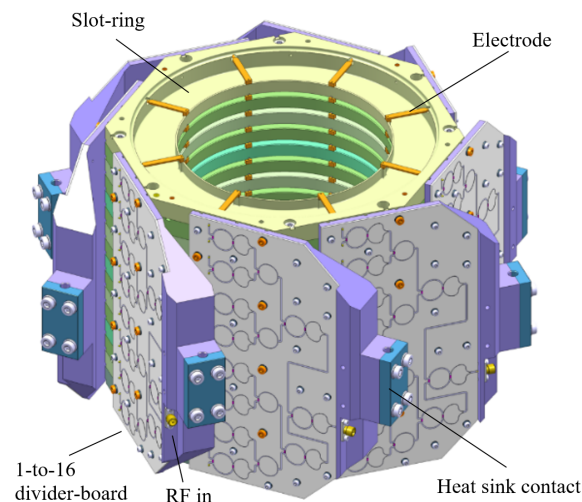


Figure 5: One stack of new CR kicker structure including divider-boards.

The slot-ring structures were optimized with CST Studio Suite for a high shunt impedance of antiprotons at a velocity of $\beta = 0.97$. The impedances are defined according to [8]. The electric fields were simulated for a cell at the centre of a long structure, and the resulting impedances were multiplied by the number of cells to obtain the total impedances shown in Table 1.

Compare to the slotline PUs from GSI, the cooling for both transverse planes can be operated at the same beam position due to the static aperture. Thus, one KI will be used for transvers cooling in both directions and one KI for longitudinal cooling. Each kicker tank contains 128 slot-

rings. Every 16 rings are hard-wired with ceramic divider-boards as a stack (see Fig. 5). The main parameters of the new structures are summarized in Table 1.

Table 1: CR Kicker Parameters

Main parameters	Value	Unit
RF frequency range	1 - 2	GHz
Particle velocity		
Rare isotope	0.83	c ₀
Anti-proton	0.97	c ₀
aperture	140	mm
No. of Slot-rings per tank	128	
Total longitudinal shunt impedance for anti-protons	2816	Ω
Total transverse shunt impedance for anti-protons	896	Ω
Total longitudinal shunt impedance for rare isotopes	1280	Ω
Total transverse shunt impedance for rare isotopes	448	Ω
Nominal power loss per divider board	15 (max. 95)	W
Nominal total power loss per tank	960	W

The Wilkinson dividers at the divider-boards use SMD resistors to dissipate the odd-mode signals coming in from the electrode side. Since the electrodes are mostly a pure inductive load, all power applied by the power amplifiers is reflected and must be dissipated in these resistors. Therefore, diamond-based resistors are used. To increase the bandwidth, mostly two-staged Wilkinson dividers are used when possible. Only the third of the four divider levels is one-staged due to space limitations. The much higher power losses at the CR divider-boards compared to the HESR requires a new cooling concept. The copper bands between the divider boards and the water cooling block have been replaced by heat pipes or heat straps respectively and extensive simulations were carried out.

The used simulation model calculates the heat flow from the resistors to the water cooling considering the detailed structure of the boards, including the strip lines and thin layers of Ag past and glue. For a constant resistor power of 15 W the maximum resistor temperature will stay below 60 °C. If the power in the resistors of a circuit board is increased to 95 W for 5 minutes, the temperature in the resistors rises to ~110 °C within 0.1 s (Fig. 6). The subsequent moderate increase, which is determined by the heating of the entire board, goes up to a maximum temperature of almost 174 °C. This is already at a critical limit. Moderate temperature increase can be handled by a temperature-measurement interlock system, but the fast increase at the beginning not.

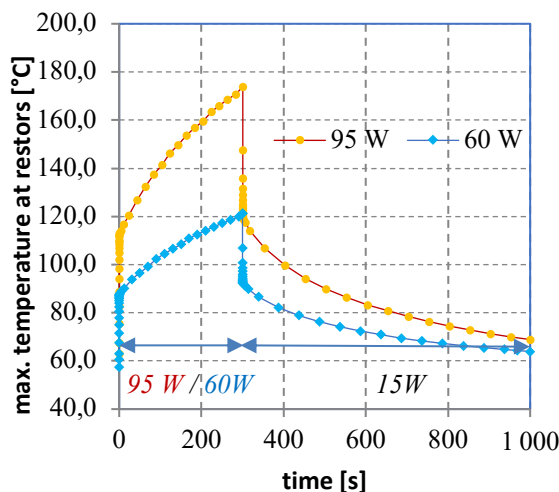


Figure 6: Simulated temperatures at resistors of the divider-boards.

The heat pipes are modelled by simplified solid bodies with high thermal conductivity, which corresponds to the heat removal capability according to the data sheet. This simplification cannot correctly describe the complex non-linear processes in the heat pipes and resulting limitations of the cooling system. This uncertainty in the parameters of the simulations require additional consideration through prototypes.

REFERENCES

- [1] “FAIR - Facility for Antiproton and Ion Research”, Green Paper - The Modularized Start Version, October 2009; http://www.faircenter.de/fileadmin/fair/publications_FAIR/FAIR_GreenPaper_2009.pdf
- [2] T. Katayama *et al.*, “Beam Accumulation with Barrier Voltage and Stochastic Cooling”, in *Proc. IPAC'10*, Kyoto, Japan, May 2010, paper MOPD065, pp. 837-839.
- [3] L. Thorndahl, “90mm Full-Aperture Structures with TM01-Mode propagation for 2-4 GHz Stochastic Momentum Cooling in HESR”, internal report, 2010.
- [4] R. Stassen, B. Breitkreutz, and N. Shurkhno, “Recent Results of HESR Original Stochastic Cooling Tanks at COSY”, in *Proc. IPAC'18*, Vancouver, Canada, Apr.-May 2018, pp. 913-915. doi:10.18429/JACoW-IPAC2018-TUPAF078
- [5] Hollow fiber lines, <http://www.nktphotonics.com/lasers-fibers/en/product/hollow-core-photon-crystal-fibers/>
- [6] B. Hetz *et al.*, “Beam and Vacuum Studies of the PANDA Cluster-Jet Target”, DPG spring meeting, Bochum, Germany, ISSN 0420-0195, 2018.
- [7] C. Zhang *et al.*, “A 1-2 GHz stochastic cooling system for antiproton and rare isotopes”, in *Proc. IPAC'23*, Venice, Italy, May 2023, pp. 1740-1743. doi:10.18429/JACoW-IPAC2023-TUPA184
- [8] D.A. Goldberg and G.R. Lambertson, “Dynamic devices. A primer on pickups and kickers.” *AIP Conference Proceedings*, vol. 249, 1992.

ELECTRON COOLING IN NICA ACCELERATION COMPLEX

A. Butenko, V. Lebedev[†], I. Meshkov, K. Osipov, Yu. Prokopjechev, V. Shpakov, S. Semenov,
 A. Sergeev, E. Syresin, R. Timonin, G. Trubnikov
 Joint Institute for Nuclear Research, Dubna, Russia
 M. Bryzgunov, A. Bublely, V. Panasyuk, V. Parkhomchuk, V. Reva
 Budker Institute for Nuclear Physics SB RAS, Novosibirsk, Russia

Abstract

The paper reports results of experimental studies of electron cooling carried out during commissioning of injection complex of NICA (the Nuclotron-based Ion Collider fAcility). Further plans of electron cooling developments and usage are also described.

NICA INJECTION COMPLEX

The Nuclotron-based Ion Collider fAcility (NICA) is in construction at JINR [1, 2]. The collider first beam tests are planned for the second half of 2024. The goal of the second stage of NICA project is to provide colliding beams for studies of collisions of heavy fully stripped ions at energies up to 4.5 GeV/u. The injection complex consists of two collider rings supporting head-on collisions in two interaction points and the injection complex [3, 4] which includes linac and two synchrotrons: Booster and Nuclotron. The injection complex is already in commissioning for few years. Stable operation of the complex has been achieved and different ion species were delivered to the BM@N and SRC experiments [5, 6] with slow beam extraction. By present time the ion beams of He, Fe, C [7] and Xe [8] were accelerated in these synchrotrons during four beam runs. With start of collider operation, the injection complex has to support both the collider operation and the fixed target experiments with slow extracted beams. Two particle detectors, a Multi-Purpose Detector (MPD) [9] and a Spin Physics Detector (SPD) [10], are located in two straight sections at the opposite sides of the collider.

The Krion-6T [11] ion source introduced into operation in Run IV will provide the beam of highly multicharged ions. $^{197}\text{Au}^{31+}$ and $^{209}\text{Bi}^{35+}$ ions are planned to be used in the collider operation. In Run IV (Sep. 2022 – Feb. 2023) we used Xe^{28+} . The same ions are expected to be used at the beginning of collider commissioning. In Run IV about a quarter of the ions extracted from the source had the targeted charge. A typical intensity was about 10^8 ions per pulse for the targeted charge. After electrostatic acceleration to 17 keV/u the beam is accelerated in the RFQ and 2 sections of heavy ion linac (HILAC) [12] to the energy of 3.2 MeV/u. Then the beam is injected into the Booster with single turn injection.

The Booster is a superconducting synchrotron designed to accelerate heavy ions to the energy of 600 MeV/u ($A/Z \approx 6$). At the Booster extraction the ions come through stripping foil where they are fully stripped and then are directed to Nuclotron for further acceleration to 3.9 GeV/u.

The collider design report [3] requires the beam intensity of about 10^9 ions per injection complex pulse with cycle duration of ~4-5 s. The beam extracted from Nuclotron will be injected into collider rings where first it is accumulated in the barrier bucket RF, then bunched and brought to collisions.

The ion xenon beam extracted from Krion-6T had ~5 charge states with the targeted charge state ($Z=28$) taking about 25%. The peak of total ion beam current at the RFQ exit is about 200 μA (curve 1, Fig.1). Since there is considerable loss for the non-target states the total beam current is significantly reduced at the linac exit (curve 2, Fig. 1). With existing instrumentation, we cannot accurately measure the actual loss of the targeted state in the course of beam acceleration in the linac. Typically, the $^{124}\text{Xe}^{28+}$ ion intensity corresponds to $5 \cdot 10^7$ ions at HILAC exit with total beam pulse duration of about 12-15 μs .

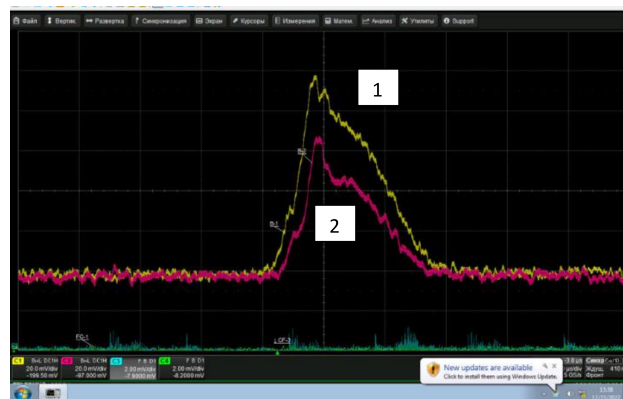


Figure1: Signals of current transformers at the RFQ exit (curve 1) and the HILAC exit (curve 2).

Curve 1 in Fig. 2 presents a typical magnetic cycle of the Booster. As one can see from curve 2, showing the beam current, the beam is injected at the first plateau, where it is adiabatically bunched at the 5th harmonic. Then the beam is accelerated to the second plateau corresponding the ion energy of 65 MeV/u, where it is adiabatically rebunched to the first harmonic. Finally, the beam is accelerated to the top energy of 205 MeV/u and extracted to Nuclotron. Typically, the accelerated to top energy $^{124}\text{Xe}^{28+}$ ions constitute about 60% of all ions at the linac exit.

Note that the electron cooling installations are important part of the accelerating complex. The first one is already installed and operates in Booster, and two others will be installed in each of the collider rings.

The intensity the of Xe^{28+} ion beam is expected to increase by a factor of 2 during next Booster Run. However,

[†] valebedev@jinr.ru

Content from this work may be used under the terms of the CC-BY-4.0 licence (© 2023). Any distribution of this work must maintain attribution to the author(s), title of the work, publisher, and DOI

this intensity still will be less than required for the collider by almost one order of magnitude [3]. To address this, we initially planned to accumulate the beam in the Booster transverse plane with multiple injections and beam damping with electron cooling [13]. Since the longitudinal cooling is faster, at the present time we plan an accumulation in the longitudinal plane.

The electron cooling in the Collider will be used for the beam accumulation and the suppression of intrabeam scattering during accumulation, bunching and collisions.

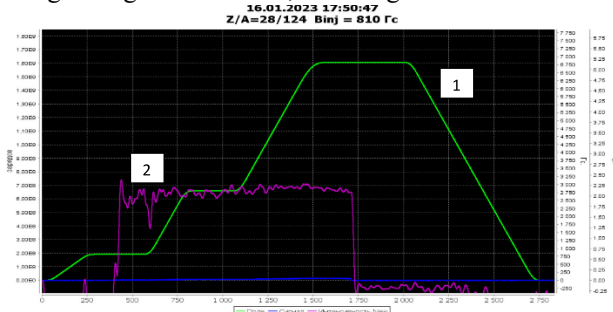


Figure 2: Magnetic field dependence on time for a typical Booster cycle (curve 1), and the number of particles in the beam measured with direct current transformer and normalized to account changes in particle velocity (curve 2); $^{124}\text{Xe}^{28+}$ ions.

BOOSTER ELECTRON COOLING

The Booster electron cooling system [14-16] designed and manufactured by BINP SB RAS has the maximum electron energy of 60 keV and cooling length 2.5 m [3]. In the collider operations it will be used at the injection energy of 3.2 MeV/u for beam accumulation and cooling. Although the Booster electron cooling was tested with multiple ion species it was not routinely used in the beam delivery to users up to almost the end of Run IV.

Investigation of Booster electron cooling was done during the 2nd [4] and 4th [8] Runs. The measurements were produced at the injection energy of 3.2 MeV/n for $^{56}\text{Fe}^{14+}$ [4] (Fig. 3) and $^{124}\text{Xe}^{28+}$ ions (Fig. 4).

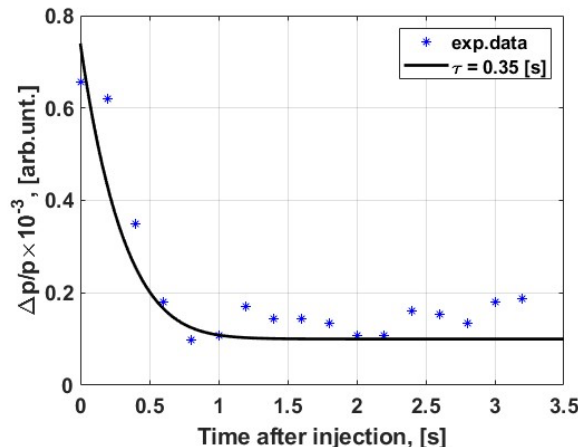


Figure 3: Dependence of ion momentum spread of $^{56}\text{Fe}^{14+}$ ion beam on time at the ion energy of 3.2 MeV/u and the electron beam current of 76 mA. The measurements were performed for continuous beam with Schottky noise.

During 4th Run the ion $^{124}\text{Xe}^{28+}$ acceleration was started in 0.23 s after beam injection. Although this is relatively short time it still was sufficient to provide cooling of ions with reduction of bunch time duration by a factor of 3 with the electron beam current of 50 mA (Figs. 4 and 5).

Dependences of bunch duration on time for cooling on (solid curve) and off (dotted curve) are shown in Fig. 5. The comparison of these curves yields the longitudinal cooling time about 70 ms.

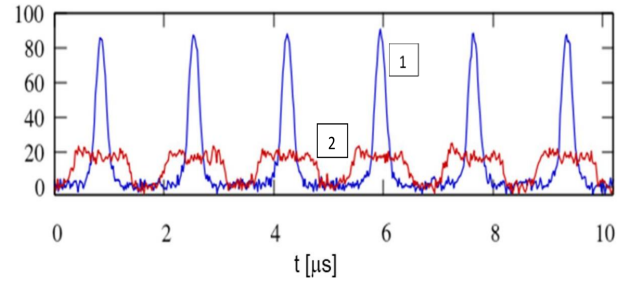


Figure 4: Longitudinal bunch profiles of $^{124}\text{Xe}^{28+}$ ion beams without (curve 2) and with (curve 1) electron cooling. The electron beam current is 50 mA. The measurements were acquired with fast beam current monitor shortly before the beam acceleration in the presence of RF voltage.

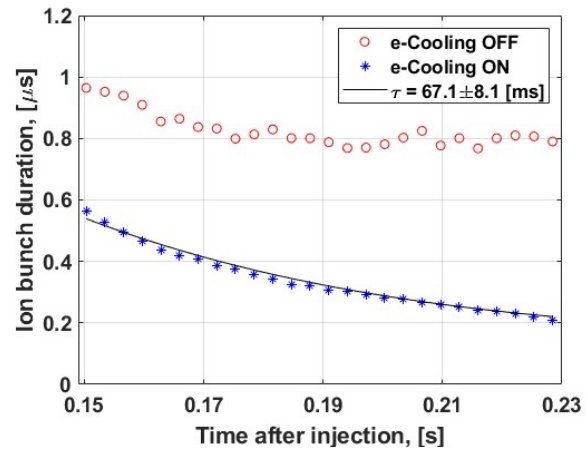


Figure 5: Dependence of bunch duration on time for cooling on (solid curve) and off (dotted curve) measured in Run IV; $^{124}\text{Xe}^{28+}$ ions.

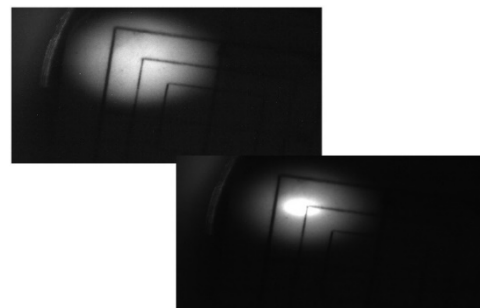


Figure 6: Transverse profiles of ion beam on the beam viewer (luminophore screen) without (upper) and with (down) cooling. The beam intensity was reduced to avoid saturation.

An effect of transverse cooling was observed on a beam viewer installed in the Booster-Nuclotron transfer line. That allows one to acquire an image of transverse distribution for the beam intensity after its acceleration. As one can see in Fig. 6 the beam cooling reduces the FWHM beam transverse sizes from 7.81 mm and 5.38 mm to 3.34 mm and 1.63 mm for horizontal and vertical planes, respectively.

The reduction of beam emittances resulted in a reduction of beam loss with subsequent doubling in the intensity for the beam extracted from the Nuclotron to BM@N experiment. As result the number of $^{124}\text{Xe}^{54+}$ nuclei reached 10^7 per pulse (Fig. 7).

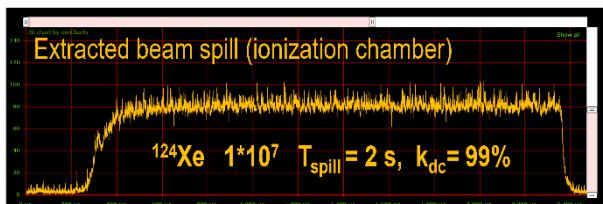


Figure 7: Dependence of beam intensity on time for the beam extracted from Nuclotron; $^{124}\text{Xe}^{54+}$ ions, extraction efficiency $\sim 30\%$, coefficient k_{dc} characterizes time uniformity of extracted beam intensity.

BEAM ACCUMULATION IN BOOSTER

To support the collider operation, we need to increase the number of ions delivered to the Nuclotron top energy by a factor of 30, which is related to a lack of the intensity in the ion source by a factor 20 in comparison with the project value. It will be achieved by the ion accumulation in the Booster with help of electron cooling and by reduction of the beam loss during beam acceleration and transfers.

Since the longitudinal cooling is much faster than transverse, we choose the beam accumulation in the longitudinal plane. In this case about half of the Booster orbit is given to the accumulated bunch, and another half is assigned for the injected beam. The electron cooling has to free the injection space before next injection. Calculations, supported by the above presented results on electron cooling, determine the optimal stacking rate of about 10 Hz; and ~ 10 -15 injections are required to obtain the beam population limited by the beam space charge at the injection energy. Thus about 1-1.5 s of 5-5.5 s acceleration cycle will be used for the beam accumulation in the Booster. A 10 Hz operation of KRION-6T ion source with 10 pulses was recently demonstrated with $^{124}\text{Xe}^{28+}$ ions. Better tuning of ion source resulted in an increase of total charge from 2.4 to 3 nC.

Next step in the ion source upgrade is aimed on shortening the pulse duration from $\sim 15 \mu\text{s}$ (the total duration) to $4 \mu\text{s}$. It will be achieved by changing shape of electrodes holding the ion column to make uniform extraction electric field. A special time program for powering the electrodes should additionally form rectangular pulse shape in time and decrease the energy spread of outgoing ions.

The low energy beam transport and powering of linac and transfer line quads were not originally built to support

10-15 linac pulses at 10 Hz operation. Therefore, a considerable number of hardware pieces has to be upgraded to withstand higher repetition rate. This work is already proceeding and we expect the linac upgrade to be complete by the end of 2023.

The beam accumulation in Booster will be done at the 1st RF harmonic. The RF bucket height of $(\Delta p/p)_{max} = 1 \cdot 10^{-3}$ was chosen to maximize the cooling rate. It requires the RF voltage of 200 V.

The half of Booster ring will be used for injection and other half for accumulation (Fig. 8). Each new injection happens after the previous one is cooled to the core. The permanently present 1st RF harmonic weakly affects high amplitude particles. The total number of accumulated ions and depth of the cooling are restricted by the ion bunch space charge. We expect to be able to store about 10^9 ions of $^{209}\text{Bi}^{35+}$.

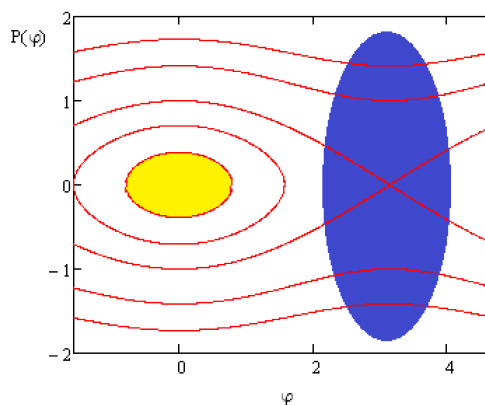


Figure 8: Sketch of Booster ion accumulation with electron cooling in longitudinal plane.

To minimize the longitudinal emittance growth, we plan to avoid rebunching in the course of beam acceleration in Booster. Thus, the entire acceleration will proceed at the first harmonic. Since at the accelerator cycle beginning the RF frequency is outside nominal operation frequency band the initial RF voltage will be lower ($\sim 1.5 \text{ kV}$). That lengthens the accelerating cycle by 300 ms – the time which otherwise will be spent for rebunching.

COLLIDER

The Collider [1-3, 7] consists of two storage rings with two interaction points (IPs). Its main parameters for operation with bismuth fully stripped ions are presented in Table 1. The collider rings have the same shape and are separated vertically. They have two arcs connected by two 109 m straight sections.

An installation of the magnetic elements of the Collider arcs began in December 2021. All dipole magnets and arc quads were assembled and tested on the cryogenic stand. Most of the arc magnets are installed in the Collider tunnel (Fig. 9). Four out of eight RF2 (22nd harmonic) and one out of two RF1 (barrier bucket) systems are also installed. Installation of the remaining four RF2 systems and RF1 system is planned for the end of 2023.

A technological run for the cryomagnetic system is planned for the autumn of 2024. In the course of this run

we plan to commission the following systems: general cryogenic system, cryostat system of magnets, power supplies for main magnets and quads, thermometry system of SC magnets, quench detection and energy evacuation system, power supplies for correctors, vacuum systems for the thermo-insulation and beam vacuum system, and monitoring and control systems.



Figure 9: Assembling of Collider arc magnets.

The first beam runs are scheduled at end 2024. For the first year of operation the beam energy will be limited to 2.5 GeV/u and the initial luminosity is expected to be about $10^{25} \text{ cm}^{-2} \text{ s}^{-1}$ (Fig. 10). Initially the luminosity will be set by the number of ions which can be accumulated in the Collider barrier buckets in the absence of cooling.

Table 1: Main Parameters of the Collider

Circumference	503.04 m
Maximum magnetic rigidity	45 T·m
Average residual gas pressure in beam chamber (room temperature equivalent)	$<10^{-10}$ Torr
Maximum field in dipole magnets	1.8 T
Kinetic energy of gold nuclei	1-4.5 GeV/u
Length of electron cooling section	6 m
Luminosity at the top energy	$10^{27} \text{ cm}^{-2} \text{ s}^{-1}$

Additionally to the electron cooling [17] the collider will have stochastic cooling systems capable to cool all three degrees of freedom. Beam cooling represents the key accelerator technology, which is critical for achieving the design luminosity of the complex. The electron cooling system [3] for the NICA Collider with 2.5 MeV electron energy is intended for accumulation and bunch formation at the ion kinetic energies in the range of 1.0 - 4.5 GeV/u. The cooling time of Au^{79+} ions is expected to be about 100 s at ion energy 3-4.5 GeV/u (Fig. 11). The solenoid cooling section has the length of 6 m and the magnetic field of 1 kGs. The maximum electron beam current is 1 A. Construction of the electron cooling system was started in

FRPAM1R2

BINP in 2016. Its commissioning will start in 2025. The stochastic cooling hardware will be installed in stages. The first stage which includes about 25% of the complete system is expected to be installed by the end of 2025.

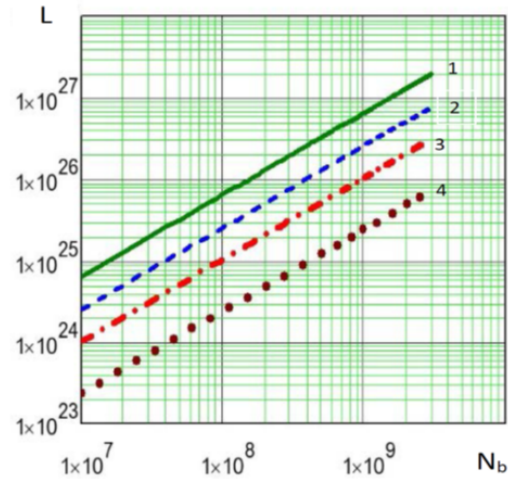


Figure 10: Dependence of luminosity on the number of ions per bunch at different energies (1) 4.5 GeV/u, (2) 3 GeV/u, (3) 2 GeV/u, (4) 1 GeV/u.

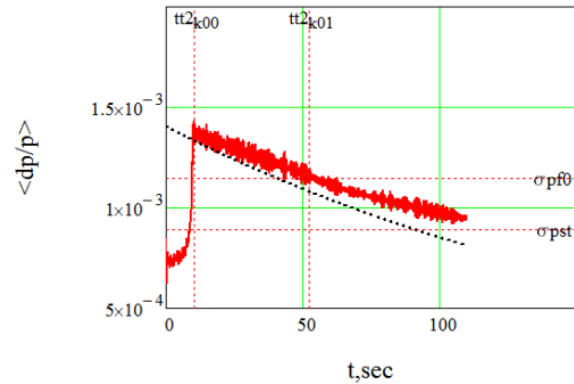


Figure 11: Dependence of ion momentum spread on time at RF3 bunching and cooling for cooling time of 100 s.

A usage of collider electron cooling system is critical to reach the ion momentum spread of $\delta p/p \approx 10^{-3}$ and bunch length of 0.6 m. Due to these reasons an effort to achieve the design luminosity of $L = 10^{27} \text{ sm}^{-2} \text{ s}^{-1}$ is expected to start after complete commissioning of RF3 and electron cooling and an installation of the full energy extraction from Nuclotron in 2026.

REFERENCES

- [1] G. V. Trubnikov *et al.*, “Project of the Nuclotron-based Ion Collider Facility (NICA) at JINR”, in *Proc. EPAC’08*, Genoa, Italy, Jun. 2008, paper WEPP029, pp. 2581-2583.
- [2] V.D. Kekelidze R. Lednicky, V.A. Matveev, *et al.*, “Three stages of the NICA accelerator complex”, *Eur. Phys. J. A*, v.52:211, pp.390, 2016.
doi:10.1088/1742-6596/668/1/012023
- [3] “Technical Project of NICA Acceleration Complex”, Dubna, 2015.

- [4] A.V. Butenko, O.I. Brovko, A.R. Galimov, *et al.*, “NICA Booster a superconducting synchrotron of new generation”, *UFN*, vol. 193, No. 2, pp. 206-225, 2023.
- [5] M. Kapishin, “The fixed target experiment for studies of baryonic matter at the Nuclotron (BM@N)”, *EPJ Web of Conferences*, vol. 182, 02061, pp.1-6, 2018.
doi:10.1051/epjconf/201818202061
- [6] M. Patsyuk, T. Atovullaev, A. Corsi, *et al.*, “BM@N data analysis aimed at studying SRC pairs: one-step single e-nucleon knockout measurement in inverse kinematic out a 48 GeV/c ¹²C nucleus”, *Phys. Part. Nuclei Lett.*, vol. 52, no. 4, pp. 631-636, 2021.
- [7] E. Syresin, O. Brovko, A. Butenko, *et al.*, “NICA ion collider and plans of its first operation”, in *Proc. IPAC'22*, Bangkok, Thailand, June 2022, pp.1819-1821.
doi:10.18429/JACoW-IPAC2022-WEPOPT001
- [8] O.I. Brovko, A.V. Butenko, A.P. Galimov, *et al.*, “NICA ion collider and its acceleration complex”, in *Proc. IPAC'23*, Venice, Italy, June 2023, pp. 616-619.
doi:10.18429/JACoW-IPAC2023-MOPL043
- [9] “Multi-purpose detector MPD”,
<https://nica.jinr.ru/projects/mpd.php>
- [10] “Spin Physics detector (SPD)”,
<https://nica.jinr.ru/projects/spd.php>
- [11] E.D. Donets, E.E. Donets, D.E. Donets, *et al.*, “ESIS ions injection, holding and extraction control system”, *EPJ Web of Conferences* 177, vol. 5, p. 08002, 2018.
doi:10.1051/epjconf/201817708002
- [12] A.V. Butenko, V.S. Aleksandrov, E.E. Donets, *et al.*, “The Heavy Ion Injector at the NICA Project”, in *Proc. LINAC'14*, Geneva, Switzerland, 2014, pp. 1068-1070.
- [13] E.M. Syresin, “Injection in NICA booster with electron cooling”, *Phys. Part. Nucl. Lett.*, vol. 12, No. 4, pp. 591-596, 2015.
doi:10.1134/S1547477115040226
- [14] M. Bryzgunov *et al.*, “Status of the electron cooler for NICA booster and results of its commissioning”, in *Proc. COOL'19*, 23-27 September, Novosibirsk, Russia, pp. 22-25, doi:10.18429/JACoW-COOL2019-TUX01
- [15] L.V. Zinovyev *et al.*, “Start of Electron Cooling System for the NICA Booster”, *Phys. Part. and Nucl. Lett.*, ISSN 1547-4771. vol. 15, No. 7, 2018, pp. 745-748.
doi:10.1134/S1547477118070737
- [16] E. Syresin, A. Baldin, A. Butenko, *et al.*, “NICA synchrotrons and their cooling systems”, in *Proc. COOL'21*, Novosibirsk, Russia, 2021, pp. 1-5.
doi:10.18429/JACoW-COOL2021-S101
- [17] M.I. Bryzgunov *et al.*, “Status of the High-Voltage Electron-Cooling System of the NICA Collider”, *Phys. Part. Nucl. Lett.*, vol. 17, vol. 4, pp. 425-428, 2020.
doi:10.1134/S1547477120040135

EXPERIMENTS ON ELECTRON COOLING AND INTENSE SPACE-CHARGE AT IOTA

N. Banerjee*, G. Stancari, Fermilab, Batavia, Illinois, USA

M.K. Bossard, J. Brandt, Y-K. Kim, The University of Chicago, Illinois, USA

S. Nagaitsev, Thomas Jefferson National Accelerator Facility, Newport News, Virginia, USA

Abstract

The Integrable Optics Test Accelerator at Fermilab will explore beam dynamics in a ring with intense space-charge using 2.5 MeV proton beams with an incoherent tune shift approaching -0.5 . We will use this machine to explore the interplay between electron cooling, intense space-charge, and coherent instabilities. In this contribution, we describe the machine setup including the design of the electron cooler and the lattice, list specific experiments and discuss the results of numerical simulations which include the effects of electron cooling and transverse space-charge forces.

INTRODUCTION

The grand challenges facing the accelerator and beam physics community include creating and sustaining beams with intensity and phase-space density an order of magnitude higher than what is achievable today [1]. In the realm of hadron storage rings, such gains are crucial for future proton drivers for neutrino generation [2], neutron sources [3] and muon colliders [4], along with heavy ion colliders for particle and nuclear physics. Specifically at Fermilab, the Accelerator Complex Evolution plan [5], which aims to provide substantially more protons on target when compared to PIP-II [6], requires the replacement of the Fermilab Booster [7] synchrotron. One class of options involves constructing a rapid cycling synchrotron which will operate at high intensity and high space-charge tune shift to sustain 2.4 MW beam power on the Long-Baseline Neutrino Facility (LBNF) target. The Integrable Optics Test Accelerator (IOTA) [8], displayed in Fig. 1, was constructed at Fermilab as part of the R&D program toward achieving multi-megawatt proton beams. Research at IOTA includes Non-linear Integrable Optics [9, 10], coherent instabilities, beam cooling [11], electron lenses [12], and more [13, 14]. IOTA was designed to operate both with 150 MeV electrons, which we have been using until now, and also 2.5 MeV protons, whose injector we are building. The proton program in IOTA is designed for experiments up to an incoherent tune shift of -0.5 to explore methods of improving the stability of bright and intense hadron beams in synchrotrons and storage rings.

The primary mechanism through which space-charge affects beam dynamics in hadron storage rings is through betatron resonance excitations [15] due to incoherent tune shifts of the particles as a function of position inside the bunch. In practice, periodic resonance crossing [16] of particles undergoing synchrotron motion in bunched beams lead to

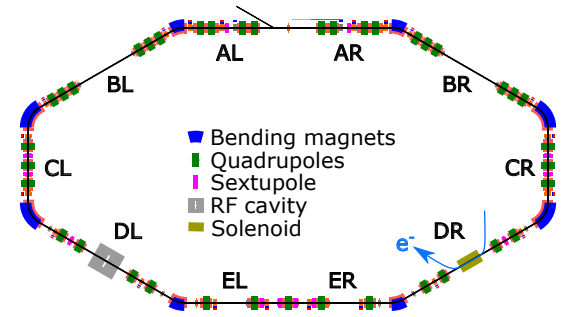


Figure 1: Layout of the Integrable Optics Test Accelerator [8] without special non-linear magnets. The beam moves clockwise. The blue arrow indicates the propagation of electrons in the cooler situated in section DR.

emittance growth and beam loss, thus limiting the maximum phase-space density which can be sustained in a ring. Studying these effects in high-energy hadron rings is complicated since the tune spread generated by space-charge dynamically changes the phase-space distribution of the bunch, which in turn influences the tune shift itself. Consequently, by using an electron cooler to enforce an equilibrium phase-space distribution in the bunch core, we can measure halo formation and beam loss in the presence of almost constant space-charge forces. Past experiments using electron cooling, seeking to maximize the Laslett tune shift of accumulated beam, found an upper limit of $|\Delta\nu_{\perp}| \sim 0.1 - 0.2$ [17, 18]. Using magnetized electron cooling of 2.5 MeV proton beams in IOTA, we seek to maximize the phase-space density of stored beam, measure beam loss and characterize the distribution.

While space charge restricts the maximum phase-space density of the beam, the onset of coherent excitations, such as the Transverse Mode Coupling Instability (TMCI), constrains the maximum current. In contrast, incoherent particle motion in the bunch with different betatron tunes results in Landau damping, which naturally restricts the growth of these instabilities. We can exploit this effect by providing non-linear focusing to the beam using octupoles [19] or electron lenses [20], and this has been instrumental in boosting the beam current in many accelerators. However, strong non-linear focusing also restricts the dynamic aperture, which constrains the maximum phase-space volume occupied by the bunch. We will explore Non-linear Integrable Optics (NIO) [21, 22] at IOTA, which can produce adjustable tune spread while ensuring stable single-particle dynamics where theoretically, the aperture is solely limited by the vacuum

* nilanjan@fnal.gov

Table 1: Proton Beam Parameters in IOTA

Parameter	Value	Unit	
Kinetic energy (K_b)	2.5	MeV	
Emittances ($\epsilon_{x,y}$)	4.3, 3.0	μm	
Momentum spread (σ_p/p)	1.32×10^{-3}		
	Coasting	Bunched	
Number of bunches	-	4	
Bunch length (σ_s)	-	0.79	m
Beam current (I_b)	5.79	1.15	mA
Bunch charge (q_b)	10.6	0.52	nC
Tune shifts ($ \Delta\nu_{x,y} $)	0.33, 0.50		
$\tau_{\text{IBS},x,y,z}$	10.2, 2.62, 14.4, 3.70,	301, 424	s

chamber. Besides dedicated non-linear optics, space-charge fields also generally provide non-linear focusing and, hence, can serve as a source of incoherent tune spread. Historically, this was believed to have a damping effect on TMCI, where increasing space-charge tune shift increases the TMCI current threshold. But recent analyses [23–25] indicate a complex interplay between space charge and wakefields. We will measure instability growth rate and damping effects using 2.5 MeV protons at IOTA with electron cooling serving as the knob for the space-charge tune shift, a digital wake-building feedback system [26] providing variable impedance, and non-linear integrable optics contributing amplitude-dependent tune spread.

The electron cooler will be realized as a specific configuration of the IOTA electron lens [12] in section DR as illustrated in Fig. 1. The electron lens consists of a low-energy (< 10 keV) magnetically confined electron beam which interacts with the recirculating beam and can be used for non-linear focusing, space-charge compensation, and electron cooling. The primary components of the setup include a thermionic electron source, a collector, and a magnetic system consisting of a main solenoid for the interaction region and transfer solenoids and toroids to guide the beam. The design of the main solenoid is constrained by the maximum axial field requirement for applying the lens to 150 MeV electrons and the strict field quality requirement dictated by electron cooling of 2.5 MeV protons. Diagnostics specific to analyzing electron cooling performance include a neutral hydrogen monitor to non-invasively measure the equilibrium proton beam profile during cooling and a cyclotron radiation emission monitor [27, 28] to measure electron density and temperature. While we already have many components from the decommissioned Tevatron electron lens, we are finalizing the design of the vacuum chambers and the transport system to meet the stringent requirements of electron cooling.

In the next section, we define the specifications for the 2.5 MeV proton beam in IOTA and the corresponding electron cooler. Then, we outline specific experiments which probe the frontier of phase-space density and intensity of the proton beam.

ELECTRON COOLING WITH 2.5 MeV PROTONS

The proton program is designed for experiments with both coasting and bunched beams, with space-charge tune shifts approaching -0.5 . The 2.5 MeV ($pc \approx 70$ MeV) beam energy has the double advantage of large tune shifts being achievable using modest bunch charges, as shown in Table 1, and simultaneously being able to produce almost no intrinsic impedance, enabling us to disentangle intensity effects. The proton injector [29] will produce the required beam parameters at a repetition rate of 1 Hz, and the beam will be injected in a single turn into section A. The IOTA rf system [30] located in section DL contains two broadband resonators driving independent accelerating gaps, one of which operates at 2.2 MHz for bunched proton beam operations at $h = 4$. The placement of linear focusing elements in IOTA preserves mirror symmetry about the vertical centerline of the layout presented in Fig. 1. However, we can independently control all magnet strengths, allowing us to set up lattices with a wide range of tunes, transverse coupling, momentum compaction, along with special configurations required for NIO. The lattice [31] for electron cooling experiments enforces zero dispersion and transverse betatron matching at the cooling solenoid and features adjustable main solenoid strength, transverse tunes, and linear coupling. The drawback of low-energy operation is the large emittance growth and loss rates driven by Intra Beam Scattering (IBS) and residual gas scattering. Consequently, electron cooling is necessary to extend the lifetime of the proton beam and maintain equilibrium conditions.

The goal of the electron cooler is to compensate for various emittance growth mechanisms and provide us with a knob to tune the equilibrium phase-space distribution for a range of proton bunch charges and energies. This trans-

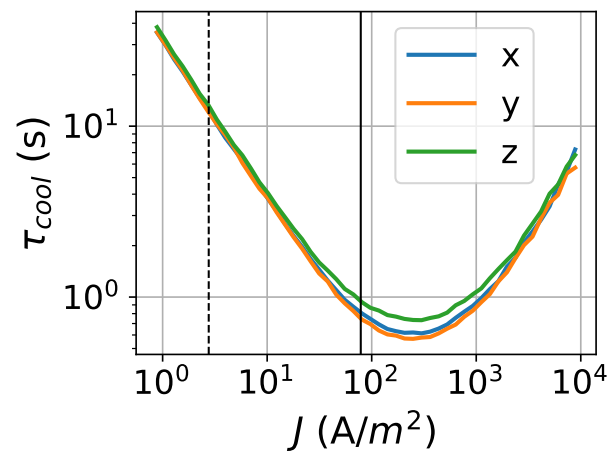


Figure 2: Cooling times of a Gaussian bunched beam as functions of electron current density in the presence of axial magnetic field of 0.1 T without any errors. The vertical lines correspond to the electron beam configurations listed in Table 2.

Table 2: Electron Cooler Parameters

Parameter	Values	Unit
Proton parameters		
RMS Size ($\sigma_{b,x,y}$)	4.43, 3.70	mm
Main solenoid parameters		
Magnetic field (B_{\parallel})	0.1 - 0.5	T
Length (l_{cooler})	0.7	m
Flatness ($\max B_{\perp}/B_{\parallel}$)	2×10^{-4}	
Electron parameters		
Kinetic energy (K_e)	1.36	keV
Temporal Profile	DC or pulsed	
Transverse Profile	Flat	
Source temp. (T_{cath})	1400	K
Current (I_e)	1.7 80	mA
Radius (a)	14 18	mm
$\tau_{\text{cool},x,y,s}$	12, 12, 13 0.79, 0.74,	s
	0.94	

lates to requiring a range of cooling time scales between 1 to 10 seconds. We opt for magnetized electron cooling with main solenoid strengths ranging between 0.1–0.5 T to boost cooling rates and provide transverse confinement to the low-energy electron beam. We calculate the cooling times of a bunched proton beam with a Gaussian distribution in all directions, assuming that (1) the velocity at the center of the electron beam matches with the average velocity of the protons, (2) the transverse distribution of the protons is matched to the beta function of the solenoid, and (3) the magnetic field at the cathode equals that at the main solenoid. Figure 2 shows the results of the cooling time calculations using the code JSPEC [32] as a function of current density of the electrons. The cooling rate increases linearly with current density for low electron currents, reaches a maximum, and then declines for high currents. This can be explained in terms of the relative contributions of space-charge, electron beam energy jitter due to power supply fluctuations, and magnetic field errors to the effective velocity in the Parkhomchuk model [33]. The cooling rate increases linearly at low electron currents ($J \lesssim 20 \text{ A/m}^2$), since the effective velocity is dominated by power supply jitter and magnetic field errors, both of which are independent of current. At higher currents, the relative motion of electrons in the beam frame, driven by space-charge forces, contributes more to the effective velocity as intensity rises. This leads to diminishing cooling rates even at larger number densities of electrons. In a practical realization, the maximum electron density will be limited by the highest betatron tune shift $\Delta\nu_{\perp,\text{cooler}}$, which can be accommodated by the lattice while retaining linear stability. In our lattice, the limit of stability corresponds to $\Delta\nu_{\perp,\text{cooler}} \sim 0.1$, which requires $J \lesssim 10^3 \text{ A/m}^2$. We chose two thermionic electron source designs [34] listed in Table 2 with an order of magnitude difference in current density to cool protons over a range of bunch charges.

We model the interplay of transverse space-charge and magnetized electron cooling using the Particle-in-Cell

code PyORBIT [35]. Our implementation [36] uses the SpaceCharge2p5D model in PyORBIT and applies multiple thin-lens kicks to the protons, which sum the contribution of the cooling and the focusing force from the electron beam as they propagate through the solenoid. We conduct bunched and coasting beam simulations to demonstrate this model, injecting a Gaussian distribution with $|\Delta\nu_y| = 0.05$ and allowing it to evolve in IOTA with and without electron cooling for 100,000 turns (183 ms). Figure 3 shows the rms emittances, transverse tune shifts at the core, and the beam losses as functions of time. In the absence of cooling, the transverse rms emittances for both coasting (blue) and bunched (green) beams rise linearly with a time scale of 1–2 seconds, which gradually reduces the incoherent tune shift of the beam. With cooling, the rms emittances of the coasting beam (orange) continue shrinking throughout the duration of the simulation, but for the bunched beam (red), they reach a minimum at 100 ms and then start expanding. In contrast, the transverse incoherent tune shifts at the bunch core increase monotonically as a function of time, where the vertical tune shift reaches 0.1 at the end of the simulation for the bunched beam and 0.08 for the coasting beam. This is consistent with the observation of growing phase-space density at the bunch core as seen in panel (d) in Fig. 3. Panel (g) shows substantial beam loss for the bunched beam with electron cooling in a relatively short period of time, which is much less for the coasting beam and completely absent in the simulations with space charge only. Periodic resonance crossing of small-amplitude particles in the bunch may explain the formation of tails and the subsequent beam loss, but more simulations are required to verify this. We will use these simulation models to optimize our experiments at IOTA and gain insight into the observations.

BEAM PHYSICS EXPERIMENTS USING ELECTRON COOLING

Space-charge-induced periodic resonance crossing is regarded as the mechanism behind emittance growth and the loss of bunched beams, hence constraining the maximum bunch charge [37] sustainable within a given emittance growth and beam loss budget. The observed maximum limit ($|\Delta\nu_{\perp}| \sim 0.1 - 0.2$) on incoherent tune shift of accumulated beam in ion rings with electron cooling is presumably due to the same mechanism. We want to measure the maximum proton bunch charge sustainable in a storage ring with electron cooling for a given duration and a fixed loss budget. We will use the typical methods, including optimization of the working point of the bare lattice and compensation of resonance driving terms [38] using sextupoles and octupoles to minimize beam loss. Figure 4 demonstrates results from a simulated low-resolution ($\Delta Q = 0.01$) scan of bare-lattice tunes over 25 synchrotron periods using a Gaussian bunched beam with $|\Delta\nu_y| = 0.05$ injected into the IOTA lattice with no magnet errors. While the vertical rms emittance grows along $Q_x - Q_y = 1$, beam loss is only appreciable along $4Q_x = 17$. In reality, the field errors in IOTA magnets will

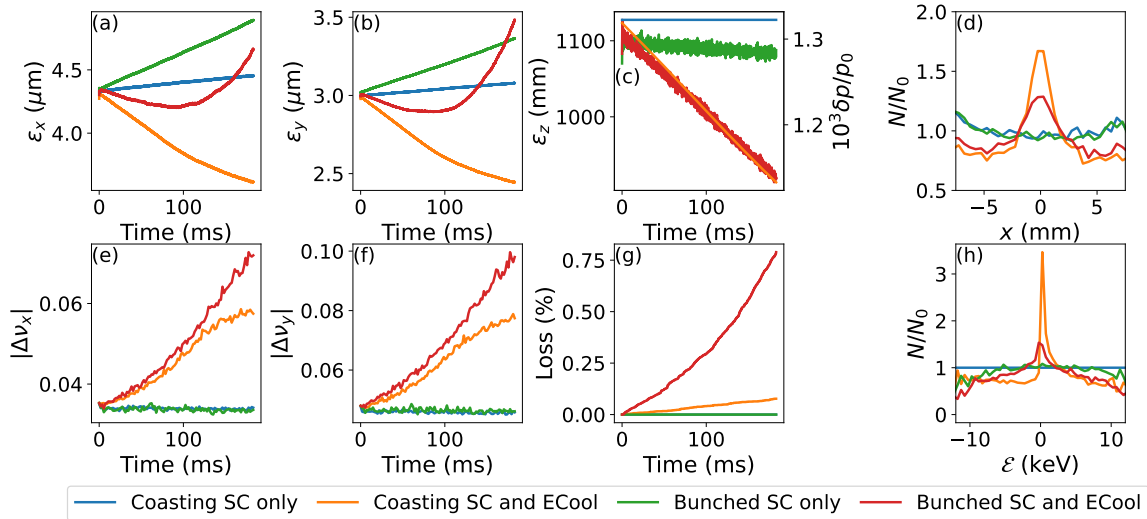


Figure 3: Evolution of beam properties in PyORBIT simulations of 2.5 MeV protons in IOTA. (a) Horizontal rms emittance. (b) Vertical rms emittance. (c) Longitudinal rms emittance. (d) Change in horizontal particle distribution $N/N_0 \equiv \{dN(t = 183 \text{ ms})/dx\} / \{dN(t = 0)/dx\}$. (e) Horizontal incoherent tune shift in the bunch core. (f) Vertical incoherent tune shift in the bunch core. (g) Percentage of beam lost. (h) Change in energy distribution $N/N_0 \equiv \{dN(t = 183 \text{ ms})/d\mathcal{E}\} / \{dN(t = 0)/d\mathcal{E}\}$. Note that the slight reduction in longitudinal emittance for the bunched beam with space-charge only (green line in panel (c)) is due to a slight mismatch of the injected distribution.

excite higher-order betatron resonances, which we will find and compensate for experimentally.

The interaction between space-charge fields within bunched beams and the wakefields originating from the vacuum chamber's structure can be understood within a parameter space where the total impedance of the ring and the incoherent tune shift, normalized to the synchrotron tune, serve as independent axes. The structure of this parameter space has been extensively explored in various theoretical models (e.g., [23–25]), all of which predict instability growth or coherent amplification in the strong space-charge regime, in line with experimental findings at the CERN SPS [39]. We propose a comprehensive study to measure the rate of instability growth and head-tail amplification. This study will be conducted as a function of variable wakefields and equilibrium tune shifts using bunched proton beams in IOTA. We will employ a digital wake-building feedback system known as the *waker* [26] to excite wakefields with arbitrary shapes and magnitudes. Subsequently, we will measure the transverse coherent oscillations as a function of longitudinal position. Concurrently, we will utilize the electron cooler to establish an equilibrium tune shift that can be maintained consistently during each observation. Such an experimental effort will enable us to compare our findings with instability models relevant to high-intensity synchrotrons and storage rings.

Mitigation techniques for coherent instabilities [40] such as TMCI include feedback systems, optics, and RF manipulations, as well as the inclusion of incoherent tune spread using chromaticity and/or dedicated non-linear focusing elements. Non-linear focusing provided by octupole magnets or Gaussian electron lenses leads to chaotic dynamics at large

amplitudes, thus increasing beam loss. The demonstration of NIO elements such as the Danilov-Nagaitsev magnets and octupole strings [21] to generate variable Landau damping while preserving stable single-particle dynamics is a fundamental goal of the Integrable Optics Test Accelerator. We can verify the preservation of the analytical invariant quantities by measuring turn-by-turn centroid positions of pencil beams kicked at variable amplitudes. Previous experiments on NIO at IOTA using electrons [9, 10] were able to collect data for a limited number of turns, as the chromatic tune spread led to the quick decoherence of the mean position signal of the bunch. Electron cooling can reduce the energy spread of protons, thus reducing the chromatic tune spread, resulting in longer turn-by-turn position datasets. Although the invariance properties of all known NIO systems are violated in the presence of non-linear space-charge forces, we can still measure the effectiveness of these elements in damping instabilities. Using electron cooling and the *waker* system, we can emulate the impedance and the space-charge tune shift of a high-energy ring and then measure the optimum non-linear focusing strength required to damp instabilities with minimum beam loss as a function of ring impedance and space-charge tune shift.

CONCLUSION

The 2.5 MeV proton program at the Integrable Optics Test Accelerator is designed to explore methods for improving the stability of hadron beams with high phase-space density and total current in synchrotrons and storage rings. The comparatively low-energy regime has the advantage of achieving transverse space-charge tune shifts close to 0.5 with almost

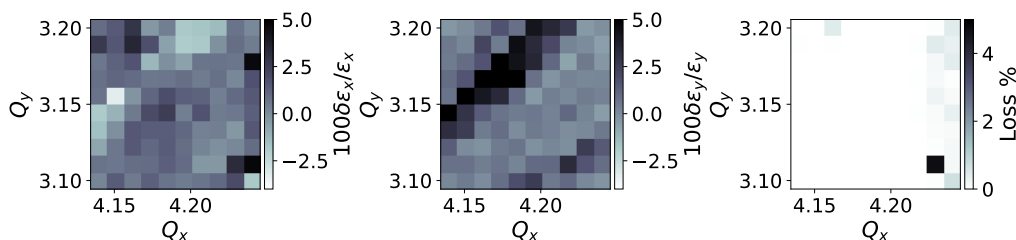


Figure 4: Simulated change of rms emittance and beam loss over 2500 turns as a function of bare-lattice tune for a bunched beam with an initial vertical space-charge tune shift of 0.05 injected into the IOTA lattice with no errors.

zero intrinsic ring impedance, providing a test bench that disentangles space-charge and intensity effects. We will use an electron cooler with cooling times adjustable between 1–10 seconds to compensate for heating mechanisms such as IBS and residual gas scattering. Cooling will enable us to maintain phase-space distributions in equilibrium, and a wake-building feedback system will allow us to generate an artificial ring impedance with arbitrary shape and magnitude. We plan to execute three broad categories of experiments: (1) Optimizing the IOTA lattice to maximize the space-charge tune shift of the circulating beam while staying within a given emittance growth and beam loss budget. (2) Measuring the dependence of coherent instability growth and head-tail amplification as a function of ring impedance and space-charge tune shift. (3) Demonstrating non-linear integrable optics to minimize instability growth and reduce beam loss in the presence of space-charge. Suitable diagnostics in the proton injector, the IOTA ring, and the electron cooler will equip us to measure beam positions, current, loss, and transverse profiles. Our ongoing work includes finalizing the design of the electron beam transport system, constructing and commissioning the proton injector with the goal of having protons in IOTA in summer 2024, and the first electron cooling in late 2025.

ACKNOWLEDGEMENT

We would like to thank A. Valishev, A. Romanov and V. Lebedev for discussions on proton operations in IOTA. R. Ainsworth and A. Burov proposed and developed the *waker* system for instability studies. This manuscript has been authored by Fermi Research Alliance, LLC under Contract No. DE-AC02-07CH11359 with the U.S. Department of Energy, Office of Science, Office of High Energy Physics. This work is also supported by the U.S. Department of Energy, Office of Science, Office of Nuclear Physics under contract DE-AC05-06OR23177. This research is also supported by the University of Chicago.

REFERENCES

- [1] J. Blazey *et al.*, “Accelerator and Beam Physics Roadmap”, DOE Accelerator Beam Physics Roadmap Workshop, 2022.
- [2] R. Garoby *et al.*, “Neutrino factory proton driver and target design”, in *Challenges and Goals for Accelerators in the XXI*

Century, World Scientific, 2016. pp. 679–697.
doi:10.1142/9789814436403_0036

- [3] J. Galambos *et al.*, “Final Design Report. Proton Power Upgrade Project”, Oak Ridge National Laboratory, Rep. ORNL/TM-2020/1570-R0, 2020.
doi:10.2172/1784163
- [4] M. Boscolo, J. P. Delahaye, and M. Palmer, “The future prospects of muon colliders and neutrino factories”, *Rev. Accel. Sci. Tech.*, vol. 10, no. 01, pp. 189–214, 2019.
doi:10.1142/9789811209604_0010
- [5] R. Ainsworth *et al.*, “Report from the Fermilab Proton Intensity Upgrade Central Design Group”, Fermi National Accelerator Laboratory, Rep. FERMILAB-FN-1229-AD-CSAID-LBNF-ND-PIP2-PPD-TD, 2023. doi:10.2172/1988511
- [6] V. Lebedev *et al.*, “The PIP-II Conceptual Design Report”, Fermi National Accelerator Laboratory, Rep. FERMILAB-DESIGN-2017-01, FERMILAB-TM-2649-AD-APC, 2017.
doi:10.2172/1346823
- [7] J. Eldred, V. Lebedev, K. Seiya, and V. Shiltsev, “Beam intensity effects in Fermilab Booster synchrotron”, *Phys. Rev. Accel. Beams*, vol. 24, p. 044001, 2021.
doi:10.1103/PhysRevAccelBeams.24.044001
- [8] S. Antipov *et al.*, “IOTA (Integrable Optics Test Accelerator): Facility and Experimental Beam Physics Program”, *JINST*, vol. 12, p. T03002, 2017.
doi:10.1088/1748-0221/12/03/t03002
- [9] A. Valishev *et al.*, “First Results of the IOTA Ring Research at Fermilab”, in *Proc. IPAC’21*, Campinas, SP, Brazil, May 2021, pp. 19–24.
doi:10.18429/JACoW-IPAC2021-MOXB02
- [10] J. Wieland *et al.*, “Improved measurements of nonlinear integrable optics at IOTA”, in *Proc. IPAC’23*, Venice, Italy, May 2023, pp. 3230–3232.
doi:10.18429/JACoW-IPAC2023-WEPL052
- [11] J. Jarvis *et al.*, “Experimental demonstration of optical stochastic cooling”, *Nature*, vol. 608, pp. 287–292, 2022.
doi:10.1038/s41586-022-04969-7
- [12] G. Stancari *et al.*, “Beam physics research with the IOTA electron lens”, *JINST* vol. 16, no. 05, p. P05002, 2021.
doi:10.1088/1748-0221/16/05/p05002
- [13] I. Lobach *et al.*, “Transverse Beam Emittance Measurement by Undulator Radiation Power Noise”, *Phys. Rev. Lett.*, vol. 126, p. 134802, 2021.
doi:10.1103/PhysRevLett.126.134802

- [14] A. Romanov *et al.*, “Experimental 3-dimensional tracking of the dynamics of a single electron in the Fermilab Integrable Optics Test Accelerator (IOTA)”, *JINST*, vol. 16, p. P12009, 2021. doi:10.1088/1748-0221/16/12/P12009
- [15] I. Hofmann and O. Boine-Frankenheim, “Space-Charge Structural Instabilities and Resonances in High-Intensity Beams”, *Phys. Rev. Lett.*, vol. 115, p. 204802, 2015. doi:10.1103/PhysRevLett.115.204802
- [16] G. Franchetti, I. Hofmann, M. Giovannozzi, M. Martini, and E. Metral, “Space charge and octupole driven resonance trapping observed at the CERN Proton Synchrotron”, *Phys. Rev. ST Accel. Beams*, vol. 6, p. 124201, 2003. doi:10.1103/PhysRevSTAB.6.124201
- [17] S. Nagaitsev *et al.*, “Space Charge Effects and Intensity Limits of Electron-Cooled Bunched Beams”, in *Proc. PAC’95*, Dallas, TX, USA, May 1995, paper RAP22, pp. 2937–2939.
- [18] M. Steck *et al.*, “Beam accumulation with the SIS electron cooler”, *Nucl. Instrum. Meth. A*, vol. 441, pp. 175–182, 2000. doi:10.1016/S0168-9002(99)01130-4
- [19] S. A. Antipov *et al.*, “Proof-of-Principle Direct Measurement of Landau Damping Strength at the Large Hadron Collider with an Antidamper”, *Phys. Rev. Lett.*, vol. 126, p. 164801, 2021. doi:10.1103/PhysRevLett.126.164801
- [20] V. Shiltsev, Y. Alexahin, A. Burov, and A. Valishev, “Landau Damping of Beam Instabilities by Electron Lenses”, *Phys. Rev. Lett.*, vol. 119, p. 134802, 2017. doi:10.1103/PhysRevLett.119.134802
- [21] V. Danilov and S. Nagaitsev, “Nonlinear accelerator lattices with one and two analytic invariants”, *Phys. Rev. ST Accel. Beams*, vol. 13, p. 084002, 2010. doi:10.1103/PhysRevSTAB.13.084002
- [22] V. V. Danilov and E. A. Perevedentsev, “Two examples of integrable systems with round colliding beams”, in *Proc. PAC’97*, Vancouver, B.C., Canada, May 1997, paper 8V001, pp. 1759–1761.
- [23] A. Burov, “Convective Instabilities of Bunched Beams with Space Charge”, *Phys. Rev. Accel. Beams*, vol. 22, no.3, p. 034202, 2019. doi:10.1103/PhysRevAccelBeams.22.034202
- [24] A. Burov, “Core-Halo Collective Instabilities”, Fermi National Accelerator Laboratory, Rep. FERMILAB-PUB-18-420-AD-APC, 2018. doi:10.48550/arXiv.1808.08498
- [25] X. Buffat, E. Métral, E. Gottlob, C. Høgh, A. Oeftiger, and T. Pieloni, “Description of beam instabilities in synchrotrons with wakefields and space charge forces using the circulant matrix model”, *Phys. Rev. Accel. Beams*, vol. 24, p. 060101, 2021. doi:10.1103/PhysRevAccelBeams.24.060101
- [26] R. Ainsworth, A. V. Burov, N. Eddy, and A. Semenov, “A Dedicated Wake-Building Feedback System to Study Single Bunch Instabilities in the Presence of Strong Space Charge”, in *Proc. HB’21*, Batavia, IL, USA, Oct. 2021, pp. 135–139. doi:10.18429/JACoW-HB2021-MOP22
- [27] D. M. Asner *et al.* (Project 8 Collaboration), “Single-Electron Detection and Spectroscopy via Relativistic Cyclotron Radiation”, *Phys. Rev. Lett.*, vol. 114, p. 162501, 2015. doi:10.1103/PhysRevLett.114.162501
- [28] C. Habfast, “Microwave diagnostics at the LEAR electron cooler”, Ph.D. Thesis, Karlsruhe University, KFK-4188, 1987.
- [29] D. Edstrom *et al.*, “IOTA Proton Injector Beamline Installation”, in *Proc. IPAC’23*, Venice, Italy, May 2023, pp. 1737–1739. doi:10.18429/JACoW-IPAC2023-TUPA183
- [30] G. M. Bruhaug and K. Carlson, “The Design and Construction of a Resonance Control System for the IOTA RF Cavity”, in *Proc. NAPAC2016*, Chicago, IL, USA, Oct. 2016, paper TUPOA74, pp. 432–434. doi:10.18429/JACoW-NAPAC2016-TUPOA74
- [31] N. Banerjee *et al.*, “Incoherent dynamics of intense proton beams under electron cooling”, in *Proc. IPAC’23*, Venice, Italy, May 2023, pp. 2237–2240. doi:10.18429/JACoW-IPAC2023-TUPM026
- [32] H. Zhang, S. V. Benson, M. W. Bruker, and Y. Zhang, “JSPEC - A Simulation Program for IBS and Electron Cooling”, in *Proc. IPAC’21*, Campinas, Brazil, May 2021, pp. 49–52. doi:10.18429/JACoW-IPAC2021-MOPAB004
- [33] V. V. Parkhomchuk, “New insights in the theory of electron cooling”, *Nucl. Instrum. Meth. A*, vol. 441, pp. 9–17, 2000. doi:10.1016/S0168-9002(99)01100-6
- [34] M. Bossard *et al.*, “Thermionic sources for electron cooling at IOTA”, in *Proc. IPAC’23*, Venice, Italy, May 2023, pp. 646–649. doi:10.18429/JACoW-IPAC2023-MOPL046
- [35] A. Shishlo, S. Cousineau, J. Holmes, T. Gorlov, “The Particle Accelerator Simulation Code PyORBIT”, *Procedia Computer Science* vol. 51, pp. 1272–1281, 2015. doi:10.1016/j.procs.2015.05.312
- [36] N. Banerjee *et al.*, “Electron Cooling With Space-Charge Dominated Proton Beams at IOTA”, in *Proc. COOL’21*, Novosibirsk, Russia, Nov. 2021, pp. 14–19. doi:10.18429/JACoW-COOL2021-S201
- [37] A. Oeftiger *et al.*, “Simulation study of the space charge limit in heavy-ion synchrotrons”, *Phys. Rev. Accel. Beams*, vol. 25, p. 054402, 2022. doi:10.1103/PhysRevAccelBeams.25.054402
- [38] F. Asvesta *et al.*, “High Intensity Studies in the CERN Proton Synchrotron Booster”, in *Proc. IPAC’22*, Bangkok, Thailand, Jun. 2022, pp. 2056–2059. doi:10.18429/JACoW-IPAC2022-WEPOTK011
- [39] H. Bartosik, “Beam dynamics and optics studies for the LHC injectors upgrade”, Ph.D. Thesis, TU Vienna, CERN-THESIS-2013-257, 2013.
- [40] E. Métral, “General mitigation techniques for coherent beam instabilities in particle accelerators”, *Eur. Phys. J. Plus*, vol. 137, no. 1, p. 47, 2022. doi:10.1140/epjp/s13360-021-02264-4

14th Int. Workshop Beam Cooling Relat. Top.
ISBN: 978-3-95450-245-5

COOL2023, Montreux, Switzerland
ISSN: 2226-0374

JACoW Publishing
doi:10.18429/JACoW-COOL2023

List of Authors

Bold papercodes indicate primary authors; ~~strike through/black~~ papercodes indicate **no submission received**

– A –			
Accettura, C.	MOPPM1R3	Du, Z.	TUPPM1R2
Ady, M.	TUPAM2R1	Duncan, M.K.	FRPAM1R3
Andelkovic, Z.	WEPAM2R2 , FRPAM1R1	Dunham, B.M.	THPOSRP17
Andreazza, W.	MOPPM1R3	Dupuy, B.	THPOSRP22
Asvesta, F.	THPAM1R3	– E –	
Aulenbacher, K.	THPAM1R2 , THPOSRP13	Eichhorn, R.G.	THPOSRP17
– B –		Eizenhöfer, N.	TUPPM2R3
Banerjee, N.	FRPAM1R3	– F –	
Bastos, W.B.	THPOSRP22	Fedotov, A.V.	MOPAM2R1 , TUPAM1R2 , WEPAM1R1 , THPAM2R2 , THPOSRP01 , THPOSRP04 , THPOSRP17
Beiser, Th.	THPAM1R2 , THPOSRP13	Fedotova, S.	WEPAM2R2 , FRPAM1R1
Benson, S.V.	MOPPM1R1 , THPOSRP14 , THPOSRP17	Ferreira Somoza, J.A.	MOPPM1R3
Bergan, W.F.	THPOSRP17	Forck, P.	TUPAM2R1
Böhm, R.M.	THPOSRP20	Franchetti, G.	THPOSRP02
Bojtár, L.	TUPAM1R3	Frassier, A.	MOPPM1R3 , THPOSRP06
Bollazzi, A.	MOPPM1R3	– G –	
Bozyk, L.H.J.	TUPPM2R3	Galante, B.	THPOSRP10
Brandt, J.A.	FRPAM1R3	Gamba, D.	MOPPM1R3 , THPAM1R3 , THPOSRP02 , THPOSRP22
Breitkreutz, B.	THPOSRP23	Ganesh, A.	TUPAM2R1
Britten, V.A.	THPOSRP03	Geithner, W.	WEPAM2R2 , FRPAM1R1
Bruker, M.W.	THPOSRP14	Greven, R.	THPOSRP23
Brutus, J.C.	TUPAM1R1 , TUPAM2R2 , WEPAM1R2	Guillot-Vignot, F.	TUPAM2R1
Bryzgunov, M.I.	FRPAM1R2	Gulliford, C.M.	THPOSRP17
Bubley, A.V.	FRPAM1R2	Gumm, J.	TUPPM2R2
Burger, S.	TUPAM2R1	Guo, J.	MOPPM1R1
Bussmann, M.H.	TUPPM2R1 , TUPPM2R2 , TUPPM2R3 , THPOSRP19	– H –	
Butenko, A.V.	FRPAM1R2	Hall, C.C.	TUPPM1R3
– C –		Hannen, V.	TUPPM2R2 , TUPPM2R3
Caspers, F.	THPOSRP22	Heber, O.	WEPAM2R1
Cenede, J.	MOPPM1R3 , TUPAM2R1 , THPOSRP06 , THPOSRP10	Herfurth, F.	WEPAM2R2 , FRPAM1R1
Chan, D.	WEPAM1R2	Hess, R.	MOPAM2R2 , WEPAM2R2 , FRPAM1R1
Chen, D.Y.	TUPPM2R1 , TUPPM2R3 , THPOSRP19	Höfle, W.	THPOSRP22
Chritin, N.S.	MOPPM1R3	Horst, M.	TUPPM2R3 , WEPAM2R2
Churchman, A.R.	TUPAM2R1	Huang, Z.	TUPPM2R1 , TUPPM2R3 , THPOSRP19
Coiffet, T.	TUPAM2R1	Hulsart, R.L.	WEPAM1R2
Conway, J.V.	THPOSRP17	– I –	
Coutron, Y.C.	MOPPM1R3	Ilardo, M.	WEPAM1R2
Curcio, A.J.	WEPAM1R2	Inacker, P.	TUPAM1R1 , TUPAM2R2 , WEPAM1R2
– D –		– J –	
Decker, K.	WEPAM1R2	Jing, Y.C.	TUPAM1R1 , TUPAM2R2 , WEPAM1R2 , THPAM2R1 , THPAM2R2
Degen, C.M.	TUPAM2R2	Jørgensen, L.V.	MOPPM1R3 , WEPAM1R3
Deitrick, K.E.	THPOSRP17	Joseph, R.	MOPAM2R2
DeSanto, L.	WEPAM1R2	– K –	
Devauchelle, W.	TUPAM2R1	Kayran, D.	MOPAM2R1 , TUPAM1R2 , WEPAM1R2 , THPAM2R2 , THPOSRP01 , THPOSRP17
Dhital, B.	MOPPM1R1	Kewisch, J.	WEPAM1R1
Di Lieto, A.	WEPAM1R2	Khatri, G.	MOPPM1R3 , THPOSRP06
Dietrich, J.	THPAM1R2 , THPOSRP13		
Dimopoulou, C.	THPOSRP20 , FRPAM1R1		
Drees, K.A.	WEPAM1R2		

Content from this work may be used under the terms of the CC-BY-4.0 licence (© 2023). Any distribution of this work must maintain attribution to the author(s), title of the work, publisher, and DOI

Kiefer, D.	TUPPM2R1, THPOSRP19	Parkhomchuk, V.V.	FRPAM1R2
Kiefer, N.	TUPPM2R3	Pekrul, W.E.	WEPAM1R2
Kim, Y.K.	FRPAM1R3	Perini, D.	TUPAM2R1
Klag, W.	THPAM1R2	Peschke, C.	MOPAM2R2, THPOSRP20
Klammes, S.	TUPPM2R1, TUPPM2R2, TUPPM2R3, THPOSRP19	Petrushina, I.	TUPAM1R1, TUPAM2R2, WEPAM1R2, THPAM2R2
Kolehmainen, A.J.	TUPAM2R1	Pikin, A.I.	MOPPM1R3
Kononov, A.	THPOSRP07	Pinayev, I.	TUPAM1R1, TUPAM2R2, WEPAM1R2, THPAM2R2
Kostroun, V.O.	THPOSRP17	Podlech, H.	THPOSRP03
Krafft, G.A.	MOPPM1R1	Ponce, L.	MOPPM1R3, THPAM1R3
Krantz, C.	WEPAM2R2, FRPAM1R1	Prokopjehev, Yu.	FRPAM1R2
Kruyt, P.M.	THPAM1R3, THPOSRP02	– R –	
Kühl, T.	TUPPM2R2, TUPPM2R3	Rausch, S.	WEPAM2R2
– L –		Reiter, A.	WEPAM2R2, FRPAM1R1
Langfeld, B.	TUPPM2R2, TUPPM2R3	Reva, V.B.	FRPAM1R2
Lebedev, V.A.	FRPAM1R2	Rey, S.F.	THPOSRP22
Lestinsky, M.	WEPAM2R2, FRPAM1R1	Ringle, R.J.	WEPAM2R1
Lin, F.	MOPPM1R1	Rogers, C.T.	THPOSRP18
Litvinenko, V.	TUPAM1R1, TUPAM2R2, THPAM2R1, THPAM2R2, WEPAM1R2	Roßbach, J.	MOPAM2R2, WEPAM2R2, FRPAM1R1
Litvinov, S.A.	MOPAM2R2	Rossi, A.	MOPPM1R3, TUPAM2R1
Löser, M.	TUPPM2R1, THPOSRP19	Russo, G.	THPAM1R3
Lorentz, B.	MOPAM2R2	– S –	
Louwerse, R.	THPOSRP22	Sadovich, S.	TUPAM2R1
– M –		Sahin, Y.E.	TUPAM2R1
Ma, F.	THPAM1R1	Sameed, M.	MOPPM1R3, TUPAM2R1
Ma, J.	TUPAM1R1, TUPAM2R2, WEPAM1R2, THPAM2R1, THPAM2R2	Sanchez Alarcon, R.M.	TUPPM2R3, FRPAM1R1
Ma, L.Y.	TUPPM1R2	Sangroula, M.P.	WEPAM1R2
Ma, X.	TUPPM2R1, TUPPM2R3, THPOSRP19	Schempp, A.	THPOSRP03
Machado, C.	MOPPM1R3	Schneider, G.	TUPAM2R1
Mahler, G.J.	WEPAM1R2	Schneider, H.	THPOSRP23
Mao, L.J.	TUPPM2R1, THPAM1R1, THPOSRP19	Schramm, U.	TUPPM2R2, TUPPM2R3, TUPPM2R1, THPOSRP19
Marqvorsen, O.	MOPPM1R3	Sedláček, O.	TUPAM2R1
Mayes, C.E.	THPOSRP17	Seletskiy, S.	MOPAM2R1, TUPAM1R2, WEPAM1R1, WEPAM1R2, THPAM2R2, THPOSRP04
Mazzoni, S.	TUPAM2R1	Semenov, S.V.	FRPAM1R2
Menz, E.	FRPAM1R1	Sequeiro, C.C.	MOPPM1R3, TUPAM2R1
Meshkov, I.N.	FRPAM1R2	Sergeev, A.S.	FRPAM1R2
Meusel, O.	THPOSRP03	Severino, F.	WEPAM1R2
Michnoff, R.J.	TUPAM2R2, WEPAM1R2	Sharma, D.	WEPAM2R1
Mohr, K.	FRPAM1R1	Shih, K.	TUPAM2R2, WEPAM1R2, THPAM2R2
Morozov, V.S.	MOPPM1R1	Shpakov, V.	FRPAM1R2
– N –		Shurkhno, N.	THPOSRP07, THPOSRP21
Nagaitsev, S.	FRPAM1R3	Sidorowski, K.	TUPAM2R1
Narayan, G.	WEPAM1R2	Siebold, M.	TUPPM2R1, TUPPM2R2, TUPPM2R3, THPOSRP19
Nguyen, L.K.	WEPAM1R2	Sinturel, A.	MOPPM1R3
Nörtershäuser, W.	TUPPM2R3, WEPAM2R2, FRPAM1R1	Skaritka, J.	WEPAM1R2
Nörtershäuser, W.	TUPPM2R3	Smart, L.	WEPAM1R2
Novotny, O.	MOPPM1R2	Smolenski, K.W.	THPOSRP17
– O –		Sorrell, Z.	WEPAM1R2
Osipov, K.G.	FRPAM1R2	Spiller, P.J.	TUPPM2R2, TUPPM2R3
– P –		Stallkamp, N.S.	WEPAM2R2
Panasyuk, V.M.	FRPAM1R2	Stancari, G.	FRPAM1R3
Paniccia, M.C.	WEPAM1R2	Stassen, R.	THPOSRP07, THPOSRP23

Steck, M.	MOPAM2R2 , TUPPM2R3	Weiss, D.	WEPAM1R2
Stöhlker, T.	TUPPM2R2, TUPPM2R3	Welker, E.-S.	THPOSRP10
Stringer, O.	TUPAM2R1	Welsch, C.P.	TUPAM2R1
Sukhanov, A.	WEPAM1R2	Wen, W.Q.	TUPPM2R1, TUPPM2R3, THPOSRP19
Syresin, E.	FRPAM1R2	Wendt, M.	TUPAM2R1
– T –		Winters, D.F.A.	TUPPM2R1, TUPPM2R2 , TUPPM2R3, THPOSRP19
Tang, M.T.	THPAM1R1	Wolters, J.	THPOSRP23
Taylor, N.W.	THPOSRP17	Wu, J.X.	TUPPM1R2, TUPPM2R1, THPOSRP19
Than, R.	WEPAM1R2	Wunderlich, S.	MOPAM2R2, THPOSRP20
Thurel, Y.	MOPPM1R3	– X –	
Timonin, R.V.	FRPAM1R2	Xu, D.	THPOSRP17
Todorcevic, T.	MOPPM1R3	– Y –	
Toscan du Plantier, M.	TUPAM2R1	Yang, J.C.	TUPPM2R1, THPAM1R1, THPOSRP18, THPOSRP19
Tranquille, G.	MOPAM1R1 , MOPPM1R3, THDMR1 , THPOSRP06, THPOSRP09 , THPOSRP10	Yang, X.D.	THPAM1R1, THPOSRP15
Trotsenko, S.	WEPAM2R2	Yin, J.	TUPPM1R2
Trubnikov, G.V.	FRPAM1R2	Yuan, Y.J.	TUPPM2R1, THPOSRP19
– U –		– Z –	
Udrea, S.	TUPAM2R1	Zajfman, D.	WEPAM2R1
Ueberholz, K.	TUPPM2R2, TUPPM2R3	Zaltsman, A.	WEPAM1R2
– V –		Zhang, C.	THPOSRP20
Veness, R.	TUPAM2R1	Zhang, D.	TUPPM2R1, THPOSRP19
von Freeden, L.	MOPPM1R3	Zhang, H.	MOPPM1R1, THPOSRP14
Vorobyev, G.	WEPAM2R2, FRPAM1R1	Zhang, H.D.	TUPAM2R1
– W –		Zhang, S.F.	TUPPM2R1, THPOSRP19
Walther, T.	TUPPM2R2, TUPPM2R3, TUPPM2R1, THPOSRP19	Zhang, Y.	MOPPM1R1, THPOSRP14
Wang, E.	THPOSRP17	Zhao, H.	THPAM1R1 , THPOSRP18
Wang, G.	TUPAM1R1, TUPAM2R2, WEPAM1R2, THPAM2R1 , THPAM2R2, THPOSRP01	Zholents, A.A.	TUPPM1R1 , TUPPM1R3
Wang, H.B.	TUPPM2R1 , TUPPM2R3, THPOSRP19	Zhou, B.	WEPAM2R2
Wang, N.	THPOSRP17	Zhu, G.	TUPPM1R2
		Zhu, R.H.	THPOSRP18

Institutes List

ANL

Lemont, Illinois, USA
• [Zholents, A.A.](#)

BINP SB RAS

Novosibirsk, Russia
• [Bryzgunov, M.I.](#)
• [Bubley, A.V.](#)
• [Panasyuk, V.M.](#)
• [Parkhomchuk, V.V.](#)
• [Reva, V.B.](#)

BNL

Upton, New York, USA
• [Bergan, W.F.](#)
• [Brutus, J.C.](#)
• [Chan, D.](#)
• [Curcio, A.J.](#)
• [Decker, K.](#)
• [Degen, C.M.](#)
• [DeSanto, L.](#)
• [Dhital, B.](#)
• [Di Lieto, A.](#)
• [Drees, K.A.](#)
• [Fedotov, A.V.](#)
• [Hulsart, R.L.](#)
• [Ilardo, M.](#)
• [Inacker, P.](#)
• [Jing, Y.C.](#)
• [Kayran, D.](#)
• [Kewisch, J.](#)
• [Litvinenko, V.](#)
• [Ma, J.](#)
• [Mahler, G.J.](#)
• [Michnoff, R.J.](#)
• [Narayan, G.](#)
• [Nguyen, L.K.](#)
• [Paniccia, M.C.](#)
• [Pekrul, W.E.](#)
• [Petrushina, I.](#)
• [Pinayev, I.](#)
• [Sangroula, M.P.](#)
• [Seletskiy, S.](#)
• [Severino, F.](#)
• [Shih, K.](#)
• [Skaritka, J.](#)
• [Smart, L.](#)
• [Sorrrell, Z.](#)
• [Sukhanov, A.](#)
• [Than, R.](#)
• [Wang, E.](#)
• [Wang, G.](#)
• [Weiss, D.](#)
• [Xu, D.](#)
• [Zaltsman, A.](#)

CASUS

Görlitz, Germany
• [Bussmann, M.H.](#)

CERN

Meyrin, Switzerland
• [Accettura, C.](#)
• [Ady, M.](#)
• [Andreazza, W.](#)
• [Asvesta, F.](#)
• [Bastos, W.B.](#)
• [Bojtár, L.](#)
• [Bollazzi, A.](#)
• [Burger, S.](#)
• [Caspers, F.](#)
• [Cenede, J.](#)
• [Chritin, N.S.](#)
• [Churchman, A.R.](#)
• [Coiffet, T.](#)
• [Coutron, Y.C.](#)
• [Devauchelle, W.](#)
• [Dupuy, B.](#)
• [Ferreira Somoza, J.A.](#)
• [Frassier, A.](#)
• [Galante, B.](#)
• [Gamba, D.](#)
• [Ganesh, A.](#)
• [Guillot-Vignot, F.](#)
• [Höfle, W.](#)
• [Jørgensen, L.V.](#)
• [Khatri, G.](#)
• [Kolehmainen, A.J.](#)
• [Kruyt, P.M.](#)
• [Louwerse, R.](#)
• [Machado, C.](#)
• [Marquersen, O.](#)
• [Mazzoni, S.](#)
• [Perini, D.](#)
• [Pikin, A.I.](#)
• [Ponce, L.](#)
• [Rey, S.F.](#)
• [Rossi, A.](#)
• [Russo, G.](#)
• [Sadovich, S.](#)
• [Sahin, Y.E.](#)
• [Sameed, M.](#)
• [Schneider, G.](#)
• [Sedláček, O.](#)
• [Sequeiro, C.C.](#)
• [Sidorowski, K.](#)
• [Sinturel, A.](#)
• [Thurel, Y.](#)
• [Todorčević, T.](#)
• [Toscan du Plantier, M.](#)
• [Tranquille, G.](#)
• [Veness, R.](#)
• [von Freedom, L.](#)
• [Welker, E.-S.](#)
• [Wendt, M.](#)

Cockcroft Institute

Warrington, Cheshire, United Kingdom
• [Sedláček, O.](#)

- Stringer, O.
- Zhang, H.D.

Cornell University
Ithaca, New York, USA

- Wang, N.

Enrico Fermi Institute, University of Chicago
Chicago, Illinois, USA

- Brandt, J.A.

Fermilab
Batavia, Illinois, USA

- Banerjee, N.
- Lebedev, V.A.
- Stancari, G.

FRIB
East Lansing, Michigan, USA

- Ringle, R.J.

FZJ
Jülich, Germany

- Greven, R.
- Schneider, H.
- Stassen, R.
- Wolters, J.

GSI
Darmstadt, Germany

- Andelkovic, Z.
- Bozyk, L.H.J.
- Breitschütz, B.
- Böhm, R.M.
- Dimopoulou, C.
- Fedotova, S.
- Forck, P.
- Franchetti, G.
- Geithner, W.
- Herfurth, F.
- Hess, R.
- Joseph, R.
- Klammes, S.
- Kononov, A.
- Krantz, C.
- Kühl, T.
- Lestinsky, M.
- Litvinov, S.A.
- Lorentz, B.
- Menz, E.
- Mohr, K.
- Nörtershäuser, W.
- Peschke, C.
- Reiter, A.
- Roßbach, J.
- Sanchez Alarcon, R.M.
- Shurkhno, N.
- Spiller, P.J.
- Steck, M.
- Stöhlker, T.
- Trotsenko, S.
- Udrea, S.
- Vorobyev, G.

- Winters, D.F.A.
- Wunderlich, S.
- Zhang, C.
- Zhou, B.

HFHF
Frankfurt am Main, Germany

- Nörtershäuser, W.
- Walther, T.

HJ
Jena, Germany

- Stöhlker, T.

HIM
Mainz, Germany

- Aulenbacher, K.
- Beiser, Th.
- Dietrich, J.
- Klag, W.

HZDR
Dresden, Germany

- Bussmann, M.H.
- Löser, M.
- Schramm, U.
- Siebold, M.

IAP
Frankfurt am Main, Germany

- Britten, V.A.
- Meusel, O.
- Podlech, H.
- Schempp, A.

IKF
Frankfurt am Main, Germany

- Stallkamp, N.S.

IMP/CAS
Lanzhou, People's Republic of China

- Chen, D.Y.
- Du, Z.
- Huang, Z.
- Ma, F.
- Ma, X.
- Mao, L.J.
- Tang, M.T.
- Wang, H.B.
- Wen, W.Q.
- Wu, J.X.
- Yang, J.C.
- Yang, X.D.
- Yin, J.
- Yuan, Y.J.
- Zhang, S.F.
- Zhao, H.
- Zhu, G.
- Zhu, R.H.

IOQ
Jena, Germany

- Stöhlker, T.

JINR

Dubna, Moscow Region, Russia

- Butenko, A.V.
- Meshkov, I.N.
- Prokopjechev, Yu.
- Semenov, S.V.
- Sergeev, A.S.
- Syresin, E.
- Timonin, R.V.
- Trubnikov, G.V.

JINR/VBLHEP

Dubna, Moscow region, Russia

- Osipov, K.G.
- Shpakov, V.

JLab

Newport News, Virginia, USA

- Benson, S.V.
- Bruker, M.W.
- Deitrick, K.E.
- Guo, J.
- Krafft, G.A.
- Nagaitsev, S.
- Zhang, H.
- Zhang, Y.

MPI-K

Heidelberg, Germany

- Novotny, O.

NWNU

Lanzhou, Gansu, People's Republic of China

- Ma, L.Y.

ORNL RAD

Oak Ridge, Tennessee, USA

- Lin, F.
- Morozov, V.S.

RadiaSoft LLC

Boulder, Colorado, USA

- Hall, C.C.

SBU

Stony Brook, New York, USA

- Shih, K.

STFC/RAL/ISIS

Chilton, Didcot, Oxon, United Kingdom

- Rogers, C.T.

Stony Brook University

Stony Brook, USA

- Litvinenko, V.

SUNY SB

Stony Brook, New York, USA

- Petrushina, I.

Technische Universität Dresden

Dresden, Germany

- Schramm, U.

The University of Liverpool

Liverpool, United Kingdom

- Sedláček, O.
- Stringer, O.
- Welsch, C.P.
- Zhang, H.D.

TU Darmstadt

Darmstadt, Germany

- Eizenhöfer, N.
- Gumm, J.
- Horst, M.
- Kiefer, D.
- Langfeld, B.
- Mohr, K.
- Nörtershäuser, W.
- Rausch, S.
- Walther, T.

TU Dresden

Dresden, Germany

- Schramm, U.

University of Chicago

Chicago, Illinois, USA

- Duncan, M.K.
- Kim, Y.K.

Universität Kassel

Kassel, Germany

- Kiefer, N.

Weizmann Institute of Science, Physics

Rehovot, Israel

- Heber, O.
- Sharma, D.
- Zajfman, D.

Westfälische Wilhelms-Universität Münster, Institut für Kernphysik

Münster, Germany

- Hannen, V.
- Ueberholz, K.

Xelera Research LLC

Ithaca, New York, USA

- Conway, J.V.
- Dunham, B.M.
- Eichhorn, R.G.
- Gulliford, C.M.
- Kostroun, V.O.
- Mayes, C.E.
- Smolenski, K.W.
- Taylor, N.W.

Xidian University

Xi'an, People's Republic of China

- Zhang, D.